



**Jain Institute of Technology, Davangere**  
(Affiliated to VTU, Belagavi)

**3.3.1: Number of Research Papers published in the Journals as notified  
on UGC Care List during AY 2019-20**



1. Performance of Building using Fluid Viscous Dampers and Shear Wall
2. Degree-based topological indices on anticancer drugs with QSPR analysis
3. Predicting physico-chemical properties of octane isomers using QSPR approach
4. Priority Assessment of Fine Aggregates for Satisfying Compressive Strength as Per IRC 44-2017 Guidelines
5. COD And Colour Removal From Distillery Spent Wash Using Metal Oxide Electrode In Electrocoagulation Process
6. A Review Paper on various control techniques for Induction Motor Drives
7. Medical Robots & its Applications in the Current Health Sector
8. Electrochemical Behavior of 1,3-bis(1-Phenylethyl) Urea as a Corrosion Inhibitor for Carbon Steel in 1 M HCl
9. Synthesis, Characterization, and Anti-corrosion Behavior of Novel Mono Azo Dyes Derived from 4,5,6,7-Tetrahydro-1,3-benzothiazole for Mild Steel in Acid Solution
10. Dakshayani Indices on Carbon and Boron Nitride Nanotubes
11. Generalized Reciprocal Sanskruti Index: Chemical Applicability and Bounds
12. Frequency dependence of AC conductivity and dielectric properties evaluation of in-situ prepared polyaniline/manganese dioxide composite
13. A comparison of features for multilingual speaker identification-A review and some experimental results
14. Hybrid location-centric e-Commerce recommendation model using dynamic behavioral traits of customer
15. Implementation of Ant-Lion Optimization Algorithm in Energy Management Problem and Comparison
16. A Research of Noise Estimation and Removal Techniques for Speech Signal
17. Improved Alpha blending algorithm for the Authentication of Medical images using LWT & QR Code
18. Comparative Study of Cutting Force Development During the Machining Of Un-Hybridized and Hybridized ZA43 Based Metal Matrix Composites
19. Investigation and study of mechanical properties of areca shell fiber and palm powder natural composites

# PERFORMNCE OF BUILDING USING FLUID VISCOUS DAMPERS AND SHEAR WALL

Namrata S Naragundkar<sup>1</sup>, Dr. H. Eramma<sup>2</sup>

P.G Student Dept. of Studies in Civil Engineering, University of B.D.T College of Engineering, Karnataka ,India.

<sup>2</sup>Professor, Dept. of Studies in Civil Engineering, University of B.D.T College of Engineering, Karnataka ,India.

\*\*\*

**Abstract** - Earthquake is one of the most terrifying and damaging phenomena of nature the after effects are terrible, during an earthquake, an abundance quantity of energy is pumped into the structure. The damage degree of the structure is determined by the way that this energy is consumed. The main purpose of a structural design is based on guaranteeing the safety and functionality of the designed buildings, in order to avoid collapse by allowing the structural elements to take and dissipate energy

The current study focused on the seismic response of high rise RC structures along with structural systems bordering on shear wall and fluid viscous dampers at various location. The building is analyzed, accordance with Indian standard code IS 1983(Part1) 2002, seismic zone V and medium soil. Equivalent static method and Response Spectrum has been employed for each model, ETABS software is used to examine the effect of structural systems on seismic parameters. From the results it's concluded that building with shear wall at core and dampers at edge have time period of 54%. Lateral displacement of 38% in x direction and 40% in y direction story drift of 48.4% .Hence shear wall at core and dampers located at edges can be used in RC multi-story buildings to reduce the response effectively

**Key Words:** ETABS, lateral load, dissipate energy, structural systems, Response spectrum, story drift, story displacement, dampers, Fluid viscous damper etc.

## 1. INTRODUCTION

India is developing country with a population of 1,380,004,385 (nearly 139 crores) according 2020 census. This rapid increase in population and low land availability have forced engineers to go for high rise building even in high seismicity zones.

Tall buildings are exposed to vibrations caused by seismic activity and wind speed due these forces huge displacement and moments are generated which lead to ultimate failure of in structure. The adobe and time of occurrence of earthquake are unpredictable, this categories them as ruin natural phenomenon.

Earth wavering caused by tectonic plates induce flouting and evolution which swifts energy rapidly discharge inside earth. During earthquake abundance amount of energy is pumped to structures,

which forces the structure to sway. The extreme force produced through the earthquake is determined by extent of damage in he uilding The intensity Of damage of structures can be reduce to by adopting various structural systems like Shear walls, dampers, bracing, etc which are usually used to oppose forces.

Dampers are the devices or any materials which are employed to absorb vibrations. Seismic dampers are mainly designed to dissipate these vibration so as to reduce the response of structures. The RC shear walls are relatively rigid in their individual plane. These transmit vibration throughout body to resist the failure.

## 1.1 Fluid Viscous Dampers

The function of this device follows principle based on flow of fluid through orifices; in a various structural applications these instruments are mounted. To withstand pressure of seismic and improve response of structure generally passive energy dissipation device is used.

Damping force is produced by flow of fluid which shifts from one case to the other case within cylinder as piston slip during earthquake. Therefore mechanical energy is transformed to thermal causing expansion and contraction of fluid. Generally highly viscous fluid like a compound of silicone or a similar kind of oil is filled in cylinder of a piston head along with orifices. While the damper undergoes compressive force it reduces the volume of fluid in cylinder due to motion of piston rod.

Viscous dampers deliver a force which can always resists the structure motion. This force stays directly proportional to relative velocity bet ween ends of damper. The damping equation stands as follows:

$$F = C|\dot{u}|\alpha \text{sgn}(\dot{u}) = CV\alpha$$

Where:

- F: amping force
- C: coefficient of amping
- V: velocity
- $\alpha$ : Damping exponent that can range from 0.01 to 1.00. (Linear behaviour equal to 1.00).

## 1.2 Shear wall

Shear walls are vertically positioned supports additionally to slabs, beams and columns, capable of resisting the lateral loads. They start at the beginning of foundation and runs from end to end of the structure. The thickness of the shear walls of size in the range of 150mm to 400mm depending on vertical elevation of the structure. RCC shear wall has high in plane stiffness, at the same time resist massive horizontal masses and support gravity masses in the direction of orientation of the walls, thereby serving merits in most of the engineering Structural applications and reducing the risk of damage in structure. Shear walls in addition gives a lateral stiffness to avoid the roof or floor on top commencing excessive side-sway.

## 2. OBJECTIVES

- To analyse the high rise buildings for seismic response, with and without FVD and shear wall.
- To study the variations in time period for different structures with combination of shear wall and FVD.
- To determine the optimum location for shear wall for a building.
- To determine displacements, storey drift, base shear variations in the structure due to introduction of FVD and shear wall.

## 3. METHODOLOGY

The forces and response of structures during seismic excitations analysed by employing response spectrum method. Analysis of the response spectrum (RSA) is an approach mainly used for design of buildings. Conceptually this method is an alternate form of modal analysis, i.e. Response History Analysis (RHA) by modal decomposition that benefits from the properties of the theory of response spectra. The goal of the approach is to provide fast peak response assessments without having to undergo historical response analysis. This is very important because the response spectrum analysis (RSA) is dependent on a set of quick and simple calculations. This approach is approximate in nature but is very beneficial because it makes the use of response spectrum to explain seismic hazard in a very comfortable manner.

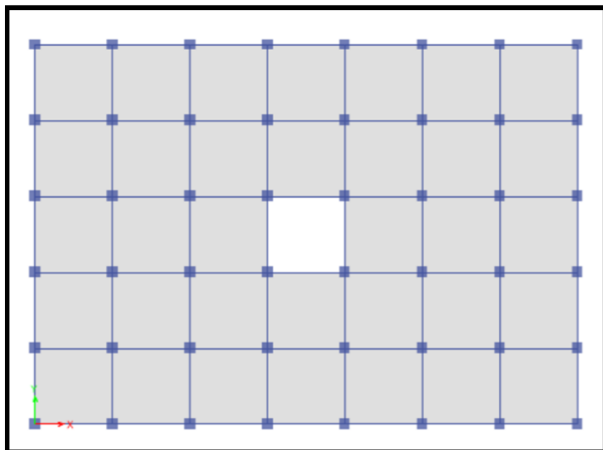
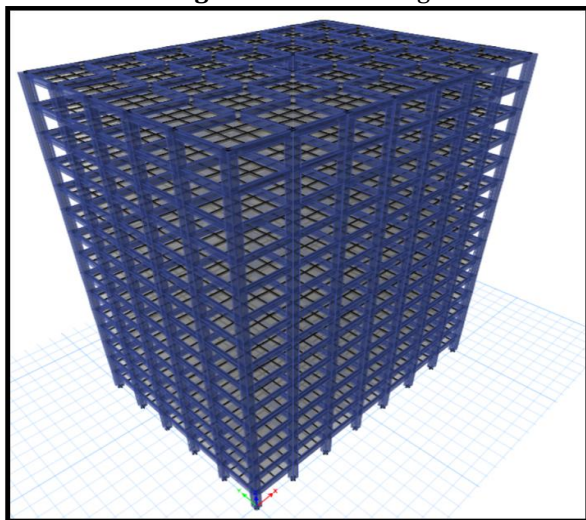
## 4. MODEL DISCRIPTION

A multistory of G+14(15) reinforced cement concrete(RCC) framed structures with plan of 5184m<sup>2</sup>.The structures is analyzed in ETABS software using response spectrum method for Indian standards .The structure presumed to be located Bhuj, Gujarat which lies in seismic and cyclone prone areas

**Table -1: Building details**

Geometric Details	
Plan dimensions	35 X25 m
Type of building plan	Regular
Height of building (m)	45
No of stores	15
Material properties	
Grade of concrete	M 30
Grade of steel	Fe 500
density of concrete	25 kN/m <sup>3</sup>
Density of brick	19 kN/m <sup>3</sup>
Section properties	
Beam size (mm)	230x500
Column size (mm)	600 x600
Slab thickness (mm)	150
Seismic properties	
Seismic zone (IS 1893-2002)	V
Seismic zone factor (Z)	0.36
Importance factor (I)	1.5
Response reduction factor(I)	5
Soil type	II
Damping ratio	0.05
Link properties	
Translational mass(kg)	44
Force (KN)	250




**Fig -1: Plan of building**

**Fig -2: 3D view of building**
**Table -2: Time period values in X and Y direction**

Type of building	Time period in X direction	Time period in Y direction
BB	3.841	3.765
DAM	2.113	2.093
SWE	2.844	2.803
SWC	2.207	2.184
SWEDM	1.943	1.932
SWCDM	1.758	1.746

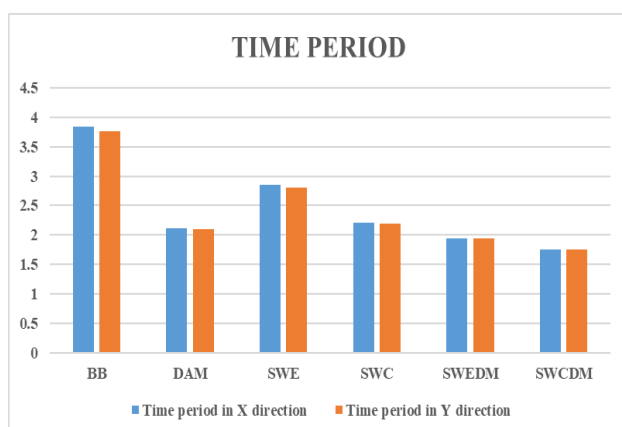
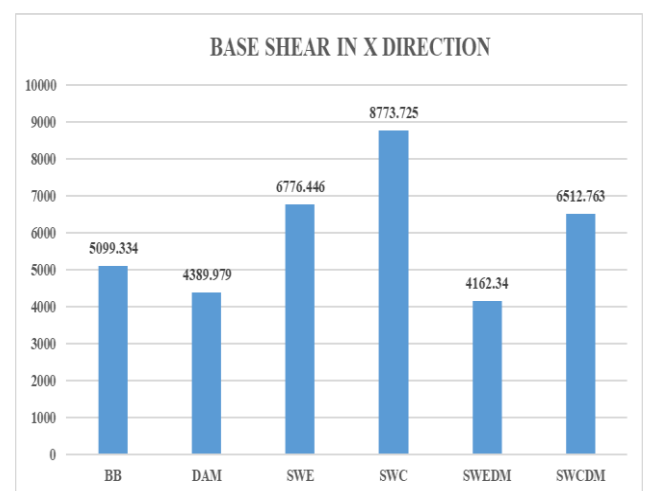
## B. Base Shear

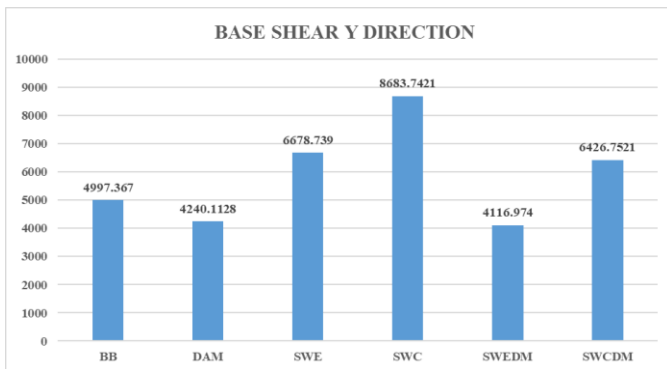
**Table -3: Base shear along X and Y direction**

Type of building	X	Y
BB	5099.33	4997.38
DAM	4389.97	4240.11
SWE	6776.45	6678.74
SWC	8773.72	8683.74
SWEDM	4162.34	4116.97
SWCDM	6512.76	6426.75

## 5. RESULTS

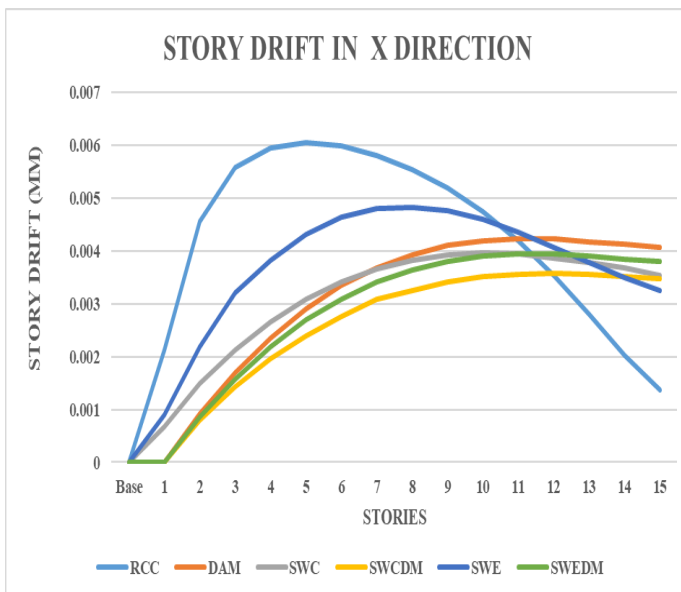
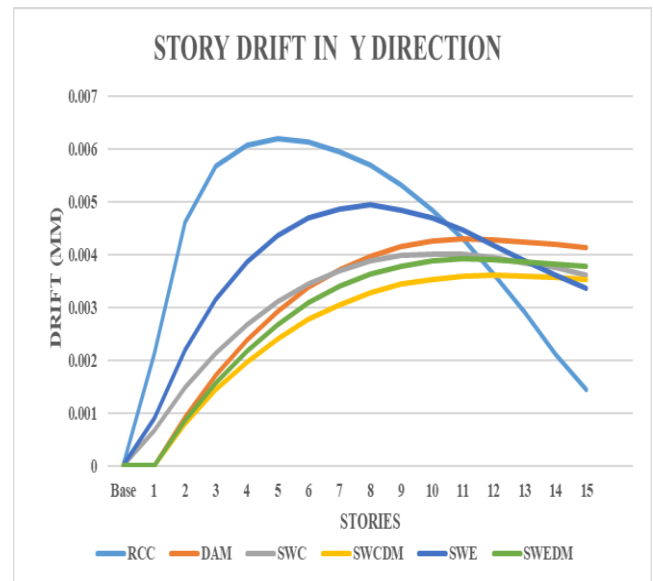
### A. Time Period


**Chart -1: Time period values in X and Y direction**

**Chart -2: Base shear along X direction**


**Chart -3:** Base shear along Y direction

### C. Story Drift

Story drift can be outlined as relative transverse displacement with respect to rates, i.e. above or below them: according to Clause No. 7.11.1 of IS 1893 (Part 1): 2002, the Story drift in any story owing a particular design oblique force with a partial load factor 1.0 shall not outstrip 0.004 times the story elevation. Regardless of column axial deformations, diagonal and girder deformations, drift in edifice frames is an outcome of flexural and shear mode contributions. Maximum permissible drift is 12 mm per modelled story height of 3 m E.g. Maximum permissible drift =  $0.004 \times 3000 = 12$  mm.


**Chart -4:** Story Drift along X Direction

**Chart -5:** Story Drift along Y Direction

**Table -4:** Story Drift along X Direction

Story Drift along X direction						
STORY NO	RCC	DAM	SWE	SWC	SWEDM	SWCDM
15	0.00136	0.004068	0.003251	0.003536	0.003806	0.003483
14	0.00202	0.004124	0.0035	0.003681	0.003855	0.003522
13	0.00279	0.004181	0.003778	0.003781	0.003904	0.003555
12	0.00353	0.004225	0.004078	0.003875	0.003939	0.003573
11	0.00418	0.004236	0.00436	0.003938	0.003943	0.00356
10	0.00474	0.004205	0.004595	0.003959	0.003904	0.003509
9	0.00519	0.004104	0.00476	0.003927	0.003809	0.00341
8	0.00555	0.003936	0.004834	0.003831	0.003649	0.003255
7	0.00582	0.003686	0.004799	0.003663	0.003414	0.003039
6	0.00599	0.003346	0.004635	0.003415	0.003097	0.002755
5	0.00606	0.002907	0.00432	0.00308	0.00269	0.002398
4	0.00597	0.002361	0.003829	0.002651	0.002187	0.00196
3	0.00558	0.0017	0.003128	0.002119	0.00158	0.001432
2	0.00456	0.000913	0.002181	0.001483	0.000856	0.000791
1	0.00213	0.000000	0.000906	0.000678	0.000000	0.000000
BASE	0.0000	0.000000	0.000000	0.000000	0.000000	0.000000

**Table -5:** Story Drift along Y Direction

Story Drift along Y Direction						
STORY NO	RCC	DAM	SWE	SWC	SWED M	SWCD M
15	0.00145	0.00414	0.003365	0.003608	0.003769	0.003522
14	0.00212	0.00419	0.003613	0.00375	0.003819	0.00356
13	0.00289	0.00424	0.003887	0.003848	0.00387	0.003592
12	0.00364	0.00428	0.004184	0.003938	0.003908	0.003607
11	0.00430	0.00429	0.004461	0.003998	0.003915	0.003592
10	0.00486	0.00425	0.004691	0.004014	0.003878	0.003538
9	0.00533	0.00415	0.004849	0.003977	0.003786	0.003436
8	0.00569	0.00397	0.004915	0.003875	0.003629	0.003278
7	0.00596	0.00372	0.004871	0.003701	0.003397	0.003058
6	0.00613	0.00337	0.004697	0.003448	0.003083	0.002771
5	0.00619	0.00293	0.00437	0.003106	0.00268	0.00241
4	0.00608	0.00238	0.003867	0.00267	0.00218	0.001969
3	0.00567	0.00171	0.003153	0.002132	0.001575	0.001438
2	0.00462	0.00092	0.002193	0.001489	0.000854	0.000794
1	0.00214	0.00000	0.000908	0.000679	0.000000	0.000000
Base	0.00000	0.00000	0.000000	0.000000	0.000000	0.000000

### D. Lateral Displacement

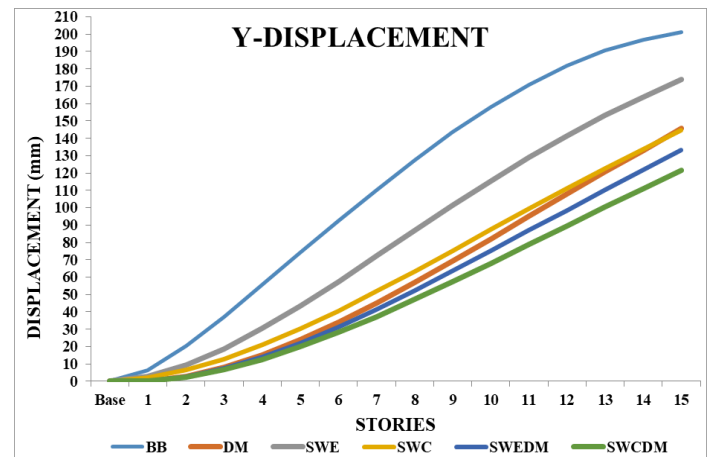
According to IS 1893-2002, permissible deflection is calculated as  $h/250$ , where 'h' is total height of edifice in millimeters (mm). Adopting the above practice, the displacements in X and Y command essential be inside 180mm.i.e.  $(45000 / 250 = 180)$  where 45000 mm is the height of construction

**Table -6:** Lateral displacement along X direction

Lateral displacement along Y direction						
Story No	RCC	DAM	SWE	SWC	SWEDM	SWCDM
15	201.16	145.62	174.07	144.7	133.029	121.693
14	196.83	133.21	163.98	133.87	121.722	111.127
13	190.48	120.64	153.14	122.62	110.264	100.448
12	181.80	107.91	141.48	111.08	98.653	89.673
11	170.89	95.059	128.92	99.266	86.93	78.852
10	157.99	82.186	115.54	87.273	75.187	68.075
9	143.34	69.435	101.47	75.23	63.553	57.46
8	127.43	56.99	86.924	63.3	52.195	47.152
7	110.36	45.066	72.178	51.675	41.309	37.318
6	92.488	33.909	57.564	40.57	31.118	28.144
5	74.098	23.79	43.474	30.228	21.867	19.831
4	55.529	15.007	30.363	20.909	13.827	12.601
3	37.282	7.879	18.763	12.899	7.288	6.693
2	20.273	2.752	9.304	6.504	2.563	2.381
1	6.421	0	2.725	2.036	0	0
Base	0	0	0	0	0	0

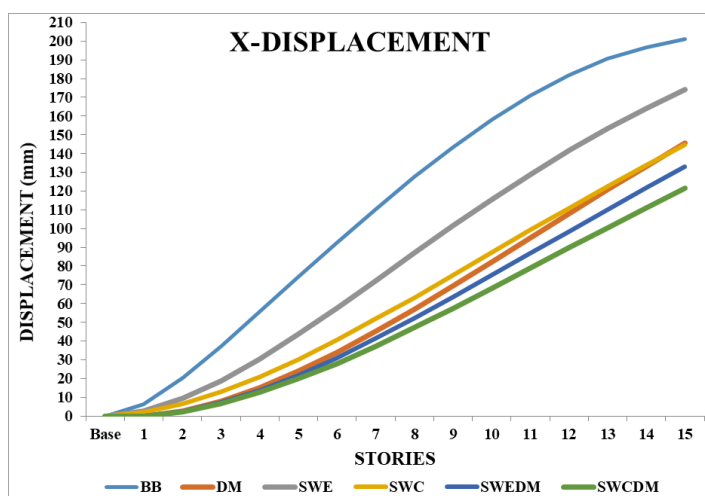
**Table -7:** Lateral displacement along X direction

Lateral Displacement along X direction						
STORY NO	RCC	DAM	SWE	SWC	SWEDM	SWCDM
15	196.44	143.967	170.856	142.857	133.896	120.72
14	192.35	131.763	161.105	132.249	122.478	110.27
13	186.26	119.392	150.604	121.205	110.914	99.708
12	177.88	106.847	139.271	109.861	99.203	89.042
11	167.28	94.171	127.036	98.236	87.387	78.325
10	154.73	81.462	113.956	86.422	75.558	67.643
9	140.53	68.861	100.172	74.544	63.846	57.116
8	124.95	56.55	85.892	62.763	52.419	46.887
7	108.30	44.743	71.391	51.27	41.473	37.122
6	90.853	33.684	56.994	40.281	31.231	28.006
5	72.878	23.646	43.09	30.034	21.94	19.742
4	54.703	14.924	30.131	20.793	13.869	12.549
3	36.808	7.841	18.645	12.84	7.307	6.669
2	20.076	2.74	9.261	6.483	2.569	2.373
1	6.385	0	2.719	2.034	0	0
Base	0	0	0	0	0	0


**Chart -7:** Lateral displacement along Y direction

## 6. CONCLUSIONS

1. The fundamental time period decreases with increasing story stiffness due to presence of different structural systems such as shear wall and fluid viscous dampers.
2. The time period of edifice with is shear wall at core and dampers is 54.23% less in x direction and 53.62% in y direction comparison to others model.
3. Base shear is increased by 20% for building with shear wall at core and dampers on comparison with bare building.
4. Lateral displacement of edifice with shear wall at core and dampers at edges is abridged by 38.5%, shear wall and dampers at edges is 31%, shear wall at core is 27.2%, and shear wall at edges is 13% and for edifice with only dampers at edges is 26.7% in x direction in comparison to bare building.
5. Lateral displacement of edifice with shear wall at core and dampers at edges is abridged by 40%, shear wall and dampers at edges is 33%, shear wall at core is 28%, shear wall at edges is 15% and for edifice with only dampers at edges is 27.6% in y direction in comparison to bare building.
6. Maximum storey drift is obtained for edifice with shear wall at core in company with dampers at corners is 48%(10.71 mm), with shear wall and dampers at edges is 35% (11.82mm), shear wall at core is 34.2% (12.03mm), shear wall at edges is 20%(14.5mm) and edifice with only dampers at corners 30% (12.7mm) along x direction.


**Chart -6:** Lateral displacement along X direction

7. Maximum storey drift is obtained for edifice with shear wall at core in company with dampers at corners is 49.08%(10.71 mm), with shear wall and dampers at edges is 36%(11.7mm), shear wall at core is 35.15%(12.04mm), shear wall at edges is 20.59%(14.70mm) and edifice with only dampers at corners is 30.67%(12.8mm) along y direction.
8. By comparison of lateral displacement, maximum story drift, and time period for edifice with shear wall at core in company with dampers at corners provides effective results.

## ACKNOWLEDGEMENT

The author wish to thank the authorities of VTU and University B.D.T College of engineering, for giving an opportunity to carry out research work in field of CAD structures. The support from Dept. of studies in civil engineering, UBDT College of engineering Davangere is gratefully acknowledges.

## REFERENCES

1. Abhijeet Koshti, Sridhar Shinde, Karthikeya Yamagar, Sagar Shegunshi(2019) published a paper entitled as "Seismic Response of Structure with Fluid Viscous Damper (FVD)" Volume-7, Issue-2, Feb.-2019
2. Abhishek Kumar Maurya, V.K. Singh (2018) "Analysis of Building Using Viscous Dampers in Seismic Zone-V". Volume-5, Issue-3, Jun.-2018.
3. Yogesh A, Dr. Jagadish, G Kori (2018) "Comparative analysis of symmetrical and unsymmetrical building using combination of dampers" Volume 5, Issue 7, July-2018.
4. Y.Sarath Kumar Reddy, M.S.Anantha Venkatesh (2018) "Vibration control of high rise building with viscous dampers using ETABS" Volume 7, Issue 6, June -2018.
5. Akash Dobariyaet, (2018) published a paper entitled as "Analysis of multi-storey building with shear wall using ETABS software".
6. Sangita C ,R.M Jadhav,S.H Patel(2018) published a paper entitled as "Dynamic analysis of multi-storeyed high rise building with different types of shear wall using E tabs"
7. Shaik Qamaruddin (2017) has proposed a paper entitled as "seismic response study of multi-storied reinforced concrete building with fluid viscous dampers"
8. Pradeep Pujar, Amaresh (2017) "Seismic Analysis of Plan Irregular Multi-Storied Building with and Without Shear Walls" Volume: 04 Issue: 08. Aug - 2017.
9. S.S. Pathan ,D.N.Kakade,A.P.Wadekar published a research paper entitled as "Comparative Study on Damper and Shear Wall in Earthquake Analysis for Multi-storey Structure" Volume 4, Issue 2.2017.
10. Kiran Tidke, Rahul Patil, Dr G.R Gandhe (2016) "Seismic Analysis of Building with and Without Shear Wall" Vol. 5, Issue 10, October 2016.
11. Nagarajan.P,( 2016) published a paper entitled as "Design Optimization and Analysis of Shear Wall in High Rise Buildings Using ETABS"
12. Puneeth Sajjan, Praveen Birada (2016) "Study on the Effect of Viscous Damper for RCC Frame Structure" Volume: 05 Issue: 09 Sep-2016.
13. Khushboo K. Soni, Dr Prakash S. Pajga (2015) "Design of Multi-storeyed Regular R.C. Buildings With and Without Shear Walls" Volume 2, Issue 5, May -2015.
14. Liya Mathew, Chandra Prabha (2014) published a paper entitled as "Effect of fluid viscous dampers in multi-storeyed buildings"
15. Vajreshwari Umachagi, Katta Venkataramana, G.R. Reddy, Rajeev Verma(2013) published a paper entitled as "Applications of Dampers for Vibration Control of Structures: An overview"
16. D.G Weng, C.Zhang, X.L.Lu, S.Zeng (2012) proposed "A simplified seismic design procedure for Retrofitting earthquake damaged frames with viscous dampers".
17. Nima Ostovar, Farzad Hejazi published a research paper entitled as "Seismic Response of Shear Wall with Viscous Damping System."
18. **IS 456-2000**, "Plain and Reinforced concrete-Code of Practice", Bureau of Indian Standards, New Delhi
19. **IS 1893-2002(Part 1)** "Criteria for earthquake resistant design of structures, General provisions and Buildings", Bureau of Indian Standards, New Delhi.
20. **IS 875 Part 1: Dead Loads--Unit Weights of Building Materials and Stored Materials (Second Revision)**
21. **IS 875 Part 2: Imposed Loads (Second Revision)** by Bureau of Indian Standards (BIS)
22. **IS 875 Part 3: Wind Loads (Second Revision)**
23. **IS 4326: Earthquake Resistant Design and Construction of Buildings--Code of Practice (Second Revision).**

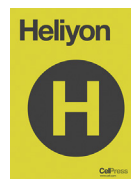




Contents lists available at ScienceDirect

Heliyon

journal homepage: [www.cell.com/heliyon](http://www.cell.com/heliyon)



## Research article

# Degree-based topological indices on anticancer drugs with QSPR analysis

M.C. Shanmukha<sup>a,b,\*</sup>, N.S. Basavarajappa<sup>b,c</sup>, K.C. Shilpa<sup>b,d</sup>, A. Usha<sup>e</sup>

<sup>a</sup> Department of Mathematics, Jain Institute of Technology, Davanagere, 577003, Karnataka, India

<sup>b</sup> Visvesvaraya Technological University, Belagavi, Karnataka, India

<sup>c</sup> Department of Mathematics, Bapuji Institute of Engineering and Technology, Davanagere, 577004, Karnataka, India

<sup>d</sup> Department of Computer Science and Engg., Bapuji Institute of Engineering and Technology, Davanagere, 577004, Karnataka, India

<sup>e</sup> Department of Mathematics, Alliance College of Engineering and Design, Alliance University, Anekal-Chandapura Road, Bangalore, Karnataka, India



## ARTICLE INFO

### Keywords:

Pharmaceutical chemistry  
Topological indices  
Anti cancer drugs  
QSPR analysis

## ABSTRACT

From last two to three decades, the world is facing the threat of finding treatment for Cancer. This disease is striking almost ten million people every year throughout the world. Anticancer drugs are those which are used to cure malignant disease i.e. Cancer. These anticancer drugs are available in different forms including alkylating agents, hormones and anti metabolites. Various examinations reveals that, there will be a adjacent relationship between the characteristics of alkanes and the anticancer drugs viz. Boiling point, melting point, enthalpy etc. with their chemical structures. In this proposed work, various topological indices are defined on some anticancer drugs to help the researchers to know the physical characteristics and chemical reaction associated with them. We also discuss the QSPR analysis of thirteen degree based topological indices. Further, we showcase that the characteristics have good correlation with physico-chemical characteristics of anticancer drugs.

## 1. Introduction and terminologies

Cancer is the rapid growth of abnormal cells in the human body. Carcinogens are the substances that causes cancer. A carcinogen is a chemical substance with certain molecules in tobacco smoke. It has a potential to spread to other parts of the body. Some of the symptoms of this disease includes lump, abnormal bleeding, prolounger cough, weight loss etc. Main causes for this malignant disease are chewing tobacco, obesity, bad diet, laziness, more intake of alcohol. This dangerous disease can be cured by several treatments like surgery, radiotherapy, chemotherapy, hormone therapy, targeted therapy and more. Anticancer drugs are those which are used to cure the disease so called cancer, which includes alkylates and metabolites. The chemical graph theory is a discipline of mathematical chemistry that deals with the chemical graphs which shows chemical system. The chemical graph theory offers defining topological indices on anticancer drugs. In this work, several drugs are taken and using the degree based calculations, few topological indices are defined on various anticancer drugs to determine physical characteristics and chemical reactions associated with them [1,2,3].

Topological indices are the important attributes to analyse the physico-chemical characteristics of chemical compound structures. There are five different types of topological indices: Degree, distance, eigenvalue, matching and mixed. In this work degree based topological indices

are stated on anticancer drugs. Generally, the chemical compound is represented as a graph where the elements denote vertices and the bonds connecting them denote edges. In a similar fashion, these anticancer drugs under this study are considered as chemical compounds and the said topological indices are defined. Graph theory offers some tools like QSAR, QSPR and QSTR where chemists or pharmacists use these data for further research work.

In this work, further we discuss QSPR analysis of said topological indices. We also show that the characteristics obtained are highly correlated with the characteristics of anticancer drugs using linear regression [4,5,6,7,8,9].

In theoretical chemistry drugs are represented as molecular graphs where vertex represents an atom and each edge represents link between the two atoms. Consider  $G(V, E)$  be a molecular graph with vertex and edge set respectively. The graphs considered are simple graphs with no cycle formation and multiple edges [4,10,11,12].

**Definition 1.1.** Estrada et al. in [13] proposed degree-based topological index  $ABC$  and defined as

$$ABC(G) = \sum_{e=vw \in E(G)} \sqrt{\frac{d_v + d_w - 2}{d_v d_w}}$$

\* Corresponding author.

E-mail address: [mcshanmukha@gmail.com](mailto:mcshanmukha@gmail.com) (M.C. Shanmukha).



**Definition 1.2.** Ghorbani et al. in [14] proposed  $ABC_4$  index and can be stated as,

$$ABC_4(G) = \sum_{e=vw \in E(G)} \sqrt{\frac{s_v + s_w - 2}{s_v s_w}}$$

**Definition 1.3.** The Randic index [15] proposed by Milan Randic and can be stated as

$$\chi(G) = \sum_{e=vw \in E(G)} \sqrt{\frac{1}{d_v d_w}}$$

**Definition 1.4.** The sum-connectivity index is proposed by Zhou and Trinjtstic [16], and is defined as

$$S(G) = \sum_{e=vw \in E(G)} \sqrt{\frac{1}{d_v + d_w}}$$

**Definition 1.5.** The GA index is proposed by Vukicevic et al. [17] as

$$GA(G) = \sum_{e=vw \in E(G)} \frac{2\sqrt{d_v d_w}}{d_v + d_w}$$

**Definition 1.6.** The  $GA_5$  index proposed by Graovac et al. [18] and is stated as

$$GA_5(G) = \sum_{e=vw \in E(G)} \frac{2\sqrt{s_v s_w}}{s_v + s_w}$$

**Definition 1.7.** The first and second Zagreb indices are proposed by Gutman and Trinajstic [19], as

$$M_1(G) = \sum_{e=vw \in E(G)} (d_v + d_w)$$

$$M_2(G) = \sum_{e=vw \in E(G)} (d_v \cdot d_w)$$

**Definition 1.8.** Fajtlowicz proposed Harmonic index in [20] as,

$$H(G) = \sum_{e=vw \in E(G)} \frac{2}{d_v + d_w}$$

**Definition 1.9.** Shirdel et al. in [21] proposed the hyper Zagreb index and is stated as,

$$HM(G) = \sum_{e=vw \in E(G)} (d_v + d_w)^2$$

**Definition 1.10.** Fath-Tabar et al. in [22] proposed the third Zagreb index as

$$ZG_3(G) = \sum_{e=vw \in E(G)} |d_v - d_w|$$

**Definition 1.11.** Furtula et al. in [23] proposed the forgotten topological index and is stated as

$$F(G) = \sum_{e=vw \in E(G)} [(d_v)^2 + (d_w)^2]$$

**Definition 1.12.** In chemical graph theory, there are some new degree-based graph types, which plays an important role in finding total surface area and heat-formation of various chemical compounds. These graphs types are as follow Symmetric division index [24],

$$SSD(G) = \sum_{e=vw \in E(G)} \left[ \frac{P}{Q} + \frac{Q}{P} \right]$$

where,  $P = \min [d_G(v), d_G(w)]$  and  $Q = \max [d_G(v), d_G(w)]$

## 2. Degree based topological indices in QSPR studies

Here we defined 13° based topological indices, Atom-bond connectivity index  $ABC(G)$ , Fourth atom-bond connectivity index  $ABC_4(G)$ , Randic index  $\chi(G)$ , Sum-connectivity index  $S(G)$ , Geometric-arithmetic index  $GA(G)$ , Fifth Geometric arithmetic index  $GA_5(G)$ , First Zagreb index  $M_1(G)$ , Second Zagreb index  $M_2(G)$ , Harmonic index  $H(G)$ , Hyper Zagreb index  $HM(G)$ , Third Zagreb index  $ZG_3(G)$ , Forgotten index  $F(G)$ , Symmetric Division index  $SSD(G)$  for modelling Five representative physical properties [Boiling point (BP), Melting point (MP), Enthalpy (E), Flash point (FP), Molar refraction (MR)] of the 17 anticancer drugs from Amathaspiramide-E to Tambjamine-K. The values for these properties are taken from Chem Spider. The above mentioned degree based topological indices and the experimental values for the physical and chemical properties of 17 anticancer drugs (Figure 1) are represented in Tables 1, 2, and 3 respectively.

From the data of above Tables 2 and 3, it has been found that all the data values are normally distributed. Hence the regression model is suitable test to adopt and analyse the data.

## 3. Regression models

The above table data shows normally distributed values. Hence the study used regression analysis for the calculation purpose. Here we have checked the linear regression model as below

$$P = A + B(TI) \quad (1)$$

where P is the Physical property of anticancer drug, A is a constant and B is the regression coefficient and TI represents the topological index. These were calculated using SPSS software for the values of five physical properties and the thirteen topological indices of seventeen anticancer drugs.

Using (1), we can get the different linear models for the defined degree based topological indices, which are as follows.

### 1. Atom-bond Connectivity index $ABC(G)$ :

$$BP = 232.702 + 18.457 [ABC(G)] \quad (2)$$

$$MP = 97.481 + 6.385 [ABC(G)] \quad (3)$$

$$E = 46.017 + 2.385 [ABC(G)] \quad (4)$$

$$FP = 105.864 + 9.791 [ABC(G)] \quad (5)$$

$$MR = 27.349 + 3.590 [ABC(G)] \quad (6)$$

### 2. Fourth Atom-bond Connectivity index $ABC_4(G)$ :

$$BP = 242.956 + 24.290 [ABC_4(G)] \quad (7)$$

$$MP = 84.818 + 9.517 [ABC_4(G)] \quad (8)$$

$$E = 46.834 + 3.081 [ABC_4(G)] \quad (9)$$

$$FP = 114.955 + 12.640 [ABC_4(G)] \quad (10)$$

$$MR = 27.134 + 4.889 [ABC_4(G)] \quad (11)$$

### 3. Randic index $\chi(G)$ :

$$BP = 207.524 + 31.676 [\chi(G)] \quad (12)$$

$$MP = 75.233 + 12.437 [\chi(G)] \quad (13)$$

$$E = 42.806 + 3.966 [\chi(G)] \quad (14)$$

$$FP = 89.052 + 17.119 [\chi(G)] \quad (15)$$

$$MR = 19.758 + 6.397 [\chi(G)] \quad (16)$$

### 4. Sum-Connectivity index $S(G)$ :

$$BP = 219.568 + 29.619 [S(G)] \quad (17)$$

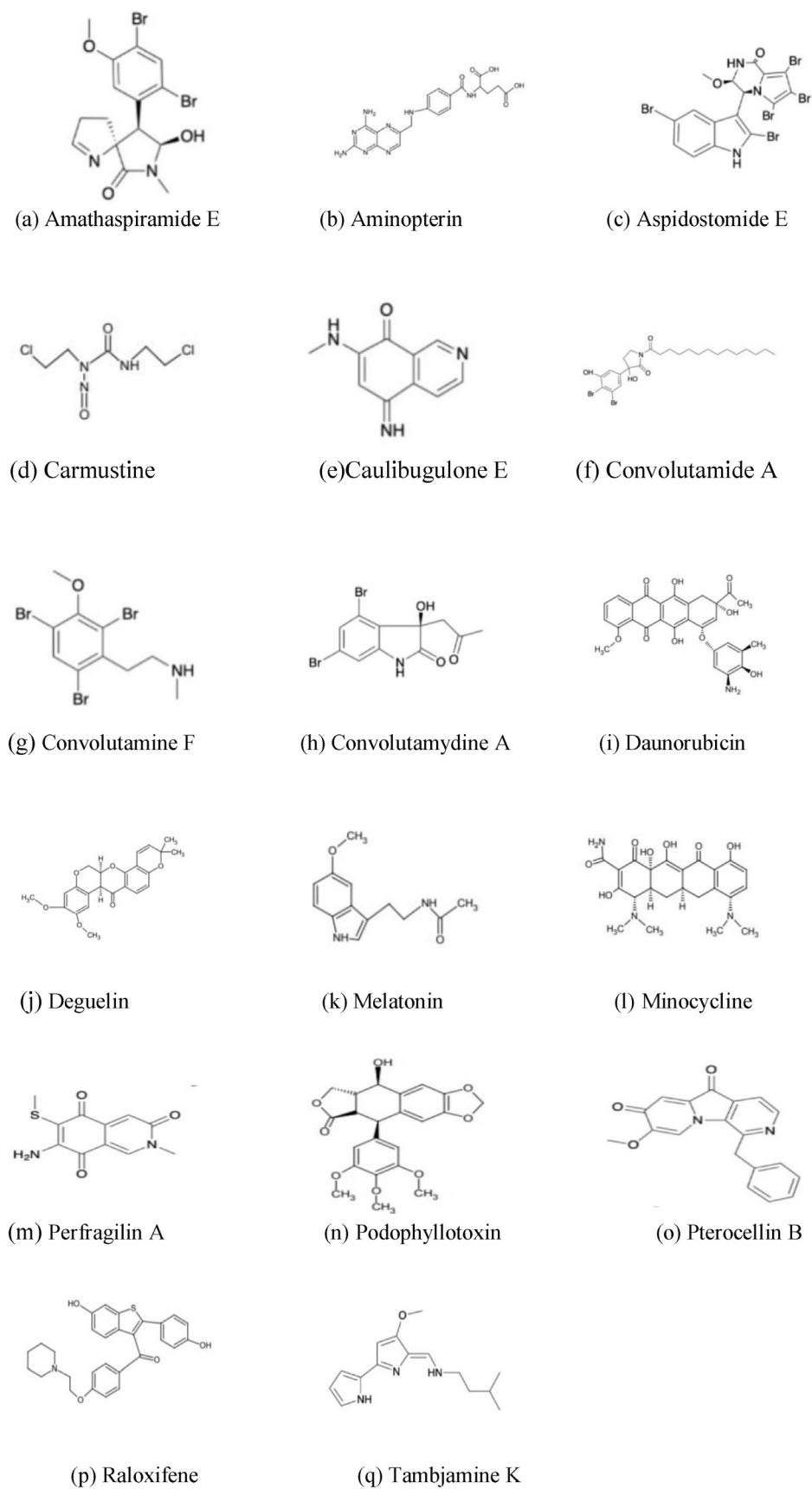


Figure 1. Molecular structures of anticancer drugs.

**Table 1.** Various Anticancer drugs with its physico-chemical properties.

S.No.	Drugs	BP	MP	E	FP	MR
1	Amathaspiramide E	572.7	209.72	90.3	300.2	89.4
2	Aminopterin	782.27	344.45			114
3	Aspidostomide E	798.8		116.2	436.9	116
4	Carmustine	309.6	120.99	63.8	141	46.6
5	Caulibugulone E	373	129.46	62	179.4	52.2
6	Convolutamide A	629.9		97.9	334.7	130.1
7	Convolutamine F	387.7	128.67	63.7	188.3	73.8
8	Convolutamydine A	504.9	199.2	81.6	259.2	68.2
9	Daunorubicin	770	208.5	117.6	419.5	130
10	Deguelin	560.1	213.39	84.3	244.8	105.1
11	Melatonin	512.8	182.51	78.4	264	67.6
12	Minocycline	803.3	326.3	122.5	439.6	116
13	Perfragilin A	431.5	187.62	68.7	214.8	63.6
14	Podophyllotoxin	597.9	235.86	93.6	210.2	104.3
15	Pterocellin B	521.6	199.88	79.5	269.2	87.4
16	Raloxifene	728.2	289.58	110.1	394.2	136.6
17	Tambjamine K	391.7		64.1	3190.7	76.6

$$MP = 86.175 + 11.026 [S(G)] \quad (18) \quad E = 45.953 + 1.745 [GA_5(G)] \quad (29)$$

$$E = 45.580 + 3.682 [S(G)] \quad (19) \quad FP = 109.675 + 7.234 [GA_5(G)] \quad (30)$$

$$FP = 97.414 + 15.829 [S(G)] \quad (20) \quad MR = 25.435 + 2.784 [GA_5(G)] \quad (31)$$

$$MR = 22.568 + 5.950 [S(G)] \quad (21) \quad \mathbf{7. First Zagreb index M_1(G):}$$

$$\mathbf{5. Geometric-Arithmetic index GA(G):} \quad BP = 232.771 + 2.686 [M_1(G)] \quad (32)$$

$$BP = 276.572 + 12.115 [GA(G)] \quad (22) \quad MP = 100.234 + 0.913 [M_1(G)] \quad (33)$$

$$MP = 90.640 + 5.053 [GA(G)] \quad (23) \quad E = 46.094 + 0.334 [M_1(G)] \quad (34)$$

$$E = 51.708 + 1.5 [GA(G)] \quad (24) \quad FP = 106.537 + 1.414 [M_1(G)] \quad (35)$$

$$FP = 134.852 + 6.163 [GA(G)] \quad (25) \quad MR = 28.756 + 0.511 [M_1(G)] \quad (36)$$

$$MR = 31.169 + 2.552 [GA(G)] \quad (26) \quad \mathbf{8. Second Zagreb index M_2(G):}$$

$$\mathbf{6. Fifth Geometric-Arithmetic index GA_5(G):} \quad BP = 250.418 + 2.138 [M_2(G)] \quad (37)$$

$$BP = 226.669 + 14.157 [GA_5(G)] \quad (27) \quad MP = 109.887 + 0.692 [M_2(G)] \quad (38)$$

$$MP = 81.299 + 5.563 [GA_5(G)] \quad (28) \quad E = 48.129 + 0.266 [M_2(G)] \quad (39)$$

**Table 2.** Various Anticancer drugs with Topological Indices values.

Drugs	ABC(G)	ABC <sub>4</sub> (G)	χ(G)	S(G)	GA(G)	GA <sub>5</sub> (G)	M <sub>1</sub> (G)
Amathaspiramide E	10.773	9.079	7.112	7.076	14.403	11.748	70
Aminopterin	24.65	18.96	15.23	15.68	32.700	33.630	162
Aspidostomide E	18.813	11.346	12.35	13.00	17.548	26.906	148
Carmustine	7.847	6.775	5.757	5.482	10.634	10.738	46
Caulibugulone E	10.664	8.342	6.736	6.946	14.574	18.966	72
Convolutamide A	24.463	19.369	17.93	17.74	35.702	34.208	167
Convolutamine F	10.773	8.616	7.113	7.077	14.403	14.599	70
Convolutamydine A	12.016	8.962	7.93	7.544	16.273	15.753	88
Daunorubicin	32.295	22.564	17.89	18.89	40.190	33.116	216
Deguelin	23.398	17.507	13.91	14.80	31.954	32.5264	168
Melatonin	12.865	9.676	8.203	8.419	17.493	17.809	84
Minocycline	26.081	19.093	15.54	16.12	34.271	35.014	184
Perfragilin A	12.992	9.836	7.968	8.171	17.172	17.491	90
Podophyllotoxin	22.02	16.42	12.95	13.86	30.090	30.53	158
Pterocellin B	19.027	11.250	11.69	12.93	26.452	20.788	132
Raloxifene	26.956	20.862	16.58	17.5	37.234	37.684	182
Tambjamine K	14.28	9.654	9.203	9.419	19.493	19.774	92

**Table 3.** Various Anticancer drugs with Topological Indices values.

Drugs	M <sub>2</sub> (G)	H(G)	HM(G)	ZG <sub>3</sub> (G)	F(G)	SSD(G)
Amathaspiramide E	81	6.767	343	12	180	35.667
Aminopterin	185	14.53	786	32	416	80.33
Aspidostomide E	186	11.767	778	22	406	55
Carmustine	48	5.533	202	8	106	25.331
Caulibugulone E	86	6.5	358	10	186	29.5
Convolutamide A	167	17.205	793	21	419	86.583
Convolutamine F	81	6.767	522	12	432	29.167
Convolutamidine A	109	6.738	468	20	250	40.083
Daunorubicin	270	16.919	1146	38	606	101.666
Deguelin	208	13.4	878	28	462	76.166
Melatonin	96	7.933	402	14	210	40.666
Minocycline	229	14.567	970	30	512	89
Perfragilin A	110	7.5	466	16	246	44
Podophyllotoxin	198	12.47	824	22	428	70.66
Pterocellin B	161	11.4	664	16	342	58.999
Raloxifene	215	16.2	890	24	460	83
Tambjamine K	104	8.933	434	14	226	44.667

$$FP = 116.671 + 1.115 [M_2(G)] \quad (40)$$

$$MR = 34.562 + 0.391 [M_2(G)] \quad (41)$$

#### 9. Harmonic index H(G):

$$BP = 218.618 + 32.191 [H(G)] \quad (42)$$

$$MP = 79.495 + 12.656 [H(G)] \quad (43)$$

$$E = 44.375 + 4.011 [H(G)] \quad (44)$$

$$FP = 96.112 + 17.286 [H(G)] \quad (45)$$

$$MR = 20.814 + 6.610 [H(G)] \quad (46)$$

#### 10. Hyper Zagreb index HM(G):

$$BP = 242.453 + 0.508 [HM(G)] \quad (47)$$

$$MP = 109.795 + 0.161 [HM(G)] \quad (48)$$

$$E = 47.199 + 0.063 [HM(G)] \quad (49)$$

$$FP = 111.462 + 0.267 [HM(G)] \quad (50)$$

$$MR = 30.608 + 0.097 [HM(G)] \quad (51)$$

#### 11. Third Zagreb index ZG<sub>3</sub>(G):

$$BP = 247.098 + 16.151 [ZG_3(G)] \quad (52)$$

$$MP = 102.564 + 5.462 [ZG_3(G)] \quad (53)$$

$$E = 47.108 + 2.087 [ZG_3(G)] \quad (54)$$

$$FP = 109.841 + 8.890 [ZG_3(G)] \quad (55)$$

$$MR = 38.887 + 2.703 [ZG_3(G)] \quad (56)$$

#### 12. Forgotten index F(G):

$$BP = 269.670 + 0.865 [F(G)] \quad (57)$$

$$MP = 123.820 + 0.257 [F(G)] \quad (58)$$

$$E = 50.889 + 0.106 [F(G)] \quad (59)$$

$$FP = 125.652 + 0.453 [F(G)] \quad (60)$$

$$MR = 33.304 + 0.172 [F(G)] \quad (61)$$

#### 13. Symmetric Division index SSD(G):

$$BP = 253.080 + 5.425 [SSD(G)] \quad (62)$$

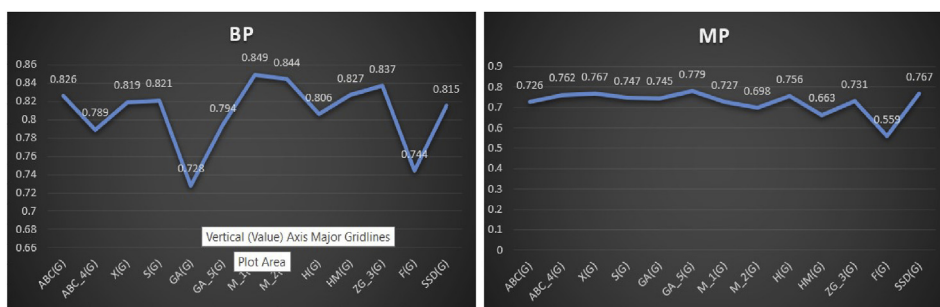
$$MP = 94.601 + 2.054 [SSD(G)] \quad (63)$$

$$E = 48.291 + 0.683 [SSD(G)] \quad (64)$$

**Table 4.** Correlation coefficients.

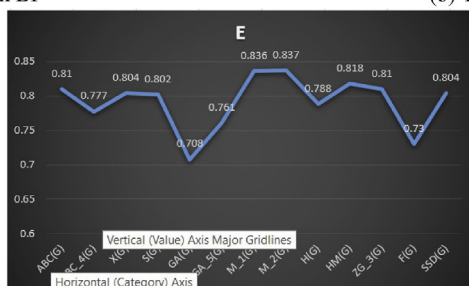
Index	Boiling Point	Melting Point	Enthalpy	Flash Point	Molar Refraction
ABC(G)	0.826	0.726	0.810	0.733	0.913
ABC <sub>4</sub> (G)	0.789	0.762	0.777	0.679	0.903
χ(G)	0.819	0.767	0.804	0.740	<b>0.941</b>
S(G)	0.821	0.747	0.802	0.735	0.938
GA(G)	0.728	0.745	0.708	0.620	0.872
GA <sub>5</sub> (G)	0.794	<b>0.779</b>	0.761	0.672	0.889
M <sub>1</sub> (G)	<b>0.849</b>	0.727	0.836	<b>0.754</b>	0.919
M <sub>2</sub> (G)	0.844	0.698	<b>0.837</b>	0.749	0.877
H(G)	0.806	0.756	0.788	0.723	<b>0.941</b>
HM(G)	0.827	0.663	0.818	0.737	0.895
ZG <sub>3</sub> (G)	0.837	0.731	0.810	0.735	0.797
F(G)	0.744	0.559	0.730	0.664	0.841
SSD(G)	0.815	0.767	0.804	0.720	0.904

The significance of bold numbers denote highest correlation value.

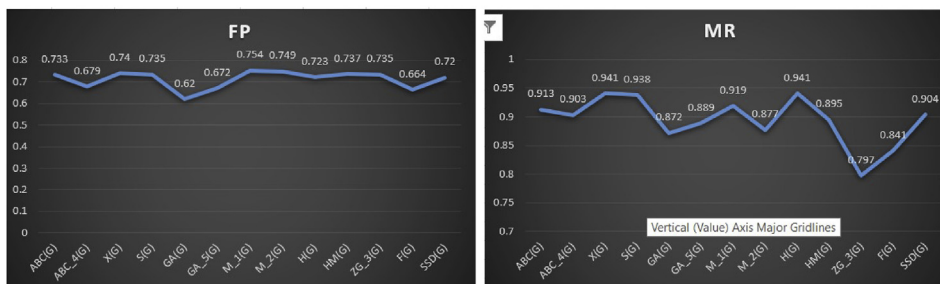


(a) TI on BP

(b) TI on MP



(c) TI on E



(d) TI on FP

(e) TI on MR

Figure 2. Physico-chemical properties with topological indices.

Table 5. Statistical parameters for the linear QSPR model For ABC(G).

Physical Properties	N	A	b	r	F	p	Indicator
Boiling Point	17	232.702	18.457	0.826	32.119	0.000	significant
Melting Point	15	97.481	6.385	0.726	13.381	0.003	significant
Enthalpy	16	46.017	2.307	0.810	26.772	0.000	significant
Flash Point	16	105.864	9.791	0.733	16.221	0.001	significant
Molar Refraction	17	27.349	3.590	<b>0.913</b>	75.573	0.000	significant

The significance of bold numbers denote highest correlation value.

Table 6. Statistical parameters for the linear QSPR model For ABC4(G).

Physical Properties	N	A	b	r	F	p	Indicator
Boiling Point	17	242.956	24.290	0.789	24.649	0.000	significant
Melting Point	15	84.818	9.517	0.762	16.580	0.002	significant
Enthalpy	16	46.834	3.081	0.777	21.267	0.000	significant
Flash Point	16	114.955	12.646	0.679	11.977	0.004	significant
Molar Refraction	17	27.134	4.889	<b>0.903</b>	66.079	0.000	significant

The significance of bold numbers denote highest correlation value.

**Table 7.** Statistical parameters for the linear QSPR model For  $\chi(G)$ .

Physical Properties	N	A	b	r	F	p	Indicator
Boiling Point	17	207.524	31.676	0.819	30.638	0.000	significant
Melting Point	15	75.233	12.437	0.767	17.167	0.001	significant
Enthalpy	16	42.806	3.966	0.804	25.674	0.000	significant
Flash Point	16	89.052	17.119	0.740	16.907	0.001	significant
Molar Refraction	17	19.758	6.347	<b>0.941</b>	116.4160.000	0.000	significant

The significance of bold numbers denote highest correlation value.

**Table 8.** Statistical parameters for the linear QSPR model For  $S(G)$ .

Physical Properties	N	A	b	r	F	p	Indicator
Boiling Point	17	219.568	29.619	0.821	31.014	0.000	significant
Melting Point	15	86.175	11.026	0.747	15.172	0.002	significant
Enthalpy	16	45.580	3.682	0.802	25.326	0.000	significant
Flash Point	16	97.414	15.829	0.735	16.448	0.001	significant
Molar Refraction	17	22.568	5.950	<b>0.938</b>	109.935	0.000	significant

The significance of bold numbers denote highest correlation value.

**Table 9.** Statistical parameters for the linear QSPR model For  $GA(G)$ .

Physical Properties	N	A	b	r	F	p	Indicator
Boiling Point	17	276.572	12.115	0.728	16.912	0.001	significant
Melting Point	15	90.640	5.053	0.745	14.93	0.002	significant
Enthalpy	16	51.708	1.5	0.708	14.098	0.002	significant
Flash Point	16	134.852	6.163	0.620	8.735	0.010	Significant
Molar Refraction	17	31.169	2.552	<b>0.872</b>	47.644	0.000	Significant

The significance of bold numbers denote highest correlation value.

**Table 10.** Statistical parameters for the linear QSPR model For  $GA_5(G)$ .

Physical Properties	N	A	b	r	F	p	Indicator
Boiling Point	17	226.669	14.157	0.794	25.640	0.000	Significant
Melting Point	15	81.229	5.563	0.779	18.506	0.001	Significant
Enthalpy	16	45.953	1.745	0.761	19.266	0.001	Significant
Flash Point	16	109.675	7.234	0.672	11.526	0.004	Significant
Molar Refraction	17	25.435	2.784	<b>0.889</b>	56.261	0.000	Significant

The significance of bold numbers denote highest correlation value.

**Table 11.** Statistical parameters for the linear QSPR model For  $M_1(G)$ .

Physical Properties	N	A	b	r	F	p	Indicator
Boiling Point	17	232.771	2.686	0.849	38.616	0.000	Significant
Melting Point	15	100.234	0.913	0.727	13.472	0.003	Significant
Enthalpy	16	46.094	0.334	0.836	32.541	0.000	Significant
Flash Point	16	106.537	1.414	0.754	18.503	0.001	Significant
Molar Refraction	17	28.756	0.511	<b>0.919</b>	81.435	0.000	Significant

The significance of bold numbers denote highest correlation value.

**Table 12.** Statistical parameters for the linear QSPR model For  $M_2(G)$ .

Physical Properties	N	A	b	r	F	p	Indicator
Boiling Point	17	250.418	2.138	0.844	37.243	0.000	Significant
Melting Point	15	109.887	0.692	0.698	11.405	0.005	Significant
Enthalpy	16	48.129	0.266	0.837	32.841	0.000	Significant
Flash Point	16	116.671	1.115	0.749	17.849	0.001	Significant
Molar Refraction	17	34.562	0.391	<b>0.877</b>	50.156	0.000	Significant

The significance of bold numbers denote highest correlation value.



**Table 13.** Statistical parameters for the linear QSPR model For H(G).

Physical Properties	N	A	b	r	F	p	Indicator
Boiling Point	17	218.618	32.191	0.806	27.735	0.000	Significant
Melting Point	15	79.495	12.656	0.756	16.024	0.002	Significant
Enthalpy	16	44.375	4.011	0.788	22.892	0.000	Significant
Flash Point	16	96.112	17.286	0.723	15.343	0.002	Significant
Molar Refraction	17	20.814	6.610	<b>0.941</b>	115.783	0.000	Significant

The significance of bold numbers denote highest correlation value.

**Table 14.** Statistical parameters for the linear QSPR model For HM(G).

Physical Properties	N	A	b	r	F	p	Indicator
Boiling Point	17	242.453	0.508	0.827	32.364	0.000	Significant
Melting Point	15	109.795	0.161	0.663	9.413	0.010	Significant
Enthalpy	16	47.199	0.063	0.818	28.407	0.000	Significant
Flash Point	16	111.462	0.267	0.737	16.689	0.001	Significant
Molar Refraction	17	30.608	0.097	<b>0.895</b>	60.345	0.000	Significant

The significance of bold numbers denote highest correlation value.

**Table 15.** Statistical parameters for the linear QSPR model For ZG<sub>3</sub>(G).

Physical Properties	N	A	b	r	F	p	Indicator
Boiling Point	17	247.098	16.151	<b>0.837</b>	35.057	0.000	Significant
Melting Point	15	102.564	5.462	0.731	13.733	0.003	Significant
Enthalpy	16	47.108	2.087	0.810	26.767	0.000	Significant
Flash Point	16	109.841	8.890	0.735	16.490	0.001	Significant
Molar Refraction	17	38.887	2.703	0.797	26.072	0.000	Significant

The significance of bold numbers denote highest correlation value.

**Table 16.** Statistical parameters for the linear QSPR model For F(G).

Physical Properties	N	a	b	r	F	p	Indicator
Boiling Point	17	269.670	0.865	0.744	18.0619	0.001	Significant
Melting Point	15	123.82	0.257	0.559	5.462	0.038	Significant
Enthalpy	16	50.889	0.106	0.730	15.942	0.001	Significant
Flash Point	16	125.652	0.453	0.664	11.012	0.005	Significant
Molar Refraction	17	33.304	0.172	<b>0.841</b>	36.186	0.000	Significant

The significance of bold numbers denote highest correlation value.

**Table 17.** Statistical parameters for the linear QSPR model For SSD(G).

Physical Properties	N	a	b	r	F	p	Indicator
Boiling Point	17	253.080	5.425	0.815	29.571	0.000	Significant
Melting Point	15	94.601	2.054	0.767	17.119	0.001	Significant
Enthalpy	16	48.291	0.683	0.804	25.633	0.000	Significant
Flash Point	16	117.165	2.87	0.720	15.055	0.002	Significant
Molar Refraction	17	31.147	1.058	<b>0.904</b>	66.734	0.000	Significant

The significance of bold numbers denote highest correlation value.

$$FP = 117.165 + 2.870 [SSD(G)] \quad (65)$$

$$MR = 31.147 + 1.058 [SSD(G)] \quad (66)$$

#### 4. Conclusion, study implications, limitations and future study

##### 4.1. Conclusion

The Table 4 and graphs (Figure 2) indicates the correlated values of Physico-chemical properties of anticancer drugs with the defined degree

based topological indices. It can be observed that  $M_1(G) = 0.849$  index shows higher significant positive correlation with Boiling point (BP), when compared with other indices.

Similarly  $GA_5(G) = 0.779$  index gives positive correlated value with melting point (MP). In case of enthalpy,  $M_2(G)$  shows highest correlated value i.e.  $r = 0.837$ .

Flashing point (FP) offers highest correlated value of 0.754 from the physico-chemical properties.

Based on molar refraction (MR),  $\chi(G)$  and  $M_2(G)$  indices depicts highest positive correlation value i.e.  $r = 0.941$ .

Hence it can be remarked that all the physical and chemical properties of anticancer drugs are positively correlate with the defined degree based topological indices.

Tables 5, 6, 7, 8, 9, 10, 11, 12, 13, 14, 15, 16, and 17 shows the regression model of various physico-chemical properties. It can be observed that the regression model value  $r$  is more than 0.6 and  $p$  value shows less than 0.05. Hence it can be concluded that all the physico-chemical properties are highly significant.

#### 4.2. Study implications

The work implies that these anti-cancer drugs may be considered for further study by pharmacists and chemists in designing the drugs using these topological indices values. May be the composition of these drugs, like the combinations may be tried for different ailments based on the range of the topological indices that are determined in the study. As the correlation coefficient has been found for the topological indices, the positively high correlated drugs may be considered for the combination of design of novel drugs.

#### 4.3. Limitations

As the range of topological indices are not published by chemists anywhere in web/internet, the mathematicians may not be able to decide upon the values they obtain for different chemical compounds whether the compounds the researchers chose have future study or not. The best solution for this would be a joint venture of the study in future may be carried out by both mathematicians/statisticians and chemists/pharmacists.

#### 4.4. Future study

In a similar fashion, a study may be carried out for different chemical structures and a conclusion may be given based on their topological indices range. May it be benzene structure or polymers or any chemical compounds can be taken for future study. A multidisciplinary project may be taken up by various disciplines researchers for a better result.

#### Declarations

#### Author contribution statement

Shanmukha M C, Basavarajappa N S, Shilpa K C, Usha A: Conceived and designed the experiments; Performed the experiments; Analyzed and interpreted the data; Contributed reagents, materials, analysis tools or data; Wrote the paper.

#### Funding statement

This research did not receive any specific grant from funding agencies in the public, commercial, or not-for-profit sectors.

#### Competing interest statement

The authors declare no conflict of interest.

#### Additional information

No additional information is available for this paper.

#### References

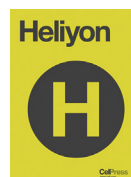
- [1] Blanca Figuerola, Conxita Avila, The phylum bryozoa as a promising source of anticancer drugs, *Mar. Drugs* 17 (2019) 477, 1-23.
- [2] W. Gao, W.F. Wang, M.R. Farahani, Topological indices study of molecular structure in anticancer drugs, *J. Chem.* (2016).
- [3] Shashank Kumar, Mohammad Kaleem Ahmad, Mohammad Waseem, Abhay K. Pandey, Drug targets for cancer treatment: an overview, *Med. Chem.* 5 (3) (2015) 115-123.
- [4] Adnan Aslam, Yasir Bashir, Safyan Ahmad, Wei Gao, On topological indices of certain dendrimer structures, *Z. Naturforsch.* 72 (6) (2017) 559-566.
- [5] S.M. Hosamani, Deepa perigidad, shruti jamagoud yallavva maled and sharada gavade, QSPR analysis of certain degree based topological indices, *J. Statist. Appl. Prob.* 6 (2) (2017) 1-11.
- [6] M. Randic, Comparative structure-property studies: regressions using a single descriptor, *Croat. Chem. Acta* 66 (1993) 289-312.
- [7] M. Randic, Quantitative Structure-Property Relationship: boiling points and planar benzenoids, *New J. Chem.* 20 (1996) 1001-1009.
- [8] M.C. Shanmukha, N.S. Basavarajappa, K.N. Anilkumar, Predicting physico-chemical properties of octane isomers using QSPR Approach, *Malaya Journal of Mathematik.* 8 (1) (2020) 104-116.
- [9] Sakander Hayat, Muhammad Imran, Jia-Bao Liu, Correlation between the Estrada index and  $[\chi]$ -electronic energies for benzenoid hydrocarbons with applications to boron nanotubes, *Int. J. Quant. Chem.* (2019).
- [10] Adnan Aslam, Safyan Ahmad, Wei Gao, On topological indices of boron triangular nanotubes, *Z. Naturforsch.* 72 (8) (2017) 711-716.
- [11] Sakander Hayat, Shaohui Wang, Jia-Bao Liu, Valency-based topological descriptors of chemical networks and their applications, *Appl. Math. Model.* (2018).
- [12] Sakander Hayat, Muhammad Imran, Jia-Bao Liu, An Efficient computational technique for degree and distance based topological descriptors with applications, 2019.
- [13] E. Estrada, L. Torres, L. Rodriguez, I. Gutman, An atom-bond connectivity index: modeling the enthalpy of formation of alkanes, *Indian J. Chem.* 37A (1998) 849-855.
- [14] M. Ghorbani, M.A. Hosseinzadeh, Computing ABC4 index of Nanostar dendrimers, *Optoelectron. Adv. Mater-Rapid Commun.* 4 (9) (2010) 1419-1422.
- [15] M. Randic, On Characterization of molecular branching, *J. Am. Chem. Soc.* 97 (1975) 6609-6615.
- [16] B. Zhou, N. Trinajstić, On general sum-connectivity index, *J. Math. Chem.* 47 (2010) 210-218.
- [17] D. Vukicevic-B. Furtula, Topological index based on the ratios of geometrical and arithmetical means of end-vertex degrees of edges, *J. Math. Chem.* 46 (2009) 1369-1376.
- [18] A. Graovac, M. Ghorbani, M.A. Hosseinzadeh, Computing Fifth Geometric-Arithmetic index for nanostar dendrimers, *J. Math. Nanosci.* 1 (2011) 33-42.
- [19] I. Gutman, Degree based topological indices, *Croat. Chem. Acta* 86 (2013) 351-361.
- [20] S. Fajtlowicz, On conjectures of graffitti II, *Congr. Numerantium* 60 (1987) 189-197.
- [21] G.H. Shirdel, H. RezaPour, A.M. Sayadi, The hyper-zagreb index of graph operations, *Iran. J. Math. Chem.* 4 (2) (2013) 213-220.
- [22] Ali Astanesh-Asl, G. H Fath-Tabar, Computing the first and third Zagreb polynomials of certain product of graphs, *Iran. J. Math. Chem.* 2 (2) (2011) 73-78.
- [23] B. Furtula, I. Gutman, A forgotten topological index, *J. Math. Chem.* 53 (2015) 213-220.
- [24] V. Alexander, Upper and lower bounds of symmetric division deg index, *Iran. J. Math. Chem.* 5 (2) (2014) 91-98.

**Update**

**Heliyon**

Volume 6, Issue 9, September 2020, Page

DOI: <https://doi.org/10.1016/j.heliyon.2020.e04754>



## Erratum to “Degree-based topological indices on anticancer drugs with QSPR analysis” [Heliyon 6 (6) (June 2020) e04235]



M.C. Shanmukha<sup>a,b,\*</sup>, N.S. Basavarajappa<sup>b,c</sup>, K.C. Shilpa<sup>b,d</sup>, A. Usha<sup>e</sup>

<sup>a</sup> Department of Mathematics, Jain Institute of Technology, Davanagere, 577003, Karnataka, India

<sup>b</sup> Visvesvaraya Technological University, Belagavi, Karnataka, India

<sup>c</sup> Department of Mathematics, Bapuji Institute of Engineering and Technology, Davanagere, 577004, Karnataka, India

<sup>d</sup> Department of Computer Science and Engg., Bapuji Institute of Engineering and Technology, Davanagere, 577004, Karnataka, India

<sup>e</sup> Department of Mathematics, Alliance College of Engineering and Design, Alliance University, Anekal-Chandapura Road, Bangalore, Karnataka, India

In the original published version of this article, errors were introduced to one equation as shown on page 2. This has now been corrected. The publisher apologizes for these mistakes. There were also typographical errors in another two equations on page 2. This has now been corrected. In addition, there was a typographical error in table 16, where a value was incorrectly listed as 180619 instead of 18.619. The author apologizes for these mistakes.

Correct versions of each equation and the table can be found below. Both the HTML and PDF versions of the article have been updated to correct the errors.

**Definition 1.4.**  $S(G) = \sum_{e=vw \in E(G)} \sqrt{\frac{1}{d_v + d_w}}$

**Definition 1.5.**  $GA(G) = \sum_{e=vw \in E(G)} \frac{2\sqrt{d_v d_w}}{d_v + d_w}$

**Definition 1.6.**  $GA_5(G) = \sum_{e=vw \in E(G)} \frac{2\sqrt{s_v s_w}}{s_v + s_w}$

Table 16: Statistical parameters for the linear QSPR model For F(G).

Physical Properties	N	a	b	r	F	p	Indicator
Boiling Point	17	269.670	0.865	0.744	18.619	0.001	Significant
Melting Point	15	123.82	0.257	0.559	5.462	0.038	Significant
Enthalpy	16	50.889	0.106	0.730	15.942	0.001	Significant
Flash Point	16	125.652	0.453	0.664	11.012	0.005	Significant
Molar Refraction	17	33.304	0.172	<b>0.841</b>	36.186	0.000	Significant

The significance of bold numbers denotes highest correlation value.

DOI of original article: <https://doi.org/10.1016/j.heliyon.2020.e04235>.

\* Corresponding author.

E-mail address: [mcsanmukha@gmail.com](mailto:mcsanmukha@gmail.com) (M.C. Shanmukha).

<https://doi.org/10.1016/j.heliyon.2020.e04754>

Received 17 August 2020; Accepted 17 August 2020

2405-8440/© 2020 Published by Elsevier Ltd. This is an open access article under the CC BY-NC-ND license (<http://creativecommons.org/licenses/by-nc-nd/4.0/>).



# Predicting physico-chemical properties of octane isomers using QSPR approach

M.C. Shanmukha<sup>1</sup>, N.S. Basavarajappa<sup>2\*</sup> and K.N. Anilkumar<sup>3</sup>

## Abstract

Topological indices are very important parameters in the QSPR study. In this paper a novel topological index named as  $RS_2$ - index has been introduced. Further, we carry QSPR analysis for the set of octane isomers. The QSPR study reveals that the performance of  $RS_2$ - index is better than the  $M_1(G)$ ,  $M_2(G)$ ,  $\overline{M}_1(G)$  and  $\overline{M}_2(G)$ .

## Keywords

Topological indices, QSPR-analysis, octane isomers.

## AMS Subject Classification

05C90, 05C35, 05C12.

<sup>1</sup> Department of Mathematics, Jain Institute of Technology, Davanagere- 577003, Karnataka, India and affiliated to Visvesvaraya Technological University, Belagavi, Karnataka.

<sup>2,3</sup> Department of Mathematics, Bapuji Institute of Engineering and Technology, Davanagere- 577004, Karnataka, India and affiliated to Visvesvaraya Technological University, Belagavi, Karnataka.

\*Corresponding author: <sup>2</sup>dr.nsbasavaraj@gmail.com; <sup>1</sup>mcshanmukha@gmail.com; <sup>3</sup>kn.anil5340@gmail.com

Article History: Received 27 October 2019; Accepted 18 November 2019

©2020 MJM.

## Contents

1	Introduction .....	104
2	QSPR Analysis $RS_2(G)$ - Index .....	105
3	Linear Regression Models .....	105
4	Quadratic Regression Models .....	105
5	Logarithmic Regression Models .....	105
6	Results and Discussions .....	106
7	The Correlations of $RS_1(G)$ with the Physico-chemical Properties of Octane isomers .....	106
8	The Correlations of $M_1(G)$ with the Physico-chemical Properties of Octane isomers .....	108
9	The Correlations of $M_2(G)$ with the Physico-chemical Properties of Octane isomers .....	110
10	The Correlations of $\overline{M}_1(G)$ with the Physico-chemical Properties of Octane isomers .....	111
11	The Correlations of $\overline{M}_2(G)$ with the Physico-chemical Properties of Octane isomers .....	113
12	Conclusion .....	115
13	Acknowledgment .....	115
	References .....	115

## 1. Introduction

Let  $G = (V, E)$  be a graph. The number of vertices of  $G$  we denote by  $n$  and the number of edges we denote by  $m$ , thus  $|V(G)| = n$  and  $|E(G)| = m$ . The degree of a vertex  $v$ , denoted by  $d_G(v)$ .

The complement of a graph  $G$ , denoted by  $\overline{G}$ , is a simple graph on the same set of vertices  $V(G)$  in which two vertices  $u$  and  $v$  are connected by an edge  $uv$ , if and only if they are not adjacent in  $G$ . Obviously,  $E(G) \cup E(\overline{G}) = E(K_n)$ , and  $\overline{m} = |E(\overline{G})| = \frac{n(n-1)}{2} - m$ . For undefined terminologies we refer the reader to [3].

There are two invariants called the first Zagreb index and second Zagreb index [1, 2, 4–6] defined as

$$M_1(G) = \sum_{u \in V(G)} d_G(u)^2$$

and

$$M_2(G) = \sum_{uv \in E(G)} d_G(u) d_G(v),$$

respectively.

In fact, one can rewrite the first Zagreb index as

$$M_1(G) = \sum_{uv \in E(G)} [d_G(u) + d_G(v)].$$

Noticing that contribution of nonadjacent vertex pairs should be taken into account when computing the weighted Wiener polynomials of certain composite graphs (see [1]) defined first Zagreb coindex and second Zagreb coindex as

$$\overline{M}_1(G) = \sum_{uv \notin E(G)} [d_G(u) + d_G(v)]$$

$$\overline{M}_2(G) = \sum_{uv \notin E(G)} d_G(u) d_G(v),$$

respectively.

It follows directly from the definition of second Zagreb coindex achieve its smallest possible value of zero. Therefore, throughout this paper, to avoid trivialities, we assume that the graphs considered have second Zagreb coindex value at least one.

Recently Hosamani et. al., [9] have put forward ten novel topological index  $S_2(G) = \sum_{uv \in E} d_G(u)^{|d_G(u)|} + d_G(v)^{|d_G(v)|}$ .

Based on this concept, here we considering the reciprocal version of  $S_2(G)$ . Which is defined as follows:

$$RS_2(G) = \frac{1}{\sum_{uv \in E} d_G(u)^{|d_G(u)|} + d_G(v)^{|d_G(v)|}}$$

## 2. QSPR Analysis $RS_2(G)$ - Index

Now, we are interested in to check the chemical applicability of  $RS_2(G)$  of molecular graph  $G$ . For this reason, we are interested to carry QSPR analysis of  $RS_2(G)$  with the set of octane isomers. The following statistical models have been used for the study:

- Linear Model:  $P = a(RS_2(G)) + b$
- Quadratic Model :  $P = a(RS_2(G))^2 + b(RS_2(G)) + c$
- Logarithmic Model:  $P = a + b \ln(RS_2(G))$

where  $P$  is a physical property,  $a, b$  and  $c$  are constants.

Here we have examined the chemical applicability of the  $RS_2$ -index and compared the values with the so called degree based topological indices, namely, first Zagreb index  $M_1(G)$ , second Zagreb index  $M_2(G)$ , first Zagreb coindex  $\overline{M}_1(G)$  and second Zagreb coindex ( $\overline{M}_2(G)$ ), for modeling ten representative physical properties [boiling points(BP), molar volumes (mv) at 20°C, molar refractions (mr) at 20°C, heats of vaporization (hv) at 25°C, surface tensions (st) 20°C and melting points (mp), acentric factor (AcentFac) and DHVAP] of octane isomers. The values are compiled in Table 1 [8].

## 3. Linear Regression Models

In this section we consider the linear regression models for  $RS_2(G)$ ,  $M_1(G)$ ,  $M_2(G)$ ,  $\overline{M}_1(G)$  and  $\overline{M}_2(G)$  as follows:

$$\begin{aligned} bp &= 106.090 + 15.401(RS_2(G)) \\ \text{Heatsofvaporization} &= -222.798 + 12.047(RS_2(G)) \\ TC &= 282.929 + 13.520(RS_2(G)) \\ PC &= 26.948 - 1.122(RS_2(G)) \\ S &= 98.878 + 13.213(RS_2(G)) \\ D &= 0.742 - 0.059(RS_2(G)) \\ \text{Radius} &= 1.403 + 0.458(RS_2(G)) \\ \text{HVAP} &= 37.829 + 1.573(RS_2(G)) \\ MV &= 160.257 + 1.649(RS_2(G)) \\ AF &= 0.283 + 0.107(RS_2(G)) \\ \text{DHVAP} &= 8.545 + 1.175(RS_2(G)) \end{aligned}$$

## 4. Quadratic Regression Models

In this section we consider the quadratic regression models for  $RS_2(G)$ ,  $M_1(G)$ ,  $M_2(G)$ ,  $\overline{M}_1(G)$  and  $\overline{M}_2(G)$  as follows:

$$\begin{aligned} bp &= 16.912(RS_2(G))^2 - 1.581(RS_2(G)) + 109.337 \\ hv &= 7.986(RS_2(G))^2 + 4.028(RS_2(G)) - 221.265 \\ tc &= 17.159(RS_2(G))^2 - 3.623(RS_2(G)) + 282.233 \\ pc &= 3.291(RS_2(G))^2 - 4.395(RS_2(G)) + 26.104 \\ s &= 25.445(RS_2(G))^2 - 12.182(RS_2(G)) + 96.539 \\ d &= -0.234(RS_2(G))^2 + 0.175(RS_2(G)) + 0.776 \\ r &= 0.147(RS_2(G))^2 + 0.310(RS_2(G)) + 1.463 \\ hvap &= -11.530(RS_2(G))^2 + 13.049(RS_2(G)) + 40.33 \\ mv &= 5.835(RS_2(G))^2 - 3.798(RS_2(G)) + 159.296 \\ af &= 0.154(RS_2(G))^2 - 0.047(RS_2(G)) + 0.274 \\ dhvap &= 0.854(RS_2(G))^2 + 0.320(RS_2(G)) + 8.607 \end{aligned}$$

## 5. Logarithmic Regression Models

In this section we consider the linear regression models for  $RS_2(G)$ ,  $M_1(G)$ ,  $M_2(G)$ ,  $\overline{M}_1(G)$  and  $\overline{M}_2(G)$  as follows:

$$\begin{aligned} bp &= 116.930 + 3.481(RS_2(G)) \\ \text{Heatsofvaporization} &= -213.886 + 3.190(RS_2(G)) \\ TC &= 293.843 + 4.566(RS_2(G)) \\ PC &= 26.410 + 0.018(RS_2(G)) \\ S &= 109.392 + 4.299(RS_2(G)) \\ D &= 0.689 - 0.027(RS_2(G)) \\ \text{Radius} &= 1.730 + 0.108(RS_2(G)) \\ \text{HVAP} &= 38.246 - 0.390(RS_2(G)) \\ MV &= 161.883 + 1.002(RS_2(G)) \\ AF &= 0.365 + 0.032(RS_2(G)) \\ \text{DHVAP} &= 9.413 + 0.310(RS_2(G)) \end{aligned}$$





## 6. Results and Discussions

The correlation coefficient( $r$ ) values for the above mentioned physical properties of octane isomers with  $RS_2(G)$ -index gives interesting results. Start from the linear regression models, The  $r$  values ranging from 0.022 to 0.597, where as the  $r$  value for the quadratic regression model ranging from 0.032 to 0.602 and for logarithmic regression model the range of  $r$  value is 0.036 to 0.687.

The correlation coefficient( $r$ ) values for the physical properties of octane isomers with  $M_1(G)$ -index as follows: Start from the linear regression models, The  $r$  values ranging from 0.038 to 0.862, where as the  $r$  value for the quadratic regression model ranging from 0.053 to 0.862 and for logarithmic regression model the range of  $r$  value is 0.050 to 0.859.

The correlation coefficient( $r$ ) values for the physical properties of octane isomers with  $M_2(G)$ -index as follows: Start from the linear regression models, The  $r$  values ranging from 0.014 to 0.902, where as the  $r$  value for the quadratic regression model ranging from 0.042 to 0.902 and for logarithmic regression model the range of  $r$  value is 0.014 to 0.897.

The correlation coefficient( $r$ ) values for the physical properties of octane isomers with  $\bar{M}_1(G)$ -index as follows: Start from the linear regression models, The  $r$  values ranging from 0.038 to 0.862, where as the  $r$  value for the quadratic regression model ranging from 0.029 to 0.861 and for logarithmic regression model the range of  $r$  value is 0.053 to 0.862.

The correlation coefficient( $r$ ) values for the physical properties of octane isomers with  $\bar{M}_2(G)$ -index as follows: Start from the linear regression models, The  $r$  values ranging from 0.027 to 0.848, where as the  $r$  value for the quadratic regression model ranging from 0.031 to 0.862 and for logarithmic regression model the range of  $r$  value is 0.043 to 0.865.

For model (1), the  $RS_2(G)$ -index shows minimum correlation with molar volume and the maximum correlation with the DHVAP of the octane isomers, the  $M_1(G)$  shows minimum correlation with HVAP and the maximum correlation with AF, the  $M_2(G)$  shows minimum correlation with HVAP and the maximum correlation with AF, the  $\bar{M}_1(G)$  shows minimum correlation with HVAP and the maximum correlation with AF and finally the  $\bar{M}_2(G)$  shows minimum correlation with HVAP and the maximum correlation with entropy.

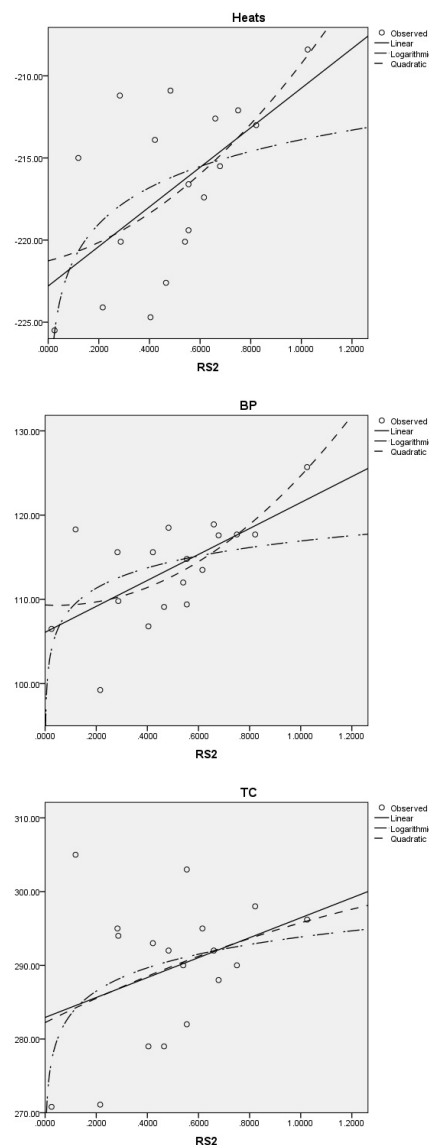
For model (2), the  $RS_2(G)$ -index shows minimum correlation with molar volume and the maximum correlation with the DHVAP of the octane isomers, the  $M_1(G)$  shows minimum correlation with MV and the maximum correlation with AF, the  $M_2(G)$  shows minimum correlation with TC and the maximum correlation with AF, the  $\bar{M}_1(G)$  shows minimum correlation with HVAP and the maximum correlation with AF and finally the  $\bar{M}_2(G)$  shows minimum correlation with TC

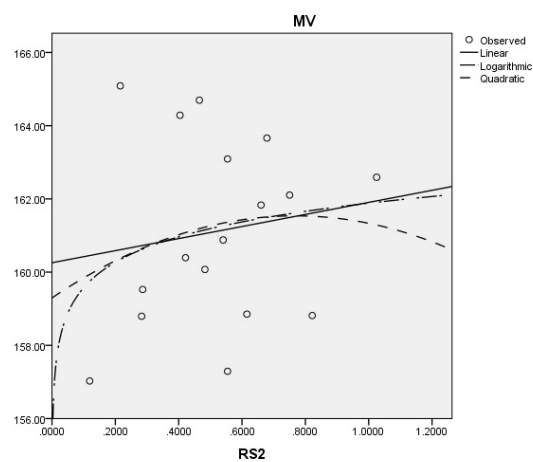
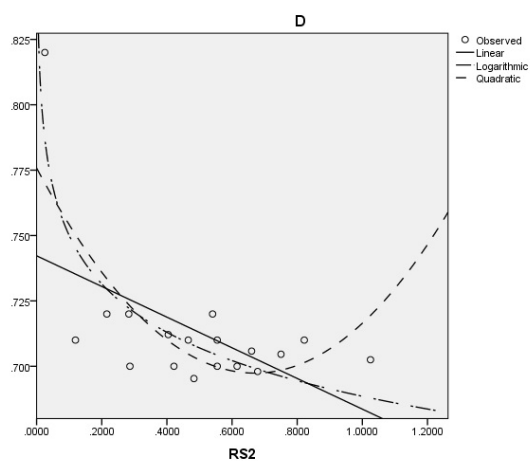
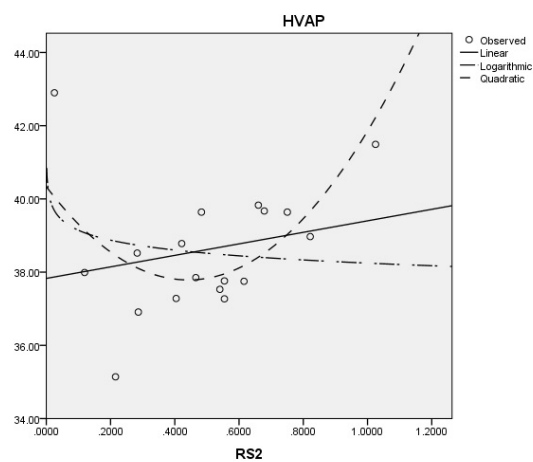
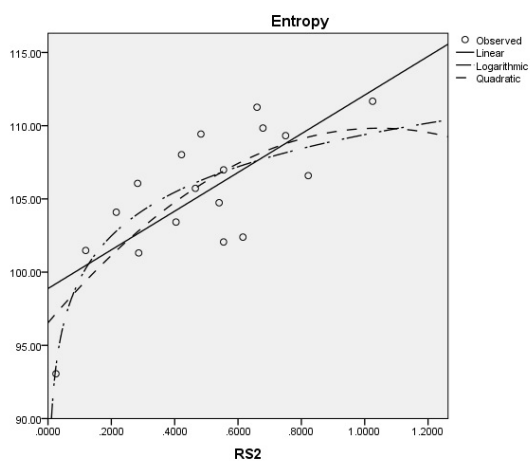
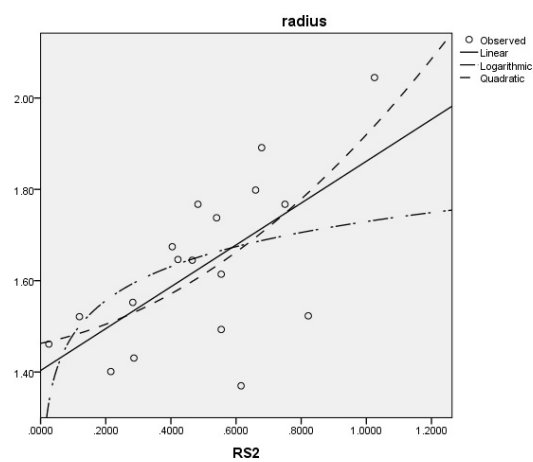
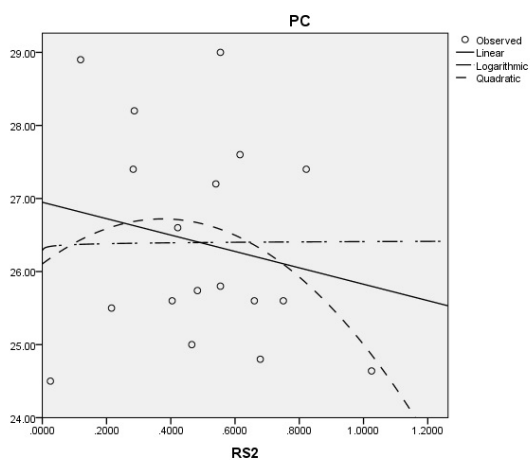
and the maximum correlation with entropy.

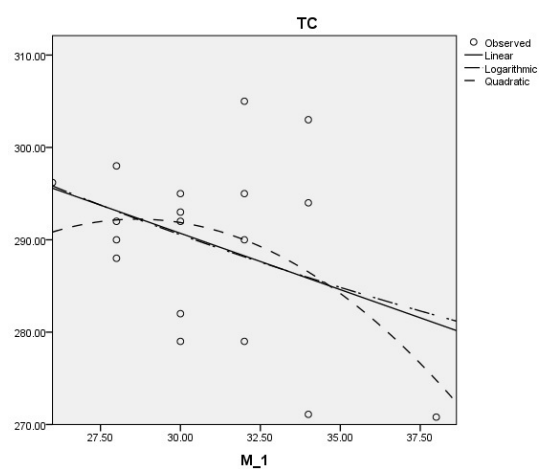
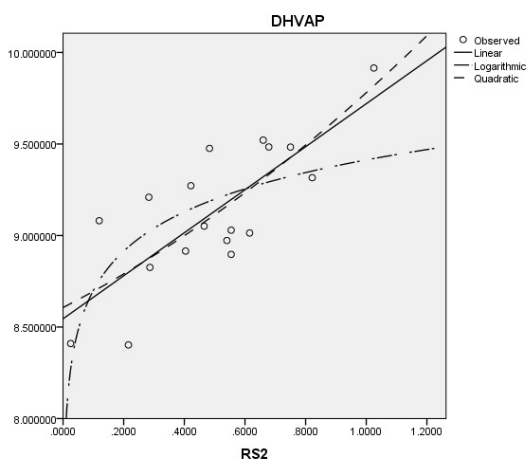
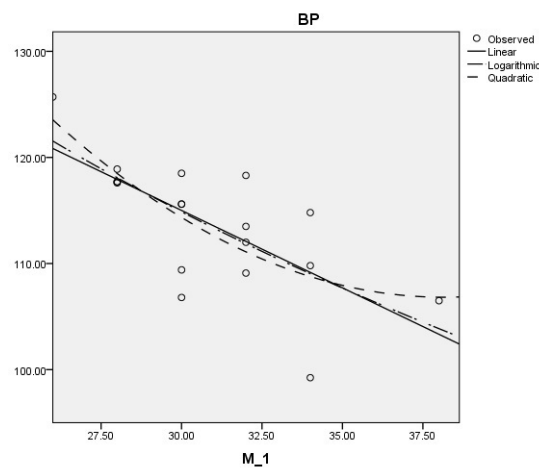
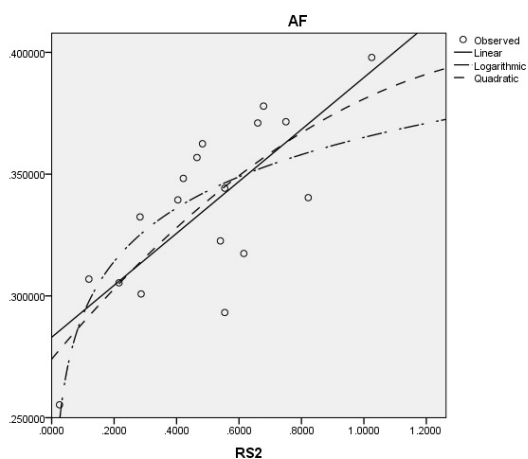
Finally, for model (3), the  $RS_2(G)$ -index shows minimum correlation with HVAP and the maximum correlation with the D of the octane isomers, the  $M_1(G)$  shows minimum correlation with MV and the maximum correlation with AF, the  $M_2(G)$  shows minimum correlation with TC and the maximum correlation with AF, the  $\bar{M}_1(G)$  shows minimum correlation with MV and the maximum correlation with AF and finally the  $\bar{M}_2(G)$  shows minimum correlation with TC and the maximum correlation with entropy.

## 7. The Correlations of $RS_1(G)$ with the Physico-chemical Properties of Octane isomers

The correlation coefficient of  $RS_2(G)$  with above mentioned physical properties are depicted in the following figures.

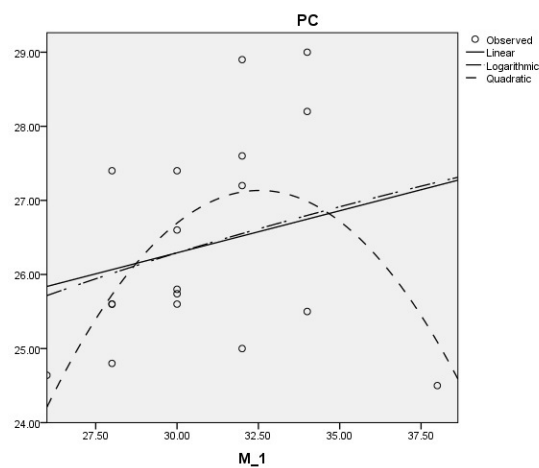
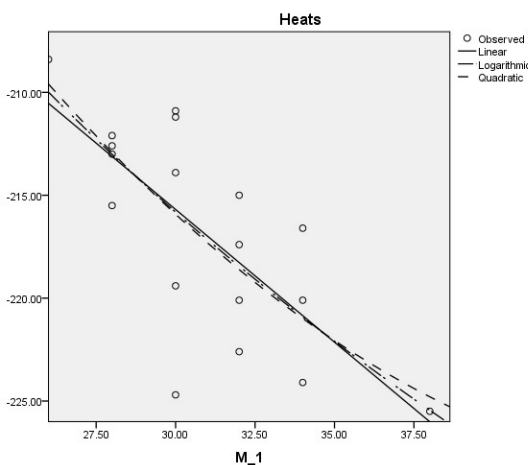


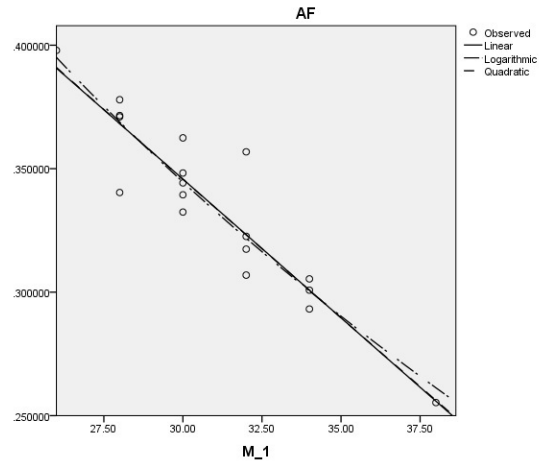
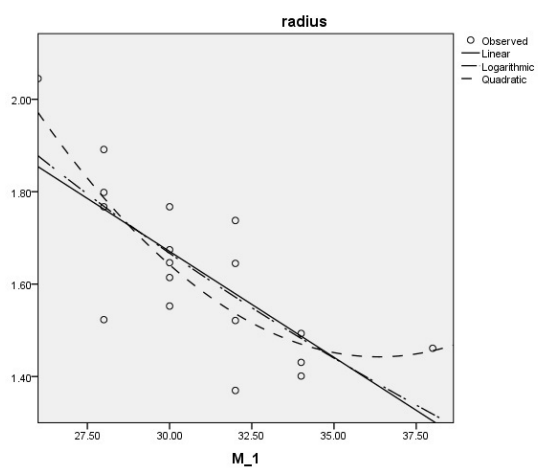
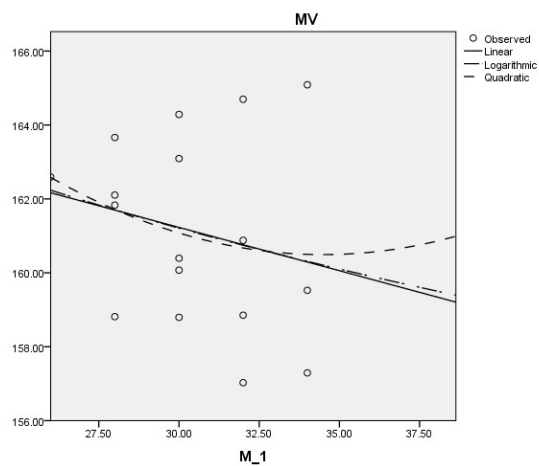
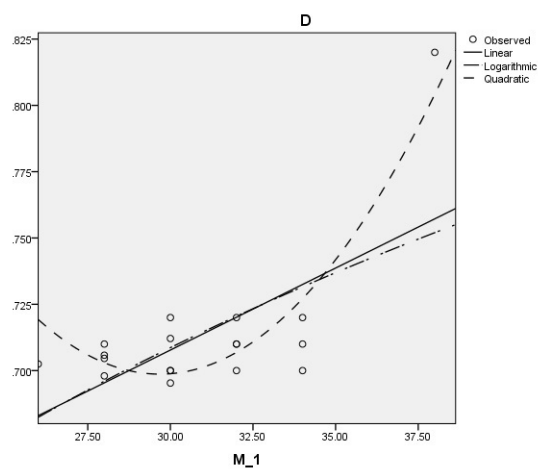
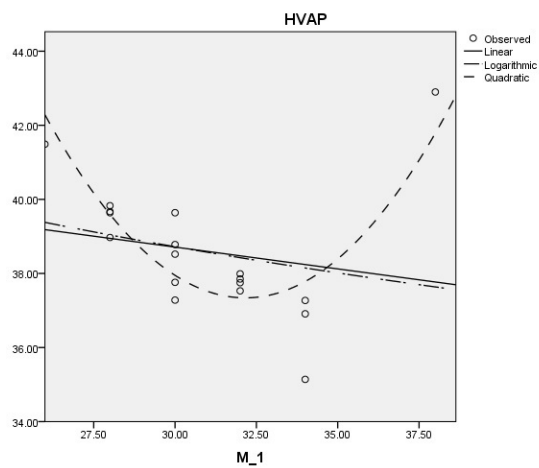
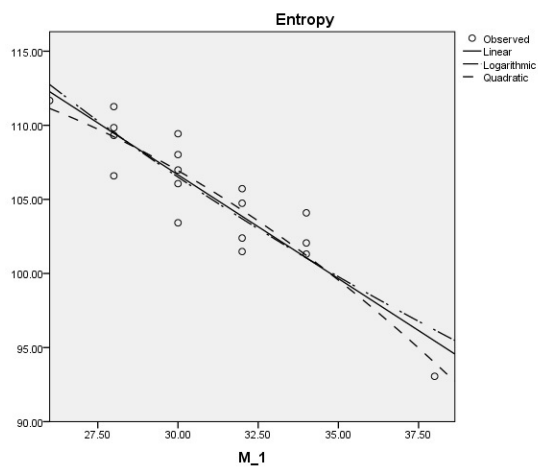


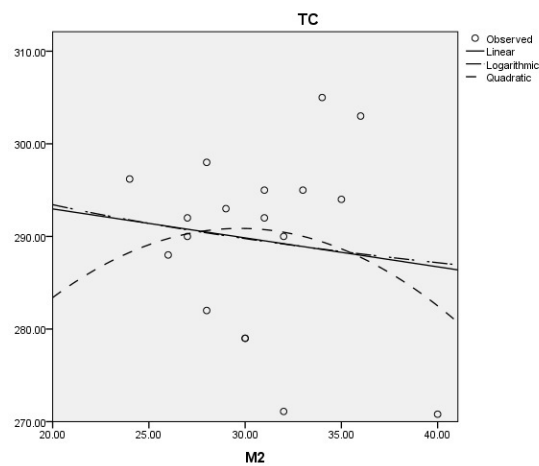
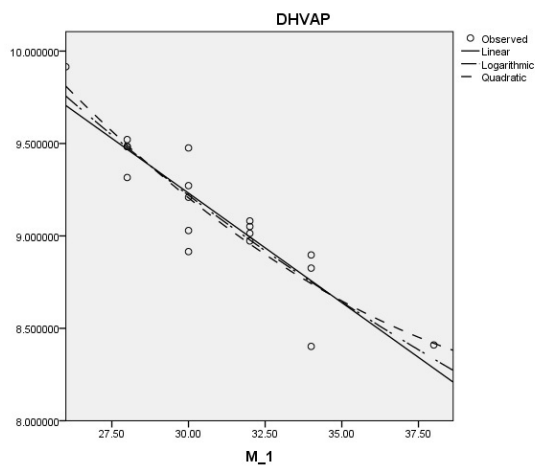


## 8. The Correlations of $M_1(G)$ with the Physico-chemical Properties of Octane isomers

The correlation coefficient of  $M_1(G)$  with above mentioned physical properties are depicted in the following figures.

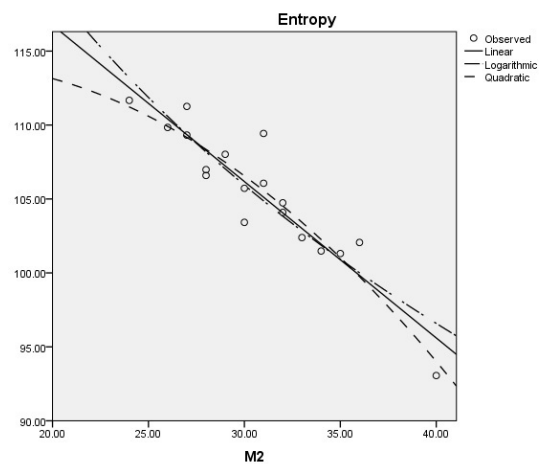
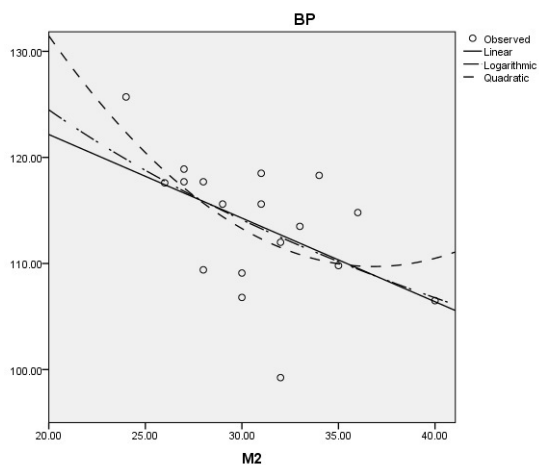
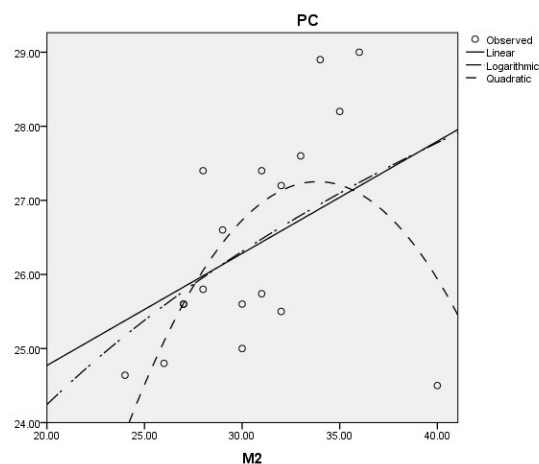
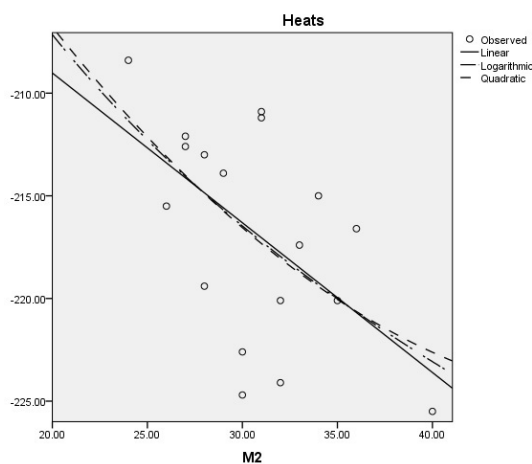


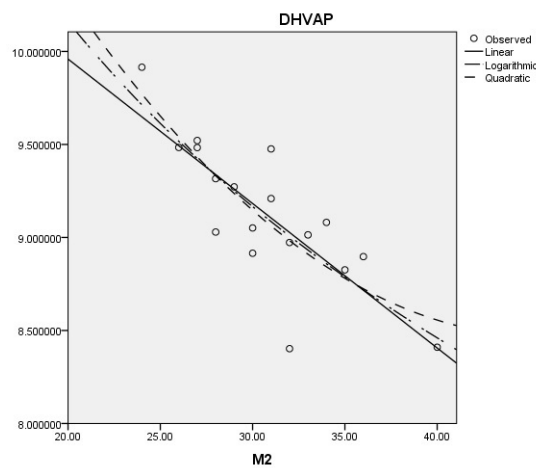
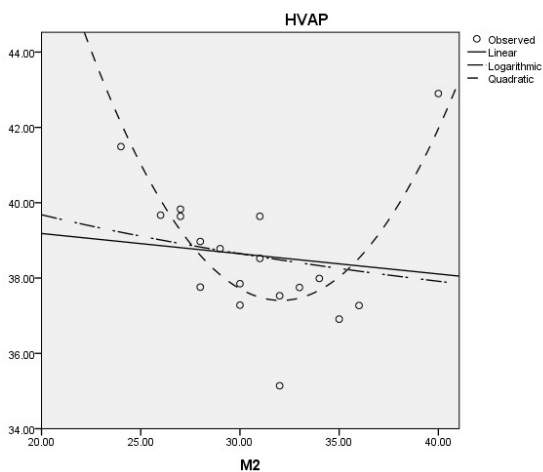
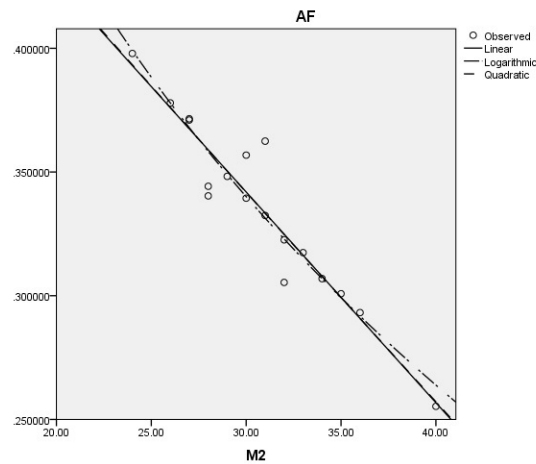
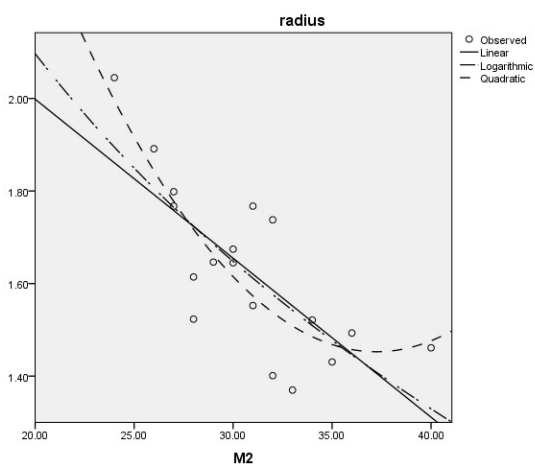
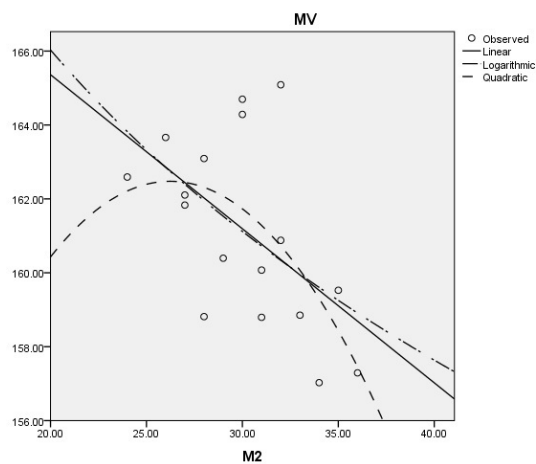
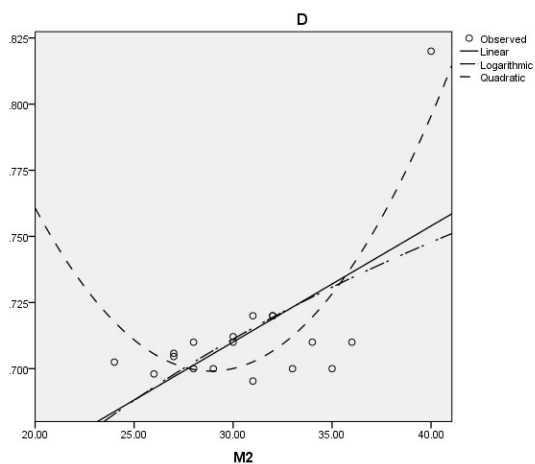




## 9. The Correlations of $M_2(G)$ with the Physico-chemical Properties of Octane isomers

The correlation coefficient of  $M_2(G)$  with above mentioned physical properties are depicted in the following figures.



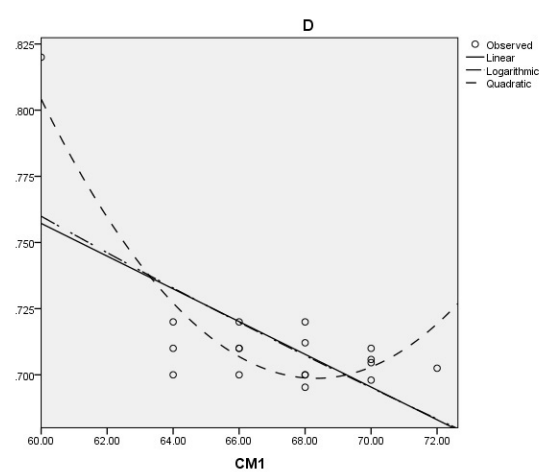
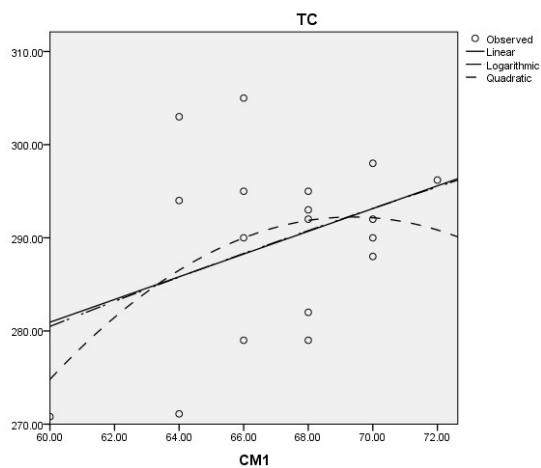
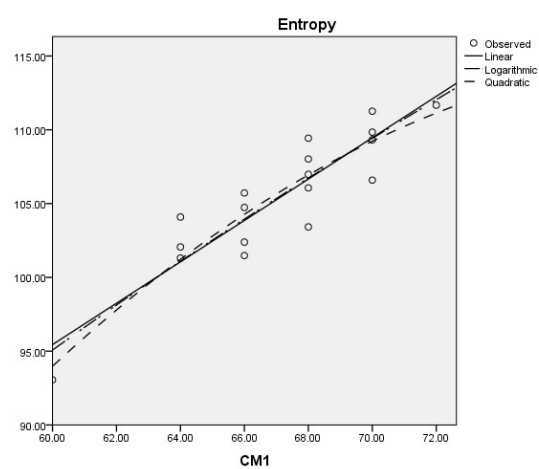
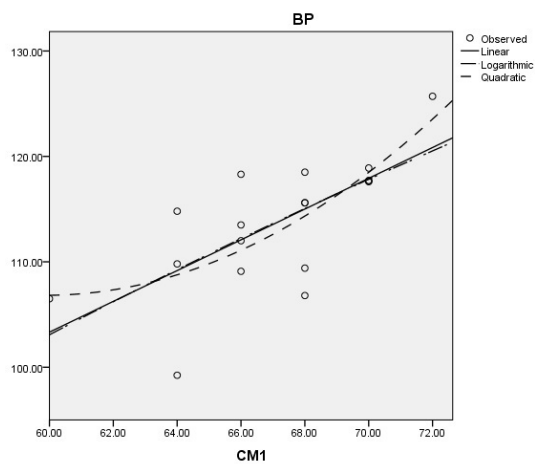
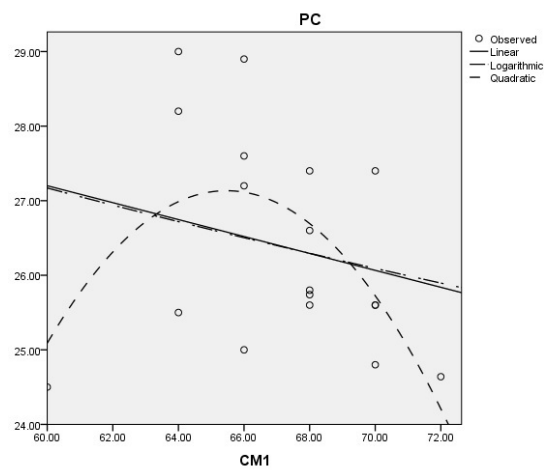
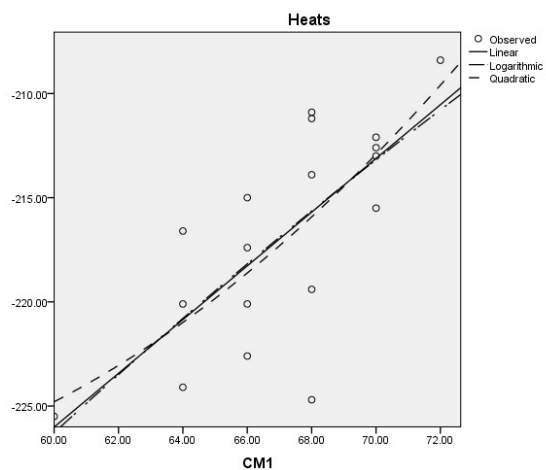


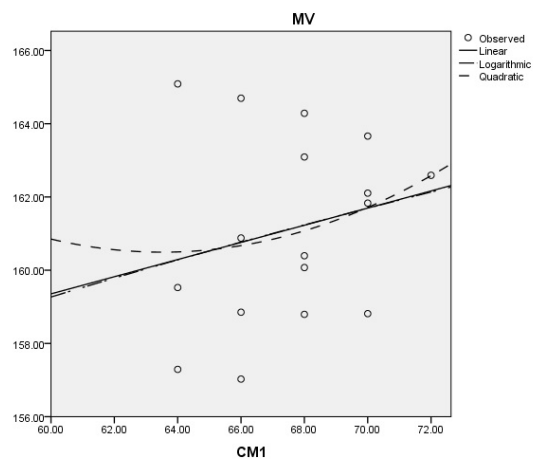
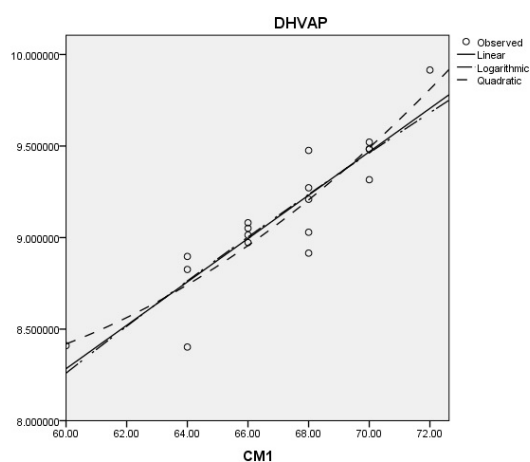
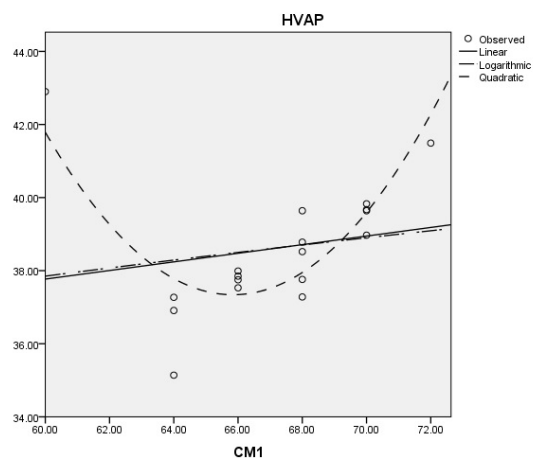
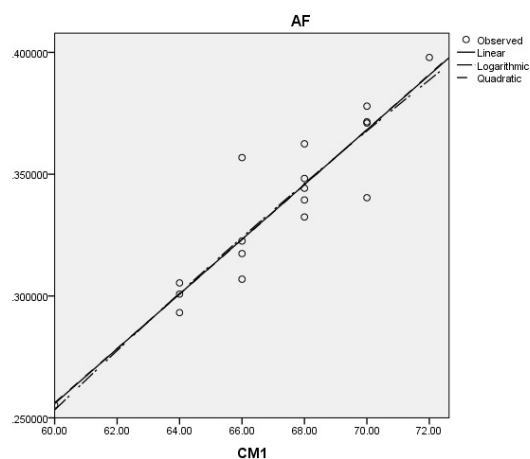
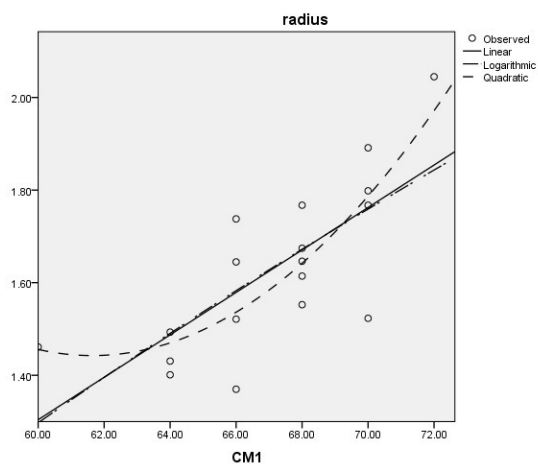
## 10. The Correlations of $\overline{M}_1(G)$ with the Physico-chemical Properties of Octane isomers

The correlation coefficient of  $\overline{M}_1(G)$  with above mentioned physical properties are depicted in the following figures.



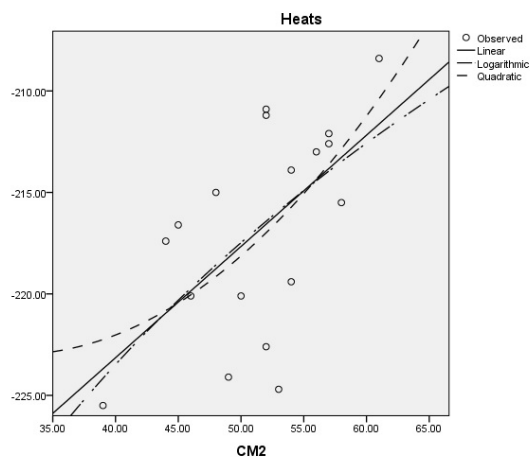


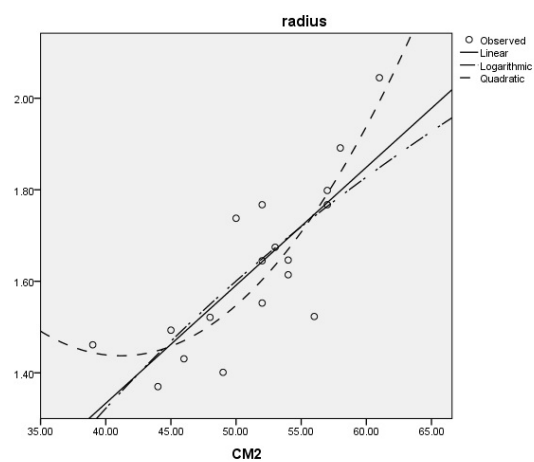
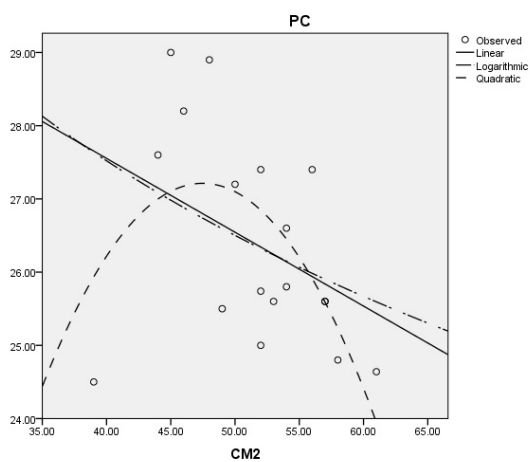
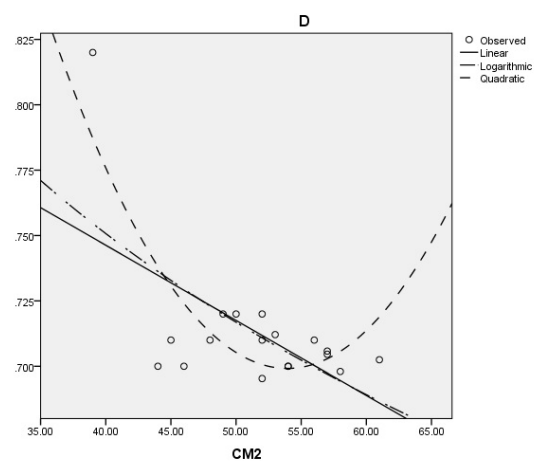
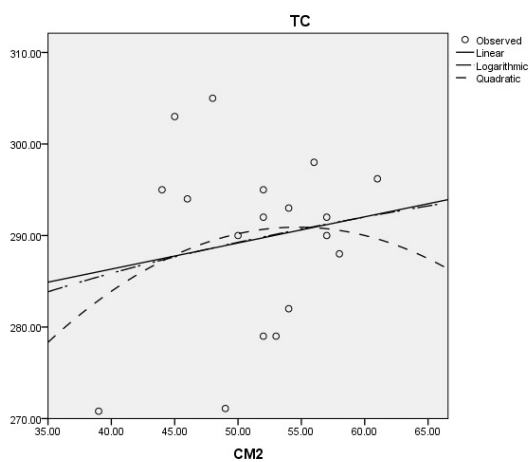
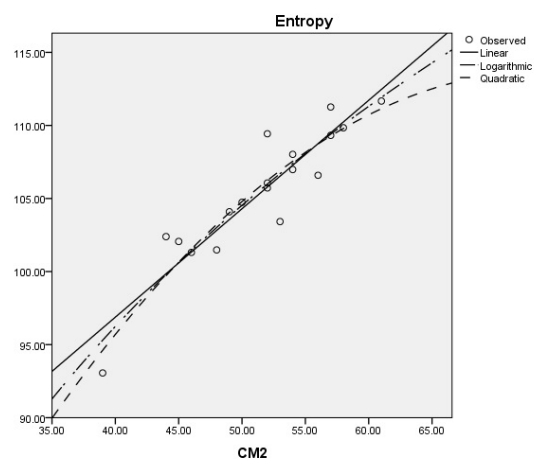
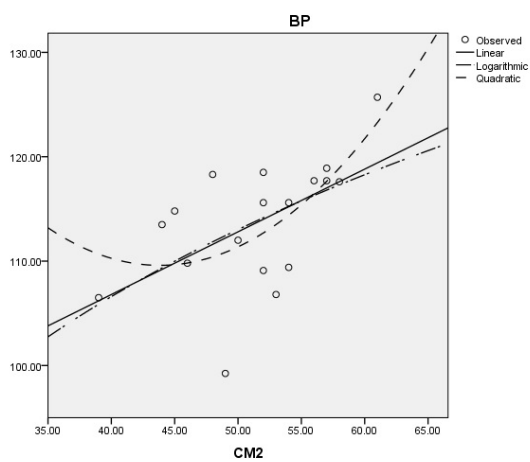


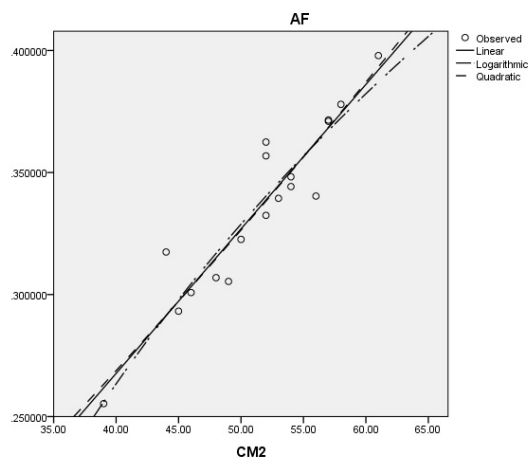
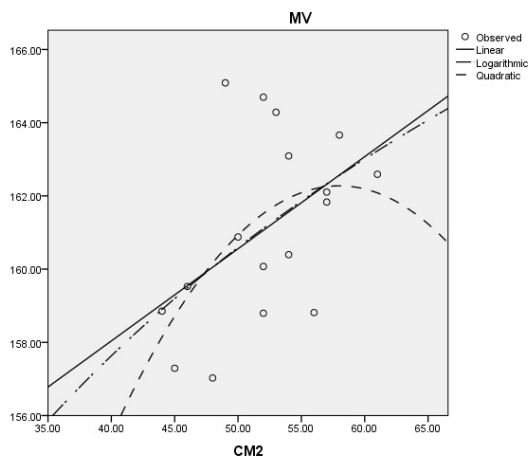
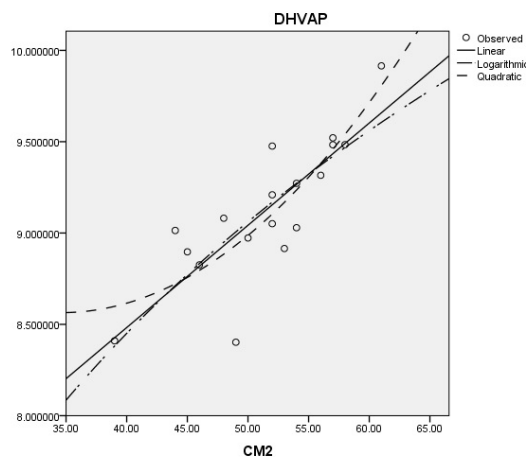
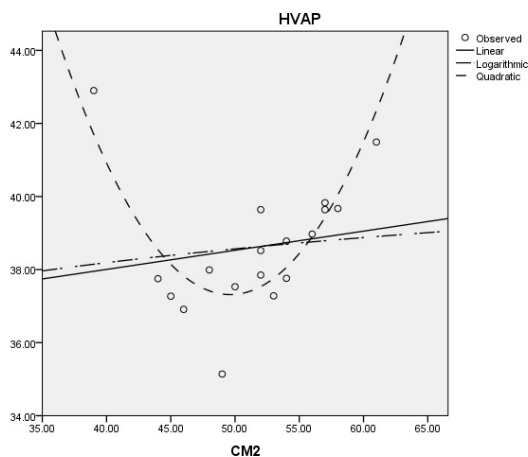


## 11. The Correlations of $\overline{M}_2(G)$ with the Physico-chemical Properties of Octane isomers

The correlation coefficient of  $\overline{M}_2(G)$  with above mentioned physical properties are depicted in the following figures.







## 12. Conclusion

The results of QSPR studies reveals that the regression models (1)-(3) are the most significant models to predict the physicochemical properties of molecular graphs.

## 13. Acknowledgment

The authors are thankful to the anonymous reviewers for their useful comments to improve the quality of the paper.

## References

- [1] A. R. Ashrafi, T. Došlić, A. Hamzeh, The Zagreb coindices of graph operations, *Discrete Appl. Math.* 158 (2010) 1571-1578.
- [2] I. Gutman, Degree-based topological indices, *Croat. Chem. Acta* 86(4)(2013) 351-361.
- [3] F. Harary, *Graph Theory*, Addison-Wesely, Reading, 1969.
- [4] S. M. Hosamani, I. Gutman, Zagreb indices of transformation and total transformation graphs, *Appl. Math. Comput.*, 247 (2014), 1156-1160.
- [5] S. M. Hosamani, B. Basavanagoud, New upper bounds for the first Zagreb index, *MATCH Commun. Math. Comput. Chem.*, 74(1)(2015), 97-101.
- [6] S. M. Hosamani, S. H. Malghan and I. N. Cangul, The first geometric-arithmetic index of graph operations, *Advances and Applications in Mathematical Sciences*, 14(6)(2015), 155-163.
- [7] S. M. Hosamani, Computing Sanskruti index of certain nanostructures, *J. Appl. Math. Comput.*, 1-9 (2016) DOI 10.1007/s12190-016-1016-9.
- [8] S. M. Hosamani Correlation of domination parameters with physicochemical properties of octane isomers. *Applied Mathematics and Nonlinear Sciences*, 1(2016), 345-352.
- [9] S. M. Hosamani, V.B. Awati and R. M. Honnamore, Estimation of numerical invariants associated with certain



nanostructures and dendrimers via degree based descriptors, *Journal of Mathematical Chemistry*, (Accepted).

- [10] M. Thakur, A. Thakur, P.V. Khadikar, QSAR study of benzene sulphonamide carbonic anhydrase inhibitors: Topological approach using Balaban index, *Bioorg. Med. Chem.*, 12(4)(2004), 789–793.
- [11] N. Trinajstić, Chemical graph theory, *CRC Press*, 1992.

\*\*\*\*\*

ISSN(P):2319 – 3786

Malaya Journal of Matematik

ISSN(O):2321 – 5666

\*\*\*\*\*



## PRIORITY ASSESSMENT OF FINE AGGREGATES FOR SATISFYING COMPRESSIVE STRENGTH AS PER IRC 44-2017 GUIDELINES

**Pruthviraj S R<sup>\*1</sup>, Maruthi T<sup>\*2</sup>, Raghavendra S<sup>\*3</sup>, Revanna E<sup>\*4</sup>**

<sup>\*1,2,3,4</sup> M-Tech Student, Department of studies in Civil Engineering, UBDTCE, DAVANAGERE,  
KARNATAKA, INDIA

### ABSTRACT

Cement, sand and combination are simple desires for any production industry. Sand is a top cloth used for instruction of mortar and urban and which performs a first-rate function in blend design. This paper presents six different types of fine aggregates which are differentiated according to the availability, Mode of generation or preparation and raw generation. The main objective of this research is to define the priority of these materials with respect to its compressive strength. Here, Each Fine aggregate is using completely for the concrete matrix to know the individual performance against compressive strength after 7, 14 and 28 days of curing. Defining the material property of each fine aggregate as per BIS was done at laboratory and according to standards fine aggregates are classified and differentiated.

**Keywords:** Sand, Alternative Material, Quarry Stone Dust, Physical Properties, Mechanical Properties.

### I. INTRODUCTION

Concrete requirements specify the best combination necessities essential to reap homogeneous, doable and sturdy concrete of good enough strength. The use of overwhelmed sand is commonly restrained because of the excessive cement paste extent had to reap a good enough workability of concrete. The quantity of extra paste content material relies upon on form, texture, grading and diploma of fineness of the sand. Mechanical houses of concrete containing great sand rely upon paste composition, paste volume, the bodily traits of the sand debris and the character of the paste-mixture interface. The growth of water call for of concrete mixtures produced via way of means of the unfavourable results of form and texture of sand may be mitigated the use of a high-variety water-lowering admixture. Several research on high-strength concrete (HSC) had been evolved with the goal of reading the impact of coarse mixture from extraordinary mineralogical re assets.

However, few researches had been conducted at the impact of sand from extraordinary re assets and the codes only consist of short necessities for great aggregates. The impact of fineness and form and floor texture of great aggregates on mechanical houses is often now no longer a aspect in traditional concretes, even though those houses may also motive an growth with inside the water call for. For those concrete, the hydrated cement paste and the transition area across the mixture are noticeably weak. Consequently, the water/cement (w/c) ratio controls the mechanical houses of concrete for the equal diploma of hydration. In many mixture quarries produce herbal sand from extraordinary mineralogical re assets. The most important goal of these studies is to offer records approximately the results of fineness and form and texture of great mixture with those observations how the electricity varies from extraordinary great aggregates on clean and hardened houses of concrete.

### Objectives

Use of eco-friendly materials is an important consideration for sustainable development. An attempt was made, in the present study, asses the compressive strength of six types of fine aggregates to get the followings.

- To achieve desired Compressive strength obtained from each type of fine aggregates.
- To make the priority out of all fine aggregates based on their Compressive strength.
- To suggest better fine aggregate for the application of road pavements.



## II. MATERIALS USED

The ingredients of concrete are

### A. Cement

It is one of the maximum crucial elements of concrete. It acts as a binder detail with inside the concrete. Indian Standards (IS) mark forty three grade cement (IS mark forty three grade approach that the compressive power of cement is forty three MPa) of ACC Brand cement changed into used for all mixes. Testing of cement was conducted as per IS: 8112 [Bureau of Indian Standards (BIS) 1989].

### B. Fine aggregate

Here, six types of fine aggregates are used as filler material. There are as follows

1. IS Sand
2. River Sand
3. Manufacturing Sand
4. Foundry Sand
5. Bottom Ash
6. Construction and Demolition Waste

#### 1. IS Sand

This Indian standard sand IS 650 is made of local Natural Silica sand(Silica Content 99%) having a water content material decrease than 0.1%. that Constituent Grains of this sand are uncrossed and of rounded form. It is packaged in 25kg.

#### 2. River Sand

River sand was used as fine aggregate. The sand was confirming to Zone II of IS 383-1978 [17]. The bulk density and specific gravity of the fine aggregate were 1.41 and 2.62.

#### 3. Manufacturing Sand

M sand approximately 20 to twenty-five in line with cent of the general manufacturing in every crusher unit is neglected because the waste cloth quarries dirt. The perfect percent of the substitute of sand with the M sand dirt is fifty five in line with cent to seventy five in line with cent in case of compressive electricity. The unique gravity of the Manufacturing sand is 2.46.

#### 4. Foundry Sand

Foundry sand India ranks fourth in phrases of general foundry manufacturing (7.eight million tonnes) in step with the forty second Census of World Casting Production of 2007. Foundry sand which could be very excessive in silica is often discarded via way of means of the metallic enterprise. Currently, there's no mechanism for its disposal, however global research say that as much as 50 in line with cent foundry sand may be applied for most cost-efficient and sustainable improvement of concrete. The unique gravity of the Manufacturing sand is 2.49.

#### 5. Bottom Ash

Aggregates offer electricity and sturdiness to the concrete. Bottom ash is used because the satisfactory aggregate. Coarse aggregates of 20mm length had been used and the unique gravity became 2.40.

#### 6. Construction and Demolition Waste

Construction and Demolition waste there is no documented quantification of quantity of production and demolition (C&D) waste being generated in India. Municipal Corporation of Delhi says it is gathering 4,000 tonnes of C&D waste day by day from the metropolis which quantities to nearly 1.5 million tonnes of waste yearly with inside the metropolis of Delhi alone. Construction and demolition waste generated via way of means of the development enterprise and which posed an environmental venture can simplest be minimized via way of means of the reuse and recycling of the waste it generates.

### C. Coarse aggregate

Machine crushed granite was used as coarse aggregate. The proportions of aggregate was passing 12.5mm sieve and retaining on 10mm sieve which consisted of 60%, while the aggregate passing 10mm sieve and retaining on 4.75mm sieve was 40%. The aggregate particles have been tested for the different properties, as per IS2386 part IV.

#### D. Water

By the process of hydration, cementitious material reacts with water and form a paste. This cement paste fills the voids and makes the aggregate together. Low water cement ratio makes a durable, strong concrete. High water cement ratio makes high slump concrete.

#### E. Super plasticizers

This is an extra component in concrete. This can also additionally or might not be used. Super plasticizers can be used with inside the concrete to decorate a few homes like strength, durability, workability, to increase or lower placing instances etc. Here, percentage of dosage of super plasticizer is 1.25% which is obtained from marsh cone test for cement paste.

### III. METHODOLOGY

#### Experimental Investigations

The experimental program was designed to evaluate the compressive strength of M30 grade concrete with six varieties of fine aggregates. The experimental work involved casting and testing of a total of 54 specimens. The specimens of standard cubes (150mm X 150mm X 150mm) were casted. All the specimens were tested in Universal Testing Machine for respective curing periods of 7, 14 and 28 days.

#### Mix design

Mix Design is a manner of selecting appropriate factor substances of concrete and determining their relative proportions as economically as viable that would fulfill the favored residences of fresh and hardened concrete as well. In this research work, IRC 44-2017 mix design procedure is used for M-30 grade concrete for the application of road pavement uses. Mix design was done for every type of fine aggregates and the mix proportion obtained is tabulated bellow.

**Table 1.** Various types of fine aggregates with proportion

Sl.no	Type of fine aggregate	Mix Proportion
1	IS Sand	1:1.96:3.34
2	River Sand	1:1.93:3.34
3	Manufacturing Sand	1:1.81:3.34
4	Foundry Sand	1:1.83:3.34
5	Bottom Ash	1:1.76:3.34
6	Construction and Demolition Waste	1:1.80:3.34

Quantity of each material obtained after mix design for each fine aggregates are tabulated bellow:

**Table 2.** Quantity of mix for all types of fine aggregates

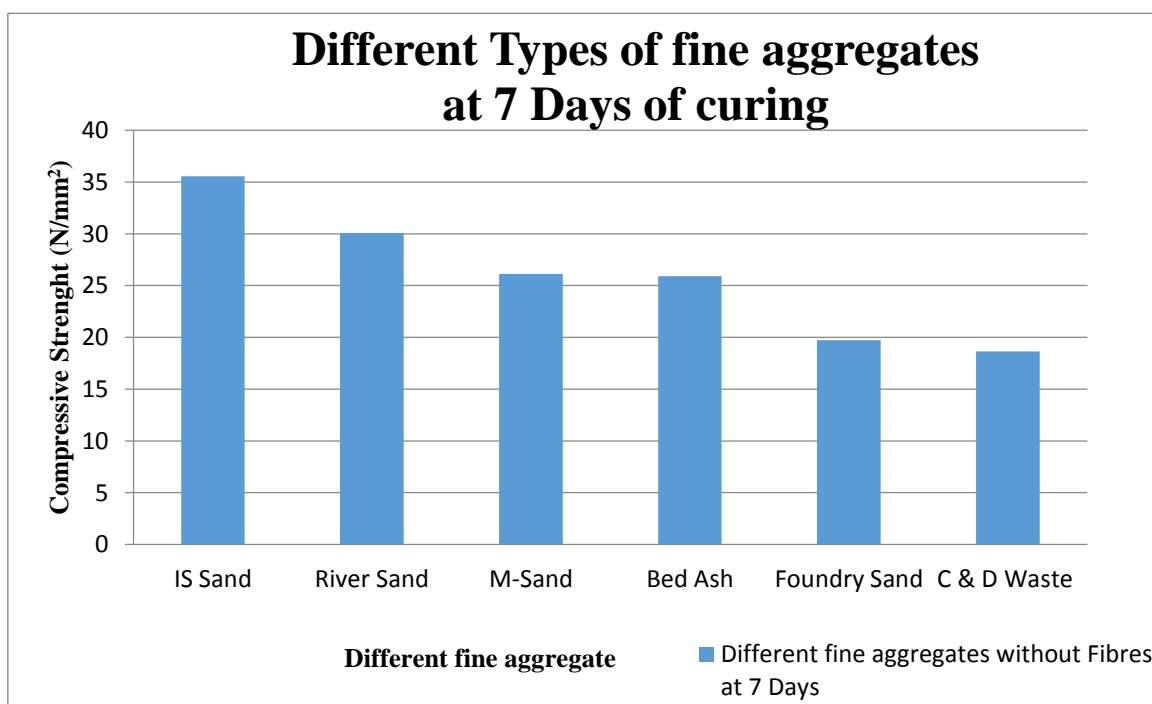
Ingredient's	IS Sand	River Sand	M- Sand	Foundry Sand	Bottom Ash	C & D Waste
Cement	360	360	360	360	360	360
Fine Aggregates	700.11	689.58	647.40	655.31	631.68	644.84
Coarse Aggregates	1193.81	1193.81	1193.81	1193.81	1193.81	1193.81
W/ C Ratio	0.421	0.421	0.421	0.421	0.421	0.421
Water	150.58	150.58	150.58	150.58	150.58	150.58
Super Plasticizer	4.46	4.46	4.46	4.46	4.46	4.46

#### IV. RESULTS AND DISCUSSION

Relation between characteristic compressive strength for the concrete mix for 7, 14 & 28 days. The quantity of amount required for casting every dice specimen thinking about the design blend as M30 grade (cement: fine aggregate: coarse aggregate) as per IRC 44-2017 specifications & tested for its strength for 7, 14 & 28 days strength for different fine aggregates in which the compressive strength by testing under compressive testing machine has given below.

**Table 3:-** Comparison of compressive strength in concrete specimens for 7 days in N/mm<sup>2</sup>

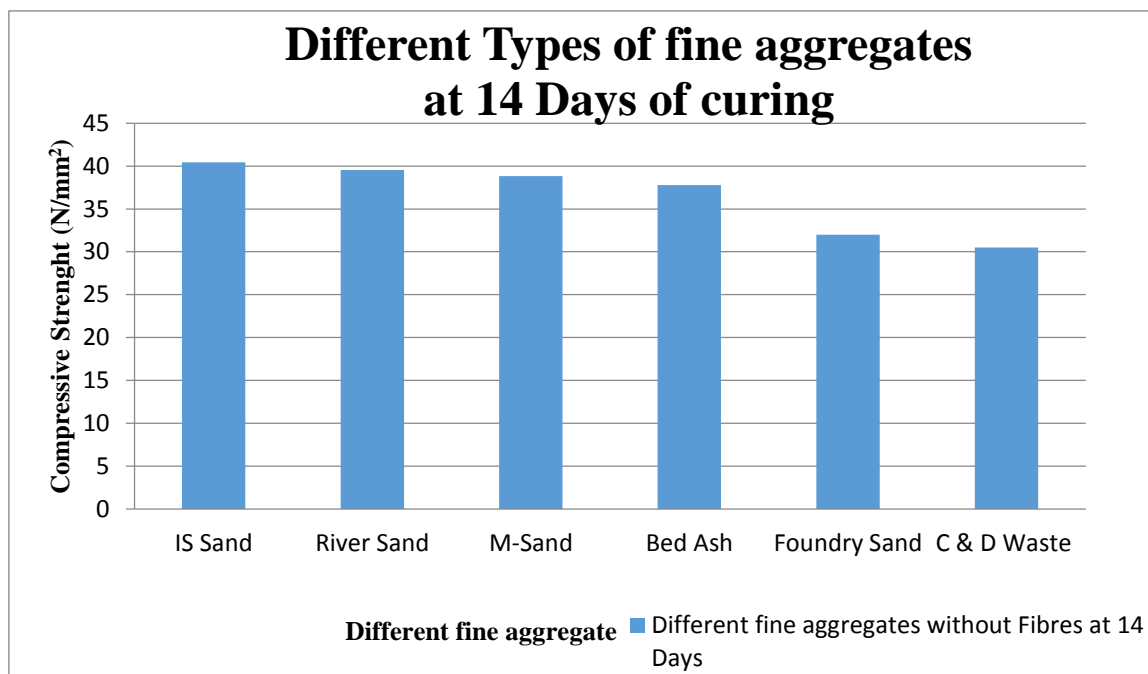
Sl.no	Different fine aggregates	Target Compressive Strength for 7 days(N/mm <sup>2</sup> )		Average Compressive Strength in (N/mm <sup>2</sup> )
		Load	Strength	
1	IS Sand	790	35.11	35.55
		830	36.88	
		780	34.66	
2	River Sand	670	29.77	30.07
		700	31.11	
		660	29.33	
3	M-Sand	580	25.77	26.14
		610	27.11	
		570	25.33	
4	Bed Ash	560	24.88	25.92
		600	26.66	
		590	26.22	
5	Foundry Sand	410	18.31	19.73
		480	21.33	
		440	19.55	
6	C & D Waste	450	20.00	18.66
		400	17.77	
		410	18.22	



**Figure 1:-** Graphical representation of Compressive Strength v/s Different fine aggregates at 7 days

**Table 4:-** Comparison of compressive strength in concrete specimens for 14 days in N/mm<sup>2</sup>

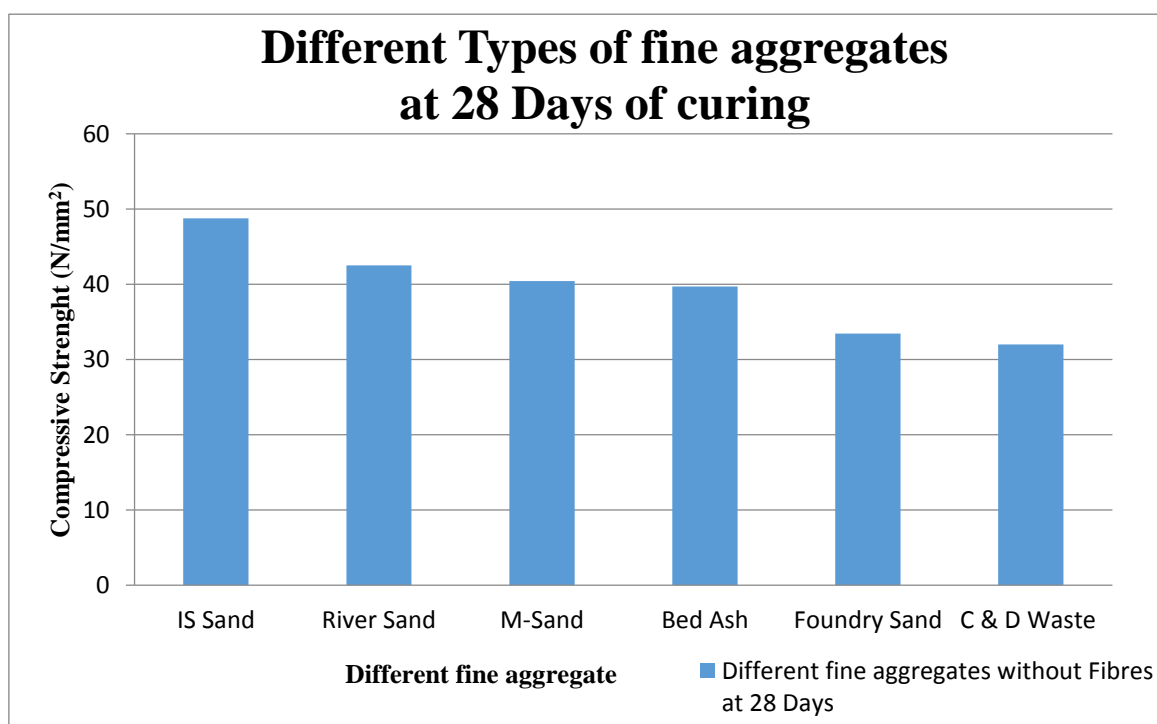
Sl.no	Different fine aggregates	Target Compressive Strength for 14 days(N/mm <sup>2</sup> )		Average Compressive Strength in (N/mm <sup>2</sup> )
		Load	Strength	
1	IS Sand	890	39.55	40.44
		910	40.44	
		930	41.33	
2	River Sand	870	38.66	39.55
		910	40.44	
		890	39.55	
3	M-Sand	900	40.00	38.81
		850	37.77	
		870	38.66	
4	Bed Ash	850	37.77	37.77
		870	38.66	
		830	36.88	
5	Foundry Sand	700	31.11	31.99
		750	33.33	
		710	31.55	
6	C & D Waste	700	31.11	30.51
		690	30.66	
		670	29.77	


**Figure 1:-** Graphical representation of Compressive Strength v/s Different fine aggregates at 14 days

**Table 5:-** Comparison of compressive strength in concrete specimens for 28 days in N/mm<sup>2</sup>

Sl.no	Different fine aggregates	Target Compressive Strength for 28 days(N/mm <sup>2</sup> )		Average Compressive Strength in (N/mm <sup>2</sup> )
		Load	Strength	
		1070	47.55	

1	IS Sand	980	43.64	48.76
		1120	49.11	
2	River Sand	970	43.11	42.51
		980	43.55	
		920	40.88	
3	M-Sand	910	40.44	40.44
		890	39.55	
		930	41.33	
4	Bed Ash	920	40.88	39.69
		870	38.66	
		890	39.55	
5	Foundry Sand	730	32.44	33.44
		770	34.22	
		760	33.66	
6	C & D Waste	690	30.66	31.99
		770	34.22	
		700	31.11	



**Figure 1:-** Graphical representation of Compressive Strength v/s Different fine aggregates at 28 days

## V. CONCLUSION

In this present study six varieties of fine aggregates are taken and basic properties of each material is tested and tabulated and also This study experimentally investigated the compressive strength of each material for 7, 14 and 28 days of curing. Priority obtained by compressive strength results are as follows.

- The Compressive strength of IS sand it shows that the highest strength and C & D waste show lower strength as compared to all six varieties of compressive strength of concrete.
- The Compressive strength of all six varieties of concrete shows decreasing in Compressive strength in sequence of orderly First IS Sand, River Sand, Manufacturing Sand, Bed ash, Foundry Sand and C&D Waste.

### **ACKNOWLEDGEMENTS**

We are grateful to our beloved Principal Dr. MALLIKARJUN S HOLI, who always been thriving for enhancement and excellence for collage, Department facilities and student welfare which a student desires. We deeply indebted to Head of the Dept. Dr. D P NAGARAJAPPA and PG Coordinator Dr. H R PRABHAKARA for his moral support and encouragement.

### **VI. REFERENCES**

- [1] American Society for Testing and Materials, 2003, C33-03 (Specification of Concrete Aggregate, Annual Book of ASTM Standard , Vol.04.01.2003.
- [2] American Society for Testing and Materials, 2005, C150-05 (Specification of Portland Cement), Annual Book of ASTM Standard , Vol.04.02.2005.
- [3] American Society for Testing and Materials, 2005, C494-05 (Specification of For Chemical Admixtures For Concrete), Annual Book of ASTM Standard , Vol.04.01.2005.
- [4] Goble, M. Cohen, 1999 (Influence of aggregate surface area on mechanical properties of mortar), ACI Mater. J. 96 (6) 657-662. 9. G. Giaccio, R. Zerbino, 1993 (Using natural and crushed gravel for made high strength concrete), Hormigón 23 (23- 42).
- [5] Al-Rawi, R. S., 2001,(Using Local Steel Slag as a Fine Aggregate in Concrete), College of Engineering, Baghdad University
- [6] J. K. Dattatreya , N. P. Rajamane, "Studies on use of Copper Slag as Replacement Material for River Sand in Building Constructions" J. Inst. Eng. India Ser. A (July-September 2014) 95(3), pp.169-177.
- [7] M. Shahul Hameed and A. S. S. Sekar, JUNE 2009," Properties Of Green Concrete Containing Quarry Rock Dust And Marble Sludge Powder As Fine Aggregate", ARPN Journal of Engineering and Applied Sciences, VOL. 4, NO. 4- ISSN 1819-6608
- [8] R. Ilangovana, N. Mahendrana and K. Nagamanib, OCTOBER 2008, " Strength And Durability Properties Of Concrete Containing Quarry Rock Dust As Fine Aggregate ", ARPN Journal of Engineering and Applied Sciences, VOL. 3, NO. 5- ISSN 1819-6608
- [9] V.R.K. Narasinha Raju1 and T. Appa Reddy, (2009)," Workability and Strength characteristics of Cement Concrete with Partial Replacement of River Sand by Manufactured Fine aggregate", International Journal of Mechanics and Solids, ISSN 0973-1881 Volume 4, Number 1, pp. 95-104



# “COD and Colour Removal from Distillery spent wash using metal oxide Electrode in Electrocoagulation process”

Soumya Patil<sup>1</sup>, Lokeshappa B<sup>2</sup>, Shanmukha N T<sup>3</sup>

<sup>1</sup>Student, <sup>2</sup>Associate Professor, <sup>3</sup>Assistant Professor

<sup>1,2</sup>University B D T of Engineering Davangere, Karnataka, India

<sup>3</sup>Government Engineering College, Ramanagara, Karnataka

\*\*\*

**Abstract** - Distillery industries are one of the oldest and heavy polluting industries in India, Categorized into red category under MoEF. They produce highly categorized Total solids, COD, BOD, and Colour. Research work has been carryout by reviewing the various research papers by considering the electrocoagulation treatment process to study the removal efficiency of COD, Colour, using four different electrodes viz Al-Al, Fe-Fe, Gr-Gr and Zn-Zn with variable parameters like electrolysis time, voltage and maintain pH constant and electrode distance is 3cm. The comparative study between electrodes Al-Al is more effective in the removal efficiency of COD 95%, Colour 98% at pH9, Voltage 20V, electrolysis time 90 min, than Fe-Fe, Graphite, and Zinc electrodes. Correspondingly the comparative analysis between Al-Al and Anodized Aluminum, Anodized Aluminum is to be more effective in removal of COD 96% and Colour 94% at pH 7, Voltage 20V, Electrolysis time 150 min. and electrode distance 2cm. Distillery spent wash discharge leads serious impact on the environment, thus process has been proved the effective removal of Colour and COD.

**Key Words:** Electrocoagulation, Aluminium, Iron, Zinc, Graphite, Anodized Aluminium, etc

## 1. INTRODUCTION

Distillery spent wash is unwanted residual liquid waste produced during alcohol production. India is a larger manufacturer and also consumer of sugar in the world (4). The generation of spent wash is mostly due to the Molasses based distillery along with their product (alcohol). Distillery spent wash are one of the main industries which release huge quantities of more strength wastewater which has more potential towards causing water pollution India produce huge quantity of spent wash whose disposable into water bodies or land causes a number of environmental complications. Spent wash generally characterized with an unpleasant odor and recalcitrant dark brown colour (11).

The spent wash effluent sample was collected from Samson Distilleries and Chemicals Limited, located nearby the city of Davanagere, Karnataka, India. The collected effluent was immediately brought to the laboratory and stored in the refrigerator at 4 °C (4) until further use in order to avoid any deterioration in the physico-chemical properties of the spent

wash. Distillery spent wash is containing greatly maximum COD, Suspended solids, Inorganic impurities, and other impurities.

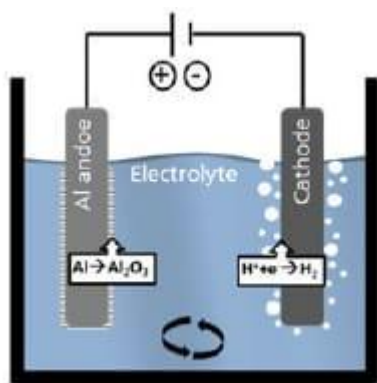
## 1.1 ELECTROCOAGULATION

Electrocoagulation is a technique used for the treatment of wastewater, electro means application of electrical charge to water, and coagulation is the process which change the charge of surface particle by permitting the suspended matter to form agglomeration. The process is performed by application of an electric current across metal electrode that are submerged in water. It is an advanced and most economical water treatment technology. A simple method and most effective in removing various heavy metals, organic substances, metalloids, etc. The metal consumption from the anode with simultaneous establishment of hydroxyl ions and hydrogen gas taking place at the cathode (12).

Electrocoagulation experiments were conducted by batch reactor. The electrochemical cell consists of two plain electrodes (5cm \*5cm\*0.5cm) of Al-Al, Fe-Fe, Graphite, and Zinc electrodes were taken. Immersed in distillery spent wash taken in 1.5L volume of a beaker. The experiments were carried out by varying time, voltage, and kept constant pH, and electrode distance at 3cm.

## 1.2 ANODIZATION

Anodization is an electrolytic passivation evolution used to expand the thickness of common oxide coat on a superficial level metal slice. The process is called anodizing in light of the fact that the portion to be dealt with structures the anode terminal of an electrical circuit. Anodizing rises the corrosion resistance and wear obstacle, and gives improved bond to paint groundwork and pastes than exposes metal. Experimental equipment used to produce anodized Aluminum oxide shown in below Figure1



**Figure1:** Experimental equipment used to produce anodized Aluminum oxide (11).

Anodization of aluminum is formed by exothermic response on the fringe surface of aluminum or aluminum combinations with the early nuclear oxygen made by the electrolysis of a watery electrolyte. The electrolyte could be acidic arrangements like sulfuric acid, chromic acid, phosphoric acid and oxalic acid. The arrangement of Anodized Aluminium Oxide layer is subject to the electrolyte synthesis, anodization time, selected voltage, temperature and pre-treatment techniques and pore size is likewise constrained by treatments like dipping in acidic electrolyte after the anodization procedure. The commendable corrosion resistance of pure aluminum is mainly owing to its liking for oxygen. This outcomes in the creation of an extremely dainty however relentless oxide film which covers the surface when a recently cut bit of metal is presented to the environment (13).

### 1.2.1 PREPARATION OF ANODIZED ELECTRODE

The Nano pores Anodized Aluminium Oxide structures were electrochemically created from Al sheet substrates by utilizing a two-advance anodizing process. The electrochemical arrangement contained 0.2 to 1M H<sub>2</sub>SO<sub>4</sub> corrosive, an anode (a pre-rewarded Al sheet of measurement 10cm x 5cm x 0.3cm) and a cathode (a Pb plate of measurement 10cm x 5cm x 1cm) most commonly.

## 2. RESULTS AND DISCUSSION

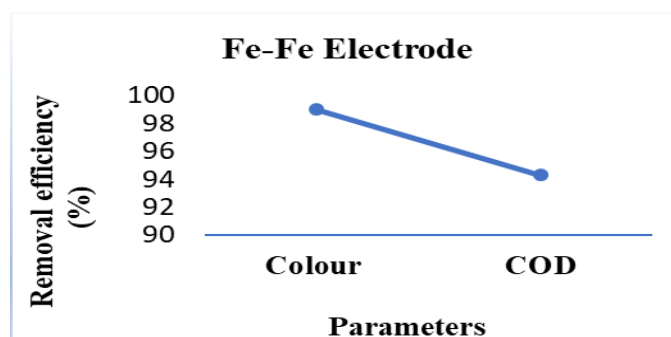
The qualities of Distillery Spent Wash were obtained and the experimental outcome on treatment of Distillery Spent Wash using Al-Al, Fe-Fe, Graphite, Zinc and Anodized electrodes by various researcher using previous research papers. The values given below are the predicted values and the various parameters monitored under electrocoagulation process are given below.

### 2.1 INITIAL CHARECHTERSTICS OF DSW

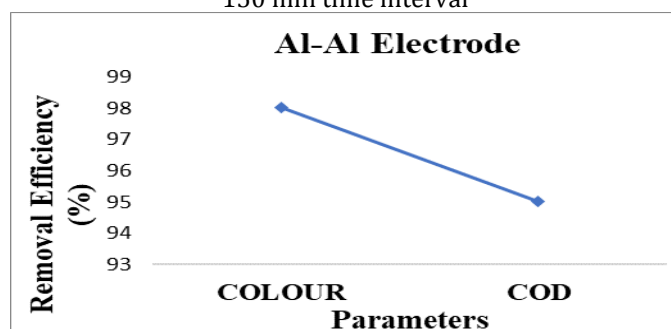
**Table -1:** Initial Characterization of DSW

SL NO	PARAMETERS	UNIT	VALUES
1	pH	-	3-4.8
2	TDS	mg/L	90,000-150,000
4	Turbidity	NTU	3,800
5	Conductivity	µs/cm	40,000
6	Colour	pt.co	3,26,000
7	EC	Ms/cm	23
8	Total hardness	mg/L	1000-1300
9	Total alkalinity	mg/L	1300-1800
10	Chlorides	mg/L	8000-8400
11	COD	mg/L	135000

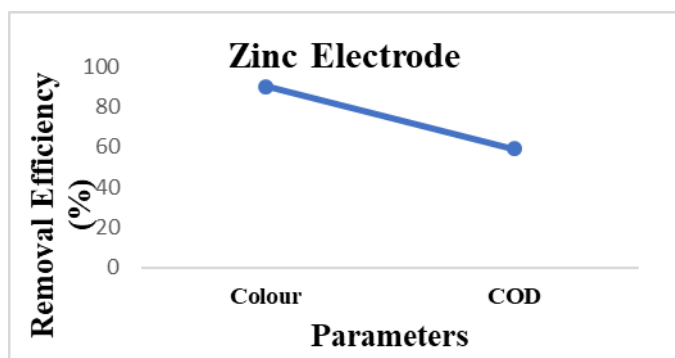
### 2.2 COD AND COLOUR REDUCTION BY ELECTROCOAGULATION USING Al-Al, Fe-Fe, GRAPHITE, AND ZINC ELECTRODE



**Figure 2:** Maximum Removal efficiencies of Fe-Fe electrodes at pH 8, 3cm electrode distance, 15 volts and 150 min time interval



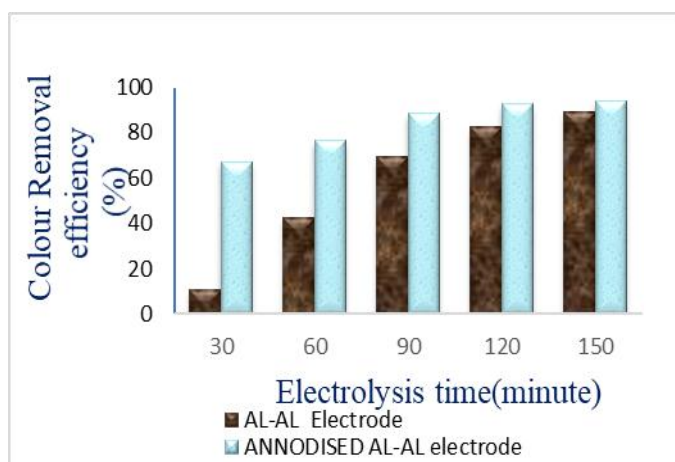
**Figure 3:** Maximum Removal efficiency of Al-Al electrodes at pH9, 3cm electrode distance, 20 volts and 90 min time interval



**Figure 4:** Maximum Removal efficiencies of zinc electrode at pH 8, 3cm electrode distance, 5 volts and 60 min time interval

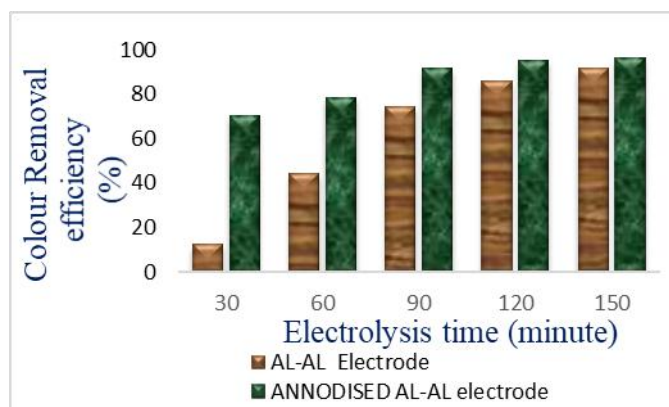
The above graphs are taken from the review values by various researcher papers initially the graphs go on increasing at the maximum time 90min, further it may probably decrease, these are the predicted values. The colour removal efficiency was not found by using Graphite electrodes and maximum COD removal efficiency found to be 85 % at pH 7, voltage 8V, time interval 90min.

## 2.2 COMPARISON OF REMOVAL EFFICIENCY



**Figure 5:** Graph depicting Comparative removal efficiency of colour employing plain Al-Al and Anodized Al-Al electrodes.

The variation in Colour removal efficiency were observed for plain Al-Al and Anodized Al-Al electrodes with different time interval are shows in the Figure 5. 89% of Colour was removed with plain Al-Al electrode and 94% of colour was removed with Anodized Aluminium at pH 7, 150 minutes, 20V and distance 2cm. Results shows that the removal efficiency of Colour is more with Anodized Aluminium electrode compared to Aluminium electrode. At neutral pH there was maximum removal of colour removal efficiency were observed in Anodized electrode.



**Figure 6:** Graph depicting Comparative removal efficiency of COD employing plain Al-Al and Anodized Al-Al electrodes

The variation in COD removal efficiency were observed for plain Al-Al and Anodized Al-Al electrodes with different time interval are shows in the Figure 6. 91% and 96 % of COD was removed with plain Al-Al electrode and Anodized aluminium electrode respectively, at the condition of 150minutes, 20V, pH 7 and 2cm distance. The maximum removal efficiency of COD was observed in Anodized aluminium electrode at pH 7.

## 3. CONCLUSION

The comparative study between all four electrodes Al-Al is more effective in the removal efficiency of COD 95%, Colour 98% at pH9, Voltage 20V, electrolysis time 90 min, than Fe-Fe, Graphite, and Zinc electrodes. Anodised electrode used in Electrocoagulation can be adopted for the attainment of higher efficiency. The comparative analysis between Al-Al and Anodized Aluminium electrodes shows aluminum oxide to be more effective with removal efficiency of COD 96% and Color 94% at a constant pH7, Voltage 20V, Electrode distance of 2cm and at a 150 minutes electrolysis time.

## REFERENCES

- [1] Barnes,D., Bliss,P, Water and waste wastewater engineering system, pitman Publishing Inc., New York.
- [2] Charles David, M. Arivazhagan, Fazaludeen Tuvakara (2015), "Decolorization of Distillery Spent Wash Effluent by Electro Oxidation (EC and EF) and Fenton Processes: A Comparative Study", Ecotoxicology and Environmental Safety, 121, 142-148.
- [3] Chen G. (2000). Separation of pollutants from restaurants wastewater by electrocoagulation, sep. purif. technolgy.,19,65-76.
- [4] Dayaca R.A, Flores. J.D, Mohammed.C.R, (2015), "An Optimization process in the reduction of Chemical Oxygen Demand from Distillery Spent Wash using Electro coagulation", Journal of Engineering science and Technology, 9(16):567-572.

- [5] F sachhi & Gpaolini(2017) "study of Anodizing of Aluminium in sulphuric acid" International Journal of surface Engineering & Tech Research.
- [6] Khandegar and Anil K.S. (2014), "Treatment of Distillery Spent Wash by Electro Coagulation", Journal of Clean Energy Technologies, 2(3): 232-238.
- [7] Krishna B M, Usha N Murthy, Manojkumar B, Lokesh K S,(2010)"Electrochemical Pretreatment Od Distillery Spentwash By Aluminium Electrodes," Application In Electrochemistry, Springer Science And Business Media, Pp. 663-673.
- [8] Manoj, P.W and Nemade.P.D (2015), "Treatment process and Technology for Decolorization and COD Removal of Distillery Spent Wash", International Journal of Innovative Research in Advanced Engineering, (2): 2349-2163.
- [9] Mr.Manoj.P.Wagh, Dr.P.D.Nemade , Mr. Sameer .R. Dhasal "Colour and COD removal of Distillery spent wash by using Electro coagulation" International Journal of Engineering Research and General Science Volume 3, Issue 3, May-June, 2015 ISSN 2091-2730
- [10] Manishankar P, Rani C , Vishvanath S," effects of halides in electrochemical treatement of distillery effluent" Department of International Chemistry sep 2003, July 2004.
- [11] Matias kamp, Axel maywald, Jonas Bartsch, "Electrochemical contact Separation for PVD Aluminium Back Contact Scholar" Fraunhofer Institute for Scholar
- [12] N. Khanna, G Karthikeyan, N. Tamilselvan, Department of chemidstry ayya nadar collage Tamilnadu,India.jan 2006. Journal of Hazardous Materials B 137 9(2006)1803-1809.
- [13] N. B Ekve, D.F Aloko, march(2013)."Anidization of Aluminium"International Journal of scientific and Research publication, volume 3 ISSN 2250-3153

PAPER • OPEN ACCESS

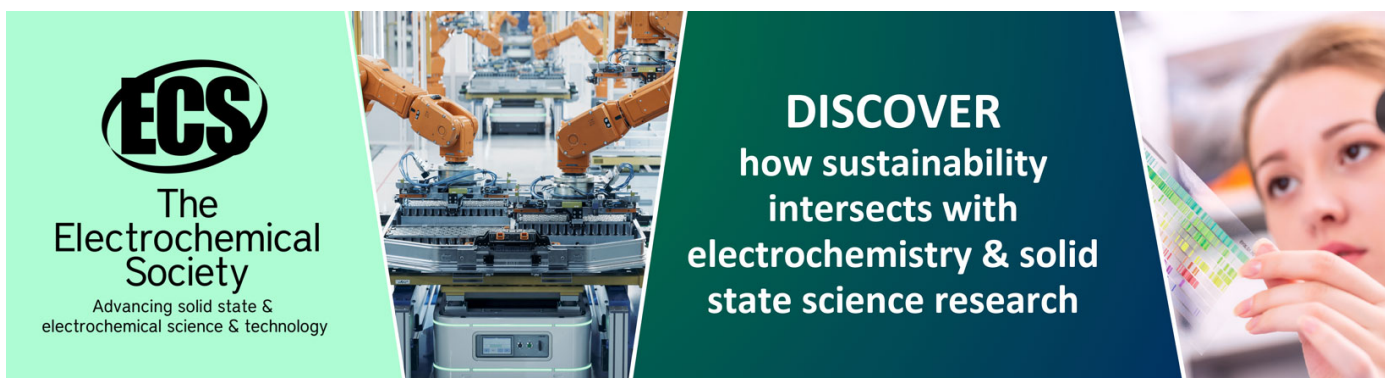
## Review on different control techniques for induction motor drive in electric vehicle


To cite this article: H B Marulasiddappa and V Pushparajesh 2021 *IOP Conf. Ser.: Mater. Sci. Eng.* **1055** 012142

View the [article online](#) for updates and enhancements.

You may also like

- [Comparative Evaluation of Control Techniques of PMSM Drive in Automotive Application](#)  
Rakesh Shrivastava, Satayjit Deshmukh, Ashwini Tidke et al.
- [Assessment of Control Drive Technologies for Induction Motor: Industrial Application to Electric Vehicle](#)  
A. Z. Ahmad Firdaus, S. A. Azmi, K. Kamarudin et al.
- [Improvement of Direct Torque Control by using a Space Vector Modulation Control of Three-Level Inverter](#)  
A Achalhi, M Bezza, N Belbounaguia et al.





The  
Electrochemical  
Society

Advancing solid state &  
electrochemical science & technology

**DISCOVER**  
how sustainability  
intersects with  
electrochemistry & solid  
state science research



# Review on different control techniques for induction motor drive in electric vehicle

Marulasiddappa H B<sup>1\*</sup> and Pushparajesh V<sup>2</sup>

<sup>1</sup> Assistant Professor, Jain Institute of Technology, Davanagere, Karnataka, India

<sup>2</sup> Associate Professor, JAIN - A Deemed to be University, Bengaluru, Karnataka, India

\*E-mail: marul.bethur@gmail.com

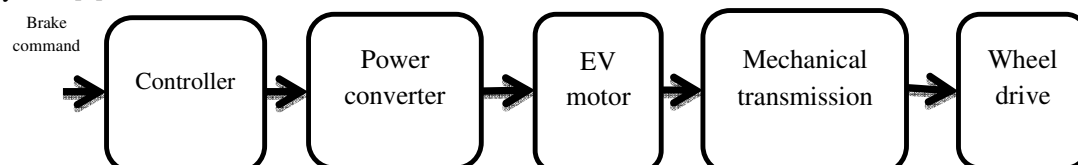
**Abstract.** Now a day Electric vehicles (EV) are called future vehicles in place of internal combustion engines because of their working with pollution free and more efficient. This paper reviews various control strategies of induction motor drives (IMD) for EV applications. Efficiency and performance are the major considerations in selecting control algorithms for induction motor drives. Basically there are scalar control and vector control methods for IMDs. Scalar control technique has drawback of low performance. Conventional direct torque control (DTC) technique is one of the most preferable control technique for controlling torque and flux independently. But due the lower switching frequency in direct torque control leads to more flux ripple and torque ripples and it leads lower performance of induction motor drives.

**Keywords.** Electric vehicle, Induction motor drive, direct torque control.

## 1. Introduction

In present days environment concerned research is going in a rapid manner to solve our environment issues such as increase of carbon dioxide level, depletion of ozone layer. Year by year there is rapid increase in production of Internal Combustion (IC) engine vehicles which increases pollution in the environment, so that there is increase in design and development of electric vehicle in automotive industries to replace IC engine vehicles.

In addition to reduced pollution in the environment, electric vehicle gives good performance in terms of its efficiency & torque [1]. The only disadvantage of EV is its cost [2]. Due to the environment concern and less fuel consumption EV are attractive than conventional IC engines [3]. For better efficiency of EV, it is necessary to choose motor drive and its control techniques properly. This means electric motor drive system is very much important and it is like heart of the entire electric vehicle system. The following figure 1 represents the block diagram of various parts of electric vehicle system [4].



**Figure 1.** Block diagram representation of electrical vehicle system

In the above fig (1), controller part, power converter part and electric motor part represents core of the drive of the EV. It consists of electric vehicle control system and battery management system works together to reduce power consumption [1, 5]. The motor that we choose must have following basic requirements which are [1].



- i. High power density and high torque density
- ii. Low losses
- iii. Good controlling property
- iv. Better dynamic performance
- v. Rugged and simple in structure
- vi. Low cost

In earlier research DC motor are preferably used in EV applications due to simple in controller design and their characteristics are well matched for electric vehicle motor. With the increase in the research advancement of controlling technique, induction motor comes into the main frame for choosing as drive motor for electric vehicle applications [6]. It is commutator less motor, it is highly reliable, rugged and maintenance free [7]. Even though it has more advantages than dc motors, it has some drawbacks like nonlinear characteristics due to this, analysis becomes complex [8, 9] and flux in the induction motor is not measurable [10]. To overcome these drawbacks, few control strategies are presented [11] and it compares among conventional controllers and intelligent controllers with respect to torque ripples. Simultaneously to reduce the torque and flux ripples and to improve the dynamic response Field Oriented Control (FOC) is established [8]. This technique decouples the torque and flux to get fast dynamic torque response [12-14] and it improves the performance of the drive system. FOC algorithm is very much sensitive to parameter variation with respect to temperature variation, which leads to reduced performance [15].

To overcome the limitations of FOC, DTC was explained by TAKANASHI [16] & DEPENDBROCK [17]. In DTC control signals are calculated directly for the inverter [18-20]. But this conventional DTC has drawbacks like more torque ripple and flux ripples in low speed region and various switching frequency, due to this torque and flux are not fully controllable [21-23]. Many modern control techniques are invented for controlling the two main parameters; those are torque and flux of IM for electric vehicle applications. In this paper section II deals with modelling of induction motor, section III explain about basic design concept of DTC, section IV deals with different control algorithm and section V ends with conclusion.

## 2. Modelling of induction motor

Analysis of induction motor is little complex due to its nonlinear characteristics. The better way to analyse the three phase induction motor is 2-phase model expressed by  $\alpha$  and  $\beta$ . The equations that represents the induction motor are along  $\alpha$  and  $\beta$  axis are [24][25]

$$\frac{d}{dt} \begin{bmatrix} i_{s\alpha} \\ i_{s\beta} \\ \varphi_{s\alpha} \\ \varphi_{s\beta} \end{bmatrix} = \begin{bmatrix} -\frac{1}{\sigma} \left( \frac{1}{T_s} + \frac{1}{T_r} \right) & -\omega_r & \frac{1}{\sigma L_s T_r} & \frac{\omega_r}{\sigma L_s} \\ \omega_r & -\frac{1}{\sigma} \left( \frac{1}{T_s} + \frac{1}{T_r} \right) & -\frac{\omega_r}{\sigma L_s} & \frac{1}{\sigma L_s T_r} \\ -R_s & 0 & 0 & 0 \\ 0 & -R_s & 0 & 0 \end{bmatrix} \begin{bmatrix} i_{s\alpha} \\ i_{s\beta} \\ \varphi_{s\alpha} \\ \varphi_{s\beta} \end{bmatrix} + \begin{bmatrix} \frac{1}{\sigma L_s} & 0 \\ 0 & \frac{1}{\sigma L_s} \\ 1 & 0 \\ 0 & 1 \end{bmatrix} \begin{bmatrix} V_{s\alpha} \\ V_{s\beta} \end{bmatrix} \quad (1)$$

Here  $\alpha$ ,  $\varsigma$ s and  $\varsigma$ r are called +ve constants

$$\sigma = 1 - \frac{M^2}{L_s L_r} \varsigma_s = \frac{R_s}{L_s} \varsigma_s = R_r / L_r$$

The following are the equations for torque and moment of inertia

$$T_{em} = (\psi_{s\alpha} i_{s\alpha} - \psi_{s\beta} i_{s\beta}) \quad (2)$$

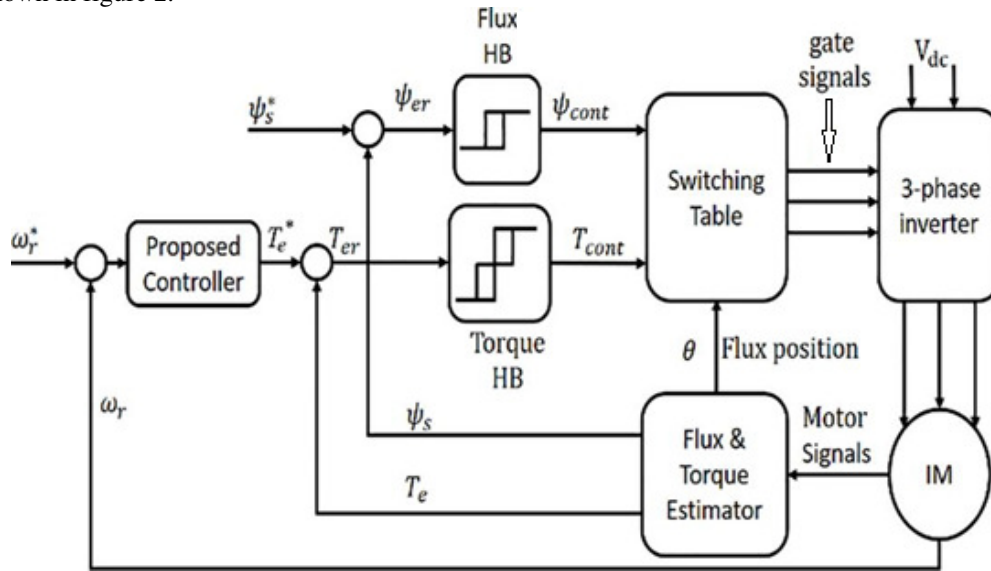
$$j \frac{d\Omega}{dt} + f\Omega = T_{em} - T_r \quad (3)$$

The transformation from three phases to two phases can be done by

$$\begin{bmatrix} X_a \\ X_b \end{bmatrix} = \sqrt{2/3} \begin{bmatrix} 1 & -1/\sqrt{2} & -1/2 \\ 0 & \sqrt{3}/2 & -\sqrt{3}/2 \end{bmatrix} \begin{bmatrix} X_a \\ X_b \\ X_c \end{bmatrix} \quad (4)$$

### 3. Direct Torque Control

Direct torque control of induction motor is initially proposed by Takahashi and Depenbrock in 1980s decade. It works on principle of direct use of control signals for power semiconductor switches of voltage source inverter. As pulse width modulation is absent in DTC, so that control strategy is simple. Figure 2 Shows electromagnetic torque and stator flux are independently controlled by hysteresis comparators. The outcomes of these two comparator decide the switching signals from switching table. It gets its attention because of its simplicity. The basic block diagram [1] which represents DTC is shown in figure 2.



**Figure 2.** Basic representation of Direct Torque Control

The design of control technique (DTC) is mainly depending on determination of torque and stator flux linkages depend on these equations. The equation for electromagnetic torque  $T_e$  is given by

$$T_e = \frac{3}{2} p (\psi_{sq} i_{sq} - \psi_{sd} i_{sd}) \quad (5)$$

$$\psi_{sd} = \int (v_{sd} - R_s i_{sd}) dt \quad (6)$$

$$\psi_{sq} = \int (v_{sq} - R_s i_{sq}) dt \quad (7)$$

Where

$P$ =number of poles

$\psi$ =flux linkage

$i_{sq}$ =quadrature axis stator current

$i_{sd}$ =direct axis stator current

$R_s$ =stator resistance

$v_{sd}$  = Quadrature axis stator voltage

$v_{sq}$  =Direct axis stator voltage

The following equations (8) & (9) used to determine the magnitude and angle of stator flux linkage

$$\psi_s = \sqrt{(\psi_{sq} + \psi_{sd})} \quad (8)$$

$$\theta = \tan^{-1} \left( \frac{\psi_{sq}}{\psi_{sd}} \right) \quad (9)$$

It can be selected directly the stator voltage vector based on comparison between reference and actual values of torque and flux linkages according to the conventional switching table [1]. Even though DTC has more advantages over other control techniques, it has some drawbacks like it generates more torque and flux ripples. To reduce or avoid these ripples many control algorithms are introduced for induction motor drives.

#### 4. Control Algorithms

There are various control techniques for induction motor drives in electric vehicle applications. They are i) Proportional Integral (PI) controller ii) PID controller iii) Sliding mode controller (SMC) iv) Fuzzy logic controller (FLC) v) Neural network controller vi) Model predictive controller vii) Hybrid controllers., and more. Few important algorithms are reviewed here. One can choose the better algorithm for controlling of induction motor drives. This paper [1] concludes that sliding mode control is well suited for electric vehicle compared to conventional proportional integral and fuzzy logic controller. This paper explains how efficiency and performance can be improved by using sliding mode controller. This paper also compares the two torque control techniques they are indirect FOC and Direct torque control. [26-29]proposes SMC which will increase the performance of the IM drive as compared to PI controllers [30,31] explains combination of SMC and FLC gives better dynamic characteristics compared to PI and FLC controller alone. In this paper [32] he proposes new controller called neural network based DTC to reduce the settling time and improve the performance of switched reluctance motor where he reduced the torque ripple of margin of 1%.This paper [33] explains the online optimization technique to vanish the flux and torque hysteresis band. It is better performance than conventional DTC as it uses the predefined switching table. This paper explains how torque ripple can be reduced using Predictive torque control (PTC) and analysis of speed response and torque ripple in the induction motor which is used in electric vehicles. Due to the complexity in calculation, settling time is more in PTC as compared to conventional DTC. He explained with result that percentage of torque ripple and current total harmonic distortion (THD) are less in PTC compared to conventional DTC.

This paper gives increase in torque and speed response of switched reluctance motor by choosing voltage vector using look up table based DTC [34]. The authors [35] proposed DTC for induction motor drives based on lookup table. By proper selection of switching table values, it is possible to improve the performance and dynamic behaviour of induction motor based electric vehicles. This paper also utilizes the regenerative braking where partial energy from the motor is used to charge the battery. This paper [36] proposes Artificial Neural Network (ANN) controller to reduce both torque and flux ripples by considering proper values for input and feedback through online mode. By using both simulation and practical it explains that proposed controller is more efficient than conventional controller. This paper [37] improvises the transient analysis by using ANN controller but no changes in torque and flux ripples. This paper [38] replaces neural controller instead of switching table and hysteresis controller to reduce the torque and flux ripples.

In this paper [39] authors explain the three different control strategies for induction motor drive based EV applications which are DTC space vector modulation (DTC-SVM), conventional DTC and FOC algorithms. By using DTC-SVM it has been noted that stator current ripples considerably decreasing hence it improves the dynamic performance of induction motor drives. [40] In this paper fast dynamic response of induction motor drive for electric vehicle is achieved by DTC-SVM in the place of voltage source inverter. This[41] paper explains on intelligent controller which is called an

better controlling technique for switched reluctance motor which reduces the overshoot time and also improves torque response of the drive system.

The following Table 1 gives comparison between five different controllers by considering different parameters.

**Table 1.** Comparison among different controllers.[1, 2, 42-49]

Parameter/ technique	Conventional DTC	SMC based DTC	DTC-MPC	Fuzzy based DTC	ANN based DTC
Torque& flux Ripple	high	medium	less	Very less	Very less
Torque response	high	high	high	Very high	Very high
Current THD	high	less	less	less	less
Switching loss	high	average	less	less	less

By considering above table we can say that conventional direct torque control algorithm has more torque and flux ripples compared to other algorithms. Depending upon parameter selection and application it is feasible to select particular algorithm for induction motor drives.

## 5. Conclusion

This paper reviews various control strategies available for IM based electric vehicle applications. The major objective of the review was to lower the flux ripple and torque ripples of induction motor drive and intern enhancing the performance of electric vehicle. The control techniques like conventional DTC, SVM-DTC, SMC-DTC, Fuzzy based DTC and ANN DTC are compared for dynamic response, torque ripple and flux ripple, total harmonic distortion and switching frequency.. These algorithms have their own advantages and drawbacks. The table 1 gives comparison among various algorithms. Therefore selection of these algorithms for induction motor is based on cost, accuracy and application. Fuzzy logic controller is used where the system behaviour is more complicated and semantic rules are necessary to explain the system. Compared to FLC artificial neural network is good for modelling in this conditions as ANN is more suitable for controlling nonlinear devices. As induction motor has a nonlinear model and therefore ANN is highly suitable for controlling induction motor drive in electrical vehicle.

## 6. References

- [1] Aktas, M., Awaili, K., Ehsani, M., and Arisoy, A. (2020). Direct torque control versus indirect field-oriented control of induction motors for electric vehicle applications. *Engineering Science and Technology, an International Journal*. **23**, Pages 1134-1143
- [2] Chau, K. T. (2015). Electric vehicle machines and drives: design, analysis and application. *John Wiley & Sons*.
- [3] Ehsani, Mehrdad, Yimin Gao, and Ali Emadi. Modern Electric, Modern Hybrid, and Fuel Cell Vehicles. *Book* (2010).
- [4] Chan, C. C. (2002). The state of the art of electric and hybrid vehicles. *Proceedings of the IEEE*, **90**(2), 247-275.
- [5] Hu, Changjian, Yimin Gao, and Q. Huang Alex (2015). Power management strategy of hybrid electric vehicles based on particle swarm optimization. *IEEE Transportation Electrification Conference and Expo (ITEC)*, pp. 1-6. IEEE, 2015.

- [6] Tabbache, B., Kheloui, A., and Benbouzid, M. E. H. (2010, September). Design and control of the induction motor propulsion of an electric vehicle. *IEEE Vehicle Power and Propulsion Conference* (pp. 1-6). IEEE.
- [7] Butler, Karen L., Mehrdad Ehsani, and Preyas Kamath. (1999) A Matlab-based modeling and simulation package for electric and hybrid electric vehicle design. *IEEE Transactions on vehicular technology* **48**, no. 6: 1770-1778.
- [8] Karagiannis, Dimitrios, Alessandro Astolfi, Romeo Ortega, and Mickaël Hilaret (2009). A nonlinear tracking controller for voltage-fed induction motors with uncertain load torque. *IEEE Transactions on Control Systems Technology* 17, no. 3: 608-619.
- [9] Sen, P. C. (1990). Electric motor drives and control-past, present, and future. *IEEE Transactions on Industrial Electronics*, **37**(6), 562-575.
- [10] Trabelsi, R., Khedher, A., Mimouni, M. F., & M'sahli, F. (2012). Backstepping control for an induction motor using an adaptive sliding rotor-flux observer. *Electric Power Systems Research*, **93**, 1-15.
- [11] Pushparajesh Viswanathan and Manigandan Thathan (2016) Torque ripple minimization of direct torque controlled four phases witched reluctance motor using artificial intelligent controller *World Journal of Modelling and Simulation*, **Vol. 12**, pp. 163-174
- [12] Amezcua-Brooks, L., Liceaga-Castro, E., Liceaga-Castro, J., & Ugalde-Loo, C. E. (2015). Flux-torque cross-coupling analysis of FOC schemes: *Novel perturbation rejection characteristics. ISA transactions*, **58**, 446-461.
- [13] El Ouanjli, N., Derouich, A., El Ghzizal, A., Chebabhi, A., & Taoussi, M. (2017, November). A comparative study between FOC and DTC control of the Doubly Fed Induction Motor (DFIM). *International Conference on Electrical and Information Technologies (ICEIT)* (pp. 1-6). IEEE.
- [14] Mehazzem, F., Nemmour, A. L., & Reama, A. (2017). Real time implementation of backstepping-multiscalar control to induction motor fed by voltage source inverter. *International Journal of Hydrogen Energy*, **42**(28), 17965-17975.
- [15] Novotny, D. W., & Lipo, T. A. (1996). Vector control and dynamics of AC drives *Oxford university press. (Vol. 41)*
- [16] Takahashi, I., & Noguchi, T. (1986). A new quick-response and high-efficiency control strategy of an induction motor. *IEEE Transactions on Industry applications*, **(5)**, 820-827.
- [17] Depenbrock, M. (1988). Direct self-control (DSC) of inverter-fed induction machine. *IEEE Transactions on Power Electronics*, **3**, 420-429.
- [18] Vaez-Zadeh, S., & Jalali, E. (2007). Combined vector control and direct torque control method for high performance induction motor drives. *Energy conversion and management*, **48**(12), 3095-3101.
- [19] El Ouanjli, N., Derouich, A., El Ghzizal, A., El Mourabit, Y., & Taoussi, M. (2017). Contribution to the improvement of the performances of doubly fed induction machine functioning in motor mode by the DTC control. *International Journal of Power Electronics and Drive Systems*, **8**(3), 1117.
- [20] Khedher, A., & Mimouni, M. F. (2010). Sensorless-adaptive DTC of double star induction motor. *Energy Conversion and Management*, **51**(12), 2878-2892.
- [21] Reza, C. M. F. S., Islam, M. D., & Mekhilef, S. (2014). A review of reliable and energy efficient direct torque controlled induction motor drives. *Renewable and Sustainable Energy Reviews*, **37**, 919-932.
- [22] Kadir, M. A., Mekhilef, S., & Ping, H. W. (2007, October). Direct torque control permanent magnet synchronous motor drive with asymmetrical multilevel inverter supply. In *2007 7th International Conference on Power Electronics* (pp. 1196-1201). IEEE.
- [23] Naik, N. V., Panda, A., & Singh, S. P. (2015). A three-level fuzzy-2 DTC of induction motor drive using SVPWM. *IEEE Transactions on Industrial Electronics*, **63**(3), 1467-1479.

- [24] Buja, G., Casadei, D., & Serra, G. (1997, July). Direct torque control of induction motor drives. In *ISIE'97 Proceeding of the IEEE International Symposium on Industrial Electronics (Vol. 1, pp. TU2-TU8)*. IEEE.
- [25] Slemon, G. R. (1989). Modelling of induction machines for electric drives. *IEEE Transactions on Industry Applications*, **25**, 1126–1131.
- [26] Abdelfatah, N., Abdeldjebar, H., Bousserhane, I. K., Hadjeri, S., & Sicard, P. (2008). Two wheel speed robust sliding mode control for electric vehicle drive. *Serbian journal of electrical engineering*, **5(2)**, 199-216.
- [27] Alagna, S., Cipriani, G., Corpora, M., Di Dio, V., & Miceli, R. (2016, November). Sliding mode torque control of an induction motor for automotive application with sliding mode flux observer. *IEEE International Conference on Renewable Energy Research and Applications (ICRERA)* (pp. 1207-1212). IEEE.
- [28] Ltifi, A., Ghariani, M., & Neji, R. (2014, December). Performance comparison of PI, SMC and PI-Sliding Mode Controller for EV. In *2014 15th International Conference on Sciences and Techniques of Automatic Control and Computer Engineering (STA)* (pp. 291-297). IEEE.
- [29] Nasri, A., Gasbaoui, B., & Fayssal, B. M. (2016). Sliding mode control for four wheels electric vehicle drive. *Procedia Technology*, **22**, 518-526.
- [30] Boumediène, A., & Abdellah, L. (2012). A novel sliding mode fuzzy control based on SVM for electric vehicles propulsion system. *ECTI Transactions on Electrical Engineering, Electronics, and Communications*, **10(2)**, 153-163.
- [31] Nasri, A., Hazzab, A., Bousserhane, I. K., Hadjeri, S., & Sicard, P. (2009). Fuzzy-sliding mode speed control for two wheels electric vehicle drive. *Journal of Electrical Engineering & Technology*, **4(4)**, 499-509.
- [32] Viswanathan, Pushparajesh, and Manigandan Thathan (2016). Minimization of Torque Ripple in Direct Torque Controlled Switched Reluctance Drive Using Neural Network. *Asian Journal of Research in Social Sciences and Humanities* **6, no. 8** :65-80.
- [33] Kousalya, V., Rai, R., & Singh, B. (2020, June). Predictive Torque Control of Induction Motor for Electric Vehicle. *IEEE Transportation Electrification Conference & Expo (ITEC)* (pp. 890-895). IEEE.
- [34] Pushparajesh, V., Balamurugan, M., & Ramaiah, N. S. (2019). Artificial Neural Network Based Direct Torque Control of Four Phase Switched Reluctance Motor. *Available at SSRN* 3371369.
- [35] Singh, B., Jain, P., Mittal, A. P., & Gupta, J. R. P. (2006, April). Direct torque control: a practical approach to electric vehicle. *IEEE Power India Conference* (pp. 4-pp). IEEE.
- [36] Bouhoune, K., Yazid, K., Boucherit, M. S., & Nahid-Mobarakeh, B. (2018, November). Simple and Efficient Direct Torque Control of Induction Motor Based on Artificial Neural Networks. *IEEE International Conference on Electrical Systems for Aircraft, Railway, Ship Propulsion and Road Vehicles & International Transportation Electrification Conference (ESARS-ITEC)* (pp. 1-7).
- [37] Zegai, M. L., M. Bendjebbar, K. Belhadri, M. L. Doumbia, B. Hamane, and P. M. Koumba (2015). Direct torque control of Induction Motor based on artificial neural networks speed control using MRAS and neural PID controller. *IEEE Electrical Power and Energy Conference (EPEC)*, pp. 320-325.
- [38] Sayouti, Y., A. Abbou, M. Akherraz, and H. Mahmoudi (2010). Real-time DSP implementation of DTC neural network-based for induction motor drive. :pp 233-233.
- [39] Prabudha, B. V., Aparna Balamurugan, T. Selvathai, Rajaseeli Reginald, and Jayashree Varadhan (2019). Evaluation of different Vector Control methods for Electric Vehicle Application. *2nd International Conference on Power and Embedded Drive Control (ICPEDC)*, pp. 273-278. IEEE, 2019.

- [40] Ellabban, Omar, Joeri Van Mierlo, and Philippe Lataire (2011). Direct torque controlled space vector modulated induction motor fed by a Z-source inverter for electric vehicles. *International Conference on Power Engineering, Energy and Electrical Drives.IEEE*.
- [41] Pushparajeshviswanathan, ManigandanThathan (2015) Hybrid Controller Based Instantaneous Torque Control of Four Phase Switched Reluctance Motor *Middle-East Journal of Scientific Research***23 (11)**: 2736-2747.
- [42] Reza, C. M. F. S., Islam, M. D., & Mekhilef, S. (2014). A review of reliable and energy efficient direct torque controlled induction motor drives. *Renewable and Sustainable Energy Reviews*, **37**, 919-932.
- [43] Sutikno, T., Idris, N. R. N., &Jidin, A. (2014). A review of direct torque control of induction motors for sustainable reliability and energy efficient drives. *Renewable and sustainable energy reviews*, **32**, 548-558.
- [44] Ammar, A., Benakcha, A., &Bourek, A. (2017). Closed loop torque SVM-DTC based on robust super twisting speed controller for induction motor drive with efficiency optimization. *international journal of hydrogen energy*, **42(28)**, 17940-17952.
- [45] Gadoue, S. M., Giaouris, D., & Finch, J. W. (2009). Artificial intelligence-based speed control of DTC induction motor drives—A comparative study. *Electric Power Systems Research*, **79(1)**, 210-219.
- [46] Gdaim, S., Mtibaa, A., & Mimouni, M. F. (2010). Direct torque control of induction machine based on intelligent techniques. *International Journal of Computer Applications*, **10(8)**, 29-35.
- [47] Lascu, C., Boldea, I., &Blaabjerg, F. (2004). Direct torque control of sensorless induction motor drives: a sliding-mode approach. *IEEE Transactions on Industry Applications*, **40(2)**, 582-590.
- [48] Kumar, R. H., Iqbal, A., & Lenin, N. C. (2017). Review of recent advancements of direct torque control in induction motor drives—a decade of progress. *IET Power Electronics*, **11(1)**, 1-15.
- [49] Niu, F., Wang, B., Babel, A. S., Li, K., &Strangas, E. G. (2015). Comparative evaluation of direct torque control strategies for permanent magnet synchronous machines. *IEEE Transactions on Power Electronics*, **31(2)**, 1408-1424.



## Medical Robots & its Applications in the Current Health Sector

T. C. Manjunath<sup>\*1</sup>, Pavithra G.<sup>2</sup>, Ravi Rayappa<sup>3</sup>, Rajasekhar Koyyeda<sup>3</sup>, Satvik M. Kusagur<sup>3</sup>, Praveen N.<sup>4</sup>

<sup>1</sup>Professor and HOD, Department of Electronics and Communication Engineering, Dayananda Sagar College of Engineering, Bangalore, Karnataka, India

<sup>2</sup>Research Consultant, Bangalore, Karnataka, India

<sup>3</sup>Research Scholars, Visvesvaraya Technological University, Belagavi, Karnataka, India

<sup>4</sup>Faculty, Department of Electrical & Electronics Engineering, Ibra College of Technology, IBRA, Sultanate of Oman, Oman

\*Corresponding Author: tmanjunath@gmail.com

### ABSTRACT

A concise survey of the nanorobots that are right now utilized in biomedical designing to fix different sorts of infections is being introduced. In the unique situation, we are completing a writing review for the therapy of malignant growth utilizing the nano-innovation idea. How we have picked is the association of nanotechnology and medication. The blend of nanotechnology into medicine is likely going to get some new challenges helpful treatment. Nanorobot is an amazing vision of medication in the future. The most excellent nanomedicine incorporates the use of nanorobots as little scope trained professionals. Headway in nanotechnology may permit us to construct fake red platelets called Respirocytes equipped for conveying oxygen and carbon dioxide atoms (i.e., elements of normal platelets). Respirocytes are nanorobots, little mechanical contraptions proposed to take a shot at the nuclear level. Respirocytes can give a short replacement to trademark platelets on the occasion of an emergency. Thusly respirocytes will change the treatment of coronary ailment. We can envision a day when you could implant billions of these nanorobots that would skim around in your body. A champion among the most reasonable and practically feasible achievements is the remedy for development which is one of the essential communities of this work. Nanorobots could convey and convey a lot of hostile to disease drugs into carcinogenic cells without hurting sound cells, lessening the results identified with flow treatments.

**Keywords--** Artery, Cancer, Coronary, Medicine, Nanorobots, Treatment

### INTRODUCTION

In this section, we give a brief introduction to what are nanobots? Nanobots à la

Michael Crichton's Prey and other sci-fi contraptions of nanoscale robots don't exist (yet).

Not to be mistaken for these anecdotal nanorobots, for clinical nanotechnology analysts a nanorobot, or nanobot, is a well-known term for atoms with an interesting property that empowers them to be customized to do a particular assignment. These nanobots are a reality and are in effect effectively investigated and created.

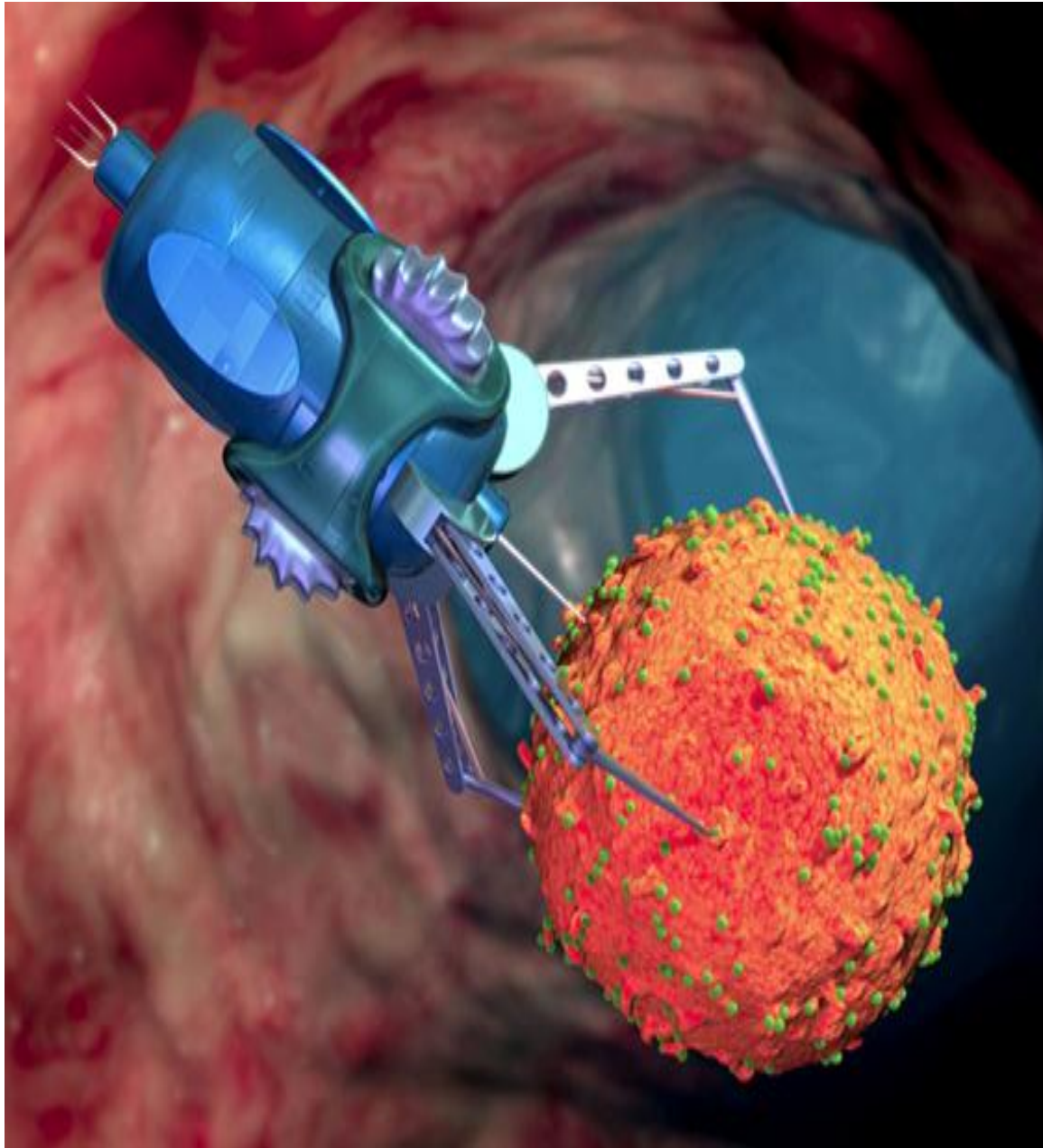
An always expanding number of examination bunches are misusing programmable self-get together properties of nucleic acids in making objectively planned nano shapes and nanomachines for various employments. That is the reason one of the most effectively investigated territories of nanorobotics today includes DNA gathering, especially a strategy called DNA origami (see underneath for additional subtleties).

In the next few paragraphs, we present what is nanorobotics. How about we start with certain rudiments: Robotics can be characterized as the hypothesis and utilization of robots, an independent electronic, electric, or mechanical gadget, to such exercises as assembling.

Scale that robot down to a couple of billionth of a meter and you are talking nanotechnology advanced mechanics; nanorobotics in short. The field of nanorobotics unites a few controls, including nanofabrication measures utilized for creating nanomotors, nano actuators, nanosensors, and actual demonstrating at nanoscales.

Nano robotic control innovations, including the get together of nanometer-sized parts, the control of natural cells or particles, and the kinds of robots used to play out these assignments likewise structure a segment of Nano robotics.

For example, analysts have interpreted the self-sufficient development directions of Nano motors into controlled surface highlights that carry a wind to customary static optical manufacture frameworks, which sets up a beginning phase approach for a Nano robotics stage for nonmanufacturing (Fig. 1).



*Figure 1: Nano robots which are Used to Attack the Cancerous Cells.*

## OVERVIEW

Nanotechnology robots are quintessential NEMS (Nano electro mechanical frameworks) and raise all the significant issues that must be tended to in NEMS configuration: detecting, incitation, control, correspondences, power, and interfacing across spatial scales and among natural and inorganic materials. Because of their size, tantamount to natural cells, Nano robots have a huge range of possible applications in fields, for example, ecological checking or medication. In any case, scientists today generally utilize the term Nano robot to depict atoms with an extraordinary property that empowers them to be modified to complete a particular assignment. We will portray

a versatile robot (Nano robot) that can be made with existing innovation that can be utilized to search out and pulverize hostile tissue inside the human body that can't be gotten to by different methods. The development and utilization of such gadgets would bring about various advantages. It would give either a fix or possibly a method for controlling or decreasing the impacts of various diseases nanotechnology can profoundly build our alternatives for anticipation, determination, and therapy of malignancy. Nanotechnology may likewise be valuable for creating approaches to kill disease cells without hurting sound, neighboring cells Nanotechnology utilizes remedial specialists that target explicit cells and convey their poison in a controlled, time-delivered way [3].



*Figure 2: Removal of cancer by surgery using the conventional method.*

### CONVENTIONAL METHODS OF CANCER THERAPY TREATMENTS

The vast majority with the disease gets a medical procedure, chemotherapy, radiation treatment, or other customary treatments sooner or later during therapy, and many will have a mix of these therapies. Infusion of medications influences both malignant and nondestructive cells in ordinary techniques. In this way, the primary kinds of malignancy therapy incorporate Surgery, Radiation Therapy, Chemotherapy, Immunotherapy, Targeted Therapy, and Hormone Therapy [4] (Fig. 2).

### DRAWBACKS & ADVANTAGES

Focal points of Nano robots over Conventional Medical Techniques: Nano robotics has been meant to defeat the accompanying disadvantages of ordinary clinical procedures.

- Entry points hurt tissue layers, which set aside a serious long effort to mend.
- Excruciating sedation is utilized to restrict the torment generally, yet it is just for a brief timeframe.

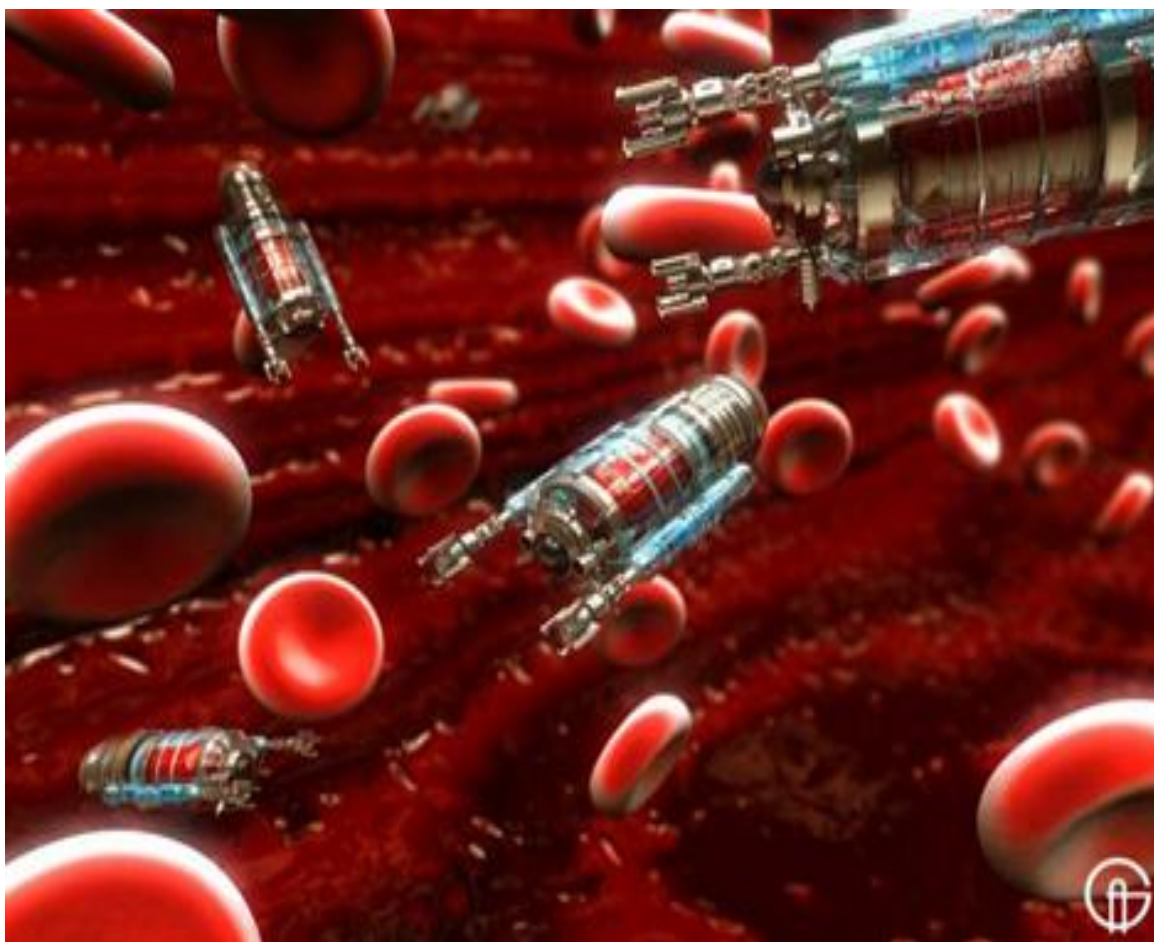
- Fragile medical procedures, for example, eye a medical procedure don't have a 100% achievement rate.
  - In any of the obtrusive procedures, the patient's life is absolutely in the possession of the administrator or specialist, or doctor. It is hazardous, as one mix-up could spell catastrophe.
  - Researchers and analysts are functions on a more vigorous, dependable, and bio-viable methodology. Rather than relieving the outside, they intend to safeguard the body from within. That is the place where clinical Nano robots come in. The significant favorable circumstances of this innovation give are
  - Negligible or no tissue injury.
  - Impressively less recuperation time.
  - Less post-treatment care is required.
  - Nonstop observing and analysis from within.
  - Fast reaction to an abrupt change.
- Some additional highlights of Nano robotics. Would likewise empower us to do the accompanying:



- It can store and handle past information, recognize designs, and subsequently, help to foresee the beginning of a disease.
- It can direct remotely or according to the program, focusing on explicit areas.
- It can convey payloads, for example, drugs, or solid cells to the particular site.
- They can explore through common organic pathways; subsequently, it very well may be redone (and frequently more sturdy) to body cells fabricated remotely.
- Hindrances of Nano robotics.
- At the point when diverse Nano robots are embedded to fix various sicknesses, the bunches might be framed inside the body.
- The establishment cost is very high.

### THE MODERN TECHNOLOGY USED TO CURE CANCER THERAPY

Nanotechnology utilizes remedial specialists that target explicit cells and convey their poison in a controlled, time-delivered way. As a needle is a today used to infuse prescription into the patient's circulatory system, tomorrow, Nano robots could ship and convey substance specialists straightforwardly to an objective cell. Nano killer (i.e., Nano robot) could discover and fix harmed organs, recognize and demolish a tumor mass. They would have the option to convey their positions, operational statuses, and the achievement or disappointment of the treatment as it advances [6].



**Figure 3:** Nano robots moving inside the bloodstream in the veins/capillaries to destroy the cancerous cells.

The utilization of functional Nano robots for medical services and medical procedure instrumentation is an arising innovation considered as a serious item at present being developed to arrive at the commercial center in the coming a very long time with possibly wide biomedical applications. The progressing improvements of sub-atomic scale gadgets, sensors, and engines are anticipated to empower tiny robots with

measurements similar to microbes. Ongoing advancements in the field of bimolecular figuring and Nano electronics hardware have shown emphatically the attainability of handling rationale assignments by bio-PCs, which are promising strides to empower Nano processors with a progressively multifaceted nature. Studies in the feeling of building biosensors and Nano-dynamic gadgets, which is needed to empower handy Nano

robot activity and movement, have been progressed as of late as well. Also, traditional protests identified with the genuine plausibility of nanotechnology, for example, quantum mechanics, warm movements, and rubbing, have been thought of and settled and conversations about the assembling of Nano devices are growing up. Creating Nano scale robots presents troublesome

manufacturing and control difficulties. The advancement of complex coordinated Nano systems and assembling of gadgets with elite can be all around explored and tended to through PC supported assembling examination, helping make ready for later utilization of Nano robots in biomedical designing issues (Fig. 3).



*Figure 4: Nano robots inside the bloodstream.*

The authors worked on the Nano issues. Nano medicine offers the possibility of groundbreaking new apparatuses for the treatment of human illnesses and the increase of human natural frameworks. Diamond-based clinical Nano robotics may offer significant upgrades in capacities over common natural frameworks, surpassing even the enhancements conceivable through tissue designing and biotechnology. Nano robots with totally counterfeit parts have not been acknowledged at this point. The dynamic territory of exploration in this field is centered around sub-atomic machines, which are completely motivated by nature's method of doing things at a Nano-scale. One illustration of the utilization of nanotechnology in medication is the nanomedical gadget known as respirocites, planned by Feynman in 1995-1996 [1-6] (Fig. 4).

Again explained the applications. He expects to copy all the significant elements of the

most well-known cells in the human body, the red platelet. The respirocites are fake red platelets containing tiny diamondoid pressure tanks that can be worked up to 1000atm of pressure. This cell is an empty, circular nanomedical gadget of 1 micron in width, a lot more modest than red cells. The respirocite is worked of 18 billion masterminded underlying iotas and holds an extra 9 billion particles when it is completely stacked. It comprises three fundamental stockpiling tanks; one for oxygen (up to ~1.5 billion atoms), another for carbon dioxide (up to ~1.5 billion particles), and a third tank for counterbalance water (up to ~6 billion particles), built with diamondoid honeycomb.

Finally, advantages were presented. It is intended to work in a way that it can convey over multiple times more respiratory gases than an equivalent volume of characteristic red platelets. Another intriguing illustration of a basic

nanorobotic application that gives a one of a kind super-biological ability is the clottocyte, counterfeit mechanical platelets [4-5]. The colonocytes are capable to work simply like some other platelets. Notwithstanding, the fake platelets could stop human seeping inside 1 second of actual injury even indecently huge wounds. Clottocytes may play out a coagulating capacity that is equal in its fundamentals to that performed by natural platelets yet at just 0.01% of the circulation system centralization of those cells or 20 Nano robots per cubic millimeter of serum. In other words, Nano robotic clottocytes reaction would be around multiple times more compelling as coagulating specialists than an equivalent volume of regular platelets.

### CONCLUSION

In this research w.r.t. the Nano technological oriented paper, we have introduced a short audit of the Nano-robots that were being utilized in the biomedical designing or restoring of the deadliest illness on the planet, i.e., the malignancy. Nature has made nanostructures for billions. Organic frameworks are current evidence of atomic nanotechnology. As opposed to focusing our eyes on the far future, let us start presently by making some real working gadgets that will permit us to fix probably the most dangerous infirmities referred to, just as advance our capacities straightforwardly, instead of as the results of different advances. There will be a day while wiping out disease cells are simple an out-quiet operation and are only a survey paper, which fills in as a reason for all the understudies, resources as a base for completing the exploration in this energizing field of nanorobotics.

### REFERENCES

1. A. Cavalcanti, R. A. Freitas Jr. (2005), Nanorobotics Control Design: A Collective Behavior Approach for Medicine, *IEEE Transactions on Nano Bio Science*, Vol. 4, no. 2, pp. 133-140, DOI: 10.1109/TNB.2005.850469.
2. R. Hariharan, J. Manohar (2011), "Nanorobotics As Medicament (Perfect Solution For Cancer)", *IEEE Emerging Trends in Robotics and Communication Technologies (INTERACT)*, DOI: 10.1109/INTERACT.2010.5706153.
3. A. Cavalcanti, L. Rosen, L. C. Kretly, M. Rosenfeld, S. Einav (2004), "Nanorobotics challenges in biomedical applications, design, and control," *IEEE ICECS International Conference on Electronics, Circuits, and Systems*, Tel-Aviv, Israel, pp. 447-450, DOI: 10.1109/ICECS.2004.1399714,
4. Sharma M. K. and Gupta R. (2016), Nanorobotics the future of medicines, *Research in Pharmacy and Health Sciences*, Available at: <https://www.rphsonline.com/wp-content/uploads/2019/07/RPHSVol2Issue1Article10.pdf>.
5. Bi C, Guix M, Johnson B, Jing W, and Cappelleri D. (2018), Design of microscale magnetic tumbling robots for locomotion in multiple environments and complex terrains, *Micromachines*, doi: 10.3390/mi9020068.
6. Mehra P and Nabhi K. (2016), A nanorobotics the changing face of dentistry, *The International Journal of Science and Research*, Available at: [https://www.ijsr.net/get\\_abstract.php?paper\\_id=NOV161810](https://www.ijsr.net/get_abstract.php?paper_id=NOV161810).



# Electrochemical Behavior of 1,3-bis(1-Phenylethyl) Urea as a Corrosion Inhibitor for Carbon Steel in 1 M HCl

B. Padmashree · K. Manjunatha · B. M. Prasanna

Submitted: 26 August 2019 / in revised form: 7 November 2019  
© ASM International 2020

**Abstract** 1,3-bis(1-Phenylethyl) urea was investigated as a good corrosion inhibitor for carbon steel by electrochemical techniques in 1 M HCl at a temperature range of 305–335 K. The investigation was done by electrochemical techniques such as potentiodynamic Tafel polarization and impedance spectroscopy. The calculated corrosion inhibition efficiency of inhibitor increases with their increasing concentrations. The Tafel polarization method reveals that the inhibitor acts as mixed type inhibitor. The inhibition effect of inhibitor attributed due to the adsorption on surface of carbon steel from 1 M HCl. The adsorption of inhibitor obeys the Langmuir's adsorption isotherm. The activation parameters indicate that the adsorption process is exothermic in nature. The scanning electron microscopic measurement gives a visual idea about the formation of protective layer on carbon steel surfaces, which retards the corrosion process.

**Keywords** 1,3-bis(1-Phenylethyl) urea · Inhibitor · Electrochemical measurements

## Introduction

Corrosion is a chemical process, which destruct the metal and alloys either by direct chemical or electrochemical reactions under the corrosive environment. The carbon steel is one of most important alloys of iron due to their superior thermal and mechanical characteristics. Therefore, carbon steel was used in enormous industrial and structural applications such as acid pickling, acid cleaning, acid descaling and oil-well acidizing [1, 2]. So, under these conditions acids provide an aggressive environment for corrosion of carbon steel. To avoid the metal dissolution due to the attack of corrosion is controlled by various techniques such as protective coatings, cathodic protection and corrosion inhibitors. Among those corrosion controlling techniques, use of corrosion inhibitors is the most convenient and practical method to retards the corrosion [3, 4].

Corrosion inhibitors are heterocyclic organic molecules, which are having electron-rich species such as N, S, O and  $\pi$ -electrons in heterocyclic ring system in its structure and are favor to act as a corrosion inhibitor due to the adsorption on surface of the metal [5]. Therefore, the adsorption of the inhibitor on surface of carbon steel which retards the corrosion. The present work concentrates on the inhibitory effect of 1,3-bis(1-phenylethyl) urea for carbon steel at a temperature range of 305–335 K in 1 M HCl by electrochemical measurements and SEM analysis. Thermodynamic and activation parameters can study the variation of inhibition efficiency with increasing temperature, and scanning electron microscopic method was used to discuss the surface analysis.

---

B. Padmashree (✉)  
Department of Chemistry, Brindavan College of Engineering,  
Bengaluru, Visvesvaraya Technological University, Belagavi,  
India  
e-mail: padmashree.ps@gmail.com

K. Manjunatha  
Department of Chemistry, Nagarjuna College of Engineering  
and Technology, Devanahalli, Bengaluru, Visvesvaraya  
Technological University, Belagavi, India

B. M. Prasanna  
Department of Chemistry, Jain Institute of Technology,  
Davanagere, Visvesvaraya Technological University, Belagavi,  
India



## Experimental

### Carbon Steel

Commercially available carbon steel was procured for all the corrosion inhibition experiments. The composition of the carbon steel is described in Table 1.

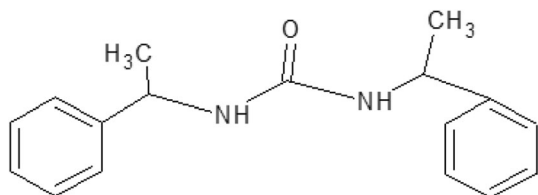
The strips of carbon steel with the dimension of  $4 \times 1 \times 0.1 \text{ cm}^3$  were used for corrosion inhibition studies by weight loss method. The electrochemical measurements were done by the same strip with  $1 \text{ cm}^2$ ; area of the metal surface was exposed (rest part was insulated by epoxy resin).

### Corrosion Inhibitor

The selected inhibitor 1,3-bis(1-phenylethyl) urea is a novel urea derivative; it was commercially purchased from Sigma-Aldrich pvt. India limited. It is a colorless amorphous derivative and highly soluble in hydrochloric acid. This inhibitor was selected for the current inhibition studies for carbon steel due to its non-toxicity and which are having electron-rich species such as N, O and  $\pi$  electrons in heterocyclic ring system. These species in the molecule facilitate adsorption onto the surfaces of carbon steel and reduces the corrosion. Hence, this molecule may behave as a good corrosion inhibitor for carbon steel in 1 M HCl. The inhibitor was dissolved in 1 M hydrochloric acid with the concentration range of 20–80 ppm as inhibited solution was used for all the experiments and molecular structure of inhibitor is shown in Fig. 1.

**Table 1** The composition of the low carbon steel

Elements	C	Mn	P	S	Fe
Percentage	0.35	0.032	0.028	0.03	Remaining



**Fig. 1** Molecular structure of 1,3-bis(1-phenylethyl) urea

### Electrochemical Measurements

A conventional three electrode system (i.e., carbon steel strip as working electrode, platinum electrode as counter electrode and SCE as reference electrode) was connected to an electrochemical Compastat.e10800 (Ivium Technologies, Netherland) for all the corrosion experiments. The potentiodynamic polarization measurements were documented at the scan rate of 1 mV/s in the given potential values. The electrochemical impedance spectra were recorded by an AC signals with amplitude of 1 mV/s at corrosion potential within the frequency range of 100–0.1 kHz.

### Scanning Electron Microscopic Measurement (SEM)

The surface morphology of carbon steel was carried out by scanning electron microscopy (JEOL JSM-840A model). The SEM micrographs were recorded without and with the optimized inhibitor concentration of 100 ppm in 1 M hydrochloric acid solution.

## Results and Discussions

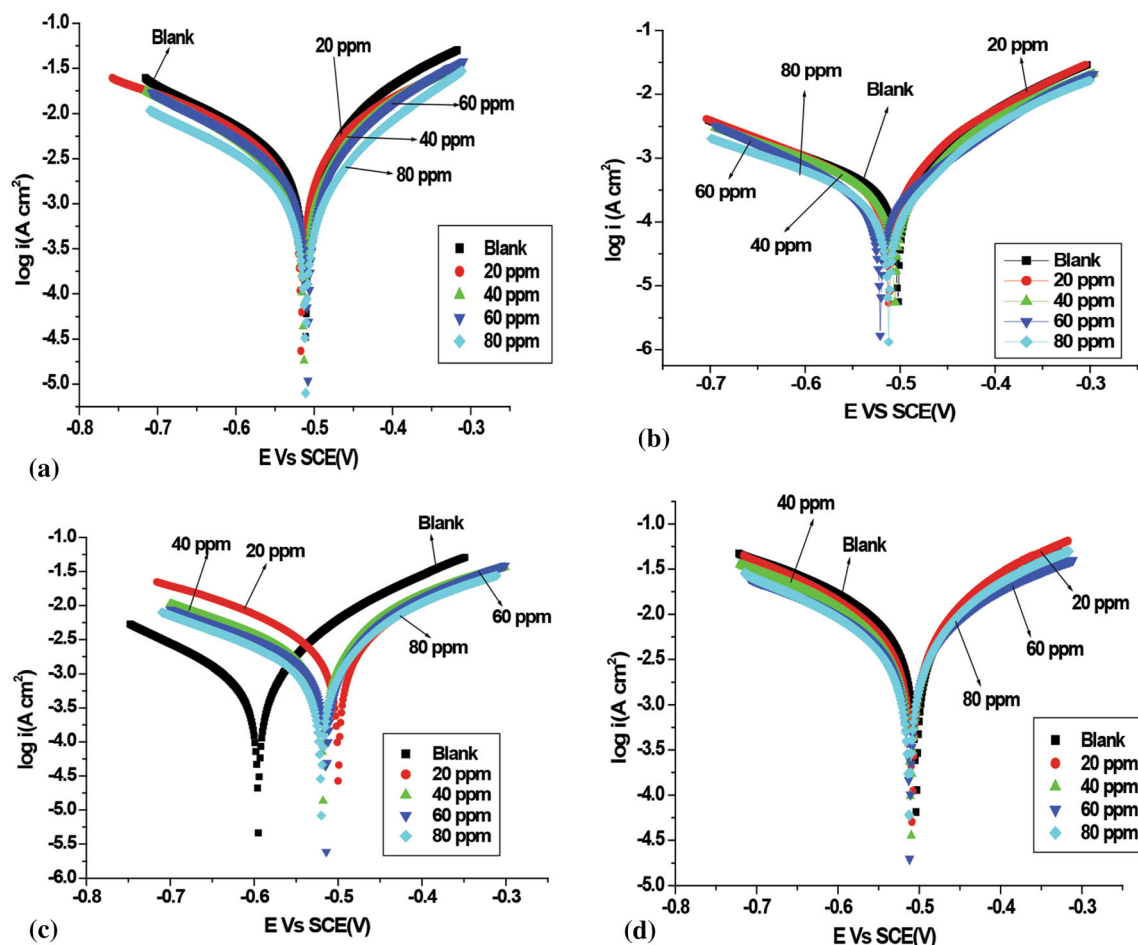
### Electrochemical Tafel Polarization Measurements

The potentiodynamic polarization behavior of carbon steel without and with the various concentration of inhibitor is shown in Fig. 2. The corrosion parameters by electrochemical polarization method viz, corrosion current density ( $i_{\text{corr}}$ ), corrosion potential ( $E_{\text{corr}}$ ), anodic Tafel slope ( $\beta_a$ ), cathodic Tafel slope ( $\beta_c$ ) and inhibition efficiency are reported in Table 1.

The following expression is used to calculate the inhibition efficiency ( $\eta_p$ ) of the inhibitor for carbon steel in 1 M hydrochloric acid as,

$$\eta_p = \frac{i^0 - i}{i^0} \times 100$$

where  $i^0$  and  $i$  are the corrosion current densities without and with the inhibitor, respectively. Results found by the Tafel polarization measurements (Table 1), the corrosion current density and corrosion rate decreases with the increasing concentration of 1,3-bis(1-phenylethyl) urea in 1 M hydrochloric acid solution. This indicates that the increasing concentration of inhibitor forms a protective layer onto the carbon steel surfaces, which retards the corrosion. As a result, there is an increasing inhibition efficiency by the addition of inhibitor in 1 M hydrochloric acid solution. The displacement of  $E_{\text{corr}}$  for inhibited solution with respect to that of uninhibited solution (i.e., Blank) was found less than 85 mV that inhibitor is



**Fig. 2** Tafel plots for carbon steel without and with the different concentrations of 1,3-bis(1-phenylethyl) urea at temperatures of (a) 303 K (b) 313 K (c) 323 K (d) 333 K

considered as mixed type, which retards the both anodic and cathodic reactions [6, 7]. There is change in  $\beta_c$  with minor extent with the increasing concentration of inhibitor reveals that there is a decreasing the hydrogen liberation due to the surface coverage on metal surface by the inhibitor molecules. And also the change in  $\beta_a$  may be reducing the reduction reaction due to the adsorption of inhibitor onto the surface of carbon steel from bulk of the solution.

#### Electrochemical Impedance Spectroscopic (EIS) Measurements

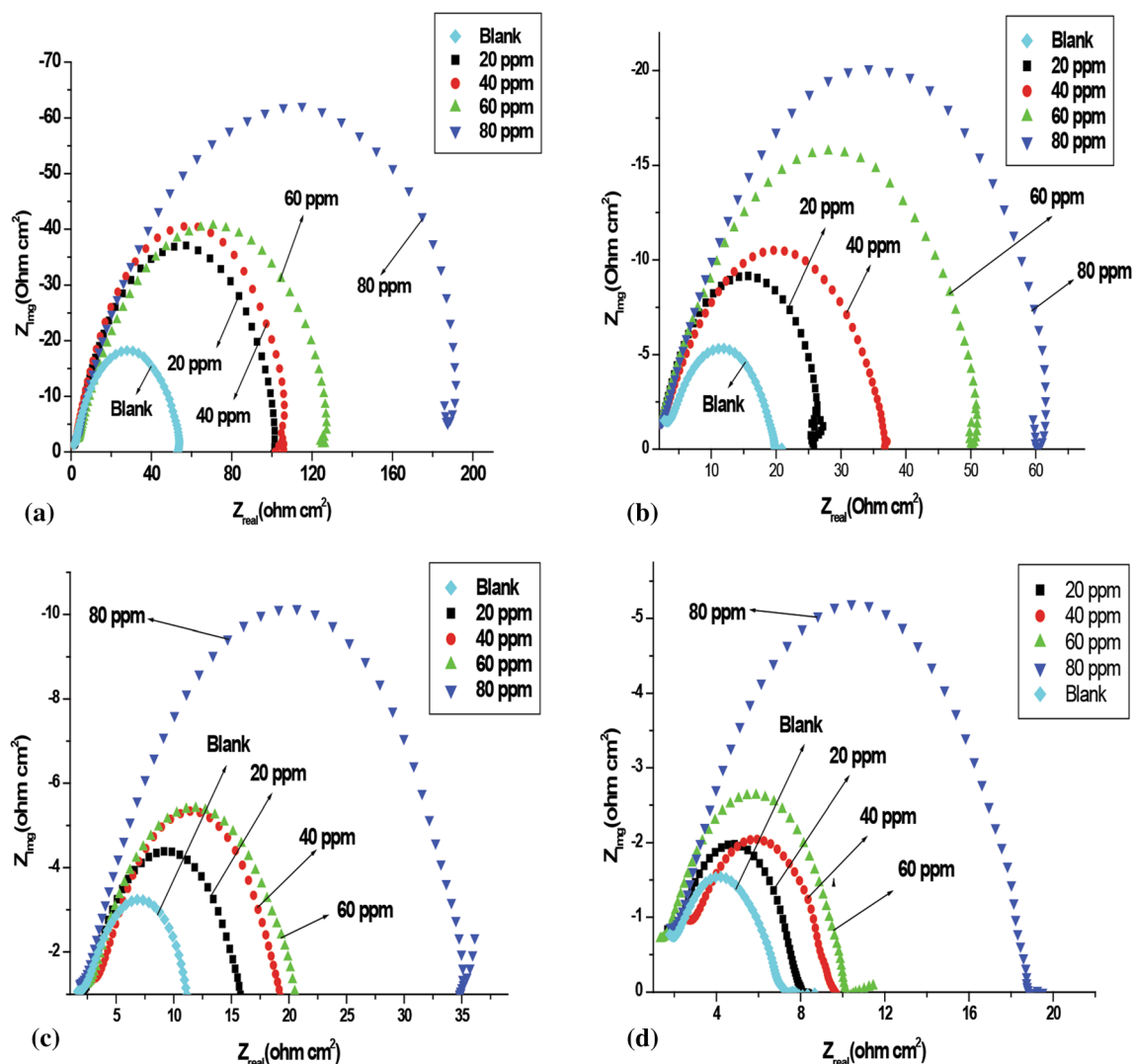
EIS is a significant method for the study of corrosion inhibitors, and results found this method are more consistent. The Nyquist plots found from this measurement are shown in Fig. 3, and the data obtained from EIS measurement are fit to an equivalent circuit as shown in Fig. 4 to compute the corrosion parameters. The computed parameters viz, polarization resistance ( $R_p$ ), double layer

capacitance ( $C_{dl}$ ) and inhibition efficiency are reported in Table 2, and the following expression was used to calculate the inhibition efficiency of the inhibitor for carbon steel in 1 M hydrochloric acid,

$$\eta_p = \frac{R_p - R_p^0}{R_p} \times 100$$

where  $R_p$  and  $R_p^0$  are the polarization resistance for carbon steel corrosion without and with the inhibitor, respectively.

The Nyquist's graphs as shown in Fig. 3 are made up of a set of semicircles with a high-frequency capacitive loop and low-frequency inductive loop. The computed corrosion parameters reveal that the addition of inhibitor increases the diameter of the semicircles, describes the polarization resistance ( $R_p$ ), which retards the metal corrosion. The increasing  $R_p$  values with the addition of inhibitor reduce the corrosion of carbon steel in 1 M hydrochloric acid through the adsorption process. Therefore, the inhibitor molecules adsorbed onto the surfaces of carbon steel



**Fig. 3** Nyquist plots for carbon steel without and with the different concentrations of 1,3-bis(1-phenylethyl) urea at temperatures of (a) 303 K (b) 313 K (c) 323 K (d) 333 K



**Fig. 4** Equivalent circuit to fit electrochemical impedance spectroscopic data

decrease the value of double layer capacitance ( $C_{dl}$ ). The decreasing  $C_{dl}$  value suggests increasing the thickness of the double layer which protect the metal by the attack of corrosion [8].

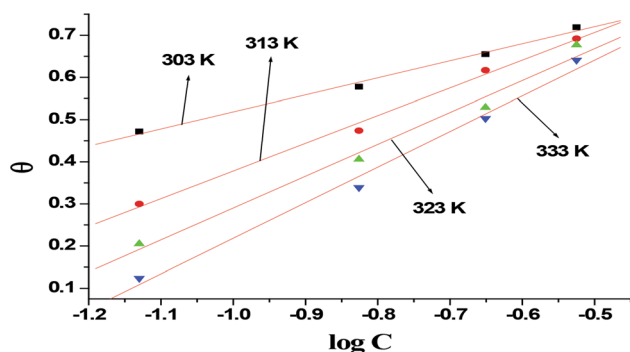
#### Adsorption Parameters (Table 3)

The inhibitory action of selected inhibitor for this current study attributed to the adsorption onto the carbon steel surface from 1 M hydrochloric acid solution. The mode of adsorption was investigated by the help of adsorption isotherm, which explains about the interaction inbetween inhibitor and surface of the metal. The current inhibition action takes place by the adsorption of inhibitor by fitting Freundlich adsorption isotherm. The calculated values of surface coverage ( $\theta$ ) are reported in Table 2, and then draw a graph of  $\theta$  against the concentrations of inhibitor (milli moles) as shown in Fig. 5, and calculated adsorption parameters are reported in Table 4.

The values of  $K_{ads}$  (Table 4) can be computed from the slope ( $K_{ads} = 1/C$ ) of the straight lines on the  $\theta$  axis. The

**Table 2** Corrosion parameters found by electrochemical Tafel polarization measurement for carbon steel without and with the different concentrations of 1,3-bis(1-phenylethyl) urea at a temperature range of 305–335 K

Temp. (K)	Concentration of 1, 3-bis(1-phenylethyl) urea (ppm)	Corrosion potential $E_{\text{corr}}$ (V)	Corrosion current density $i_{\text{corr}}$ ( $10^{-6}$ A cm $^{-2}$ )	Corrosion rate $v$ (mpy)	$\beta_c$ (mV/decade)	$\beta_a$ (mV/decade)	Inhibition efficiency $\eta_p$ (%)
305	Blank	− 0.511	0.196	26.85	− 5.29	7.18	–
	20	− 0.517	0.134	15.74	− 5.35	6.08	31.63
	40	− 0.513	0.102	13.72	− 5.98	7.25	47.95
	60	− 0.508	0.097	12.19	− 5.91	7.62	50.51
	80	− 0.511	0.055	11.18	− 5.51	7.89	71.93
315	Blank	− 0.502	0.210	40.50	− 5.64	9.45	–
	20	− 0.512	0.140	27.30	− 6.25	9.38	33.33
	40	− 0.506	0.102	22.30	− 5.82	9.68	51.42
	60	− 0.521	0.085	21.25	− 7.24	10.62	59.52
	80	− 0.512	0.062	17.30	− 5.87	11.08	70.47
325	Blank	− 0.595	0.241	60.50	− 6.30	8.83	–
	20	− 0.500	0.180	47.00	− 5.94	6.89	25.31
	40	− 0.518	0.142	33.20	− 5.13	6.94	41.07
	60	− 0.514	0.126	30.00	− 5.13	7.61	47.71
	80	− 0.520	0.075	24.70	− 5.42	7.69	68.87
335	Blank	− 0.504	0.340	73.50	− 5.44	5.98	–
	20	− 0.509	0.277	70.05	− 5.82	6.84	18.50
	40	− 0.510	0.246	46.98	− 5.73	6.23	27.64
	60	− 0.512	0.227	43.17	− 5.27	6.18	33.23
	80	− 0.512	0.138	32.47	− 5.52	6.63	59.41

**Fig. 5** Langmuir's adsorption isotherm

adsorbed inhibitor molecules onto the surface of the carbon steel are represented by the value of  $K_{\text{ads}}$ . The increasing values of  $K_{\text{ads}}$  decide the increasing the inhibition action for the metal by the better adsorption. Therefore, as on temperature increases from 305 to 335 K, which decreases the values of  $K_{\text{ads}}$ , this effect may be the fact that the inhibition effect of inhibitor decreases due to the increasing the temperature. After that, the value of free energy change

of adsorption  $\Delta G_{\text{ads}}^0$  calculated by the following expression as,

$$\Delta G_{\text{ads}}^0 = -\ln(K_{\text{ads}} \times 55.5) \times R \times T$$

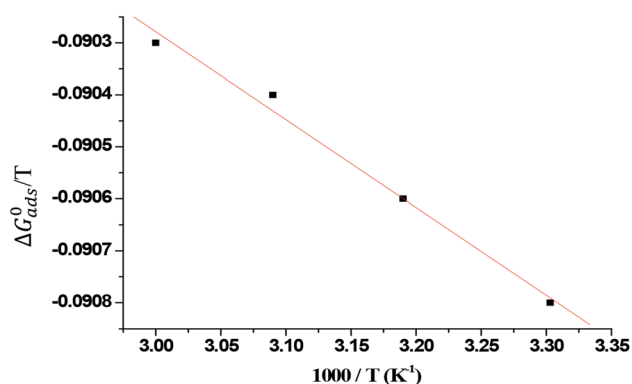
where  $R$  is the universal gas constant with the value of 8.314 kJ/Kg/K and  $T$  is the temperature in K. The measured values of  $\Delta G_{\text{ads}}^0$  are tabulated in Table 4, the negative value of  $\Delta G_{\text{ads}}^0$  is an indication of spontaneous adsorption of inhibitor with stabilized adsorbed layer onto the surface of carbon steel [9].

The value of  $\Delta G_{\text{ads}}^0$  also explains about the mode of adsorption by the inhibitor onto the carbon steel surfaces from bulk of the solution. There are two possible modes of adsorption; one is the electrostatic interaction between the inhibitor and surface of the carbon steel (i.e., physisorption), and another mode is the inhibitor adsorbed chemically onto the carbon steel surfaces (i.e., chemisorption). The chemisorption process involves the following points as,

- The replacement of water molecules from the surface of carbon steel by the inhibitor molecules

**Table 3** Thermodynamic parameters

Temperature (K)	$K_{\text{ads}}$ ( $\text{kJ mol}^{-1}$ )	$\Delta G_{\text{ads}}^0$ ( $\text{kJ mol}^{-1}$ )	$\Delta H_{\text{ads}}^0$ ( $\text{kJ mol}^{-1}$ )	$\Delta S_{\text{ads}}^0$ ( $\text{kJ mol}^{-1}$ )
305	1084	− 27.90	− 16.90	0.0360
315	966	− 28.51		0.0368
325	961	− 29.41		0.0384
335	941	− 30.25		0.0398

**Fig. 6** Graph of  $1000/T$  vs.  $\Delta G_{\text{ads}}^0$ 

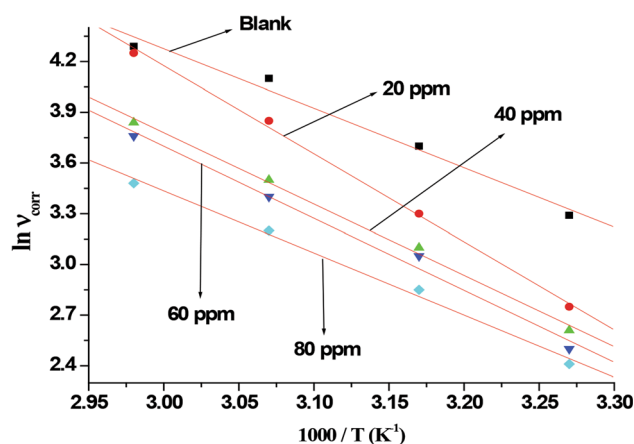
- The electronic interaction between  $\pi$  electrons from the inhibitor molecule and vacant d orbital of the surface of carbon steel.

If the value of  $\Delta G_{\text{ads}}^0$  is more than  $-40$  kJ/mol, the adsorption of inhibitor occurs only through the chemisorption. Suppose  $\Delta G_{\text{ads}}^0$  values lie in between  $-20$  kJ/mol and  $-40$  kJ/mol, the adsorption occurs through the both physisorption as well as chemisorption [10, 11]. In the present work, we found  $\Delta G_{\text{ads}}^0$  value is around  $-30$  kJ/mol. Hence, the adsorption process is the mixture of physisorption and chemisorption. At the same time, the  $\Delta G_{\text{ads}}^0$  value is close toward  $-40$  kJ/mol and indicates that the adsorption may occur predominantly in chemisorption process.

A graph of  $1000/T$  versus  $\Delta G_{\text{ads}}^0/T$  is shown in Fig. 6, the slope value is described as enthalpy of adsorption  $\Delta H_{\text{ads}}^0$ , and entropy of adsorption  $\Delta S_{\text{ads}}^0$  was calculated by the following equation,

$$\Delta S_{\text{ads}}^0 = \frac{(\Delta H_{\text{ads}}^0 - \Delta G_{\text{ads}}^0)}{T}$$

The computed values of  $\Delta H_{\text{ads}}^0$  and  $\Delta S_{\text{ads}}^0$  are reported in Table 4. The negative value of  $\Delta H_{\text{ads}}^0$  suggests that the

**Fig. 7** Arrhenius plot

adsorption process of inhibitor molecule is an exothermic in nature. The positive value of  $\Delta S_{\text{ads}}^0$  reveals that the reactions suffer a loss of degrees of freedom during the complex formation. And also the increasing in entropy is the indication of decreasing the inhibition effect as temperature increases from 305 to 335 K.

#### Activation Parameters

The study of the influence of temperature on the action of inhibitor for carbon steel corrosion in 1 M hydrochloric acid was investigated by the data obtained by Tafel polarization measurement (Table 1) at 305–335 K. From the results, we can observe in the temperature range of 305–335 the inhibition efficiency gradually decreases with the increasing temperature [12]. This observation was investigated by activation parameters by the help of Arrhenius and Transition plots. The significant activation parameter such as apparent activation energy ( $E_a^*$ ) was computed by the following Arrhenius equation as,

$$\ln v_{\text{Corr}} = \ln A - \frac{E_a^*}{RT}$$

**Table 4** Corrosion parameters found by EIS measurement for carbon steel without and with the different concentrations of 1,3-bis(1-phenylethyl) urea at a temperature range of 305–335 K

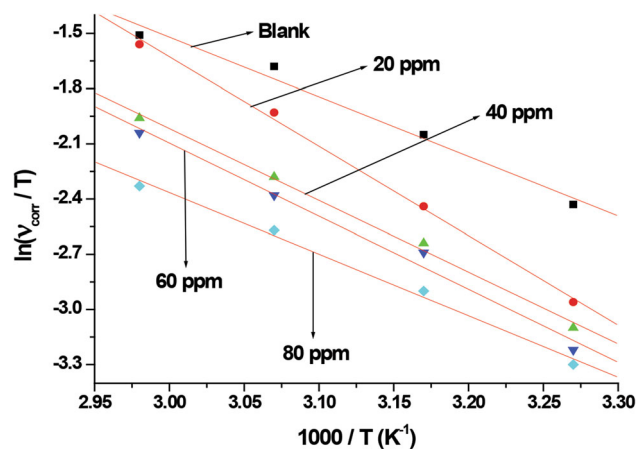
Temperature (K)	Inhibitor concentration (ppm)	Polarization resistance $R_p$ ( $\Omega$ cm <sup>2</sup> )	Double layer capacitance $C_{dl}$ ( $\mu$ F cm <sup>-2</sup> )	Inhibition efficiency $\eta_z$ (%)	Surface coverage ( $\theta$ )
305	Blank	51.00	0.0287	–	
	20	96.72	0.0275	47.27	0.472
	40	102.3	0.0255	50.14	0.501
	60	120.1	0.0196	57.53	0.575
	80	182.00	0.0163	71.97	0.719
315	Blank	17.81	0.0649	–	
	20	25.45	0.0615	30.01	0.300
	40	33.92	0.0535	47.49	0.474
	60	47.79	0.0274	62.73	0.627
	80	57.95	0.0192	69.26	0.692
325	Blank	10.58	0.0312	–	
	20	14.61	0.0249	27.58	0.275
	40	17.83	0.0296	40.66	0.406
	60	19.21	0.0262	44.92	0.449
	80	32.85	0.0156	67.79	0.677
335	Blank	6.05	0.0627	–	
	20	6.91	0.0382	12.41	0.124
	40	7.56	0.0342	19.94	0.199
	60	9.51	0.00029	36.39	0.363
	80	16.9	0.00013	64.18	0.641

**Table 5** Activation parameters for carbon steel in the absence and the presence of various concentrations of 1,3-bis(1-phenylethyl) urea at the temperature range of 305–335 in 1 M hydrochloric acid

Inhibitor concentration (ppm)	Apparent activation energy ( $E_a^*$ ) (kJ/mol)	Arrhenius pre-exponential factor ( $\text{kJ mol}^{-1}$ )	Enthalpy of activation ( $\Delta H^*$ ) (kJ mol <sup>-1</sup> )	Entropy of activation ( $\Delta S^*$ ) (J mol <sup>-1</sup> K <sup>-1</sup> )
Blank	– 29.23	$27.30 \times 10^5$	26.85	– 15.62
20	– 43.33	$40.12 \times 10^7$	40.40	– 10.86
40	– 35.09	$13.79 \times 10^6$	32.42	– 14.13
60	– 35.43	$21.42 \times 10^6$	33.00	– 13.99
80	– 31.31	$19.05 \times 10^6$	27.76	– 16.14

where  $v_{\text{Corr}}$  is the corrosion rate,  $R$  is the universal gas constant,  $T$  is temperature in K and  $A$  is the Arrhenius pre-exponential factor. A graph of  $v_{\text{Corr}}$  versus  $1000/T$  provides a set of straight lines which are having slope of  $-\frac{E_a^*}{R}$  and intercept of  $\ln A$  is described in Fig. 7. The calculated values of  $E_a^*$  and  $A$  are reported in Table 3.

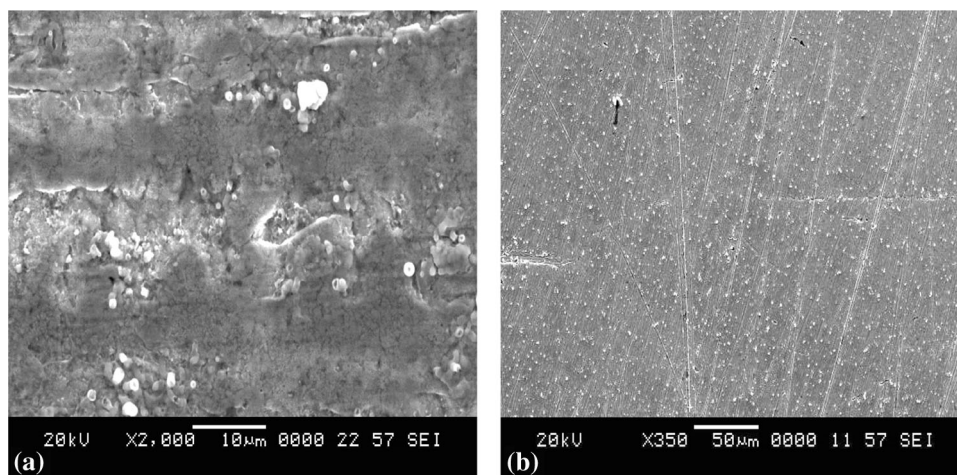
The values of  $E_a^*$  and  $A$  for inhibited solutions are higher than that of the uninhibited solution. This is attributed due

**Fig. 8** Transition state plot

to the addition of inhibitor hinders the metal dissolution in 1 M hydrochloric acid due to the adsorption onto the surfaces of the carbon steel. And also the value of  $E_a^*$  for the corrosion in the absence and the presence of various concentrations of 1,3-bis(1-phenylethyl) urea is greater than 20 kJ/mol and is an indication of the whole process of



**Fig. 9** SEM micrographs of carbon steel surface in (a) the absence of inhibitor (b) in the presence of 1,3-bis(1-phenylethyl) urea in 1 M hydrochloric acid



corrosion inhibition is controlled by surface reaction (Table 5).

The transition state equation as shown in below equation describes the variation in enthalpy ( $\Delta H^*$ ) and entropy ( $\Delta S^*$ ) of activation as,

$$\frac{\ln v_{\text{corr}}}{T} = \left[ \ln \frac{Rh}{Nh} + \frac{\Delta S^*}{R} \right] - \frac{\Delta H^*}{R}$$

where  $h$  is the Planck's constant,  $N$  is the Avogadro's number. The graph of  $\ln (v_{\text{corr}}/T)$  against  $1000/T$  is described in Fig. 8. Therefore, the plot provides a set of straight lines with the slope equal to  $\Delta H^*$ . The +ve value of  $\Delta H^*$  suggests that the metal dissolution reaction is endothermic in nature in the absence and the presence of inhibitor. And also the increasing  $\Delta S^*$  values indicate that the activated complex in the rate determining step characterizes a dissociation rather than association; it means that there is a decrease in disordering takes place going from reactants to activated complex [13, 14].

#### Scanning Electron Microscopic (SEM) Measurement

The surface characterization of the carbon steel was investigated by SEM as described in Fig. 9. The SEM micrographs of carbon steel strip in 1 M hydrochloric acid have large number of pits due to the attack of corrosion. But the same strip after the immersion of optimized uninhibited solution avoided by the attack of corrosion due to the formation of protective layer on metal surface by the inhibitor molecules.

#### Conclusions

- The inhibition efficiency of 1,3-bis(1-phenylethyl) urea for carbon steel increases with increasing concentration as on 20–80, but it decreases with increasing temperature as on 305–335 K.

- The inhibition efficiency of inhibitor attributed due to adsorption process and the present investigation obeys the Freundlich adsorption isotherm model.
- Adsorption parameters reveal that the inhibitor acts as mixed type and adsorbed spontaneously to retards the corrosion process.
- SEM micrographs visually give an idea of inhibition effect due to the formation of protective film on carbon steel surfaces.

#### References

1. H.L. Fan, H.B. Zheng, Inhibition of mild steel in hydrochloric acid solution by a mercapto-triazole compound. *J. Mater. Chem. Phys.* **77**, 655–661 (2002)
2. M. Yadav, D. Behera, U. Sharma, Nontoxic corrosion inhibitors for N80 steel in hydrochloric acid. *Chem. Sin.* **3**, 262–268 (2012)
3. I. Ahamad, M.A. Quraishi, Bis (benzimidazol-2-yl) disulphide: an efficient water soluble inhibitor for corrosion of mild steel in acid media. *Corros. Sci.* **51**, 2006–2013 (2009)
4. Q.B. Zhang, Y.X. Hua, Carbon steel corrosion behavior in aqueous carbonated solution of MEA/[bmim] [DCA]. *Electrochim. Acta* **54**, 1881–1887 (2009)
5. B.M. Prasanna, B.M. Praveen, N. Hebbar, T.V. Venkatesha, H.C. Tandon, Inhibition study of mild steel corrosion in 1 M hydrochloric acid solution by 2-chloro 3-formyl quinolone. *Int. J. Ind. Chem.* **7**(1), 9–19 (2016)
6. S.A. Ali, A.M. El-Shareef, R.F. Al-Ghandi, M.T. Saeed, The isoxazolidines: the effects of steric factor and hydrophobic chain length on the corrosion inhibition of mild steel in acidic medium. *Corros. Sci.* **47**, 2659–2678 (2005)
7. D. Jayaperumal, Effects of alcohol-based inhibitors of corrosion of mild steel in hydrochloric acid. *Mater. Chem. Phys.* **119**, 478–484 (2010)
8. E.S. Ferreira, C. Giancomlli, F.C. Giacomlli, A. Spinelli, Evaluation of the inhibitor effect of L-ascorbic acid on the corrosion of mild steel. *Mater. Chem. Phys.* **83**, 129–134 (2004)
9. A.M. Badiea, K.N. Mohana, Effect of temperature and fluid velocity on corrosion mechanism of low carbon steel in presence of 2-hydrazino-4,7-dimethylbenzothiazole in industrial water medium. *Corros. Sci.* **51**, 2231–2241 (2009)



10. B.M. Prasanna, B.M. Praveen, Hebbar Narayana, T.V. Venkatesha, H.C. Tandon, Ketosulfone drug as a green corrosion inhibitor for mild steel in acidic medium. *I&EC Res.* **53**, 8436–8444 (2014)
11. B.M. Prasanna, B.M. Praveen, N. Hebbar, Theoretical and experimental approach of inhibition effect by sulfamethoxazole on mild steel corrosion in 1 M HCl. *Surf Interface Anal.* (2018). <https://doi.org/10.1002/sia.6457>
12. A. Ostovari, S.M. Hoseinieh, M. Peikari, S. Hashemi, Corrosion inhibition of mild steel in 1 M HCl solution by henna extract: a comparative study of the inhibition by henna and its constituents (Lawsone, Gallic acid,  $\alpha$ -D-Glucose and Tannic acid). *J. Corros. Sci.* **51**, 1935–1949 (2009)
13. E.E. Oguzie, V.O. Njoku, C.K. Enenebeaku, C.O. Akalezi, C. Obi, Effect of hexamethylpararosaniline chloride (crystal violet) on mild steel corrosion in acidic media. *Corros. Sci.* **50**, 3480–3486 (2008)
14. S. Martinez, I. Stern, Thermodynamic characterization of metal dissolution and inhibitor adsorption processes in the low carbon steel/mimosa tannin/sulfuric acid system. *Appl. Surf. Sci.* **199**, 83–89 (2002)

**Publisher's Note** Springer Nature remains neutral with regard to jurisdictional claims in published maps and institutional affiliations.



# Synthesis, Characterization, and Anti-corrosion Behavior of Novel Mono Azo Dyes Derived from 4,5,6,7-Tetrahydro-1,3-benzothiazole for Mild Steel in Acid Solution

N. M. Mallikarjuna<sup>1</sup> · J. Keshavayya<sup>1</sup> · B. M. Prasanna<sup>2</sup> · B. M. Praveen<sup>3</sup> · H. C. Tandon<sup>4</sup>

Received: 27 September 2019 / Revised: 2 November 2019 / Accepted: 11 November 2019  
© Springer Nature Switzerland AG 2019

## Abstract

The present study describes the use of 4,5,6,7-tetrahydro-1,3-benzothiazole incorporated azo dyes as anti-corrosive agents and dissolution protection of mild steel from 1 M HCl solution. The inhibition efficiency of the azo dyes is determined by potentiodynamic polarization technique and electrochemical impedance spectroscopic studies. Based on these experimental results, it is noted that, the azo dye **T<sub>1</sub>** is an effective inhibitor and the inhibition efficiency of the azo dyes is found to be in the following order **T<sub>1</sub>** > **T<sub>2</sub>** > **T<sub>3</sub>**. From the polarization measurements, it is noted that, these azo dyes are mixed type of inhibitors in 1 M HCl. The inhibition efficiency was increased as the concentration of the inhibitors increased and attains a maximum value of 83.81% for **T<sub>1</sub>** at 2.5 ppm concentration. The quantum chemical study was used to explain better about the structural and electronic effects in relation to the inhibition efficiencies. Further, the surface morphology of the tested mild steel samples was examined by scanning electron microscopy and energy-dispersive X-ray analysis with and without inhibitors in 1 M HCl solution. The results of the analysis showed the effective corrosion inhibition properties after the deposition of the inhibitors on to the metal surface.

**Keywords** Azo dye · Benzothiazole · Corrosion inhibition · Quantum studies

## 1 Introduction

Azo colorants are the important class of organic molecules having –N=N– chromophoric group in their structures and found to have a variety of applications in different fields [1, 2]. Azo dyes were the largest used molecules among the class of dyes and pigments due to their variations in the chemical structure and method of applications which are quite simple. The presence of heterocyclic ring systems in

their structure exhibits a wide spectrum of colors and therefore they found to have applications in various fields such as the textile industry, designing of optical storage devices, non-linear optical (NLO) materials, and also in many biological reactions [3–7]. Due to their high thermal stability and sensitivity, they are widely used in the design of photo switches, electro-optic modulators [8–11], chemo sensors, and photochemical molecular switches [12].

From the literature survey, it is observed that many of the organic colorants were used as effective corrosion inhibitors to protect the metals from the aggressive media [13]. Particularly, the heterocyclic azo dyes were used to be efficient inhibitors for metals to avoid corrosion from acid solutions [14, 15]. It is an important and effective protection technique and is widely used in chemical, petroleum, and other industries. There are a good number of organic inhibitors widely using throughout the world, but some of the compounds fail to act effectively to protect the surface of the metals and also they can cause severe environmental problems due to toxicity, lack of inhibition efficiency, high cost in the production. Therefore, researchers are trying to overcome these impeding challenges and to

✉ J. Keshavayya  
jathikeshavayya1959@gmail.com

<sup>1</sup> Department of PG Studies and Research in Chemistry, School of Chemical Sciences, Kuvempu University, Jnana Sahyadri, Shankaraghatta, Karnataka 577451, India

<sup>2</sup> Department of Chemistry, Jain Institute of Technology, Davanagere, Karnataka 577003, India

<sup>3</sup> Department of Chemistry, College of Engineering and Technology, Srinivas University, Mukka, Mangalore, Karnataka 574146, India

<sup>4</sup> Department of Chemistry, Sri Venkateswara College, Dhula Kuan, New Delhi 110021, India

improve the efficiency of the inhibitors [16, 17]. The protective coatings, cathodic protection, use of organic inhibitors, etc. are the important corrosion control techniques to avoid corrosion of the surface of the metals and also helps in avoiding the metal dissolution [18, 19]. Among those, the use of heterocyclic compounds as corrosion inhibitors is the most convenient and practical method to control the corrosion [20]. Normally the heterocyclic compounds containing N, S, O, and P atoms and aromatic conjugated systems permit the lone pair of electrons and  $\pi$ -electrons to adsorb on to the metal surface, respectively [21]. Adsorption is a physico-chemical phenomenon wherein the loosely bound electrons on the heteroatoms of the inhibitor interact with the d-orbitals of the metal and forms a protective film on to the metal surface thereby protect the metal surface from corrosion [22–24]. The experimental techniques in the development of corrosion inhibitors are more effective but their mechanism of inhibition to prevent the corrosion of metallic surfaces from the external factors was not studied in detail [25]. Usually, the mechanism of action was illustrated by the nature of the protecting layer developed on the metal surface and the inhibition efficiency of the adsorbed compounds.

To achieve maximum inhibition efficiency of the applied compounds and to develop effective corrosion inhibitors, chemists have tried to explain the mechanism through molecular modeling (Quantum Chemical Calculations). Such theoretical methodologies are to provide a detailed explanation from the experimental techniques to find out the effective inhibition mechanism of the inhibitors [26]. Quantum chemical methods played a very significant role not only to develop effective corrosion inhibitors but also used in the study of the inhibition mechanism. Some of the parameters such as  $E_{\text{HOMO}}$ ,  $E_{\text{LUMO}}$ , electronegativity, electron affinity, global hardness, etc. signify the structural properties of the heterocyclic molecules, then the comparison of these structural properties with the experimental results will have an influence on the mechanism of corrosion inhibition [27, 28]. Therefore, these theoretical studies will greatly help to design and develop efficient and eco-friendly corrosion inhibitors for the protection of metals and alloys from aggressive media.

From all these extensive observations, we have attempted to synthesize novel azo dyes and their corrosion inhibitory effect over mild steel in 1 M HCl solution by electrochemical and quantum chemical methods. The chemical structures of all the newly synthesized azo dyes were elucidated by various physico-chemical techniques. The electrochemical measurements include potentiodynamic polarization and electrochemical impedance spectroscopy (EIS) and quantum chemical calculations were done by the PM3 method. Further, the corrosion inhibition efficiency evaluated from the above experimental techniques was compared with the

quantum chemical study and they were discussed in detail at the end of the results and discussion section.

## 2 Experimental

All the solvents and chemicals used in the present study were analytical grade (AR) and purchased from Sigma-Aldrich Chemical Company and used without further purification. The completion of the reaction was monitored by thin-layer chromatography and performed on silica gel plates purchased from Merck. Melting points of the synthesized compounds were determined by using an electro-thermal melting point apparatus and are uncorrected. UV–Vis spectra were recorded on Elico-SL 164 double-beam spectrophotometer in the range 200–800 nm using ca.  $10^{-6}$  M solution in four different solvents like ethanol, tetrahydrofuran, *N,N*-dimethyl formamide, and dimethyl sulfoxide. FT-IR spectra of the compounds were recorded as KBr pellets on a Perkin-Elmer-spectrum RX-IFTIR instrument in the region 4000–400  $\text{cm}^{-1}$ . The  $^1\text{H}$  NMR spectra were recorded on the FT-NMR spectrometer model Bruker Avance II, 400 MHz using  $\text{DMSO}-d_6$  as solvent. ESI–MS spectra of the compounds were recorded on a mass spectrometer equipped with electrospray ionization (ESI) source having a mass range of 4000 amu in quadrupole and 20,000 amu in ToF. The quantum chemical parameters of the azo dyes were obtained in the gas phase from the parametric method 3 (PM3) by using Hyperchem 7.5 package program.

### 2.1 Synthesis of 4,5,6,7-Tetrahydro-1,3-benzothiazol-2-amine (2)

The starting material 4,5,6,7-tetrahydro-1,3-benzothiazol-2-amine (2) was synthesized as per reported literature [29, 30]. To the hot solution of cyclohexanone (4.5 mL, 0.05 mol) in 25 mL ethanol, thiourea (6 g, 0.1 mol) and iodine (12.7 g, 0.05 mol) were added and the reaction mixture was stirred for 5 h at reflux temperature. Then the reaction mixture was cooled to room temperature and 100 mL distilled water was added. The obtained solution was basified by the addition of aqueous ammonia and extracted with ethyl acetate. The organic layer (ethyl acetate layer) was washed several times with water and then finally filtered to remove insoluble solids. The ethyl acetate extract was concentrated to two-third of its volume and we obtained pure red syrup as the final compound.

Red syrup, yield: 82%, m.p. 62–65 °C, IR (KBr,  $\text{cm}^{-1}$ ): 3364 (NH), 2963 (aliphatic  $\text{CH}_2$ ), 1625 ( $\text{C}=\text{N}$ ).  $^1\text{H}$  NMR ( $\text{DMSO}-d_6$ , ppm): 6.63 (s, 2H,  $\text{NH}_2$ ), 2.51–2.36 (d, 4H,  $\text{CH}_2$ ), 1.70 (s, 4H,  $\text{CH}_2$ ). Anal. Calcd. For  $\text{C}_7\text{H}_{10}\text{N}_2\text{S}$ : C, 54.51; H, 6.54; N, 18.16. Found: C, 54.47; H, 6.12; N, 18.02. MS: 155 m/z ( $\text{M}+1$ )<sup>+</sup>.

## 2.2 General Procedure for the Synthesis of Azo Dyes ( $T_1$ – $T_3$ )

A 2 mmol of the well-cooled solution of 4,5,6,7-tetrahydro-1,3-benzothiazol-2-amine (**2**) in 5 mL HCl was added drop wise into the previously cooled solution of sodium nitrite in 2 mL  $H_2SO_4$  (nitrosyl sulphuric acid) and was kept on an ice-salt bath till the reaction mixture was attained the temperature 0–5 °C. After completion of the addition, the reaction mixture was stirred continuously for 2 h to complete the diazotization. The resulting reaction mixture was then poured into the ice-cold solution of coupling components (2 mmol) (**a–c**) in acetic acid (8 mL). Furthermore, the reaction mixture was stirred for an additional 2 h in the ice-salt bath. The pH of the reaction mixture was maintained at 5–6 by adding the required volume of saturated sodium bicarbonate solution. The obtained product was collected by filtration, washed with cold water and finally, the product was dried. The pure compounds ( $T_1$ – $T_3$ ) were obtained by recrystallizing in ethanol [31]. The schematic representation of the synthesis of azo dyes was depicted in Scheme 1.

### 2.2.1 Synthesis of 4-[3a, 4 5,6,7,7a-hexahydro-1,3-benzothiazol-2-ylidiazenyl]-5-methyl-2-phenyl-2,4-dihydro-3H-pyrazol-3-one ( $T_1$ )

Orange-red solid, yield: 72%, m.p. 193–5 °C, IR (KBr,  $cm^{-1}$ ): 3065, 1801 (C=N), 2938 (Ar-H), 1661 (C=O), 1495 (N=N), 1158, 838 (C=S).  $^1H$  NMR (DMSO- $d_6$ , ppm): 7.92–7.91 (d, 2H, Ar-H), 7.43–7.39 (t, 2H,

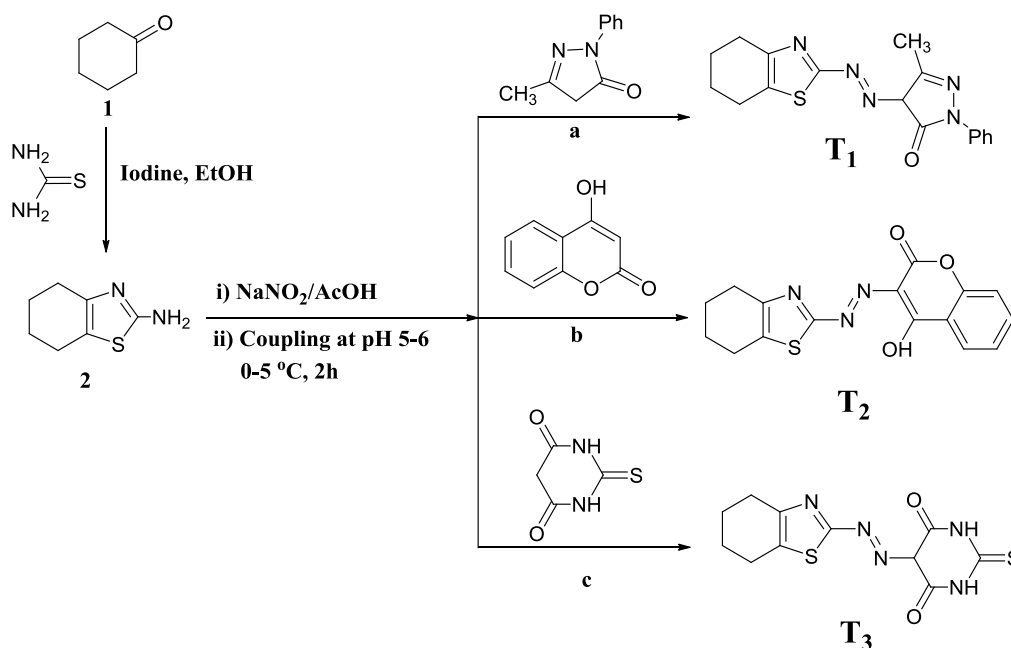
Ar-H), 7.22–7.18 (t, 1H, Ar-H), 2.72–2.68 (d, 4H,  $CH_2$ ), 2.33 (s, 3H,  $CH_3$ ), 1.87 (s, 5H,  $CH_2$ ). Anal. Calcd. For  $C_{17}H_{17}N_5OS$ : C, 60.16; H, 5.50; N, 20.63. Found: C, 59.96; H, 5.46; N, 20.25. MS:  $m/z$  340 ( $M+1$ ) $^+$ .

### 2.2.2 Synthesis of 4-Hydroxy-3-[4,5,6,7-tetrahydro-1,3-benzothiazol-2-ylidiazenyl]-2H-chromen-2-one ( $T_2$ )

Brick red solid, yield: 78%, m.p. 196–8 °C, IR (KBr,  $cm^{-1}$ ): 3434 (OH), 3061, 1814 (C=N), 2932 (Ar-H), 1663 (C=O), 1465 (N=N), 1247 (C–O), 1180, 867 (C=S).  $^1H$  NMR (DMSO- $d_6$ , ppm): 7.97–7.95 (d, 1H, Ar-H), 7.51–7.49 (t, 1H, Ar-H), 7.21–7.19 (t, 1H, Ar-H), 7.17–7.13 (d, 1H, Ar-H), 2.72–2.65 (d, 4H,  $CH_2$ ), 1.84 (s, 4H,  $CH_2$ ). Anal. Calcd. For  $C_{16}H_{13}N_3O_3S$ : C, 58.70; H, 4.00; N, 12.84. Found: C, 58.43; H, 5.62; N, 12.67. MS:  $m/z$  328 ( $M+1$ ) $^+$ .

### 2.2.3 Synthesis of 5-[4,5,6,7-Tetrahydro-1,3-benzothiazol-2-ylidiazenyl]-2 thioxodihydropyrimidine 4,6(1H, 5H)-dione ( $T_3$ )

Dark red solid, 75%, m.p. 192–4 °C, IR (KBr,  $cm^{-1}$ ): 3043 (NH), 2940 (Ar-H), 1683 (C=O), 1480 (N=N), 1149, 852 (C=S).  $^1H$  NMR (DMSO- $d_6$ , ppm): 12.59 (s, 2H, NH), 2.7 (s, 2H,  $CH_2$ ), 2.60 (s, 2H,  $CH_2$ ), 1.79 (s, 5H,  $CH_2$ ). Anal. Calcd. For  $C_{11}H_{11}N_5O_2S_2$ : C, 42.71; H, 3.58; N, 22.64. Found: C, 42.68; H, 3.43; N, 22.13. MS:  $m/z$  310 ( $M+1$ ) $^+$ .



Scheme 1 Synthesis of azo dyes ( $T_1$ – $T_3$ )

## 2.3 Corrosion Inhibition Measurements

The inhibition effect of synthesized azo dyes ( $T_1$ – $T_3$ ) on the corrosion of mild steel in 1 M HCl solution was studied by both experimental and theoretical methods. The working electrode (mild steel strip), the counter electrode (platinum) and a reference electrode (SCE) were used for the measurements. The mild steel strip (working electrode) was mechanically cut into 1 cm × 1 cm × 1 cm dimensions with an exposed area of 1 cm<sup>2</sup> and the rest of the area was coated with Araldite resin. Before performing the electrochemical measurements, the mild steel strip was abraded by different grade emery papers from 100 to 2000, finally washed with acetone and dried. The commercially available mild steel strips (composition in %: C = 0.16, Mn = 0.35, Si = 0.016, P = 0.01, S = 0.029, Cr = 0.06, Cu = 0.1 and the remaining is Fe) were used for all the experimental methods [32–34]. The various concentrations of inhibitor solutions were prepared in 1 M HCl solution.

The experimental methods such as potentiodynamic polarization and electrochemical impedance spectroscopy were carried out by an electrochemical work station CHI608D with the three-electrode system at 303 K. Before the start of each electrochemical measurement, the working electrode was allowed to stand for about 30 min to establish the open circuit potential (OCP). In the potentiodynamic polarization measurement, the potential/current curves were recorded at a scan rate of 0.001 Vs<sup>−1</sup> with respect to OCP. Impedance measurements were recorded with an AC signal at an amplitude of 5 mV at OCP in the given frequency range from 100 kHz to 10 mHz. The quantum chemical calculation of the inhibitors was performed in the gaseous

phase using parametric method 3 (PM3) by the Hyper Chem 7.5 package program.

## 2.4 Investigation of surface morphology

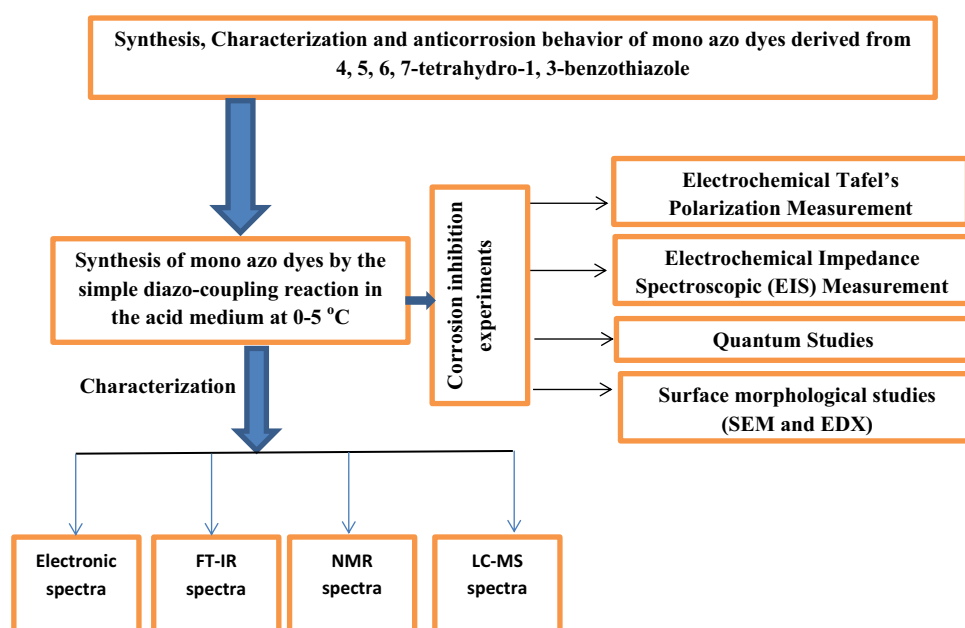
The mild steel samples were used for the surface analysis and immersed in 1 M HCl solution in the absence and presence of inhibitors ( $T_1$ – $T_3$ ) for 4 h. After 4 h of immersion, the samples were washed with distilled water and dried. Then the samples were studied for their surface morphology with the help of scanning electron microscopy (SEM). The elemental composition on the surface of the samples was evaluated by energy-dispersive X-ray (EDX) spectroscopy (GEMINI, Ultra 55).

The entire experimental program was shown in the form of flowchart as depicted in Fig. 1.

## 3 Results and Discussion

The present work mainly focuses on the design of novel heterocyclic azo dyes by conventional diazo-coupling reaction of 4,5,6,7-tetrahydro-1,3-benzothiazol-2-amine (**2**) with three coupling components such as 5-methyl-2-phenyl-2,4-dihydro-3H-pyrazol-3-one (**a**), 4-hydroxy-2H-chromen-2-one (**b**) and 2-thioxodihydropyrimidine-4,6(1H, 5H)-dione (**c**) at 0–5 °C and to measure the corrosion inhibition efficiency on mild steel in 1 M HCl solution by experimental and theoretical methods. All the newly synthesized azo dyes were characterized by various analytical and spectroscopic techniques. The physical and analytical data of the azo dyes are presented in Table 1. The structures of the newly

**Fig. 1** Flow chart for the synthesis, structural characterization and anti-corrosion behavior of azo dyes ( $T_1$ – $T_3$ )



**Table 1** Physical and analytical data of the synthesized azo dyes (**T**<sub>1</sub>–**T**<sub>3</sub>)

Compounds	Mol. formula	Mol. (wt)	M. P. (°C)	Color	Elemental analysis (%) calc (found)		
					C	H	N
<b>T</b> <sub>1</sub>	C <sub>17</sub> H <sub>17</sub> N <sub>5</sub> OS	339.41	193–5	Orange-red	60.16 (59.96)	5.50 (5.46)	20.63 (20.25)
<b>T</b> <sub>2</sub>	C <sub>16</sub> H <sub>13</sub> N <sub>3</sub> O <sub>3</sub> S <sub>3</sub>	327.35	196–8	Brick red	58.70 (58.43)	4.00 (5.62)	12.84 (12.67)
<b>T</b> <sub>3</sub>	C <sub>11</sub> H <sub>11</sub> N <sub>5</sub> O <sub>2</sub> S <sub>2</sub>	309.36	192–4	Dark red	42.71 (42.68)	3.58 (3.43)	22.64 (22.13)

synthesized azo dyes were found to be in good agreement with the spectral data.

The presence of a typical carbonyl functional group in all the synthesized azo dyes (**T**<sub>1</sub>–**T**<sub>3</sub>) was confirmed by the infrared spectra are displayed at the 1661–1683 cm<sup>−1</sup> region. The spectra showed the existence of azo (–N=N–) group at 1465–1495 cm<sup>−1</sup> in all the dyes [35]. The aromatic CH stretching vibrations and C=S groups in all the compounds appeared in the region 2932–2940 cm<sup>−1</sup> and 1149–1180 cm<sup>−1</sup>, respectively. The absorption band of the OH group in compound **T**<sub>2</sub> appeared at 3434 cm<sup>−1</sup> region.

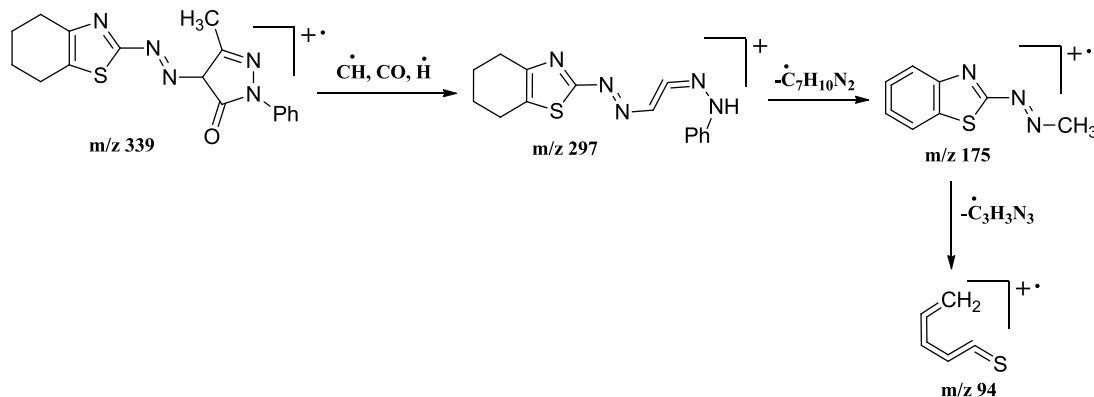
In the <sup>1</sup>H NMR spectra of dyes (**T**<sub>1</sub>–**T**<sub>3</sub>) recorded in DMSO-*d*<sub>6</sub> displayed signals of the respective protons based on their chemical shifts and multiplicities. In the <sup>1</sup>H NMR spectra of **T**<sub>1</sub> and **T**<sub>2</sub>, the aromatic protons have resonated in the region 7.92–7.18 and 7.97–7.13 ppm respectively. In the spectra of all azo dyes (**T**<sub>1</sub>–**T**<sub>3</sub>), the protons appeared in the region 2.70–1.79 ppm corresponds to the aliphatic protons of the tetrahydro benzothiazole moiety. Furthermore, the two NH protons of the thiobarbitone ring in the compound **T**<sub>3</sub> appeared as a singlet at 12.59 ppm.

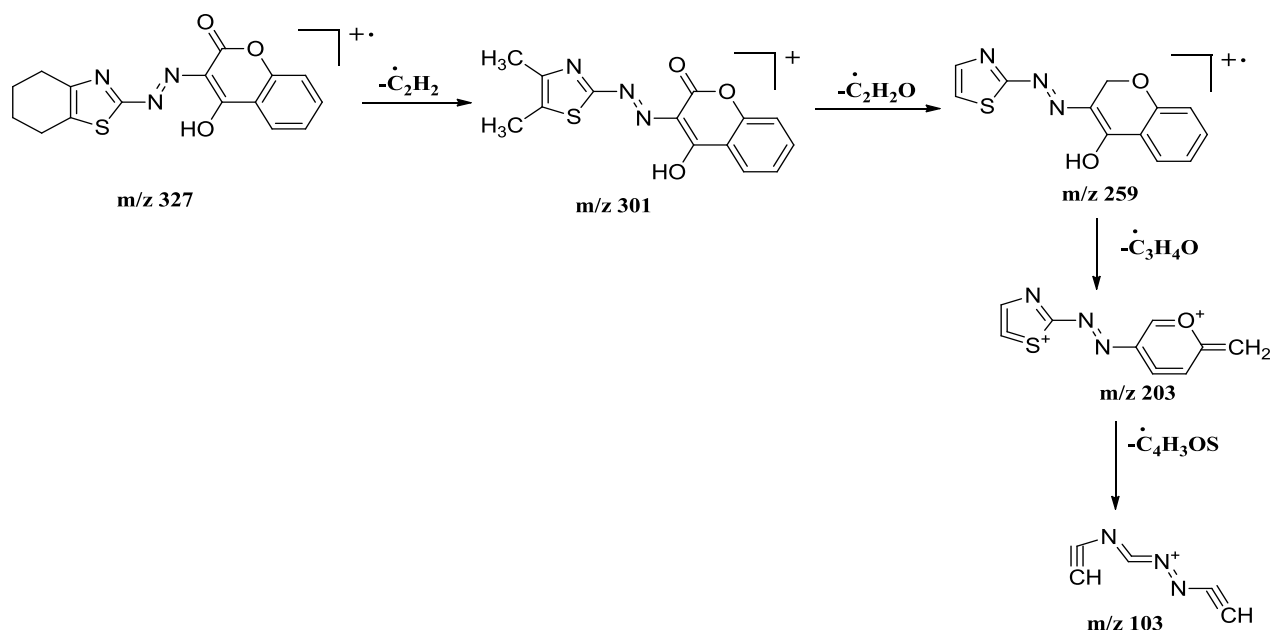
The ESI-mass spectra of azo dyes (**T**<sub>1</sub>–**T**<sub>3</sub>) have been recorded for their mass spectral studies and their tentative mass spectral fragmentation is given in Schemes 2, 3 and 4. The mass spectra of the azo dyes showed molecular ion peaks equivalent to their molecular mass along with other fragment peaks. The mass spectra of synthesized azo dyes **T**<sub>1</sub>, **T**<sub>2</sub> and **T**<sub>3</sub> exhibited their molecular ion peaks recorded

at *m/z* 340, 328 and 310 respectively. From the above spectral studies, it is noted that the obtained spectroscopic results are in accordance with the proposed chemical structures of the synthesized azo dyes.

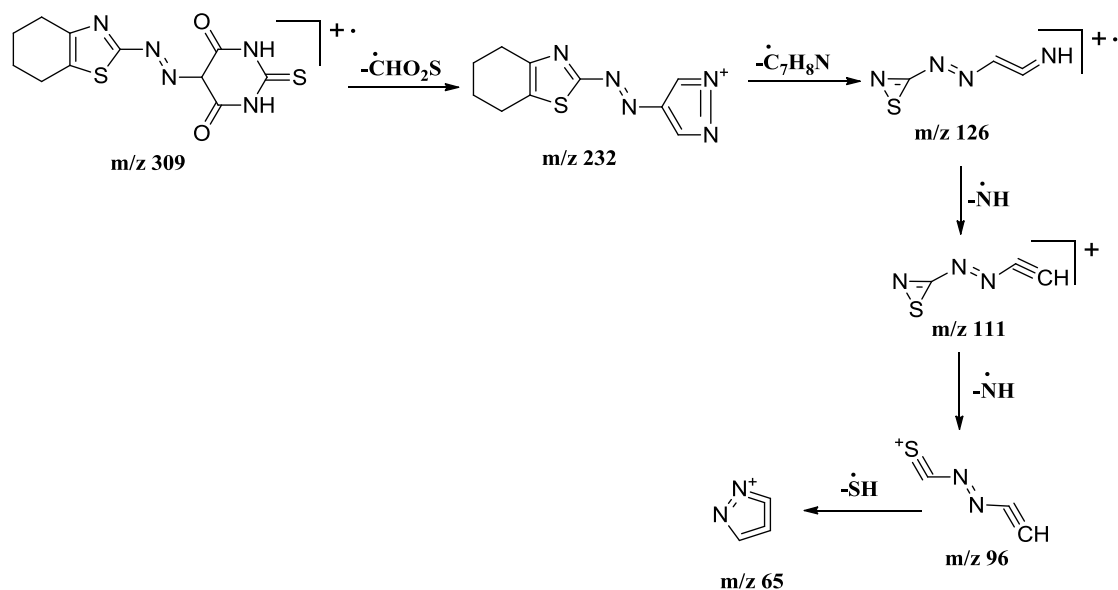
### 3.1 Electronic Absorption Spectra and Substituent Effect

Generally, the polarity of the solvent molecules and the electronic substituents present on the diazo components influence the values of the absorption maxima ( $\lambda_{\max}$ ). Therefore, in order to measure the effect of solvent polarity on the electronic spectra of the azo dyes, we recorded their absorption spectra (Figs. 2, 3, and 4) in four different solvents (Ethanol, tetrahydro furan, *N,N*-dimethyl formamide, and dimethyl sulphoxide) in the range 200–800 nm at  $\sim 10^{-6}$  M concentration and the results obtained are presented in Table 2. From the electronic spectral results it is evident that, the absorption spectra of the azo dyes (**T**<sub>1</sub>–**T**<sub>3</sub>) in different solvents exhibited absorption maxima in the region 365–442 nm due to  $\pi \rightarrow \pi^*$  or  $n \rightarrow \pi^*$  transition of the azo group. From Table 2, it is observed that, as the polarity of the solvent molecules increases (Ethanol > THF > DMF > DMSO), the value of  $\lambda_{\max}$  also increases indicating a bathochromic shift in all the studied azo compounds. For example, in the case of ethanol, the observed values of  $\lambda_{\max}$  for the compounds (**T**<sub>1</sub>–**T**<sub>3</sub>) are in the range of 364–366 nm. In the case of THF, DMF, and DMSO the wavelengths of absorptions of compounds

**Scheme 2** Tentative mass spectral fragmentation of the azo dye **T**<sub>1</sub>



**Scheme 3** Tentative mass spectral fragmentation of the azo dye **T<sub>2</sub>**

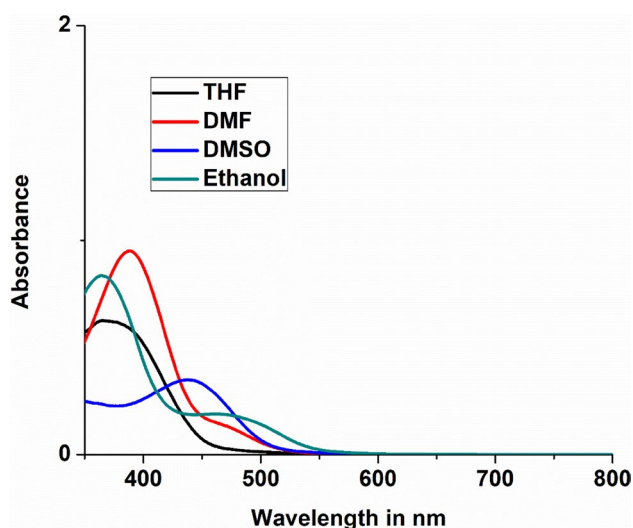
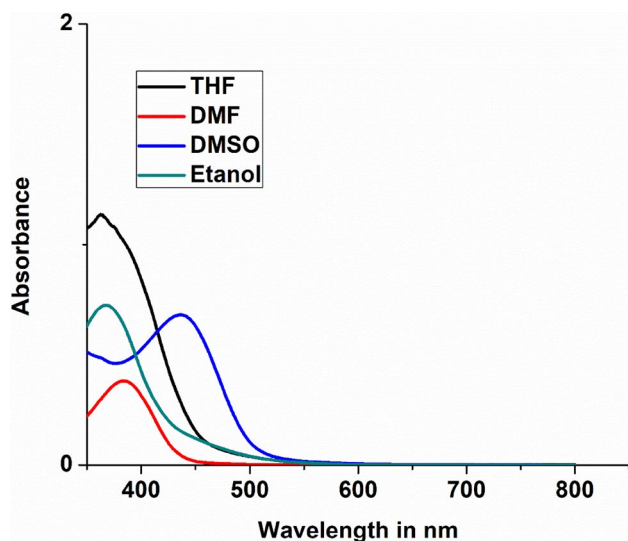


**Scheme 4** Tentative mass spectral fragmentation of the azo dye **T<sub>3</sub>**

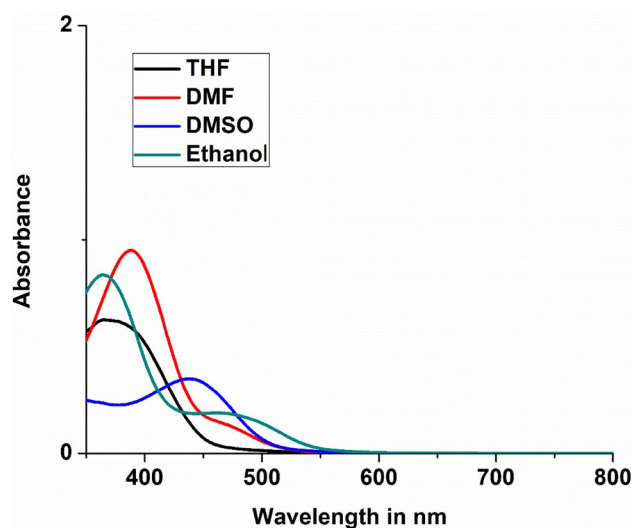
(**T<sub>1</sub>**–**T<sub>3</sub>**) appeared in the range of 367–378, 384–394, and 439–442 nm, respectively. Therefore, from our studies, it is inferred that the polarity of the solvents will play a crucial role in the interpretation of the electronic spectra of the studied azo dyes. Particularly, in more polar solvents the  $\lambda_{\text{max}}$  significantly shifted towards longer wavelengths. This observed bathochromic shift of molecules can be attributed to the interaction of solvent molecules with the lone pair of electrons on the nitrogen atom of the azo group that causes

extended conjugation via increased polarity [36]. The difference in the value of  $\lambda_{\text{max}}$  for the studied azo dyes can be attributed to the electron releasing and withdrawing properties of the substituents present on the conjugated system. By the close observation of Table 2, the introduction of electron-donating  $-\text{H}$ ,  $-\text{CH}_3$  and  $-\text{C}_6\text{H}_5$  groups in the benzene ring resulted in a bathochromic shift in all the solvents. Electron withdrawing substituents caused hypsochromic shift when there is a change of polar to non-polar solvents



Fig. 2 Electronic spectrum of compound  $T_1$ Fig. 3 Electronic spectrum of compound  $T_2$ 

[37]. In the present case, the presence of methyl and phenyl groups in the compound  $T_1$  showed a stronger bathochromic shift nearly in all solvents than  $T_2$  and  $T_3$ . This is a result of the effective interaction of the solvent molecules with the compounds demonstrate that different substituents on the benzene ring significantly change the extent of conjugation in the molecules. From the above discussion, it is concluded that both the polarity of the solvent and electronic effects are the two major factors that will directly influence the position of the absorption maxima in the electronic spectra of the organic molecules. Therefore, an increase in the solvent polarity and enhancement of electron density on the diazo component will significantly produce a bathochromic effect

Fig. 4 Electronic spectrum of the compound  $T_3$ 

i.e., shifts in the absorption maxima towards longer wavelength was observed.

## 3.2 Corrosion Inhibition Studies

### 3.2.1 Polarization Measurement

The polarization curves for mild steel in 1 M HCl are given in Fig. 5. From polarization curves, the electrochemical parameters such as corrosion potential ( $E_{\text{corr}}$ ) and corrosion current density ( $i_{\text{corr}}$ ) values were calculated by the Tafel plot analysis. Cathodic and anodic Tafel slopes ( $\beta_c$  and  $\beta_a$ ) are calculated by the extrapolation of the linear part of the Tafel lines. Table 3 consists of computed corrosion parameters by polarization measurement [38]. The inhibition efficiency of the inhibitors was calculated by the following expression,

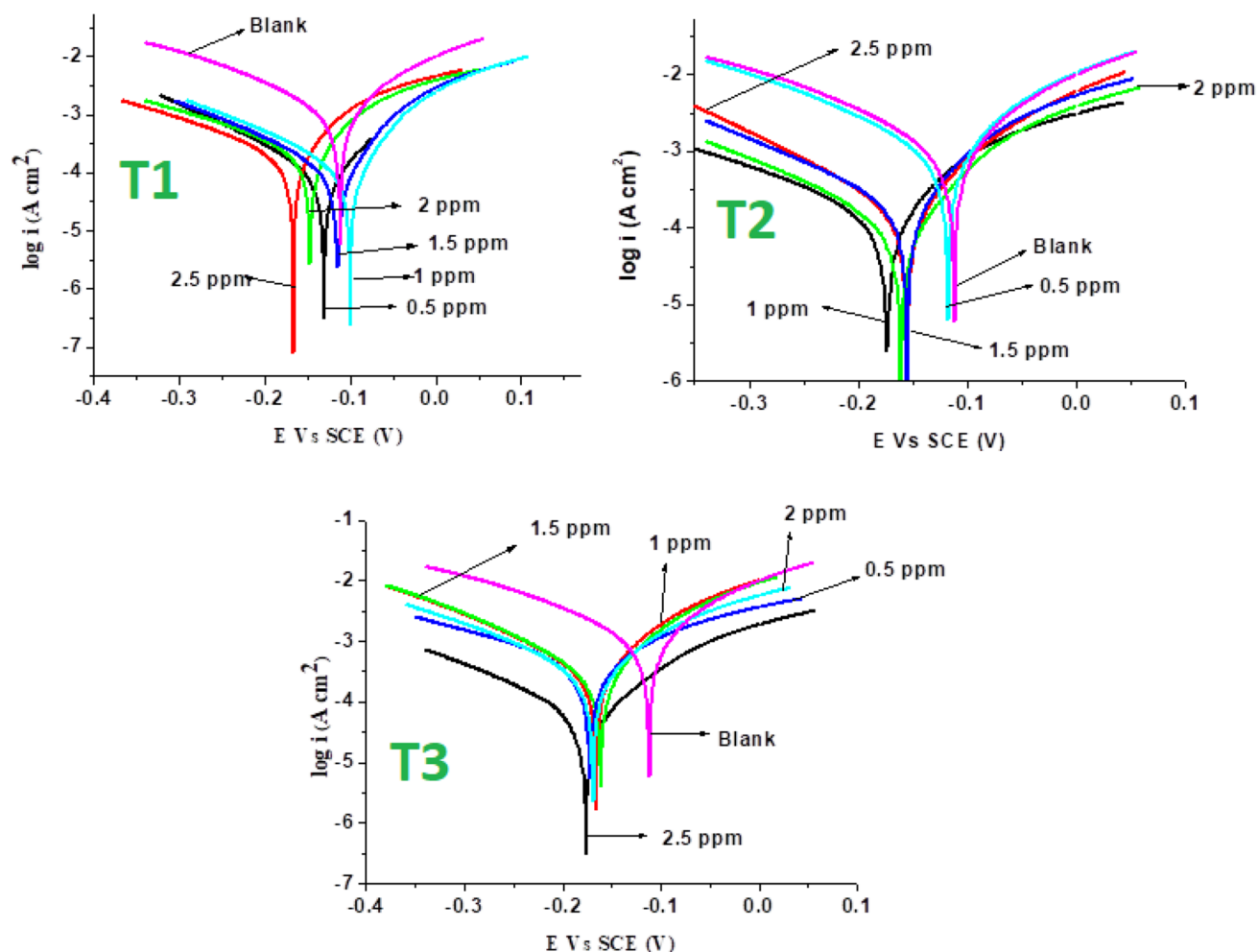
$$\eta_p = \frac{i_{\text{corr}}^0 - i_{\text{corr}}}{i_{\text{corr}}^0} \times 100. \quad (1)$$

By the close observation of results obtained by the Tafel polarization method (Table 3), the corrosion current density and rate of corrosion mild steel gradually decreases with the increasing of inhibitors concentration because of which are gets adsorbed on the surface of mild steel. Therefore, the inhibition efficiency ( $\eta_p$ ) increases with the increase of inhibitor concentrations.

The corrosion potential ( $E_{\text{corr}}$ ) of the inhibited solution with respect to the uninhibited solution is less than 80 mV. This result is an indication of the inhibitor acts as mixed type (both anodic and cathodic), because of the displacement in  $E_{\text{corr}}$  is less than  $\pm 85$  mV, the inhibitor is considered as mixed type. The cathodic Tafel slope ( $\beta_c$ ), changes with a minor extent with the increase of inhibitor

**Table 2** Electronic spectral data of the azo dyes  $T_1$ – $T_3$  in different solvents

Compounds	$\lambda_{\max}$ (nm)				log $\epsilon$			
	Ethanol	THF	DMF	DMSO	Ethanol	THF	DMF	DMSO
$T_1$	366	378	389	442	5.91	5.79	5.95	5.53
$T_2$	364	368	384	439	5.85	6.04	5.57	5.83
$T_3$	365	367	394	441	5.92	5.79	5.97	5.55

**Fig. 5** Tafel plots for the mild steel in the presence and absence of various concentrations of azo dyes ( $T_1$ – $T_3$ ) in 1 M HCl at 303 K

concentration is an indication of the hydrogen evolution (reduction) was controlled by the surface coverage by the inhibitor. The corrosion rate of the inhibitor gradually increases with the increasing concentrations of inhibitors due to the adsorption of inhibitor onto the surface of mild steel. The change in anodic Tafel slope ( $\beta_a$ ) may be reducing the reduction reaction due to the adsorption of inhibitor on the mild steel surface. The inhibitor  $T_1$  shows the maximum inhibition efficiency of 81.53% for 2.5 ppm of the inhibitor from the bulk of the solution than  $T_2$  and  $T_3$ . This is attributed due to the inhibitor  $T_1$  get adsorbed

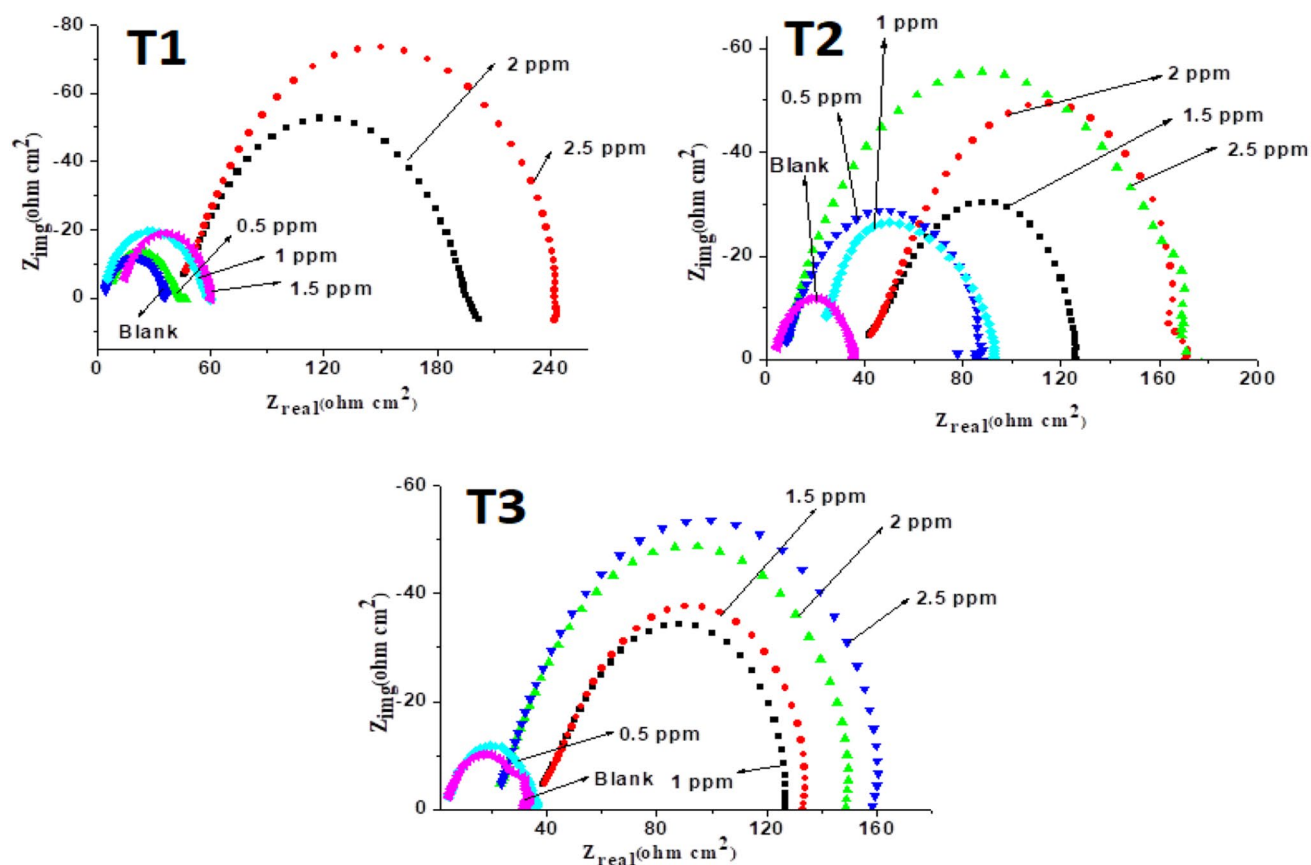
strongly on mild steel surfaces than that of the adsorption of the other two inhibitors ( $T_1$  and  $T_2$ ).

### 3.2.2 Electrochemical Impedance Spectroscopy (EIS)

The corrosion behavior of mild steel in 1 M HCl media in the absence and presence of the inhibitors ( $T_1$ – $T_3$ ) was studied by EIS after immersion for 30 min at 303 K. The typical Nyquist's and Bode plots obtained for the uninhibited and inhibited acid solution containing synthesized azo dyes in various concentrations are presented in Figs. 6 and

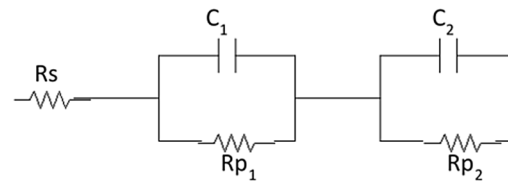
**Table 3** Electrochemical Tafel polarization parameters for mild steel in the absence and presence of azo dyes ( $T_1$ – $T_3$ ) in 1 M HCl at 303 K

Compounds	Inhibitor concn. (ppm)	$E_{\text{corr}}$ (V)	$i_{\text{corr}}$ ( $\mu\text{A cm}^{-2}$ )	Corrosion rate (mpy)	$\beta_c$ (mV/dec)	$\beta_a$ (mV/dec)	Inhibition efficiency ( $\eta_p$ (%))
$T_1$	Blank	−0.112	0.065	47.28	6.592	7.494	–
	0.5	−0.131	0.059	23.92	7.365	7.453	9.23
	1.0	−0.100	0.051	18.50	6.699	9.467	21.53
	1.5	−0.155	0.025	16.42	6.859	9.862	61.53
	2.0	−0.147	0.022	12.45	5.241	6.996	66.15
	2.5	−0.167	0.012	10.12	5.564	7.235	81.53
$T_2$	Blank	−0.112	0.065	48.92	6.592	7.494	–
	0.5	−0.118	0.060	43.38	6.579	7.557	7.69
	1.0	−0.174	0.051	24.84	5.664	7.656	21.53
	1.5	−0.161	0.037	15.46	6.645	9.918	43.07
	2.0	−0.155	0.033	10.07	6.366	8.487	49.23
	2.5	−0.155	0.021	7.42	7.423	9.633	67.69
$T_3$	Blank	−0.112	0.095	47.28	6.592	7.494	–
	0.5	−0.172	0.075	18.70	4.997	6.191	21.05
	1.0	−0.166	0.066	14.73	7.548	8.670	30.52
	1.5	−0.161	0.065	13.08	7.782	8.882	31.57
	2.0	−0.169	0.053	13.60	6.761	7.684	44.21
	2.5	−0.176	0.041	8.062	7.085	9.846	56.84

**Fig. 6** Nyquist plots for the corrosion of mild steel in the absence and presence of different concentrations of azo dyes ( $T_1$ – $T_3$ ) in 1 M HCl at 303 K

7, respectively. The electrical layer developed on the steel surface can be shown by the electrical equivalent circuit diagrams to model the metal/solution interface. The model used for the fitting of the EIS results is shown in Fig. 8. EIS parameters such as charge transfer resistance which is equal to polarization resistance ( $R_p$ ), double-layer capacitance ( $C_{dl}$ ), surface coverage and inhibition efficiency are calculated and reported in Table 4. The Nyquist plots (Fig. 6) consist of semicircles with their centers on the real axis. These are described as polarization resistance ( $R_p$ ). The  $R_p$  value increases with the increase in the inhibitor concentrations. These semicircles are not perfect, and there is a frequency dispersion effect due to the roughness and inhomogeneity nature of the working electrode (mild steel). The increase in  $R_p$  value is an indication of the corrosion inhibition of mild steel due to the formation of the protective layer by the adsorption of inhibitor molecules onto the surface of the mild steel. The decrease in the  $C_{dl}$  values (Table 3) with the addition of inhibitor is attributed due to the increase in the electric double layer on the metal surface [39]. The inhibition efficiency of the compound  $T_1$  shows maximum due to the strong adsorption onto the mild steel surface.

The Bode plots as depicted in Fig. 7 show that the impedance values over the whole frequency range increased



Where  $R$ - Solution resistance,  $R_{p1}$  and  $R_{p2}$  are the polarization resistances,  $C1$  and  $C2$  are the capacitances

Fig. 8 Equivalent circuit used to fit the EIS results

greatly with increasing the inhibitor concentration. It can be obtained from Bode phase plots that the corrosion process taking place at the electrode surface has two relaxation time constants. One is related to the relaxation of an electrical double layer capacitor, and the other is associated with the relaxation process of the adsorbed inhibitor. It is also observed that increasing the concentration of inhibitor results in an increase in the maximum phase angle, which indicates inhibition of the corrosion process [40]. The inhibitor  $T_1$  shows the highest phase angle around  $80^\circ$  for 2.5 ppm of the inhibitor from the bulk of the solution than  $T_2$  and  $T_3$ . This is attributed due to the inhibitor  $T_1$  get adsorbed

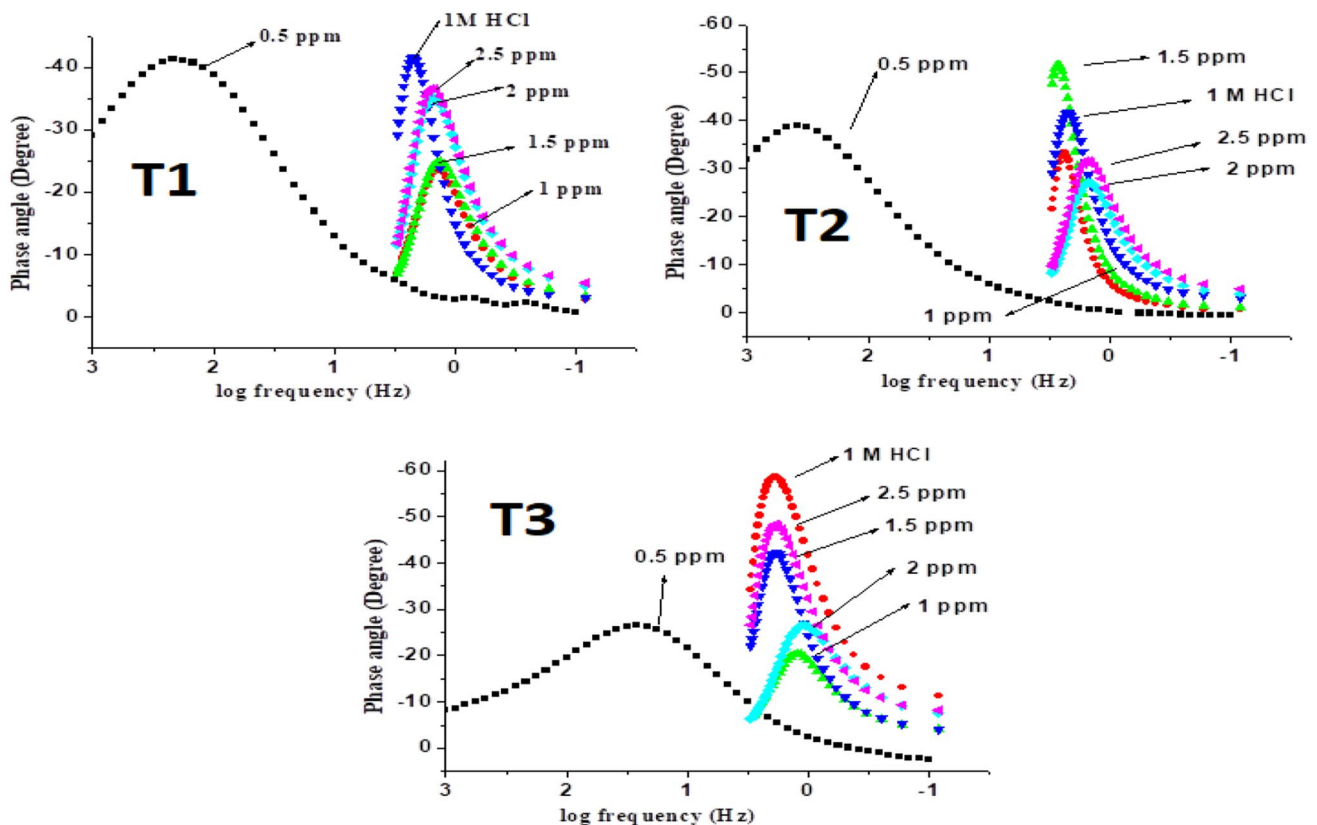


Fig. 7 Bode plots for the corrosion of mild steel in the absence and presence of different concentrations of azo dyes ( $T_1$ – $T_3$ ) in 1 M HCl at 303 K

**Table 4** Electrochemical impedance spectroscopic parameters for the corrosion of mild steel in the absence and presence of azo dyes (**T**<sub>1</sub>–**T**<sub>3</sub>) in 1 M HCl at 303 K

Compounds	Inhibitor concn. (ppm)	Polarization resistance $R_p$ ( $\Omega$ cm <sup>2</sup> )	Double-layer capacitance $C_{dl}$ ( $\mu$ F cm <sup>-2</sup> )	Inhibition efficiency ( $\eta_z$ (%))
<b>T</b> <sub>1</sub>	Blank	30.63	289.1	–
	0.5	36.19	40.51	15.36
	1.0	45.91	34.55	31.71
	1.5	52.65	26.25	41.82
	2.0	142.52	25.67	78.50
	2.5	189.21	23.37	83.81
<b>T</b> <sub>2</sub>	Blank	30.63	249.1	–
	0.5	76.60	244.2	60.01
	1.0	81.46	134.4	62.40
	1.5	122.56	66.27	75.00
	2.0	147.72	51.98	79.26
	2.5	154.78	50.42	80.21
<b>T</b> <sub>3</sub>	Blank	28.53	289.1	–
	0.5	30.90	183.3	7.67
	1.0	86.42	136.5	66.70
	1.5	92.55	107.9	69.17
	2.0	123.45	49.59	76.88
	2.5	132.93	53.20	78.53

strongly on mild steel surfaces than that of the adsorption of the other two inhibitors (**T**<sub>2</sub> and **T**<sub>3</sub>).

### 3.2.3 Quantum Chemical Measurement

Quantum chemical analysis is a powerful tool, which is used to design the structural study of the molecules as corrosion inhibitors using the distribution of electron density for different molecular geometries. The highest occupied molecular orbitals (HOMOs) and lowest unoccupied molecular orbitals (LUMOs) are the orbitals together referred as frontier molecular orbitals (FMOs) will play an important role in determining the electronic density on the molecule and to compare most of the physical properties with the energy difference between these HOMO and LUMO. They are also referred to as electron donor and acceptors respectively. The difference in energy between the HOMO and LUMO will play an important role in obtaining the various parameters like chemical reactivity, kinetic stability, polarizability, dipole moment, and optical properties of the molecules. The energy gap between HOMO and LUMO is small indicating the energy required to promote an electron from HOMO to LUMO is less, then the molecule becomes more reactive, having low kinetic stability and highly polarizable. Therefore, the electron density on the whole molecular system will be greatly increased and thus more reactive towards any molecular reactions. If the energy gap is high, the promotion of an electron from HOMO to LUMO is difficult and therefore

the molecule will be less reactive, kinetically stable and less polarization. This indicates that the molecule has less electron density and become less reactive towards chemical reactions. Further, the HOMO and LUMO correspond to ionization potential and electron affinity of a molecule. Overall, the ability of a molecule that means potentiality can be expressed in terms of some parameters such as chemical potential ( $\alpha$ ), hardness ( $\eta$ ) and Electrophilicity index ( $\omega$ ) and these parameters were evaluated from HOMO–LUMO energies obtained from PM3 method and their mathematical expressions were represented below,

$$\text{Energy gap } (\Delta E) = E_{\text{HOMO}} - E_{\text{LUMO}}, \quad (2)$$

$$\text{Electronegativity } (\chi) = \frac{(I + A)}{2}, \quad (3)$$

$$\text{Chemical potential } (\alpha) = -\frac{(I + A)}{2}, \quad (4)$$

$$\text{Hardness } (\eta) = \frac{(I - A)}{2}, \quad (5)$$

$$\text{Electrophilicity index } (\omega) = \frac{\alpha^2}{2\eta}, \quad (6)$$

where  $I$  and  $A$  are electron affinity and ionization potential and which are given by the expressions,

$$\text{Electron affinity (I)} = -E_{\text{LUMO}} \quad (7)$$

$$\text{Ionization potential (A)} = -E_{\text{HOMO}} \quad (8)$$

The optimized molecular structures of the inhibitors (**T**<sub>1</sub>–**T**<sub>3</sub>) are as shown in Fig. 9 and Table 5 is the computed quantum chemical parameters for the inhibitor molecules. The structures of HOMO and LUMO are presented in Figs. 10, 11 respectively.

Inhibitor molecules are adsorbed on the metal surface by the donor–acceptor interactions between inhibitor molecules and metal surface.  $E_{\text{HOMO}}$  relates the electron-donating ability of the inhibitor and higher values of  $E_{\text{HOMO}}$  indicate high tendencies of inhibitor molecules to donate electrons to the acceptor molecules.  $E_{\text{LUMO}}$  relates the ability of a metal/molecule to accept electrons and the lower value of  $E_{\text{LUMO}}$  indicates the easier acceptance of electrons from the metal surface [41]. The molecules with lower  $\Delta E$  values give higher inhibition efficiencies because the excitation energy gap is more polarizable and is generally associated with chemical reactivity [42]. Lower  $\Delta E$  values aid an electron transfer process between inhibitor molecules and mild steel surface.

The calculated  $\Delta E$  values for the inhibitors are justifying the results. The inhibition efficiency of these inhibitors decreased with an increase in  $\Delta E$  values. Zhang et al. studied the corrosion inhibition performance of imidazoline phosphate and they found  $\Delta E$  value of 8.838 eV with inhibition efficiency of 95% [43]. Nataraj et al. studied few organic compounds and they found  $\Delta E$  values of 8.13 eV 6.56 eV, 5.47 eV for HYD, TAD, TRD respectively [44]. Generally, in the previous studies, corrosion inhibition efficiency

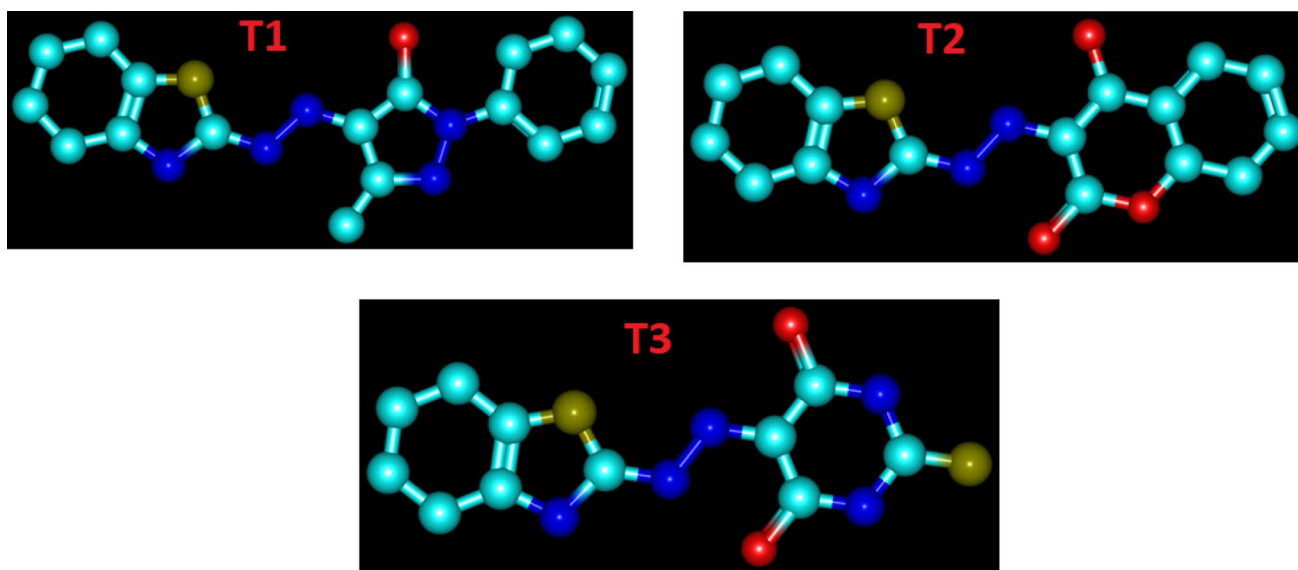
**Table 5** Calculated quantum chemical parameters for the azo dyes (**T**<sub>1</sub>–**T**<sub>3</sub>) by PM3 method

Electronic parameters	<b>T1</b>	<b>T2</b>	<b>T3</b>
$E_{\text{HOMO}}$ (eV)	−8.78	−9.07	−9.33
$E_{\text{LUMO}}$ (eV)	−1.26	−1.45	−1.33
$E_{\text{HOMO}}-E_{\text{LUMO}}$ (eV)	7.53	7.62	8.00
Electronegativity ( $\chi$ )	5.02	5.26	5.33
Chemical potential ( $\alpha$ )	−5.02	−5.26	−5.33
Hardness ( $\eta$ )	3.76	3.81	4.00
Electrophilicity index ( $w$ )	3.35	3.63	3.55
Ionization potential (A)	8.78	9.07	9.33
Electron affinity (I)	1.26	1.45	1.33
Dipole moment ( $\mu$ ) D	6.23	3.14	3.14

decreased with an increase in  $\Delta E$  values. The inhibitor **T**<sub>1</sub> shows maximum inhibition efficiency due to a higher  $\Delta E$  value of 8.0 eV. Dipole moment ( $\mu$ ) is another important parameter to decide the adsorption inhibitor molecule on the mild steel surface. Higher dipole moment increases the adsorption of inhibitors on the mild steel surface and increases the inhibition efficiency. The calculated dipole moment ( $\mu$ ) of **T**<sub>1</sub> is 6.23 D. The quantum studies concluded that comparatively **T**<sub>1</sub> is the better corrosion inhibitor than **T**<sub>2</sub> and **T**<sub>3</sub>.

### 3.2.4 SEM and EDX Analysis

To understand the type of interaction between the metal surface and the deposited organic inhibitor, the tested steel samples were examined by SEM and EDX techniques and



**Fig. 9** Optimized molecular structures of azo dyes (**T**<sub>1</sub>–**T**<sub>3</sub>)



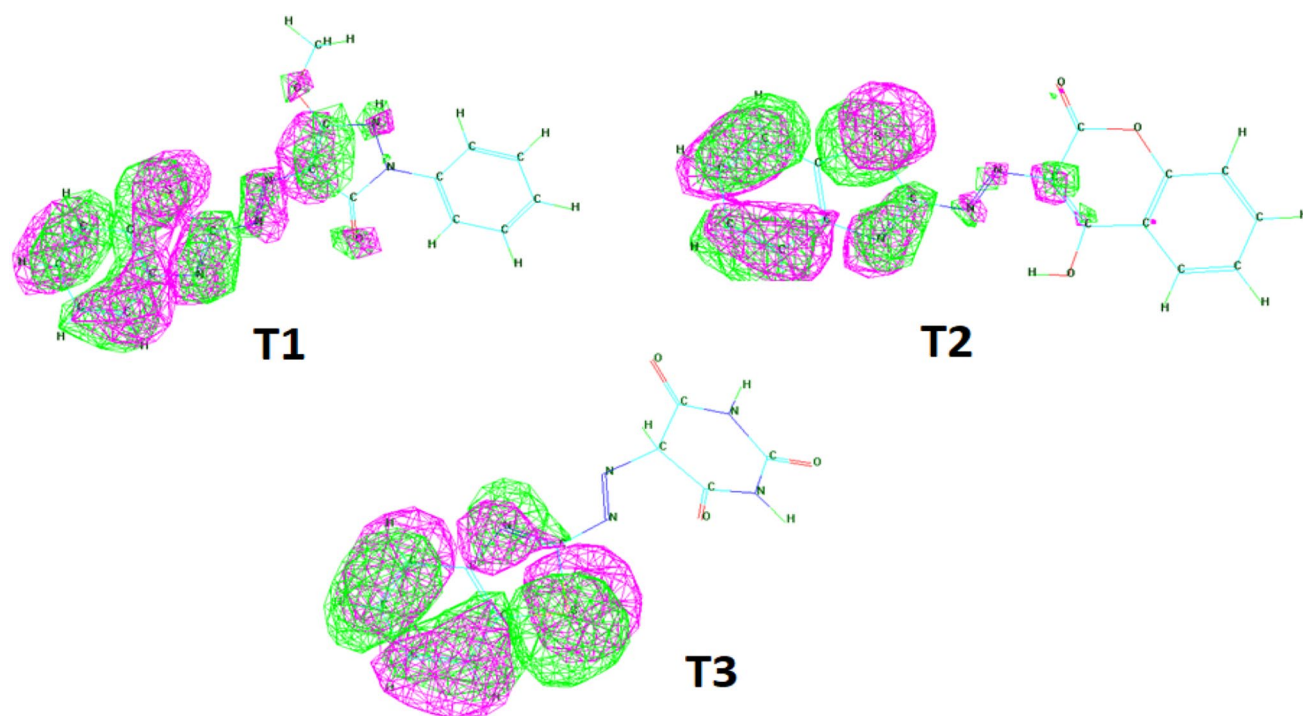


Fig. 10 Structures of HOMO energy states of azo dyes (T<sub>1</sub>–T<sub>3</sub>)

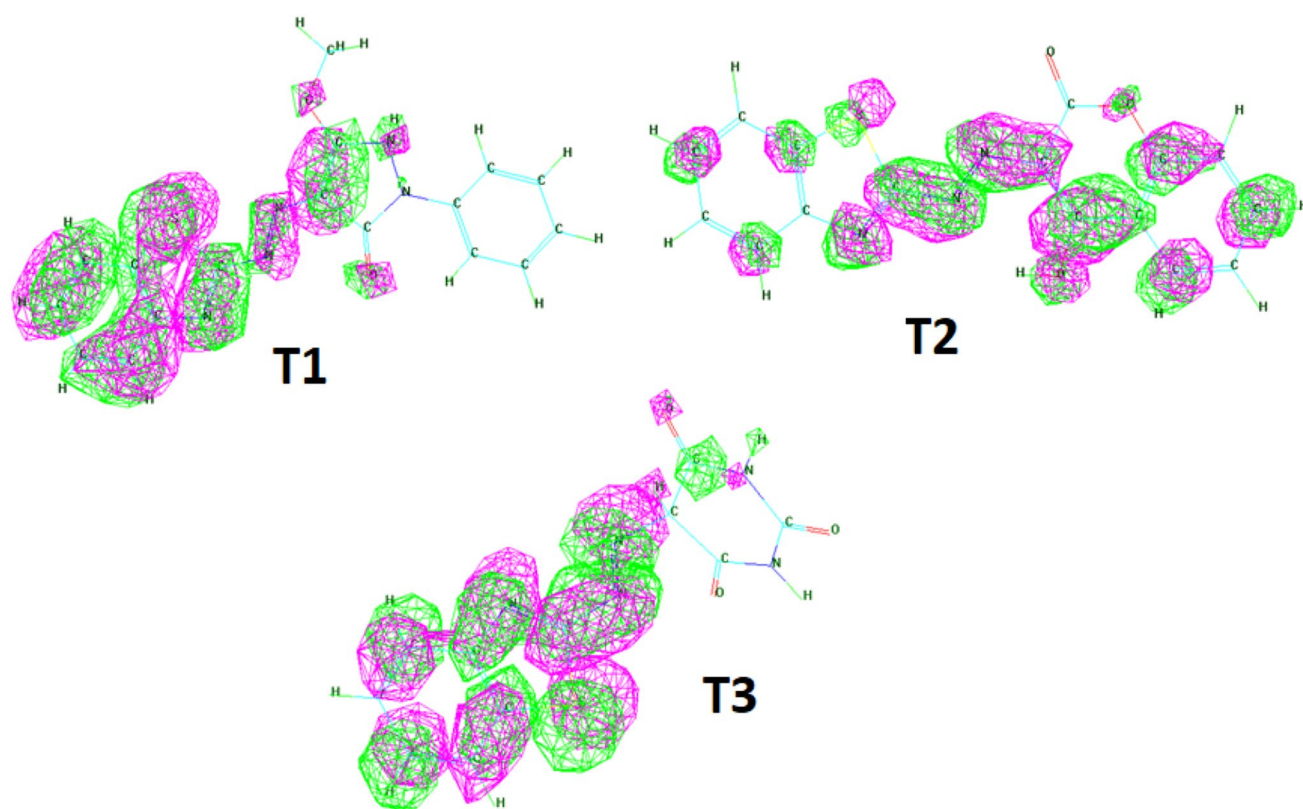


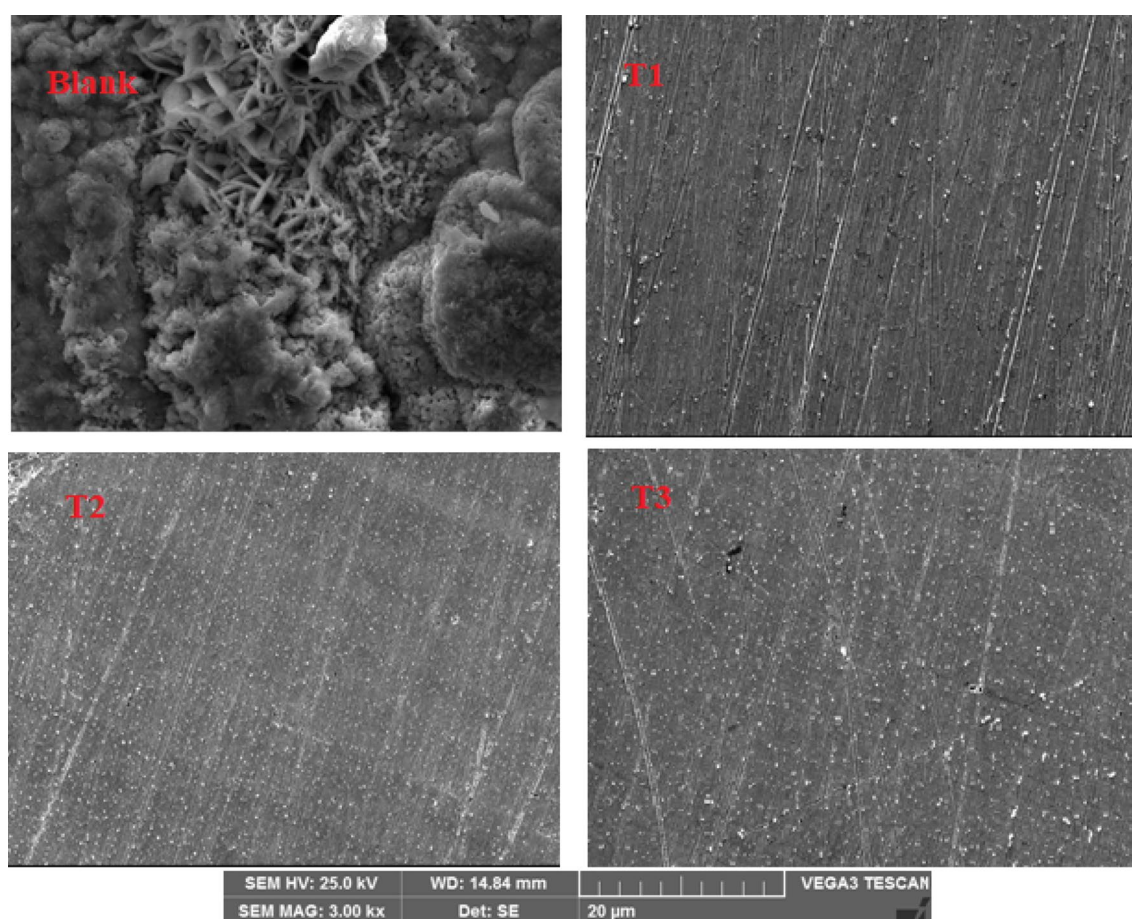
Fig. 11 Structures of LUMO energy states of azo dyes (T<sub>1</sub>–T<sub>3</sub>)



the surface morphology was analyzed in the absence and presence of inhibitors ( $T_1$ – $T_3$ ) at ambient temperature. The SEM images of the mild steel with and without the presence of inhibitors were recorded and are depicted in Fig. 12. From the analysis of SEM images of the steel sample in 1 M HCl solution (as shown in Fig. 12 Blank) in the absence of inhibitors exhibited rough surface and damaged due to the corrosion by aggressive media. In the same Fig. 12 the images  $T_1$ ,  $T_2$  and  $T_3$  are showing smooth surface due to the deposition of the inhibitors on to the steel surface and protect it by corrosion. This effective deposition of the inhibitors on to the metal surface often explained by the interaction between the iron and the electron-rich species in the azo molecules. These groups block the metal sites against corrosion and helpful in protecting the surface of the metal by metal dissolution caused by the acid solution [45].

The energy-dispersive X-ray analysis (EDX) was carried out to evaluate the elemental composition of the coated inhibitors on to the metal surface. The spectra were recorded after 2 h immersion of the steel samples with and

without inhibitors in 1 M HCl solution. The results of the EDX analysis were obtained in terms of Weight (wt%) and Atomic (at.%) percentages of elements obtained from steel samples in the absence and presence of inhibitors ( $T_1$ – $T_3$ ) are shown in Table 6. The analysis of Table 6 indicated that, the peak corresponding to the oxygen atom in the presence of inhibitors was gradually decreased as compared to the steel samples without inhibitors. This suggests that, the inhibitors on the steel samples will not allow forming the iron oxide on the metal surface while the percentage of O on the steel without inhibitors (Blank) is more. So, the EDX analysis will reveal the effective coatings on the metal surface in turn suggesting the enhanced inhibition efficiency as the azo dye molecule adsorb on to the metal surface. Finally, it is the presence of inhibitors that protects the surface from the aggressive or acid solutions, as also indicated by the SEM images. These two morphological evaluations signify the effective adsorption of inhibitor molecules on the steel surface forming a protective film [46–48].



**Fig. 12** The SEM images of the steel samples recorded in 1 M HCl with and without inhibitors ( $T_1$ – $T_3$ ) at room temperature

**Table 6** The results of the EDX spectral analysis in terms of weight (wt) and atomic (at.) percentages of elements of steel samples in 1 M HCl with and without inhibitors (**T**<sub>1</sub>–**T**<sub>3</sub>) at room temperature

Element	Blank		<b>T</b> <sub>1</sub>		<b>T</b> <sub>2</sub>		<b>T</b> <sub>3</sub>	
	wt%	at. %	wt%	at. %	wt%	at. %	wt%	at. %
Fe	53.26	23.71	57.45	27.19	60.92	30.17	61.60	30.96
C	6.52	13.50	4.05	8.92	3.55	8.18	2.45	5.72
O	38.01	59.07	36.16	59.75	33.76	58.37	33.81	59.32
N	2.01	3.56	2.08	3.93	1.58	3.12	1.88	3.78
S	0.20	0.16	0.26	0.21	0.19	0.17	0.25	0.22

## 4 Conclusion

The present work describes the synthesis of four novel disperse azo dyes derived from 4,5,6,7-tetrahydro-1,3-benzothiazole and their corrosion inhibition behavior over the mild steel in 1 M HCl solution. From overall observations, the following conclusions were made.

- The chemical structures of the newly synthesized azo dyes (**T**<sub>1</sub>–**T**<sub>3</sub>) derived from 4,5,6,7-tetrahydro-1,3-benzothiazole were elucidated by various physico-chemical techniques.
- All the studied azo compounds showed efficient corrosion inhibition properties in 1 M HCl solution. The inhibition efficiency was increased with the increase of inhibitor concentration.
- From the polarization measurements, it is concluded that the azo dyes are behaving as a mixed type of inhibitors affecting both anodic and cathodic corrosion processes.
- EIS study revealed that polarization resistance increases relatively and double-layer capacitance decreases with increasing inhibitors concentration.
- Among the studied compounds, **T**<sub>1</sub> exhibited maximum inhibition efficiency of 83% at 2.5 ppm of inhibitor in 1 M HCl compared to **T**<sub>2</sub> and **T**<sub>3</sub>.
- The quantum chemical studies strengthening the experimental results for corrosion protection study. **T**<sub>1</sub> shows lesser  $\Delta E$  value (7.53 eV) and a higher dipole moment ( $\mu$ -6.23 D) shows that higher inhibition efficiency.
- The SEM and EDX analyses were carried out to study the surface morphology and elemental composition on the surface of the mild steel in the absence and presence of the inhibitors in the 1 M HCl solution. The results indicated that the effective adsorption of the azo dyes on the surface of the metal and the EDX also confirmed the interaction of the atoms of the inhibitors with the iron.

From the overall study, it is concluded that the present work described the effective corrosion inhibition properties of the newly synthesized azo dyes by both experimental and theoretical methods. The present work mainly carried out to understand the how heteroatoms containing organic systems enhance the corrosion inhibition in an aggressive medium

at room temperature. The recent developments showed that some of the organic compounds can also be more effective in controlling the corrosion at elevated temperatures. So that our future aim is to design the compounds to act as efficient, eco-friendly corrosion inhibitors for metals and alloys to protect from the aggressive media at higher temperatures.

**Acknowledgement** Authors are thankful to the Department of chemistry, Kuvempu University, Shimoga and Srinivas School of Engineering, Mukka, Mangalore for providing laboratory and instrumental facility, respectively. Authors are also grateful to SAIF and CIL Panjab University, Chandigarh for providing spectral data.

## Compliance with Ethical Standards

**Conflict of interest** On behalf of all authors, the corresponding author states that there is no conflict of interest.

## References

1. Jelena M, Jelena L, Milka AI, Dušan M (2014) Electro oxidative behaviour of arylazo pyridone dyes and their inclusion complexes on gold electrode in 0.1 M NaOH. *Electrochim Acta* 137:705–713
2. Chudgar RJ, Oakes J, Dyes AZO (2003) Kirk–Othmer encyclopedia of chemical technology. Wiley Interscience, New York, pp 1–81
3. Sawant VA, Bapu AY, Sanjay SC (2010) Manganese (II), cobalt (II) and nickel (II) complexes with 2-phenyl-3-(benzylamino)-1, 2-dihydroquinazolin-4 (3H)-one, pseudohalides and some bidentate N-donor ligands. *Transit Met Chem* 35(3):357–361
4. Ulusoy M, Hasan K, Rafet K, Muhittin A, Bekir C, Santiago G-G (2010) Co (II) and Cu (II) Schiff base complexes of bis (N-(4-diethylamino-2-methylphenyl)-3, 5-di-tert-butylsalicylaldehyde): electrochemical and X-ray structural study. *Struct Chem* 19:749–755
5. Ikeda T, Osamu T (1995) Optical switching and image storage by means of azobenzene liquid-crystal films. *Science* 268:1873–1875
6. Rageh NM (2004) Tautomeric structures, electronic spectra, acid–base properties of some 7-aryl-2, 5-diamino-3 (4-hydroxyphenylazo) pyrazolo [1, 5-a] pyrimidine-6-carbonitriles, and effect of their copper (II) complex solutions on some bacteria and fungi. *Spectrochimica. Acta Part A* 60:1917–1924
7. Tunçel M, Hülya K, Mehmet C (2008) Synthesis, characterization, and histological activity of novel polydentate azo ligands and their cobalt (II), copper (II) and nickel (II) complexes. *Transit Met Chem* 33:605–613
8. Chen W, Yiqun W, Donghong G, Fuxi G (2007) Synthesis, optical and thermal characterization of novel thiazolyl heterocyclic azo dye. *Mater Lett* 61:4181–4184

9. Li XY, Wu YQ, Gu DD, Gan FX (2009) Optical characterization and blue-ray recording properties of metal (II) azo barbituric acid complex films. *Mater Sci Eng B* 158:53–57
10. Rivera E, Del Pilar Carreón-Castro M, Rodríguez L, Cedillo G, Fomine S, Morales-Saavedra OG (2007) Amphiphilic azo-dyes (RED-PEGM). Part 2: charge transfer complexes, preparation of Langmuir–Blodgett films and optical properties. *Dyes Pigm* 74:396–403
11. Huang F, Y Wu, Donghong G, Fuxi G (2005) Synthesis, spectroscopic and thermal properties of nickel (II)–azo complexes with blue-violet light wavelength. *Dyes Pigm* 66:77–82
12. Merino E (2011) Synthesis of azo benzenes: the coloured pieces of molecular materials. *Chem Soc Rev* 40:3835–3853
13. Singh AK, Quraishi MA (2010) The effect of some bis-thiadiazole derivatives on the corrosion of mild steel in hydrochloric acid. *Corros Sci* 52:1373–1385
14. Bentiss F, Bouanis M, Mernari B, Traisnel H, Vezin M, Lagrenee M (2007) Understanding the adsorption of 4H-1, 2, 4-triazole derivatives on mild steel surface in molar hydrochloric acid. *Appl Surf Sci* 253:3696–3704
15. Popova A, Christov M, Zvetanova A (2007) Effect of the molecular structure on the inhibitor properties of azoles on mild steel corrosion in 1 M hydrochloric acid. *Corros Sci* 49:2131–2143
16. Avci G (2008) Corrosion inhibition of indole-3-acetic acid on mild steel in 0.5 M HCl. *Colloids Surf A* 317:730–736
17. Solmaz R, Kardaş G, Culha B, Yazıcı B, Erbil M (2008) Investigation of adsorption and inhibitive effect of 2-mercaptothiazoline on corrosion of mild steel in hydrochloric acid media. *Electrochim Acta* 53:5941–5952
18. Quraishi MA, Rana Sardar, Danish Jamal (2001) Corrosion inhibition of mild steel in hydrochloric acid by some aromatic hydrazides. *Mater Chem Phys* 71:309–313
19. Yurt A, Balaban A, Kandemir SU, Bereket G, Erx B (2005) Investigation on some Schiff bases as HCl corrosion inhibitors for carbon steel. *Mater Chem Phys* 85:420–426
20. Matad PB, Mokshanatha PB, Hebbar N, Venkatesha V, Tandon HC (2014) Ketosulfone drug as a green corrosion inhibitor for mild steel in acidic medium. *Ind Eng Chem Res* 53:8436–8444
21. Gowda J, Khadar AMA, Kalluraya B, Kumari NS (2010) Microwave assisted synthesis of 1,3,4-oxadiazoles carrying benzimidazole moiety and their antimicrobial properties. *Indian J Chem B* 49:1130–1134
22. Masoud MS, Awad MK, Shaker MA, El-Tahawy MMT (2010) The role of structural chemistry in the inhibitive performance of some amino pyrimidines on the corrosion of steel. *Corros Sci* 52:2387–2396
23. Quartarone G, Bonaldo L, Tortato C (2006) Inhibitive action of indole-5-carboxylic acid towards corrosion of mild steel in deaerated 0.5 M sulfuric acid solutions. *Appl Surf Sci* 252:8251–8257
24. Obot IB, Obi-Egbedi NO, Umoren SA (2009) Antifungal drugs as corrosion inhibitors for aluminium in 0.1 M HCl. *Corros Sci* 51:1868–1875
25. Obot IB, Gasem ZM (2014) Theoretical evaluation of corrosion inhibition performance of some pyrazine derivatives. *Corros Sci* 83:359–366
26. Allis DG, Hakey PM, Kortner TM (2008) The solid-state terahertz spectrum of MDMA (Ecstasy): a unique test for molecular modeling assignments. *Chem Phys Lett* 463:353–356
27. Murulana LC, Singh AK, Shukla SK, Kabanda MM, Ebenso EE (2012) Experimental and quantum chemical studies of some bis(trifluoromethyl-sulfonyl) imide imidazolium-based ionic liquids as corrosion inhibitors for mild steel in hydrochloric acid solution. *Ind Eng Chem Res* 51:13282–13299
28. Yadav DK, Maiti B, Quraishi MA (2010) Electrochemical and quantum chemical studies of 3, 4-dihydropyrimidin-2(1H)-ones as corrosion inhibitors for mild steel in hydrochloric acid solution. *Corros Sci* 52:3586–3598
29. Naik SJ, Halkar UP (2005) Synthesis and application of novel 4,5,6,7 tetrahydro benzothiazole based azo disperse dyes. *Arxivoc* 13:141–149
30. Adki N, Ravi G, Kumar SS, Rao GN (2012) Synthesis of new biologically active compounds containing linked thiazolyl-thiazolidinone heterocycles. *Organ Commun* 5(4):160–170
31. Nagesh GY, Raj KM, Mruthyunjayaswamy BHM (2018) Synthesis, characterization, thermal and biological evaluation of Cu (II), Co (II) and Ni (II) complexes of azo dye ligand containing sulfamethoxazole moiety. *J Mol Struct* 1165:28–36
32. Khajuria A, Kumar R, Bedi R, Swaminathan J, Albert DKS (2018) Impression creep studies on simulated reheated HAZ of P91 and P91B steels. *Int J Modern Manuf Technol* 1:50–56
33. Akhtar M, Khajuria A, Sahu JK, Swaminathan J, Kumar R, Bedi R, Albert SK (2018) Phase transformations and numerical modelling in simulated HAZ of nanostructured P91B steel for high temperature applications. *Appl Nanosci* 8(7):1669–1685
34. Khajuria A, Kumar R, Bedi R (2019) Effect of boron addition on creep strain during impression creep of P91 steel. *J Mater Eng Perform* 28(7):4128–4142
35. Mallikarjuna NM, Keshavayya J, Ravi BN (2018) Synthesis, spectroscopic characterization, antimicrobial, antitubercular and DNA cleavage studies of 2-(1H-indol-3-ylidiazonyl) 4,5,6,7-tetrahydro-1,3-benzothiazole and its metal complexes. *J Mol Struct* 1173:557–566
36. Mallikarjuna NM, Keshavayya J (2018) Synthesis, spectroscopic characterization and pharmacological studies on novel sulfamethoxazole based azo dyes. *J King Saud Univ Sci*. <https://doi.org/10.1016/j.jksus.2018.04.033>
37. Kumar V, Keshavayya J, Pandurangappa M, Ravi BN (2018) Synthesis, characterization and electrochemical investigations of azo dyes derived from 2-amino-6-ethoxybenzothiazole. *Chem Data Collect* 17–18:13–29
38. Prasanna BM, Praveen BM, Hebbar N, Venkatesha TV (2016) Experimental and theoretical studies of hydralazine hydrochloride as corrosion inhibitor for mild steel in HCl acid medium. *Anti-corrosion Methods Mater* 63:47–55
39. Prasanna BM, Praveen BM, Hebbar N, Venkatesha TV, Tandon HC (2016) Inhibition study of mild steel corrosion in 1 M hydrochloric acid solution by 2-chloro 3-formyl quinoline. *Int J Ind Chem* 7:9–19
40. Sherif ESM, Erasmus RM, Comins JD (2008) Inhibition of copper corrosion in acidic chloride pickling solutions by 5-(3-aminophenyl)-tetrazole as a corrosion inhibitor. *Corros Sci* 50:3439–3445
41. Mu GN, Li X, Li F (2004) Synergistic inhibition between o-phenanthroline and chloride ion on cold rolled steel corrosion in phosphoric acid. *Mater Chem Phys* 86:59–68
42. Ji G, Shukla SK, Dwivedi P, Sundaram S, Prakash R (2011) Inhibitive effect of argemone mexicana plant extract on acid corrosion of mild steel. *Ind Eng Chem Res* 50:11954–11959
43. Zhang J, Gong XL, Yu MD (2011) The inhibition mechanism of imidazoline phosphate inhibitor for Q235 steel in hydrochloric acid medium. *Corros Sci* 53:3324–3330
44. Nataraja SE, Venkatesha TV, Manjunatha K, Boja P, Pavithra MK, Tandon HC (2011) Inhibition of the corrosion of steel in hydrochloric acid solution by some organic molecules containing the methylthiophenyl moiety. *Corros Sci* 58:2651–2659
45. Mahdi M, Rafiee E, Rashed G, Ashassi-Sorkhabi H, Behpour M (2013) Corrosion inhibition of mild steel by safflower (*Carthamus tinctorius*) extract: polarization, EIS, AFM, SEM, EDS, and artificial neural network modelling. *J Dispers Sci Technol* 34:964–973
46. Idouhli R, N'Ait Ousidi A, Koumya A, Abouelfida Y, Benyaich A, Auhmani A, Ait Itto MY (2018) Electrochemical studies of

- monoterpenic thiosemicarbazones as corrosion inhibitor for steel in 1 M HCl. Int J Corros. <https://doi.org/10.1155/2018/9212705>
47. Kumari PP, Shetty P, Rao SA (2017) Electrochemical measurements for the corrosion inhibition of mild steel in 1 M hydrochloric acid by using an aromatic hydrazide derivative. Arab J Chem 10:653–663
48. Chellouli M, Chebabe D, Dermaj A, Erramli H, Bettach N, Hajjaji N, Casaletto MP, Cirrincione C, Privitera A, Srhiri A (2016)

Corrosion inhibition of iron in acidic solution by a green formulation derived from *Nigella sativa* L. Electrochim Acta 204:50–59

**Publisher's Note** Springer Nature remains neutral with regard to jurisdictional claims in published maps and institutional affiliations.

# Dakshayani Indices on Carbon and Boron Nitride Nanotubes

Basavarajappa N S<sup>1</sup>, Shanmukha M C<sup>2,\*</sup> , Niranjana K M<sup>3</sup>, Shilpa K C<sup>1</sup>

<sup>1</sup> Department of Mathematics and Computer Science Engg, Bapuji Institute of Engineering and Technology, Davanagere-577004, Karnataka, India

<sup>2</sup> Department of Mathematics, Jain Institute of Technology, Davanagere-577003, Karnataka, India

<sup>3</sup> Department of Mathematics, UBDT College of Engineering, Davanagere-577004, Karnataka, India

\* Correspondence: mcshanmukha@gmail.com;

Scopus Author ID 57217312072

Received: 30.07.2020; Revised: 20.08.2020; Accepted: 22.08.2020; Published: 25.08.2020

**Abstract:** Chemical graph theory is a discipline of graph theory deals with the study of chemical compounds using simple connected graphs. In computational chemistry, the properties of chemical compounds are determined using a numerical value called the topological index. Topological indices are widely applicable in QSAR and QSPR modeling. In this proposed work, we have used topological index like Neighborhood Dakshayani index on nanostructures called Carbon nanotube and Boron nitride nanotubes. Carbon nanotube has its various applications in air and water filtration, field emission, and biomedical applications. Boron nitride nanotubes are used in aerospace to automotive and defense to biomedical.

**Keywords:** Nanostructures; Neighborhood Dakshayani indices; Carbon nanotubes; Boron nitride nanotubes.

© 2020 by the authors. This article is an open-access article distributed under the terms and conditions of the Creative Commons Attribution (CC BY) license (<https://creativecommons.org/licenses/by/4.0/>).

## 1. Introduction

Graph theory is used in almost all fields of studies. Chemical graph theory deals with the discussion of chemical compounds using simple graphs. The graph  $G$  includes vertices and edges such that chemical compound atoms can be represented by vertices and the links between the atoms as edges. The total graphs number of edges in association with the vertices known as the degree of a vertex. The chemists use graph theory as a computing measure to determine the organization of chemical compounds since the valency of an atom is the degree of a vertex. The chemical graph theory offers the study of characteristics of chemical compounds. The topological indices are the numerical quantities used to determine the properties of chemical compounds. In the molecular graph, the vertices are denoted as atoms, and the edges are denoted by the links connecting the vertices. Chemical graph theory has its application in the development of chemical science and medical science. The mathematical chemistry offers several topological indices used in QSAR/QSPR study. For the discussion of topological indices, see [5, 6, 13, 14, 15, 17].

Nanosystem includes various organic and inorganic compounds that are responsible for their characteristics whose size varies from 1 to 100 nm. Examples of nanostructures include nano-torus, nanotubes, etc. So far, the work has been done on neighborhood degree-based indices in [8, 9, 10, 11, 16]. In this proposed work, we use a few defined degree-based



topological indices such as the first and second neighborhood Dakshayani indices, the first and second hyper neighborhood Dakshayani indices, and the minus and square neighborhood Dakshayani indices on nanostructures like carbon nanotube and boron nitride nanotube [4, 7].

Here we have considered finite, simple, and connected graphs. Consider a graph  $G$  with a set of vertices and edges  $V(G)$  and  $E(G)$ , respectively. The degree of a vertex  $w$  is denoted by  $d_G(w)$ . The set of all vertices adjacent to  $w$  are called the open neighborhood of  $w$  and denoted by  $N_G(w)$ . The closed neighborhood of  $w$  is the set  $N_G[w] = N_G(w) \cup \{w\}$ . The set  $N_G[w]$  is the set of closed neighborhood vertices of  $w$ . Let  $D_G(w) = d_G(w) + \sum_{v \in N_G(w)} d_G(v)$  be the degree sum of closed neighborhood vertices of  $w$ .

**Definition 1.1.** The first and second neighborhood Dakshayani indices are stated as  $ND_1(G) = \sum_{vw \in E(G)} [D_G(v) + D_G(w)]$ ,  $ND_2(G) = \sum_{vw \in E(G)} [D_G(v) D_G(w)]$

**Definition 1.2.** The first and second hyper neighborhood Dakshayani indices are stated as

$$HND_1(G) = \sum_{vw \in E(G)} [D_G(v) + D_G(w)]^2, \quad HND_2(G) = \sum_{vw \in E(G)} [D_G(v) D_G(w)]^2$$

**Definition 1.3.** The Minus and Square neighborhood Dakshayani indices of a graph  $G$  is stated as

$$MND(G) = \sum_{vw \in E(G)} |D_G(v) - D_G(w)|, \quad QND(G) = \sum_{vw \in E(G)} |D_G(v) - D_G(w)|^2$$

**Definition 1.4.** The  $F_1$  neighborhood Dakshayani index of a graph  $G$  is stated as

$$F_1ND(G) = \sum_{vw \in E(G)} [D_G(v)^2 + D_G(w)^2]$$

For the computation of topological indices on nanostructures, see [1, 2, 12]. In this paper, we carry forward the work done in [3] by using Neighborhood Dakshayani indices on carbon nanotube and Boron- nitride nanotube.

## 2. Materials and Methods

Our main results consist of degree-based neighborhood topological indices of carbon nanotubes and boron nitride nanotubes. To calculate the results, vertex partition, edge partition, analytical techniques, graph-theoretical tools, and a sum of degrees of neighbor methods are used.

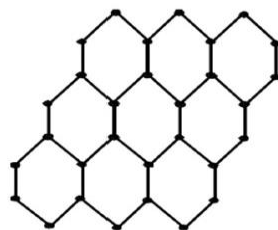
## 3. Results and Discussion

### 3.1. Boron-nitride graph.

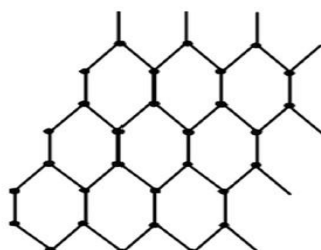
In inorganic chemistry, the boron-nitride graph is a simple, connected, and planar graph. The symbolic representation of boron-nitride is BN. The BN horizontal and vertical rings of are  $p \times p$ .  $2p^2 + 4p$  is the order of graph,  $O|G|$  and is as shown in Figure 2 and  $3p^2 + 4p - 1$  is the size of the graph  $E|G|$ . The 2D BN graph is classified as Cubic BN and Hexagonal BN. In this proposed work, the hexagonal BN graph is considered. The BN consists of boron and nitrogen atoms, joined alternatively to form a hexagonal structure. The hexagons are formed such that an equal number of atoms of Boron (B) and nitrogen(N) are involved in the formation. 0.145 nm is the bond-length between the atoms. The angle between Boron-Nitrogen-Boron or Nitrogen-Boron-Nitrogen is  $120^\circ$ . The hexagonal BN structure consists of a single layer and is found in nanotubes.

The edge classification based on the neighbor sum of the degrees of the end vertices of each edge of  $BN(G)$  is denoted in Table 1.





**Figure 1.**  $3 \times 3$ , hexagonal Boron nitride graph.



**Figure 2.**  $p \times p$ , hexagonal Boron nitride graph.

**Table 1.** The edge partition of  $BN(G)$  For  $p \geq 2$ .

$E(v,w)$ Where $vw \in E(G)$	No. of Edges
$E(4,5)$	4
$E(5,5)$	2
$E(5,7)$	8
$E(6,7)$	$8(p-2)$
$E(7,9)$	$4(p-1)$
$E(9,9)$	$(p-1)(3p-5)$

**Theorem 2.1.** The first neighborhood Dakshayani index of hexagonal boron nitride nano-tube graph  $\{BNT(G)\}$  for  $p \geq 2$  is  $54p^2 + 24p - 34$

*Proof.*

$$\begin{aligned}
 ND_1(G) &= \sum_{vw \in E(G)} [D_G(v) + D_G(w)] \\
 &= E(4,5) (4 + 5) + E(5,5) (5 + 5) + E(5,7) (5 + 7) + E(6,7) (6 + 7) + E(7,9) (7 + 9) \\
 &\quad + E(9,9) (9 + 9) \\
 &= 4(9) + 2(10) + 8(12) + (8p - 16)(13) + (4p - 4)(16) + (3p^2 - 8p + 5)(18) \\
 &= 54p^2 + 24p - 34.
 \end{aligned}$$

**Theorem 2.2.** The second neighborhood Dakshayani index of hexagonal boron nitride nanotube graph  $\{BNT(G)\}$  for  $p \geq 2$  is  $243p^2 - 60p - 109$

*Proof.*

$$\begin{aligned}
 ND_2(G) &= \sum_{vw \in E(G)} [D_G(v)D_G(w)] \\
 &= E(4,5) (4 \times 5) + E(5,5) (5 \times 5) + E(5,7) (5 \times 7) + E(6,7) (6 \times 7) + E(7,9) (7 \times 9) \\
 &\quad + E(9,9) (9 \times 9) \\
 &= 243p^2 - 60p - 109.
 \end{aligned}$$

**Theorem 2.3.** The first hyper neighborhood Dakshayani index of hexagonal boron nitride nanotube graph  $\{BNT(G)\}$  for  $p \geq 2$  is  $972p^2 - 216p - 500$

*Proof.*

$$\begin{aligned}
 HND_1(G) &= \sum_{vw \in E(G)} [D_G(v) + D_G(w)]^2 \\
 &= E(4,5) (4 + 5)^2 + E(5,5) (5 + 5)^2 + E(5,7) (5 + 7)^2 + E(6,7) (6 + 7)^2 + E(7,9) (7 + 9)^2 \\
 &\quad + E(9,9) (9 + 9)^2
 \end{aligned}$$

$$= 972p^2 - 216p - 500.$$

**Theorem 2.4.** The first hyper neighborhood Dakshayani index of hexagonal boron nitride nano-tube graph  $\{BNT(G)\}$  for  $p \geq 2$  is  $19683p^2 - 22500p + 4355$

*Proof.*

$$\begin{aligned} HND_2(G) &= \sum_{vw \in E(G)} [D_G(v)D_G(w)]^2 \\ &= E(4,5)(4 \times 5)^2 + E(5,5)(5 \times 5)^2 + E(5,7)(5 \times 7)^2 + E(6,7)(6 \times 7)^2 + E(7,9)(7 \times 9)^2 \\ &\quad + E(9,9)(9 \times 9)^2 \\ &= 19683p^2 - 22500p + 4355. \end{aligned}$$

**Theorem 2.5.** The minus neighborhood Dakshayani index of hexagonal boron nitride nanotube graph  $\{BNT(G)\}$  for  $p \geq 2$  is  $16p - 4$

*Proof.*

$$\begin{aligned} MND(G) &= \sum_{vw \in E(G)} |D_G(v) - D_G(w)| \\ &= E(4,5)|(4 - 5)| + E(5,5)|(5 - 5)| + E(5,7)|(5 - 7)| + E(6,7)|(6 - 7)| + E(7,9)|(7 - 9)| \\ &\quad + E(9,9)|(9 - 9)| \\ &= 16p - 4. \end{aligned}$$

**Theorem 2.6.** The square neighborhood Dakshayani index of hexagonal boron nitride nanotube graph  $\{BNT(G)\}$  for  $p \geq 2$  is  $24p + 4$

*Proof.*

$$\begin{aligned} QND(G) &= \sum_{vw \in E(G)} |D_G(v) - D_G(w)|^2 \\ &= E(4,5)|(4 - 5)|^2 + E(5,5)|(5 - 5)|^2 + E(5,7)|(5 - 7)|^2 + E(6,7)|(6 - 7)|^2 + E(7,9)|(7 - 9)|^2 \\ &\quad + E(9,9)|(9 - 9)|^2 \\ &= 24p + 4. \end{aligned}$$

**Theorem 2.7.** The  $F_1$  neighborhood Dakshayani index of hexagonal boron nitride nano-tube graph  $\{BNT(G)\}$  for  $p \geq 2$  is  $486p^2 - 96p - 214$

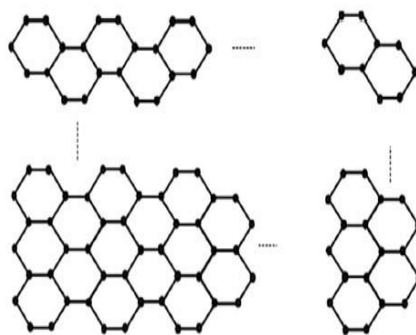
*Proof.*

$$\begin{aligned} F_1ND(G) &= \sum_{vw \in E(G)} [D_G(v)^2 + D_G(w)^2] \\ &= E(4,5)(4^2 + 5^2) + E(5,5)(5^2 + 5^2) + E(5,7)(5^2 + 7^2) + E(6,7)(6^2 + 7^2) + E(7,9)(7^2 + 9^2) \\ &\quad + E(9,9)(9^2 + 9^2) \\ &= 486p^2 - 96p - 214. \end{aligned}$$

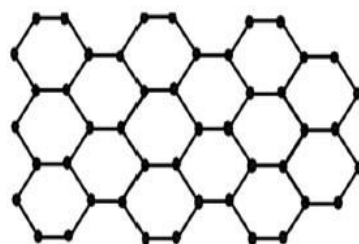
### 3.2. Carbon nanotube graph.

The carbon nanotube (CNT) graph is a simple, connected, and planar graph, as depicted in figure 3 and figure 4. The CNT consists of two sets of rings viz. vertical and horizontal rings. The first one consists of  $p$  vertical rings, and the other one consists of  $p - 1$  horizontal rings. It consists of  $4p^2 + 4p - 1$  vertices, and  $6p^2 + 3p - 2$  edges. The CNT's have a diameter approximately equal to 1 nm. The structure of CNT affects the length and angle between the carbon atoms. In our work, we considered the  $p \times p$ , ( $p=q$ ) rectangular section of the CNT graph for all  $p \geq 3$ .

The edge classification based on the neighbor sum of the degrees of the end vertices of each edge of  $CNT(G)$  is denoted in Table 2.



**Figure 3.** Carbon nanotube graph.



**Figure 4.** Carbon nanotube graph with  $p=3$ .

**Theorem 3.1.** The first neighborhood Dakshayani index of Carbon nano-tube graph  $\{CNT(G)\}$  for  $p \geq 3$  is  $108p^2 - 14p - 40$

*Proof.*

$$\begin{aligned}
 ND_1(G) &= \sum_{vw \in E(G)} [D_G(v) + D_G(w)] \\
 &= E(4,5) (4 + 5) + E(5,5) (5 + 5) + E(5,7) (5 + 7) + E(5,8) (5 + 8) + E(6,7) (6 + 7) \\
 &+ E(7,9) (7 + 9) \\
 &+ E(8,8) (8 + 8) + E(8,9) (8 + 9) + E(9,9) (9 + 9) \\
 &= 4(9) + 2p(10) + 8(12) + (4p - 4)(13) + (4p - 10)(13) + (2p - 1)(16) + (2p - 2)(16) \\
 &+ (4p - 4)(17) + (6p^2 - 15p + 7)(18) \\
 &= 108p^2 - 14p - 40.
 \end{aligned}$$

**Table 2.** The edge partition of  $CNT(G)$  For  $p \geq 3$ .

$E(v,w)$ Where $vw \in E(G)$	No. of Edges
$E(4,5)$	4
$E(5,5)$	$2p$
$E(5,7)$	8
$E(5,8)$	$4(p - 1)$
$E(6,7)$	$2(2p - 5)$
$E(7,9)$	$(2p - 1)$
$E(8,8)$	$2(p - 1)$
$E(8,9)$	$4(p - 1)$
$E(9,9)$	$6p^2 - 15p + 7$

**Theorem 3.2.** The second neighborhood Dakshayani index of Carbon nano-tube graph  $\{CNT(G)\}$  for  $p \geq 3$  is  $486p^2 - 295p - 132$

*Proof.*

$$\begin{aligned}
 ND_2(G) &= \sum_{vw \in E(G)} [D_G(v)D_G(w)] \\
 &= E(4,5) (4 \times 5) + E(5,5) (5 \times 5) + E(5,7) (5 \times 7) + E(5,8) (5 \times 8) + E(6,7) (6 \times 7) + \\
 &E(7,9) (7 \times 9)
 \end{aligned}$$

$$+ E(8,8) (8 \times 8) + E(8,9) (8 \times 9) + E(9,9) (9 \times 9) \\ = 486p^2 - 295p - 132.$$

**Theorem 3.3.** *The first hyper neighborhood Dakshayani index of Carbon nano-tube graph  $\{CNT(G)\}$  for  $p \geq 3$  is  $1944p^2 - 112p - 546$*

*Proof.*

$$HND_1(G) = \sum_{vw \in E(G)} [D_G(v) + D_G(w)]^2 \\ = E(4,5) (4 + 5)^2 + E(5,5) (5 + 5)^2 + E(5,7) (5 + 7)^2 + E(5,8) (5 + 8)^2 + E(6,7) (6 + 7)^2 \\ + E(7,9) (7 + 9)^2 + E(8,8) (8 + 8)^2 + E(8,9) (8 + 9)^2 + E(9,9) (9 + 9)^2 \\ = 1944p^2 - 112p - 546.$$

**Theorem 3.4.** *The first hyper neighborhood Dakshayani index of Carbon nano-tube graph  $\{CNT(G)\}$  for  $p \geq 3$  is  $39366p^2 - 46843p + 390$*

*Proof.*

$$HND_2(G) = \sum_{vw \in E(G)} [D_G(v)D_G(w)]^2 \\ = E(4,5) (4 \times 5)^2 + E(5,5) (5 \times 5)^2 + E(5,7) (5 \times 7)^2 + E(5,8) (5 \times 8)^2 + E(6,7) (6 \times 7)^2 \\ + E(7,9) (7 \times 9)^2 + E(8,8) (8 \times 8)^2 + E(8,9) (8 \times 9)^2 + E(9,9) (9 \times 9)^2 \\ = 39366p^2 - 46843p + 390.$$

**Theorem 3.5.** *The minus neighborhood Dakshayani index of Carbon nano-tube graph  $\{CNT(G)\}$  for  $p \geq 3$  is  $12p + 10$*

*Proof.*

$$MND(G) = \sum_{vw \in E(G)} |D_G(v) - D_G(w)| \\ = E(4,5)|(4 - 5)| + E(5,5)|(5 - 5)| + E(5,7)|(5 - 7)| + E(5,8)|(5 - 8)| + E(6,7)|(6 - 7)| \\ + E(7,9)|(7 - 9)| + E(8,8)|(8 - 8)| + E(8,9)|(8 - 9)| + E(9,9)|(9 - 9)| \\ = 12p + 10$$

**Theorem 3.6.** *The square neighborhood Dakshayani index of Carbon nano-tube graph  $\{CNT(G)\}$  for  $p \geq 3$  is  $16p + 24$*

*Proof.*

$$QND(G) = \sum_{vw \in E(G)} |D_G(v) - D_G(w)|^2 \\ = E(4,5)|(4 - 5)|^2 + E(5,5)|(5 - 5)|^2 + E(5,7)|(5 - 7)|^2 + E(5,8)|(5 - 8)|^2 + E(6,7)|(6 - 7)|^2 \\ + E(7,9)|(7 - 9)|^2 + E(8,8)|(8 - 8)|^2 + E(8,9)|(8 - 9)|^2 + E(9,9)|(9 - 9)|^2 \\ = 16p + 24.$$

**Theorem 3.7.** *The first neighborhood Dakshayani index of Carbon nanotube graph  $\{CNT(G)\}$  for  $p \geq 3$  is  $972p^2 - 538p - 282$*

*Proof.*

$$F_1ND(G) = \sum_{vw \in E(G)} [D_G(v)^2 + D_G(w)^2] \\ = E(4,5) (4^2 + 5^2) + E(5,5) (5^2 + 5^2) + E(5,7) (5^2 + 7^2) + E(5,8) (5^2 + 8^2) + E(6,7) (6^2 \\ + 7^2) \\ + E(7,9) (7^2 + 9^2) + E(8,8) (8^2 + 8^2) + E(8,9) (8^2 + 9^2) + E(9,9) (9^2 + 9^2) \\ = 972p^2 - 538p - 282.$$

#### 4. Conclusions

In the proposed work, we have calculated the values of Neighborhood Dakshyani indices for nanostructures such as hexagonal boron nitride nanotubes and carbon nanotubes. The results obtained are used to analyze the properties of nanotubes. Using Neighborhood Dakshyani indices to determine the properties of nanostructures includes various applications in biomedical, aerospace, water filtration, etc.

## Funding

This research received no external funding.

## Acknowledgments

This research has no acknowledgment.

## Conflicts of Interest

The authors declare no conflict of interest.

## References

1. Aslam, A.; Ahmad, S.; Gao, W.J.Z.f.N.A. On certain topological indices of boron triangular nanotubes. **2017**, *72*, 711-716.
2. Akhter, S.; Imran, M. On molecular topological properties of benzenoid structures. *Canadian Journal of Chemistry* **2016**, *94*, 687-698, <https://doi.org/10.1139/cjc-2016-0032>.
3. Yousaf, A.; Alolaiyan, H.; Nadeem, M.; Razaq, A. Topological analysis of carbon and boron nitride nanotubes. *Scientific Reports* **2020**, *10*, 1-9, <https://doi.org/10.1038/s41598-020-58372-1>.
4. De, N. On Molecular Topological Properties of  $TiO_2$  Nanotubes. *J. Nanosci.* **2016**, 1-5, <https://doi.org/10.1155/2016%2F1028031>.
5. Gutman, I.; Polansky, O.E. *Mathematical Concepts in Organic Chemistry*. Springer, Berlin, **1986**.
6. Hayat, S.; Imran, M. Computation of topological indices of certain networks. *Applied Mathematics and Computation* **2014**, *240*, 213-228, <https://doi.org/10.1016/j.amc.2014.04.091>.
7. Liu, J.-B.; Gao, W.; Siddiqui, M.K.; Farahani, M.R. Computing three topological indices for Titania nanotubes. *AKCE International Journal of Graphs and Combinatorics* **2016**, *13*, 255-260, <https://doi.org/10.1016/j.akcej.2016.07.001>.
8. Kulli, V.R. Neighbourhood Dakshayani indices. *International Journal of Mathematical Archive* **2019**, *10*, 23-31.
9. Kulli, V.R. Some Multiplicative Neighbourhood Dakshayani Indices of Certain Nanostructures. *International Journal of Mathematics and its Applications* **2019**, *7*, 209-217.
10. Kulli, V.R.  $F_1$ -Neighbourhood and square neighbourhood Dakshayani indices of some nano structures. *International journal of engineering sciences and research technology* **2019**, *8*, 126-138.
11. Mondal, S.; Bhosale, A.; De, N.; Pal, A. Topological properties of some nanostructures. *Nanosystems: Physics, Chemistry, Mathematics* **2020**, *11*, 14-24, <https://doi.org/10.17586/2220-8054-2020-11-1-14-24>.
12. Nadeem, M.; Yousaf, A.; Alolaiyan, H.; Razaq, A. Certain polynomials and related topological indices for the series of benzenoid graphs. *Scientific Reports* **2019**, *9*, 1-5, <https://doi.org/10.1038/s41598-019-45721-y>.
13. Shanmukha, M.C.; Basavarajappa, N.S.; Anilkumar, K.N. Predicting physico-chemical properties of octane isomers using QSPR approach. *Malaya Journal of Matematik* **2020**, *8*, 104-116, <https://doi.org/10.26637/MJM0801/0018>.
14. Shanmukha, M.C.; Basavarajappa, N.S.; Shilpa, K.C.; Usha, A. Degree-based topological indices on anticancer drugs with QSPR analysis. *Heliyon* **2020**, *6*, 1-9, <https://doi.org/10.1016/j.heliyon.2020.e04235>.
15. Anil Kumar, K.N.; Basavarajappa, N.S.; Shanmukha, M.C. QSPR analysis of Alkanes with certain degree based topological indices. *Malaya Journal of Matematik* **2020**, *8*, 314-330, <https://doi.org/10.26637/MJM0802/0003>.
16. Mondal, S.; De, N.; Pal, A. On Some New Neighborhood Degree-Based Indices for Some Oxide and Silicate Networks. *J* **2019**, *2*, 384-409, <https://doi.org/10.3390/j2030026>.
17. Trinajstić, N. *Chemical Graph Theory*. CRC Press, Boca Raton, FL. **1992**.

# Generalized Reciprocal Sanskruti Index: Chemical Applicability and Bounds

Shanmukha M C <sup>1,\*</sup> , Basavarajappa N S <sup>2</sup>, Anil Kumar K N <sup>2</sup>, Shilpa K C <sup>3</sup>

<sup>1</sup> Department of Mathematics, Jain Institute of Technology, Davanagere-577003, Karnataka, India

<sup>2</sup> Department of Mathematics, Bapuji Institute of Engineering and Technology, Davanagere-577004, Karnataka, India

<sup>3</sup> Department of Computer Science & Engineering, Bapuji Institute of Engineering and Technology, Davanagere-577004, Karnataka, India

\* Correspondence: [mcshanmukha@gmail.com](mailto:mcshanmukha@gmail.com);

Scopus Author ID 57217312072

Received: 30.07.2020; Revised: 15.08.2020; Accepted: 16.08.2020; Published: 19.08.2020

**Abstract:** In this paper, we put forward the generalization of reciprocal Sanskruti index  $\mathcal{RS}^\alpha$  for some  $\alpha \in \mathbb{Z}^+$ . For  $\alpha = 3$  the prediction potentiality of  $\mathcal{RS}^3$  is discussed with the physicochemical properties of the set of octane isomers. And also we study the mathematical properties of  $\mathcal{RS}^3$ .

**Keywords:** Topological indices; Sanskruti index; Reciprocal Sanskruti index.

© 2020 by the authors. This article is an open-access article distributed under the terms and conditions of the Creative Commons Attribution (CC BY) license (<https://creativecommons.org/licenses/by/4.0/>).

## 1. Introduction

Let  $G = (V, E)$  be a simple graph with  $|V| = n$  and  $|E| = m$ . Let  $\Delta = \deg(v_1) \geq \deg(v_2) \geq \deg(v_3) \geq \dots \geq \deg(v_n) = \delta$  be vertex degree sequence and let  $\Delta' = \sigma(v_1) \geq \sigma(v_2) \geq \sigma(v_3) \geq \dots \geq \sigma(v_n) = \delta'$  be neighborhood degree sequence of  $G$  respectively. Where  $\sigma(u) = \sum_{v \in N(u)} \deg(v)$  and  $N(u) = \{v \mid uv \in E(G)\}$ .  $S(G)$  and  $L(G)$  denote the subdivision and line graph of  $G$ , respectively.

A Topological Index of a graph is a numerical value that is invariant under the automorphism of graphs. Due to numerous applications in chemistry as a molecular structure descriptors, topological indices gained considerable popularity in the field of mathematical chemistry. These topological indices are used in QSAR/QSPR [1, 4, 12, 16, 17] studies to predict the physicochemical characteristics and biological activities of chemical compounds using a molecular graph. Topological indices can be classified into several distinct categories. One of the widely used group is the so-called degree-based topological indices. A large number of degree-based topological indices have been studied so far [2-10, 13-15, 18], and references are cited therein.

The most studied topological indices are the Zagreb indices.

$$M_1(G) = \sum_{v \sim u} d_G(v)^2 \quad (1)$$

$$M_2(G) = \sum_{v \sim u} d_G(v)d_G(u) \quad (2)$$

The Sanskruti index [11] is defined as

$$S(G) = \sum_{v_i \sim v_j} \left( \frac{v_i v_j}{v_i + v_j - 2} \right)^3 \quad (3)$$

Motivated by the previous research on Sanskruti index, here we propose the following topological indices:

- Generalized Reciprocal Sanskruti Index:



$$\mathcal{RS}(G)^\alpha = \sum_{v_i \sim v_j} \left( \frac{v_i + v_j - 2}{v_i v_j} \right)^\alpha \quad (4)$$

- For  $\alpha = 1$ ,

$$\mathcal{RS}(G) = \sum_{v_i \sim v_j} \left( \frac{v_i + v_j - 2}{v_i v_j} \right) \quad (5)$$

- Randic type reciprocal Sanskruti index:

$$RT = \sum_{v_i \sim v_j} \frac{1}{v_i v_j} \quad (6)$$

- Reduced Sanskruti index:

$$RSI = \sum_{v_i \sim v_j} \frac{v_i + v_j}{v_i v_j} \quad (7)$$

In this paper we are interested to work on the reciprocal sanskruti index for  $\alpha = 3$ . Which is defined as follows:

$$\mathcal{RS}(G)^3 = \sum_{v_i \sim v_j} \left( \frac{v_i + v_j - 2}{v_i v_j} \right)^3 \quad (8)$$

Whenever we introduced a new topological index, it is mandatory to check its applicability in chemistry as a molecular structure descriptor. Therefore, in the following section, we investigate the applicability of  $\mathcal{RS}(G)^3$  index.

## 2. Materials and Methods

### 2.1. On chemical applicability of the $\mathcal{RS}(G)^3$ -Index.

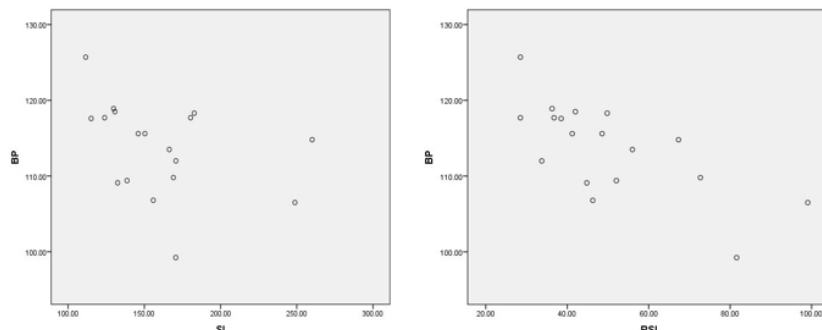
Here we have examined the chemical applicability of the reciprocal Sanskruti  $\mathcal{RS}(G)^3$  – index and compared the values with the Sanskruti  $\mathcal{S}(G)$  – index for modeling the physical and chemical properties [boiling points(BP), molar volumes (mv) at 20°C, molar refractions (mr) at 20°C, heats of vaporization (hv) at 25°C, surface tensions (st) 20°C and melting points (mp), acentric factor (AcentFac), and DHVAP] of octane isomers. The  $\mathcal{RS}(G)^3$  was tested using a data set of octane isomers found at (<http://www.moleculardescriptors.eu/dataset.htm>). The values are compiled in Table 1.

**Table 1.** Physico-chemical properties of octane isomers.

Alkane	AF	DHVAP	BP	TC	PC	S	D	$R_m^2$	$-\Delta H_f$	$-\Delta H_v$
n-octane	0.3978	9.915	125.70	296.20	24.64	111.67	0.7025	2.0449	208.6	41.49
2M	0.3779	9.484	117.6	288.0	24.80	109.84	0.6980	1.8913	215.4	39.67
3M	0.3710	9.521	118.9	292.0	25.60	111.26	0.7058	1.7984	212.5	39.83
4M	0.3715	9.483	117.7	290.0	25.60	109.32	0.7046	1.7673	210.7	39.64
3E	0.3624	9.476	118.5	292.0	25.74	109.43	0.7136	1.7673	210.7	39.64
22MM	0.3394	8.915	106.8	279.0	25.60	103.42	0.6953	1.6744	224.6	37.28
23MM	0.3482	9.272	115.6	293.0	26.60	108.02	0.7121	1.6464	213.8	38.78
24MM	0.3442	9.029	109.4	282.0	25.80	106.98	0.7004	1.6142	219.2	37.76
25MM	0.3568	9.051	109.1	279.0	25.00	105.72	0.6935	1.6449	222.5	37.85
33MM	0.3225	8.973	112.0	290.8	27.20	104.74	0.7100	1.7377	220.0	37.53
34MM	0.3403	9.316	117.7	298.0	27.40	106.59	0.7200	1.5230	212.8	38.97
2M3E	0.3324	9.209	115.6	295.0	27.40	106.06	0.7193	1.5525	211.0	38.52
3M3E	0.3068	9.081	118.3	305.0	28.90	101.48	0.7274	1.5212	214.8	37.99
223MMM	0.3008	8.826	109.8	294.0	28.20	101.31	0.7161	1.4306	220.0	36.91
224MMM	0.3053	8.402	99.24	271.1	25.50	104.09	0.6919	1.4010	224.0	35.14
233MM	0.2931	8.897	114.8	303.0	29.00	102.06	0.7262	1.4931	216.3	37.27
234MMM	0.3174	9.014	113.5	295.0	27.60	102.39	0.7191	1.3698	217.3	37.75
2233MMMM	0.2552	8.41	106.5	270.8	24.50	93.06	0.8242	1.4612	225.6	42.90

Surprisingly, we can see that the correlation coefficient value of  $\mathcal{RS}(G)^3$  for the boiling points of octane, the isomer is  $r = 0.701$ , whereas for  $\mathcal{S}(G)$  the correlation coefficient value is  $r = 0.366$ . Similarly for other physical properties of octane isomers such as heats, critical

temperature, critical pressure, density, entropy and mean radius, the correlation coefficient value for  $\mathcal{RS}(G)^3$  is  $r = 0.670, 0.473, 0.636, 0.810$  and  $0.687$  respectively, where as for  $\mathcal{S}(G)$  the correlation coefficient value is  $r = 0.435, 0.010, 0.611, 0.857$  and  $0.669$  respectively. Clearly, the reciprocal Sanskruti index  $\mathcal{RS}(G)^3$  shows a better correlation than  $\mathcal{S}(G)$ . In Figure 1, the correlation coefficient of  $\mathcal{RS}(G)^3$  and  $\mathcal{S}(G)$  are depicted.



**Figure 1.** Correlation coefficient.

### 3. Results and Discussion

#### 3.1. Mathematical properties of $\mathcal{RS}(G)^3$ .

Since,  $\left(\frac{v_i + v_j - 2}{v_i v_j}\right)^3$  is equal for all edges if a graph  $G$  is regular or biregular. Therefore we have the following axillary results:

**Proposition 1.** For any  $r$ -regular graph  $G$ ,  $\mathcal{S}^3(G) = \frac{4n(r^2-1)^3}{r^{11}}$

*Proof.* Let  $G$  be a  $r$ -regular graph. Then for every  $v \in V(G)$ ,  $v_j = r^2$ . Further, every  $r$ -regular graph containing  $\frac{nr}{2}$  edges. Therefore we have,

$$\begin{aligned}\mathcal{RS}(G)^3 &= \sum_{v_i \sim v_j} \left(\frac{v_i + v_j - 2}{v_i v_j}\right)^3 \\ &= \frac{nr}{2} \left(\frac{r^2 + r^2 - 2}{r^4}\right)^3 \\ &= \frac{4n((n-1)^2 - 1)^3}{r^{11}}\end{aligned}$$

**Proposition 2.**

- (a) For a complete graph  $K_n$ ,  $\mathcal{S}^3(K_n) = \frac{4n((n-1)^2-1)^3}{(n-1)^{11}}$
- (b) For cycle graph  $C_n$ ,  $\mathcal{S}^3(C_n) = \frac{27n}{512}$
- (c) For path graph  $P_n$ ,  $\mathcal{S}^3(P_n) = \frac{27n+47}{512}$
- (d) For the wheel graph  $W_n$ ,  $\mathcal{S}^3(W_n) = (n-1) \left[ \left(\frac{4n-6}{3(n-1)^2}\right)^3 + \left(\frac{n+8}{n+5}\right)^3 \right]$
- (e) For complete bipartite graph  $K_{r,s}$ ;  $2 \leq r < s$ ,  $\mathcal{S}^3(K_{r,s}) = \frac{8(rs-1)^3}{rs^5}$

*Proof.* (a) and (b) follows by Proposition 1, putting  $r = n-1$  and  $r = 2$  respectively.

(c) Let  $V(P_n) = \{v_1, v_2, v_3, \dots, v_n\}$  where  $v_1$  and  $v_n$  are pendent vertices of  $P_n$ . Then for every  $v \in V\{v_1, v_n\}$ ,  $v_j = 4$  and  $\sigma(v_1) = 5 = \sigma(v_n)$ . Since  $E(P_n) = n - 1$ , therefore, we have

$$\begin{aligned}\mathcal{RS}(P_n)^3 &= \sum_{v_i \sim v_j} \left( \frac{v_i + v_j - 2}{v_i v_j} \right)^3 \\ &= (n-3) \left( \frac{4+4-2}{4^2} \right)^3 + 2 \left( \frac{2+3-2}{2 \times 3} \right)^3 \\ &= \frac{27n+47}{512}\end{aligned}$$

(d) Let  $V(W_n) = \{v_1, v_2, v_3, \dots, v_n\}$  where  $v_1$  is a central vertex of  $W_n$ . Then for every  $v \in V \setminus \{v_1\}$ ,  $v_j = n+5$  and  $\sigma(v_1) = 3(n-1)$ . Since  $E(W_n) = 2(n-1)$ , therefore, we have

$$\begin{aligned}\mathcal{RS}(W_n)^3 &= \sum_{v_i \sim v_j} \left( \frac{v_i + v_j - 2}{v_i v_j} \right)^3 \\ &= (n-1) \left( \frac{3(n-1)+(n-1)-2}{3(n-1)^2} \right)^3 + (n-1) \left( \frac{(n+5)+(n+5)-2}{(n+5)^2} \right)^3 \\ &= (n-1) \left[ \left( \frac{4n-6}{3(n-1)^2} \right)^3 + \left( \frac{n+8}{n+5} \right)^3 \right]\end{aligned}$$

(e) Let  $V(K_{r,s}) = v_1 \cup v_2$  where  $v_1 = \{v_1, v_2, v_3, \dots, v_r\}$  and  $v_2 = \{v_{r+1}, v_{r+2}, v_{r+3}, \dots, v_s\}$ . Clearly, every  $v \in v_1$ ,  $v_j = rs$  and  $u \in v_2$ ,  $v_i = sr$ . Since  $E(K_{r,s}) = rs$  therefore, we have

$$\begin{aligned}\mathcal{RS}(K_{r,s})^3 &= \sum_{v_i \sim v_j} \left( \frac{v_i + v_j - 2}{v_i v_j} \right)^3 \\ &= rs \left( \frac{rs+sr-2}{rs^2} \right)^3 \\ &= \frac{8(rs-1)^3}{rs^5}\end{aligned}$$

We need the following well-known results to obtain bounds for  $RS(G)^3$ .

**Lemma 1** ([19]). Let  $a_i$ ,  $i = 1, 2, 3, \dots, m$  be a positive real number sequence. Then for any real  $r$ ,  $r \geq 1$  or  $r \leq 0$ , the following inequality holds

$$\sum_{i=1}^m a_i^r \geq m^{1-r} \left( \sum_{i=1}^m a_i \right). \quad (9)$$

Equality holds if and only if  $a_1 = a_2 = \dots = a_m$ .

**Lemma 2** ([20]). Let  $a_i$  and  $b_i$ ,  $i = 1, 2, 3, \dots, m$  be a positive real number sequences. Then for any real  $r \geq 0$  the following inequality holds

$$\sum_{i=1}^m \frac{a_i^{r+1}}{b_i^r} \geq \frac{\left( \sum_{i=1}^m a_i \right)^{r+1}}{\left( \sum_{i=1}^m b_i \right)^r} \quad (10)$$

Equality holds if and only if  $\frac{a_1}{b_1} = \frac{a_2}{b_2} = \dots = \frac{a_m}{b_m}$ .

### 3.2. Bounds for $RS(G)^3$ .

Next, we have the following lower bound for  $RS(G)^3$  in terms of maximum degree and the size of a graph  $G$ .

**Theorem 3.** For any graph  $G$  without isolated vertices,

$$RS(G)^3 \geq 8m \left( \frac{1}{\Delta^2} - \frac{1}{\Delta^4} \right)^3 \quad (11)$$

*Proof.* Let  $G$  be graph without isolated vertices of size  $m$  and maximum degree  $\Delta$ . Since for any  $v \in V$ ,  $v_j \leq \Delta^2$ . Therefore, we have,

$$RS(G)^3 = \sum_{v_i \sim v_j} \left( \frac{v_i + v_j - 2}{v_i v_j} \right)^3 \geq m \left( \frac{\Delta^2 + \Delta^2 - 2}{\Delta^4} \right)^3$$

$$= 8m \left( \frac{\Delta^2 - 1}{\Delta^4} \right)^3$$

$$= 8m \left( \frac{1}{\Delta^2} - \frac{1}{\Delta^4} \right)^3$$

In the following results, we obtain lower bound for  $RS(G)^3$  in terms of maximum degree  $\Delta$ .

**Theorem 4.** For any  $n$ -vertex graph  $G$  and maximum degree  $\Delta$ , we have

$$RS(G)^3 \geq \frac{8(\Delta^4 - 1)^3}{\Delta^{12}(\Delta^2 + 1)^3} \quad (12)$$

*Proof.* Let  $G$  be a  $n$ -vertex graph with a maximum degree  $\Delta$ , we have

$$RS(G)^3 = \sum_{v_i \sim v_j} \left( \frac{v_i + v_j - 2}{v_i v_j} \right)^3 \quad (13)$$

$$= \sum_{v_i \sim v_j} \left( \frac{v_i v_j - 1}{v_i v_j} \right)^3 \left( \frac{v_i + v_j - 2}{v_i v_j - 1} \right)^3 \quad (14)$$

Since  $(v_i - v_j)^2 \geq 0$ , therefore it is easy to check that

$$\frac{v_i + v_j - 2}{v_i v_j - 1} = \frac{1}{v_i + 1} + \frac{1}{v_j + 1}. \quad (15)$$

Since  $v_i \leq \Delta^2$  therefore (15) becomes

$$\frac{v_i + v_j - 2}{v_i v_j - 1} = \frac{1}{\Delta^2 + 1} + \frac{1}{\Delta^2 + 1} \quad (16)$$

Employing (16) in (14), we get

$$RS(G)^3 \geq \left( \frac{\Delta^2 \Delta^2 - 1}{\Delta^4} \right)^3 \left( \frac{2}{\Delta^2 + 1} \right)^3$$

$$= \frac{8(\Delta^4 - 1)^3}{\Delta^{12}(\Delta^2 + 1)^3}$$

**Theorem 5.** Let  $G$  be a graph without isolated vertex. Then

$$RS(G)^3 \geq \frac{(RSI - 2RT)^3}{m^2}$$

*Proof.* Let  $G$  be a graph without isolated vertex. Then set  $r = 3, a_i = \frac{v_i + v_j - 2}{v_i v_j}$  where the summation is performed over all edges of  $G$  then (9) is transformed into

$$\sum_{v_i \sim v_j} \left( \frac{v_i + v_j - 2}{v_i v_j} \right)^3 \geq m^{1-3} \sum_{v_i \sim v_j} \left( \frac{v_i + v_j - 2}{v_i v_j} \right)^3$$

$$\geq \left( \sum_{v_i \sim v_j} \frac{v_i + v_j}{v_i v_j} - \sum_{v_i \sim v_j} \frac{2}{v_i v_j} \right)^3$$

$$= \frac{(RSI - 2RT)^3}{m^2}$$

**Theorem 6.** Let  $G$  be a graph without isolated vertex with size at least 2.

Then

$$RS(G)^3 \leq (2M_2 - 2m)^3 (RT)^3$$

*Proof.* Observe that the following identity holds

$$2M_2 - 2m = \sum_{v_i \sim v_j} (v_i + v_j) - 2m$$

$$= \sum_{v_i \sim v_j} v_i + v_j - 2$$

$$(2M_2 - 2m)^3 = \sum_{v_i \sim v_j} \frac{\left(\frac{v_i + v_j - 2}{v_i v_j}\right)^3}{\left(\frac{1}{v_i v_j}\right)^3}$$

Set  $r = 2$ ,  $a_i = \frac{v_i + v_j - 2}{v_i v_j}$  and  $b_i = \frac{1}{v_i v_j}$  in (10), we get

$$\sum_{v_i \sim v_j} \frac{\left(\frac{v_i + v_j - 2}{v_i v_j}\right)^3}{\left(\frac{1}{v_i v_j}\right)^3} \times \frac{1}{v_i v_j} \geq \frac{\left(\sum_{v_i \sim v_j} \left(\frac{1}{v_i v_j}\right)\right)^3}{\left(\sum_{v_i \sim v_j} \frac{1}{v_i v_j}\right)^2}$$

$$(2M_2 - 2m)^3 RT \geq \frac{RS(G)^3}{(RT)^\epsilon}$$

$$RS(G)^3 \leq (2M_2 - 2m)^3 (RT)^3.$$

#### 4. Conclusions

Inspired by the work on the Sanskruti index, the reciprocal Sanskruti index is proposed. The value of the reciprocal Sanskruti index is calculated for octane isomers. The chemical applicability is compared to model the physical and chemical properties of octane isomers. The reciprocal Sanskruti index gives better results than the Sanskruti index.

#### Funding

This research received no external funding.

#### Acknowledgments

This research has no acknowledgment.

#### Conflicts of Interest

The authors declare no conflict of interest.

#### References

1. Anil Kumar, K.N.; Basavarajappa, N.S.; Shanmukha, M.C. QSPR analysis of Alkanes with certain degree based topological indices. *Malaya Journal of Matematik* **2020**, *8*, 314-330, <https://doi.org/10.26637/MJM0802/0003>.
2. Estrada, E. Atom-bond connectivity and the energetic of branched alkanes. *Chemical Physics Letters* **2008**, *463*, 422-425, <https://doi.org/10.1016/j.cplett.2008.08.074>.
3. Fath-Tabar, G. Old and New Zagreb Indices of Graphs. *MATCH - Communications in Mathematical and in Computer Chemistry* **2011**, *65*, 79-84.
4. Randic, M. Quantitative Structure-Property Relationship: boiling points and planar benzenoids. *New. j. Chem.* **1996**, *20*, 1001-1009.
5. Furtula, B.; Graovac, A.; Vukićević, D.; Augmented Zagreb index. *Journal of Mathematical Chemistry* **2010**, *48*, 370-380.
6. Aslam, A.; Bashir, Y.; Ahmad, S.; Gao, W. On Topological Indices of Certain Dendrimer Structures. *ADS* **2017**, *72*, 559-566, <https://doi.org/10.1515/zna-2017-0081>.
7. Gutman, I. Selected properties of the Schultz molecular topological index. *Journal of Chemical Information and Computer Sciences* **1994**, *34*, 1087-1089, <https://doi.org/10.1021/ci00021a009>.
8. Gutman, I.; Furtula, B.; Vukićević, Ž.; Popivoda, G. On Zagreb Indices and Coindices. *Match* **2015**, *74*, 5-16.
9. Harary, F. *Graph Theory*. Addison-Wesely, Reading Mass **1969**.
10. Hosamani, S.M.; Basavanagoud, B.; New upper bounds for the first Zagreb index. *MATCH Commun. Math. Comput. Chem.* **2015**, *74*, 97-101.

11. Hosamani, S.M. Computing Sanskruti index of certain nanostructures. *Journal of Applied Mathematics and Computing* **2017**, *54*, 425-433, <https://doi.org/10.1007/s12190-016-1016-9>.
12. Hosamani, S.; Perigidad, D.; Jamagoud, S.; Maled, Y.; Gavade, S. QSPR Analysis of Certain Degree Based Topological Indices. *Journal of Statistics Applications & Probability* **2017**, *6*, 1-11, <https://doi.org/10.18576/jsap/060211>.
13. Liu, B.; Gutman, I. Upper bounds for Zagreb indices of connected graphs. *MATCH - Communications in Mathematical and in Computer Chemistry* **2006**, *55*, 439-446.
14. Hayat, S.; Imran, M.; Liu, J.-B. Correlation between the Estrada index and  $\pi$ -electronic energies for benzenoid hydrocarbons with applications to boron nanotubes. *International Journal of Quantum Chemistry* **2019**, *119*, <https://doi.org/10.1002/qua.26016>.
15. Chen, J.; Liu, J.; Guo, X. Some upper bounds for the atom–bond connectivity index of graphs. *Applied Mathematics Letters* **2012**, *25*, 1077-1081, <https://doi.org/10.1016/j.aml.2012.03.021>.
16. Shanmukha, M.C.; Basavarajappa, N.S.; Anilkumar, K.N. Predicting physicochemical properties of octane isomers using QSPR approach. *Malaya Journal of Matematik* **2020**, *8*, 104-116.
17. Shanmukha, M.C.; Basavarajappa, N.S.; Shilpa, K.C.; Usha, A. Degree-based topological indices on anticancer drugs with QSPR analysis. *Heliyon* **2020**, *6*, 1-9, <https://doi.org/10.1016/j.heliyon.2020.e04235>.
18. Usha, A.; Ranjini, P.S.; Lokesh, V.; Harish. Bounds of Harmonic index. *Contemporary Studies in Discrete Mathematics* **2018**, *2*, 1-4.
19. Nadeem, M.F.; Zafar, S.; Zahid, Z. On topological properties of the line graphs of subdivision graphs of certain nanostructures. *Applied Mathematics and Computation* **2016**, *273*, 125-130, <https://doi.org/10.1016/j.amc.2015.10.010>.
20. Ranjini, P.S.; Veera, L.; Rajan, M.A.; Raju, M.P. On the Shultz index of the subdivision graphs. *Advanced Studies in Contemporary Mathematics (Kyungshang)* **2011**, *3*, 279-290.





# Frequency dependence of AC conductivity and dielectric properties evaluation of in-situ prepared polyaniline/manganese dioxide composite

Yankappa A. Kulakarni<sup>1</sup> · M. R. Jagadeesh<sup>2</sup> · Sahebagoada Jambaladinni<sup>3</sup> · H. M. Suresh Kumar<sup>4</sup> · M. S. Vasanthkumar<sup>5</sup> · S. Shivakumara<sup>6</sup>

Received: 23 December 2019 / Accepted: 21 March 2020 / Published online: 6 April 2020  
© Springer Science+Business Media, LLC, part of Springer Nature 2020

## Abstract

In the present study, polyaniline/manganese dioxide (PANI/MnO<sub>2</sub>) nanocomposite has been synthesised by in-situ redox method. MnO<sub>2</sub> nanostructures are formed in PANI matrix via simple redox reaction between KMnO<sub>4</sub> and aniline monomer at ambient conditions. The composite formation, structural and morphological changes in MnO<sub>2</sub> and PANI/MnO<sub>2</sub> were characterised by Fourier transform infrared spectroscopy (FT-IR), powder X-ray diffraction (PXRD) and scanning electron microscopy (SEM) analysis. The PXRD and FT-IR patterns of the PANI/MnO<sub>2</sub> nanocomposites confirm the presence of  $\alpha$ -MnO<sub>2</sub> nanostructures in polymer matrix. SEM images of the composite showed that MnO<sub>2</sub> nanostructures were dispersed uniformly in polymer matrix. AC conductivity and dielectric properties of MnO<sub>2</sub> nanostructures and PANI/MnO<sub>2</sub> nano composite were studied in the frequency range 10–100 MHz. AC conductivity of the nano composite obeyed the power law indicating the universal behaviour of disordered structures.

## 1 Introduction

Conducting polymers are the class of organic materials with a potential application in many technologies including energy storage [1], molecular recognition [2],

electromagnetic interference shielding [3], electrochemical sensors [4] and opto-electronic devices [5]. The conducting polymers have conjugated structures consisting of an alternate single and double bonds which is one of the basic requirement for the electrical conductivity. During oxidative polymerisation process, some of the pi-bonds are broken, releasing electron which further increases their conductivity [4, 6]. The electron transport in polymeric materials has become an area of interesting research because these materials have great potential for the fabrication of solid-state devices. There are many conducting polymers including polypyrrole, polythiophene, poly(3, 4-ethylenedioxythiophene), Polyaniline, etc., reported in literature and these polymers have been used in various applications [1, 3–5]. All these conducting polymers exhibit highly redox behaviour in the presence of heteroatom and polymer conjugation present in the respective polymer [4]. Moreover, these kind of polymers were used as electrode materials to study sensors and catalytic applications [4, 5, 7]. Among all conducting polymers, polyaniline (PANI) has attracted many researchers due to its high conductivity, unique conduction mechanism, easy preparation, simple polymerization, good thermal stability and environmental friendly impact [4, 5, 7]. PANI has been used as a conducting mediator material to contact between the atoms present in most of

✉ M. R. Jagadeesh  
jmrshyagale@gmail.com

✉ S. Shivakumara  
elessk@gmail.com

<sup>1</sup> Department of Physics, BLDEA's Vachana Pitamaha Dr. P.G. Halakatti College of Engineering and Technology, Bijapur, affiliated to Visvesvaraya Technological University, Belgavi, Karnataka 586103, India

<sup>2</sup> Department of Physics, Jain Institute of Technology, Davangere, affiliated to Visvesvaraya Technological University, Belgavi, Karnataka 577003, India

<sup>3</sup> Department of Physics, Government Engineering College, Huvinahadagali, Karnataka 583219, India

<sup>4</sup> Department of Physics, Siddaganga Institute of Technology, Tumakuru, Karnataka 572103, India

<sup>5</sup> Department of Physics, Acharya Institute of Technology, Soladevanahalli, Bangalore, Karnataka 560107, India

<sup>6</sup> Department of Chemistry, REVA University, Kattigenahalli, Yelahanka, Bangalore, Karnataka 560064, India

the semiconductor metal oxides [3, 4]. PANI has been used to enhance the electrical conductivity of metal oxide and increases overall performance of the electrode material [1, 4, 5]. There are several authors have been reported to synthesize nanocomposites using conducting polymer with metal oxide nanostructures such as ferrates, ZnO, MnO<sub>2</sub>, SnO<sub>2</sub>, TiO<sub>2</sub>, etc. [7–16] to enhance the electrical conductivity of nanocomposites.

Among the available metal oxides, manganese dioxide received much attention due to its potential applications in various fields [17–20]. Manganese dioxide is cheap, abundantly available, and relatively non-toxic in nature [17–21]. MnO<sub>2</sub> possesses different crystallographic forms such as  $\alpha$ -,  $\beta$ -,  $\gamma$ -,  $\delta$ - and  $\epsilon$ - type made of [MnO<sub>6</sub>] octahedral with different connectivity. Among these crystallographic forms,  $\alpha$ - (tunnel type structure) and  $\delta$ -MnO<sub>2</sub> (layered type structure) are great interest and these materials have been reported for supercapacitor, sensor and battery applications [18–21]. One of the disadvantages of the manganese dioxide is poor conducting nature. The poor conducting nature of manganese dioxide can be further improved by the introduction of organic conducting matrix such as conducting polymers [21, 22]. Extensive research reports have been published in the literature to improve the conductance of manganese dioxide using conducting polymers [20–22]. The nanostructured PANI/MnO<sub>2</sub> composites exhibit enhanced performance compared to pure manganese oxide [22]. PANI/MnO<sub>2</sub> nanocomposites have been received greater interest due to low cost and environmentally friendly nature.

To the best of the author's knowledge, AC conductivity studies on PANI/MnO<sub>2</sub> nanocomposites are rarely reported. There are many methods available in the literature for the preparation of PANI/MnO<sub>2</sub> nanocomposites including chemical and electrochemical synthetic routes. In the present study, an attempt has been made to prepare PANI/MnO<sub>2</sub> nanocomposites by using simple reduction–oxidation reaction at ambient conditions. Herein, the simultaneous oxidation of aniline to polyaniline and reduction of KMnO<sub>4</sub> to MnO<sub>2</sub> (VII to IV) and as a result of this redox reaction, MnO<sub>2</sub> nanoparticles embedded in polyaniline matrix thus form PANI/MnO<sub>2</sub> nanocomposites [22]. Thus, polyaniline acts as conducting support to the poor conducting MnO<sub>2</sub> and further increases the performance. The resultant nanocomposite has been subjected to AC impedance spectroscopy to test the material conductivity behaviour at room temperature.

## 2 Experimental

### 2.1 Preparation of polyaniline/manganese dioxide nanostructures

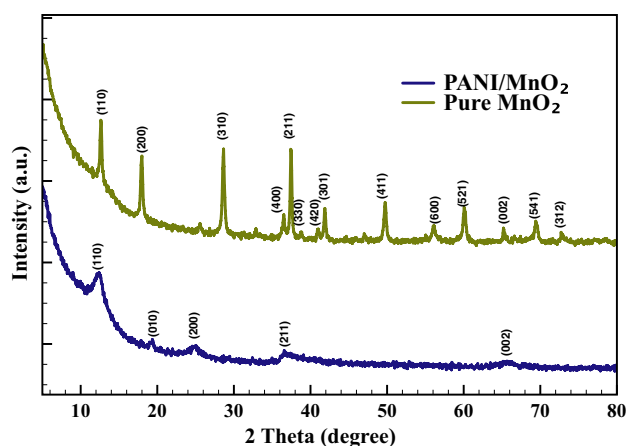
All chemicals used were of analytical grade and they were used as received. In a typical preparation of polyaniline/manganese dioxide (PANI/MnO<sub>2</sub>) nanocomposite, 3.16 g of KMnO<sub>4</sub> was dissolved in 250 mL of distilled water [7]. To the above pink-coloured solution, 1 mL of aniline monomer was added upon stirring for about 30 min. The pink-coloured solution disappears and a blackish-brown coloured precipitate was formed indicates the reduction of Mn (VII) to Mn (IV). At the same time, aniline gets oxidized to polyaniline, the obtained precipitate was washed with large amount distilled water for several times followed by ethanol. Finally, filtered and dried at 100 °C overnight. For the preparation of pure MnO<sub>2</sub> nanostructures, the as-prepared PANI/MnO<sub>2</sub> nanocomposite was heated at 600 °C for 3 h under air atmosphere. The prepared samples were used for further physico-chemical characterization and electrical properties studies.

### 2.2 Characterization methods

Powder X-ray diffraction (XRD) patterns of the precursor and the final products were recorded using Bruker D8 advance diffractometer with monochromatized Cu K $\alpha$  ( $\lambda = 1.5418$  Å) incident radiation as the source. IR absorption spectrum was recorded in a FT-IR spectrum 1000 PERKIN ELMER spectrometer on dried sample using KBr pellet. Brunauer–Emmett–Teller (BET) surface area and pore size distribution of the samples were measured using Micromeritics surface area analyzer model ASAP 2020. The microscopy studies were examined by using scanning electron microscopy (SEM, FEI Co. model Sirion). AC conductivity and dielectric properties of the samples were carried out using Agilent 4294A analyser.

### 2.3 Preparation of electrodes and AC conductivity measurements

Room temperature AC conductivity properties of samples were examined using Agilent 4294A precision impedance analyser in the frequency range 10 Hz to 100 MHz. The voltages across the known range resistor and the DUT are measured and the impedance of the latter can be estimated. A variable frequency signal source section generates the test signals applied to the material being investigated. For impedance measurements, the samples were prepared in circular geometry with 10 mm diameter and 1 mm thickness and were coated with the silver on both sides. For



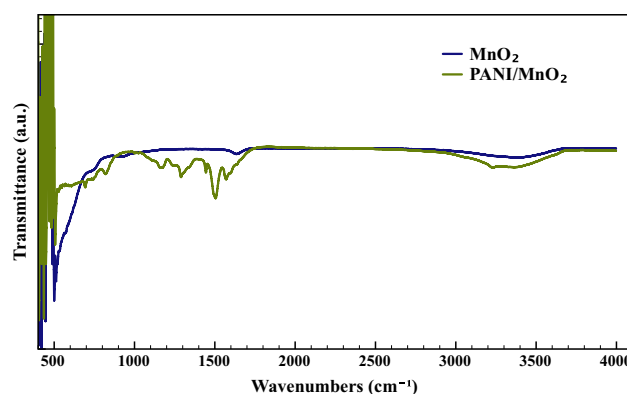
**Fig. 1** XRD of PANI/MnO<sub>2</sub> nanocomposite and pure MnO<sub>2</sub> samples

measurements, the copper wire contacts were drawn from the silver-coated surface using fine enamelled copper wire of grade 38 AWG (0.1 mm diameter) and conductive silver paint.

### 3 Results and discussion

The X-ray diffraction patterns (XRD) of the pure MnO<sub>2</sub> nanostructures and PANI/MnO<sub>2</sub> nanocomposite are shown in Fig. 1. The diffraction patterns of PANI/MnO<sub>2</sub> nanocomposite exhibit three broad peaks at 12.6°, 37.5° and 65.1° (2 $\theta$ ) corresponding to (110), (211) and (002) reflection planes of MnO<sub>2</sub>, respectively. The two broad diffraction peaks at 19.34° and 24.9° correspond to (010) and (200) reflection planes of PANI in PANI/MnO<sub>2</sub> nanocomposite revealing the poor crystalline nature of the sample [18, 20, 22]. The series of diffraction peaks for pure MnO<sub>2</sub> at 12.7°, 18°, 37.4°, 42°, 49.8°, 56°, 60.2°, 65.3° and 69.6° degree correspond to (110), (200), (310), (211), (301), (411), (600), (521), (002) and (541) reflection planes, respectively, indexing the tetragonal structure (space group I4/m) of  $\alpha$ -MnO<sub>2</sub> phase with lattice constants of  $a = 9.8172$  and  $c = 2.8582$  which are in good agreement with the reported values referring to JCPDS card number 44-0141 [18, 19, 22]. The diffraction peaks are sharp and intense, indicating that upon heating the PANI/MnO<sub>2</sub> nanocomposite sample at 600 °C under air atmosphere, the amorphous phase is converted to crystalline phase. Moreover, the PANI present in composite was removed by heating at 600 °C and hence pure form of MnO<sub>2</sub> was obtained at the end. The obtained samples were used for the further characterisation.

To know intermolecular interactions, the prepared samples were subjected to Fourier transform infrared spectroscopic (FT-IR) technique. The prepared PANI/MnO<sub>2</sub> nanocomposite and pure MnO<sub>2</sub> samples were recorded in the

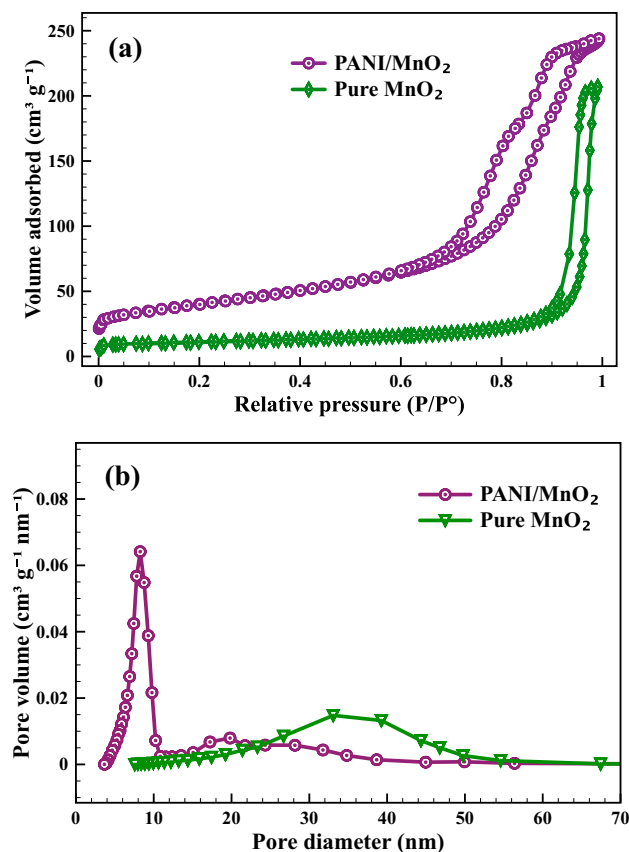


**Fig. 2** FT-IR spectra of PANI/MnO<sub>2</sub> nanocomposite and pure MnO<sub>2</sub> samples

range 4000 to 450 cm<sup>-1</sup> and are shown in Fig. 2. The bands at 1569, 1506, 1290 and 820 cm<sup>-1</sup> of PANI are assigned to the C=C stretching vibrations of quinoid and benzenoid rings, the C–N stretching vibration and C–H out of plane bending vibrations, respectively [22]. The broad absorption band at 3380 cm<sup>-1</sup> in the spectra of both materials can be assigned to the O–H stretching vibration. The absorption band at 500 cm<sup>-1</sup> is ascribed to the contribution of the Mn–O vibrations that confirms the formation of MnO<sub>2</sub> [21, 22]. The PANI/MnO<sub>2</sub> nanocomposite spectrum shows all the absorption bands due to MnO<sub>2</sub> (500 cm<sup>-1</sup>) and absorption bands due to PANI (1569, 1506, 1290 and 820 cm<sup>-1</sup>) that confirms the existence of PANI in PANI/MnO<sub>2</sub> nanocomposite.

To evaluate the surface area and porous nature of the PANI/MnO<sub>2</sub> nanocomposite and MnO<sub>2</sub> nanostructures, N<sub>2</sub> adsorption–desorption isotherms were recorded (Fig. 3a). The specific surface area was calculated using the Brunauer–Emmett–Teller (BET) method from adsorption branch of isotherm in  $p/p^0$  range of 0.1–0.2. The isotherms of all samples resemble type IV isotherm with hysteresis in the  $p/p^0$  range of 0.5–0.99 [19, 20]. The adsorption–desorption loop indicates the presence of mesopores in the samples. Barrett–Joyner–Halenda (BJH) curves from desorption branch of isotherms are presented in Fig. 3b. The as-prepared PANI/MnO<sub>2</sub> nanocomposite exhibits pores with a pore size distribution of 9.3 nm, whereas pure MnO<sub>2</sub> nanostructures exhibit large pore of 35 nm. The BET surface area is 203 m<sup>2</sup> g<sup>-1</sup> highlighting the overall formation of PANI/MnO<sub>2</sub> nanocomposite. For the pure MnO<sub>2</sub> nanostructures sample prepared at 600 °C, the surface area was found to be low (18 m<sup>2</sup> g<sup>-1</sup>) due to increased crystallinity.

Surface morphology notably influences the properties of the materials. The scanning electron micrographs (SEM) of PANI/MnO<sub>2</sub> nanocomposite and pure MnO<sub>2</sub> nanostructures are shown in Fig. 4. PANI/MnO<sub>2</sub> nanocomposite (Fig. 4a) is spongy in nature without clear boundary of particles. This is due to the amorphous nature of the material, which

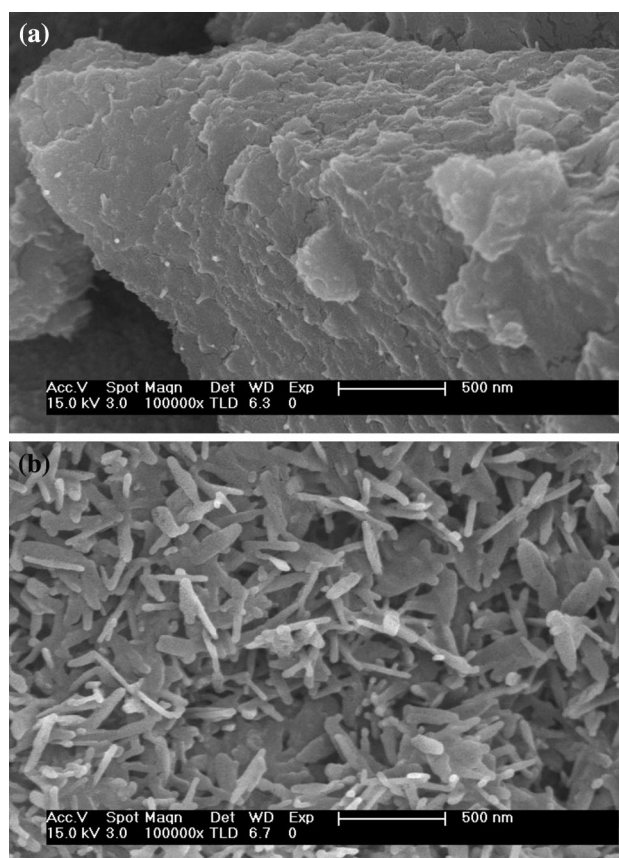


**Fig. 3** N<sub>2</sub> adsorption–desorption, **a** BJH curves, **b** of PANI/MnO<sub>2</sub> nanocomposite and pure MnO<sub>2</sub> samples

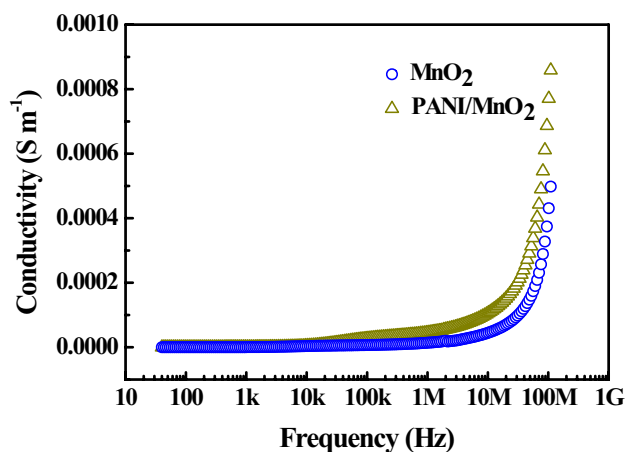
is reflected in the XRD pattern (Fig. 1). The morphology image of PANI/MnO<sub>2</sub> nanocomposite clearly reflects that the whole MnO<sub>2</sub> is covered with PANI. Upon heating at 600 °C, the morphology of PANI/MnO<sub>2</sub> composite interestingly changes into clear crystalline MnO<sub>2</sub> nanoplatelets. The morphology changes from particles to platelet nanostructures as observed in Fig. 4b.

#### 4 Conductivity studies

Figure 5 shows the variation of AC conductivity as a function of frequency for pure MnO<sub>2</sub> nanostructures and PANI/MnO<sub>2</sub> nanocomposite. At higher frequencies, more than 80 MHz, the conductivity increases because of the contribution of polarons which are moving along shorter distances in the polymer chain. The increasing AC conductivity at higher frequencies is attributed to charge motion in the amorphous regions and this supports the presence of isolated polarons and bipolarons in this region [9–11]. It is observed from the figure that the conductivity of the PANI/MnO<sub>2</sub> nanocomposite and pure MnO<sub>2</sub> nanostructures remains constant up to 10 kHz and thereafter, the conductivity of PANI/MnO<sub>2</sub> nanocomposite increases



**Fig. 4** Scanning electron micrographs of PANI/MnO<sub>2</sub> nanocomposite **(a)** and pure MnO<sub>2</sub> **(b)** samples



**Fig. 5** AC conductivity measurement of PANI/MnO<sub>2</sub> nanocomposite and pure MnO<sub>2</sub> nanostructures

steeply, which is the characteristic feature of disordered materials. At high frequencies, AC conductivity increases due to the contribution of polarons, which are moving along smaller and smaller distances in a polymer chain [4]. Increase of AC conductivity at higher frequencies is due to the charge motion

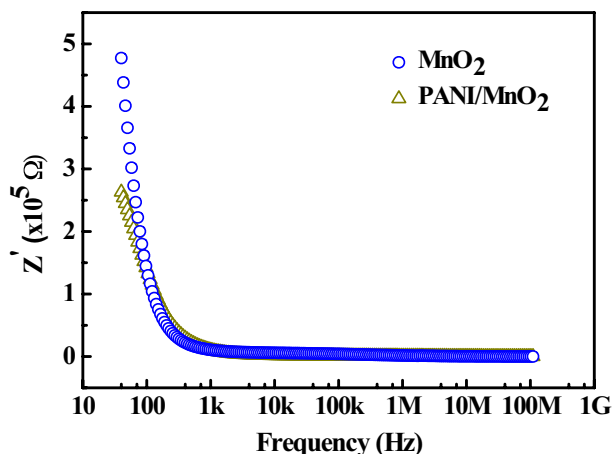


in the amorphous region and this supports the presence of isolated polarons in this region. The high conductivity of about  $0.0009 \text{ S cm}^{-1}$  is for the sample PANI/MnO<sub>2</sub> nanocomposite whereas conductivity  $0.0005 \text{ S cm}^{-1}$  is observed for the pure MnO<sub>2</sub> nanostructures.

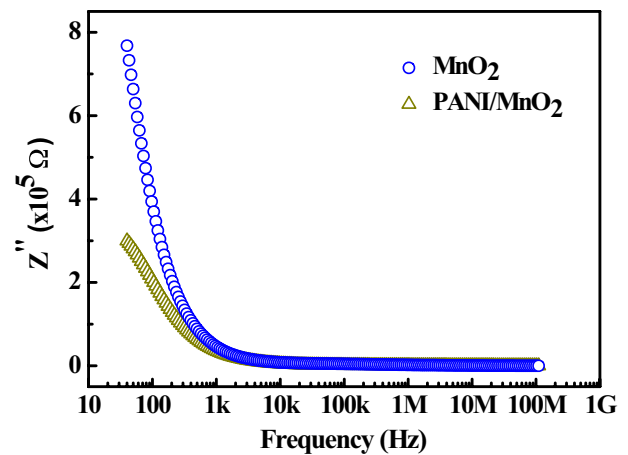
Figure 6 shows the variation of real part of impedance ( $Z'$ ) as a function of frequency varied from 50 Hz to 100 MHz at room temperature. The pattern shows the variation of  $Z'$  as a function of frequency in the low-frequency region followed by the saturation in the high-frequency region. The decrease in magnitude of  $Z'$  is with increase in frequency for both pure MnO<sub>2</sub> nanostructures and PANI/MnO<sub>2</sub>. This suggests the presence of polarization behaviour in the material, such as electronic, dipolar and orientation polarization. It can be observed from the plot that conductivity of PANI/MnO<sub>2</sub> nano composite is more than that of pure MnO<sub>2</sub> nanostructures. The  $Z'$  values merge at high frequency due to the release of space charge as a result of reduction in barrier properties of the material and are responsible factor for the enhancement of AC conductivity of the PANI/MnO<sub>2</sub> nanocomposite material.

Figure 7 presents the variation of imaginary part of impedance ( $Z''$ ) as a function of frequency. The imaginary part of impedance ( $Z''$ ) decreased with increase in frequency in both the cases. The higher electrical resistance of pure MnO<sub>2</sub> nanostructures may be due to the absence of the PANI polymer chain. On the other hand, the electrical resistance dramatically decreased in the case of PANI/MnO<sub>2</sub> nanocomposite which may be due to the presence of conducting PANI polymeric chains [16]. In PANI/MnO<sub>2</sub>, the PANI facilitating the charge carrier motion, decreases the resistance and increases conductivity.

The complex impedance analysis is another approach to predict electrical properties of the material and it is shown in Fig. 8. The resistive nature of the sample with semicircular



**Fig. 6** Real part of impedance vs frequency measurement of PANI/MnO<sub>2</sub> nanocomposite, pure MnO<sub>2</sub> nanostructures

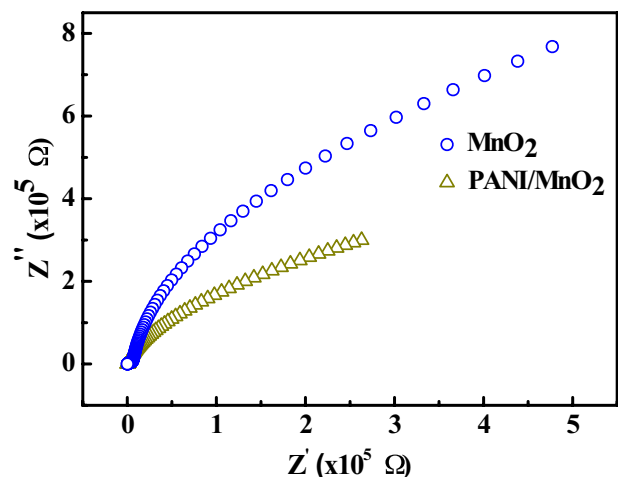


**Fig. 7** Imaginary part of impedance vs frequency measurement of PANI/MnO<sub>2</sub> nanocomposite and pure MnO<sub>2</sub> nanostructures

arcs was observed. The X-axis represents the real part, while y-axis shows the imaginary part of the Nyquist plot. From these plots, it is clearly seen that the contribution of PANI in PANI/MnO<sub>2</sub> nanocomposites exhibit more conductivity than the pure MnO<sub>2</sub> nanostructures. On the other hand, the pure MnO<sub>2</sub> nanostructures exhibit maximum resistance than that of the PANI/MnO<sub>2</sub> nanocomposites which indicates that in the presence of PANI the resistivity of MnO<sub>2</sub> decreased and conductivity increased [21, 22].

## 5 Conclusions

Porous PANI/MnO<sub>2</sub> nanocomposite was prepared under ambient conditions. It was found that the change in morphology, crystal structure of PANI/MnO<sub>2</sub> nanocomposite



**Fig. 8** Complex impedance spectra of PANI/MnO<sub>2</sub> nanocomposite and pure MnO<sub>2</sub> nanostructures

when heated at high temperature and it was converted to crystalline pure  $\alpha$ - $\text{MnO}_2$ . There was a notable change in the electrical properties for PANI/ $\text{MnO}_2$  nanocomposite, and pure  $\text{MnO}_2$  nanostructures were observed. The AC electrical conductivity of PANI/ $\text{MnO}_2$  nanocomposite is found to be more than the pure  $\text{MnO}_2$  and the conductivity increased as a function of increase in frequency. The high electrical conductivity of PANI/ $\text{MnO}_2$  nanocomposite is due to the conducting polymer support to the  $\text{MnO}_2$ . As the synthesis method is simple and cost effective, the synthesis method can be used to prepare PANI/ $\text{MnO}_2$  nanocomposite in large scale.

## References

1. S. Chen, G. Meng, B. Kong, B. Xiao, Z. Wang, Z. Jing, Y. Gao, G. Wu, H. Wang, Y. Cheng, *Chem. Eng. J.* **387**, 123662 (2020)
2. W. Wu, C. Yu, J. Chen, Q. Yang, *Int. J. Environ. Anal. Chem.* **100**, 324–332 (2019)
3. A. Feng, M. Ma, Z. Jia, M. Zhang, G. Wu, *RSC Adv.* **9**, 25932 (2019)
4. M.H. Naveen, N.G. Gurudatt, Y.-B. Shim, *Appl. Mater. Today* **9**, 419–433 (2017)
5. Z. Jia, B. Wang, A. Feng, J. Liu, M. Zhang, Z. Huang, G. Wu, *J. Alloys Compd.* **799**, 216–223 (2019)
6. H. Khan, K. Malook, M. Shah, *J. Mater. Sci.* **29**, 9090–9098 (2018)
7. B.K. Sharma, A.K. Gupta, N. Khare, S. Dhawan, H. Gupta, *Synth. Met.* **159**, 391–395 (2009)
8. A. Vijayamari, K. Sadayandi, S. Sagadevan, P. Singh, *J. Mater. Sci.* **28**, 2739–2746 (2017)
9. Q. Yu, C. Wang, X. Li, Z. Li, L. Wang, Q. Zhang, G. Wu, Z. Li, *Fuel* **239**, 1240–1245 (2019)
10. R.E. John, A. Chandran, M. Samuel, M. Thomas, K.C. George, *Physica E* **116**, 113720 (2020)
11. S. Palsaniya, H.B. Nemade, A.K. Dasmahapatra, *Carbon* **150**, 179–190 (2019)
12. H. Khan, K. Malook, M. Shah, *J. Mater. Sci.* **29**, 1990–1998 (2018)
13. S. Manjunath, A.K. Koppalkar, M.V.N. Ambika Prasad, *Ferroelectrics* **366**, 22–28 (2008)
14. S. Manjunath, A.K. Koppalkar, M.V.N. Ambika Prasad, *Ferroelectr. Lett.* **35**, 36–46 (2008)
15. G.D. Prasanna, H.S. Jayanna, A.R. Lamani, M.L. Dinesha, C.S. Naveen, G.J. Shankaramurthy, *Chin. Phys. Lett.* **28**, 117701 (2011)
16. B.P. Prasanna, D.N. Avadhani, H.B. Muralidhara, K. Chaitra, V.R. Thomas, M. Revanasiddappa, N. Kathyayini, *Bull. Mater. Sci.* **39**, 667–675 (2016)
17. S. Shivakumara, T.R. Penki, N. Munichandraiah, *Solid State Electrochem.* **18**, 1057–1066 (2014)
18. S. Devaraj, N. Munichandraiah, *J. Phys. Chem. C* **112**, 4406–4417 (2008)
19. P. Ragupathy, H.N. Vasan, N. Munichandraiah, *J. Electrochem. Soc.* **155**, A34–A40 (2008)
20. S. Shivakumara, N. Munichandraiah, *J. Alloys Compd.* **787**, 1044–1050 (2019)
21. V.C. Lokhande, A.C. Lokhande, C.D. Lokhande, J.H. Kim, T. Ji, *J. Alloys Compd.* **682**, 381–402 (2016)
22. M.M. Mezgebe, K. Xu, G. Wei, S. Guang, H. Xu, *J. Alloys Compd.* **794**, 634–644 (2019)

**Publisher's Note** Springer Nature remains neutral with regard to jurisdictional claims in published maps and institutional affiliations.



# A Comparison of Features for Multilingual Speaker Identification - A Review and Some Experimental Results

Pritam Limbaji Sale, Spoorti J Jainar, B.G. Nagaraja

**Abstract:** Countries like India, Canada, Malaysia, etc. are multilingual in nature. People in multilingual countries have habituated to use several languages. Due to the increased number of multilingual speaker identification system applications, the interest in the area has grown notably in recent years. The accuracy of speaker recognition system is severely degraded if training and testing speech languages are different. In speaker recognition area, researchers have made many attempts to tackle language mismatch issues. Choosing a suitable feature extraction method for obtaining appropriate information using speech signal is an essential task. This paper reports a concise experimental review of ten feature extraction techniques for the multilingual scenario. The monolingual, crosslingual and multilingual speaker identification studies are carried out using randomly selected 50 speakers from the IITG multi-variability speaker recognition (IITG-MV) database. Comparative results indicate that subband centroid frequency coefficients (SCFC), linear frequency cepstral coefficients (LFCC) and multitaper Mel frequency cepstral coefficients (MFCC) features are considerably more useful in all the speaker identification. Further, concluding any relation to speaker identification performance in the language mismatch environment is identification as the distribution of speakers in different languages is non-uniform.

**Keywords:** Speaker identification, monolingual, cross lingual, multilingual, LPCC, MFCC, IMFCC, LFCC, RFCC, multitaper MFCC, SCFC, SSFC, GMM-UBM.

## I. INTRODUCTION

Speaker recognition is one among the important problems in speech signal processing. Speaker recognition system, carry out either speaker verification or speaker identification tasks [1], [2]. The speaker identification task results in the best match for an unknown voice from the database, whereas speaker verification task is either to accept/reject a claimed identity. Based on the languages used for the study, speaker recognition can be done in monolingual, crosslingual and multilingual modes [3]. In the monolingual mode, same language is considered for both training and testing. In crosslingual speaker recognition, training and testing are carried out with different languages. In multilingual mode, speaker-dependent models are trained using single language and tested for several languages [3], [4]. Monolingual and

crosslingual speaker recognitions are a subset of multilingual speaker recognition.

In [5], speaker discriminative power of Mel frequency cepstral coefficients (MFCC), anti-MFCC, and linear frequency cepstral coefficients (LFCC) was examined using telephone speech data. It was demonstrated that LFCCs perform considerably better than MFCCs for speaker recognition systems using the nasal and non-nasal consonant broad phonetic regions. MFCC performs better in the lower frequency region, but in the higher frequency regions, it does not capture speaker characteristics effectively and hence its performance degrades [6].

A new speaker recognition system was introduced based on MFCC and back-propagation neural networks [6]. It was observed from the results that proposed system was feasible and fairly successful. A robust speaker recognition system based on multi-stream features (spectral centroid frequency and power normalized cepstral coefficients) was proposed in [7]. Three types of fusion technique were introduced and compared. Results proved the effectiveness of proposed multi-stream features for speaker recognition system. In [8], a new type of feature was proposed based on gammatone frequency cepstral coefficients (GFCC) by introducing technologies like multitaper estimation, smooth amplitude envelope, mean subtraction, variance normalization and autoregressive moving average filter. The experimental results using TIMIT database showed that under different noise and different signal-to-noise ratio, the proposed GFCC performs better than the MFCC.

For multilingual countries, the impact of different languages on speaker recognition system needs to be studied. Non-availability of the standard multilingual database for Indian languages is the major difficulty for carrying out speaker recognition research in multilingual/language mismatched scenario. In this direction, a study on the effect of language mismatch on speaker identification and speaker verification task was carried out in [9]. The speech data (100 speakers) was recorded in three languages, viz., the local language of Arunachal Pradesh, Hindi, and Indian English. It was studied that the impact of language variability in intra-group and inter-group were nearly same. A study in [10], focused on the speaker recognition performance under language mismatch environment.

Further, the consequence of language mismatch was also described for a single language and multiple languages together.

Manuscript published on 30 December 2019.

\*Correspondence Author(s)

Pritam Limbaji Sale, Research Scholar, VTU, Belagavi.

Spoorti J. Jainar, Research Scholar, VTU, Belagavi.

B.G. Nagaraja, Professor & Head, Dept. of E&CE, JIT, Davangere.

© The Authors. Published by Blue Eyes Intelligence Engineering and Sciences Publication (BEIESP). This is an open access article under the CC-BY-NC-ND license <http://creativecommons.org/licenses/by-nc-nd/4.0/>

The experiments were demonstrated using 13 Indian languages. It was observed that the impact of language mismatch was less significant in speaker identification task compared to speaker verification. Literature reveals that the most of the investigations are restricted to a single language environment. It is essential to know which type of feature is more beneficial for a multilingual speaker recognition. In this work, we provide a brief overview of the feature extraction techniques for speaker identification systems. Following this overview, we will experimentally compare 10 front-end speech features for multilingual speaker identification using Gaussian mixture model with universal background model (GMM-UBM).

In the rest of this paper, Section 2 describes the different front-end feature extraction techniques for speaker recognition. A database used for the study and the experimental setups are provided in Section 3. Section 4 discusses the monolingual, crosslingual and multilingual speaker identification results. The paper concludes in Section 5.

## II. FEATURE EXTRACTION TECHNIQUES

### 2.1 Linear prediction cepstral coefficients (LPCC)

The cepstral features obtained from either filter-bank approach or a linear prediction analysis are relatively treated as state-of-the-art front-end features for speaker identification. In linear prediction (LP) speech analysis, every sample is approximated as a linear weighted sum of the past speech samples. In LPCC, the power spectrum is computed from the smoothed auto-regressive power spectral estimate instead of the periodogram estimate technique. The order of the linear prediction analysis denotes the number of peaks in an all-pole model. The predictor coefficients  $a_k$  are transformed into robust cepstral coefficients. The relationship between predictor coefficients,  $a_k$  and cepstral coefficients,  $C_n$  is characterized by the following recursive relation [11] given as:

$$C_0 = \ln G \quad (1)$$

$$C_n = a_n + \sum_{k=1}^{n-1} \left(\frac{k}{n}\right) c_k a_{n-k}; \quad 1 \leq n \leq p \quad (2)$$

Where  $G$  is the gain factor in the LP model,  $n$  is an index and  $p$  is the LP order.

### 2.2 MFCC

The MFCC feature extraction method consists of windowing (Hamming) the signal to minimize the spectral distortion, applying the discrete Fourier transform (DFT) to obtain the magnitude frequency response. To compute the log energy, frame magnitude spectra is multiplied with the set of Mel-scale triangular filters. Finally, inverse discrete cosine transform of filter bank coefficients is calculated to get the cepstral coefficients. The mapping of perceived frequency ( $f_{mel}$  in mels) with respect to the physical frequency ( $f$  in Hz) scale is given by [12]:

$$f_{mel} = 2595 \log_{10} \left(1 + \frac{f}{700}\right) \quad (3)$$

### 2.3 Sine-weighted cepstrum estimator (SWCE) multitaper MFCC

From a statistical perspective, the MFCC feature extraction using windowed DFT is not favorable due to large variance of the spectrum approximation [13]. Efforts

have been made to improve the MFCC robustness. A study in [13]-[15] described the multitaper MFCC feature extraction technique for speaker recognition. In order to lower the variance of the MFCC estimator, multiple window (multitaper) spectrum estimates was used. In multitapering technique, analysis frame is passed through different window functions and the final spectrum estimate was computed using a weighted mean of the individual sub-spectra. Every individual spectral contribute to a final spectral envelope for each component.

Thomson multitaper [16], multipeak multitaper [17] and SWCE multitaper [18] are the popular multitapering techniques. In [13], it was described that the choice of the number of tapers  $K$  was more important than the choice of multitaper type. Further, the best results were obtained for  $3 \leq K \leq 8$ . Our previous results showed that the SWCE multitaper MFCC ( $K = 6$ ) can be used to improve the speaker identification performance for language mismatched scenario [4]. In this work, SWCE multitapers are used with  $K = 6$  windows. The weights employed in the SWCE multitaper method are described by the following closed-form expression [13]:

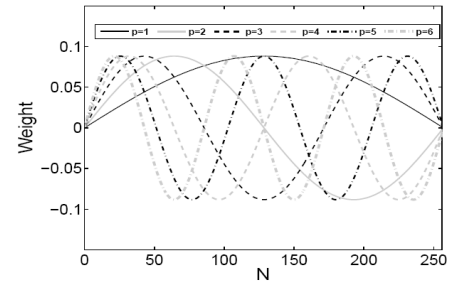


Figure 1: SWCE method for six sine tapers,  $p$  is the taper number and  $N = 256$  window length.

$$\lambda(p) = \frac{\cos\left(\frac{2\pi(p-1)}{K/2}\right) + 1}{\sum_{p=1}^K \left(\cos\left(\frac{2\pi(p-1)}{K/2}\right) + 1\right)} : p = 1 \dots \dots \dots K \quad (4)$$

The Figure 1 shows the sine tapers of the SWCE multitaper method for  $K = 6$ .

### 2.4 $\tau$ th - order MFCC

A novel type of windowing technique to extract MFCC features for speaker recognition task was presented in [19]. The new window technique uses differentiation in the frequency domain property of discrete time Fourier transforms. Let  $\omega(n)$  be the Hamming window function, the proposed window function ( $\hat{\omega}(n)$ ) for  $\tau^{\text{th}}$  - order is obtained as:

$$\hat{\omega}(n) = n^\tau \omega(n) \quad (5)$$

Then windowed speech frame is described as:

$$\hat{x}(n) = \hat{\omega}(n)x(n) \quad (6)$$

where  $x(n)$  is a raw speech frame. The Hamming window can be analyzed as zero order window ( $\tau = 0$ ) of proposed family. Figure 2 shows the frequency and time domain representation of  $\hat{\omega}(n)$  window function for 160 samples. In this work,  $\tau^{\text{th}}$  - order MFCC are computed for  $\tau = 2$ .

## 2.5 Inverted Mel frequency cepstral coefficients (IMFCC)

In [12], IMFCC features were proposed for speaker identification. IMFCC features efficiently capture high-frequency formants, which are neglected by the conventional MFCC. In IMFCC, the complete filter bank structure is inverted so that

the upper-frequency width averages by more precisely located filters and in the lower frequency range lesser number of widely located filters are utilized. Inverted Mel scale ( $\hat{f}_{mel}$ ) is defined as [12]:

$$\hat{f}_{mel} = 2195.2860 - 2595 \log_{10} \left( 1 + \frac{4031.25 - f}{700} \right) \quad (7)$$

## 2.6 LFCC

Based on the theory of human speech production, several speakers specific information connected with the vocal tract structure, mainly, length of the vocal tract are distributed more in the higher frequency region. Hence, linear frequency scale may offer various benefits in speech/speaker recognition in comparison with the conventional Mel frequency scale. In this direction, a study in [20] compared the LFCC and MFCC features using the NIST speaker recognition evaluation (SRE) 2010 extended-core task database. Results using SRE10 showed that the LFCC constantly perform better than the MFCC due to its higher recognition for the female subjects. The feature extraction methodology of LFCC is almost similar to MFCC. The only difference is that the Mel-scale filters are replaced by linear space triangular filter bank [21].

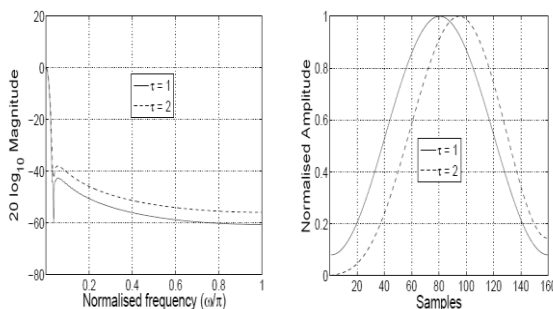


Figure 2: Frequency and time domain representation of  $\hat{\omega}(n)$  window function for 160 samples.

## 2.7 Rectangular filter-bank cepstral coefficient (RFCC)

RFCC feature was originally proposed for robust automatic speech recognition in noisy/Lombard speech conditions [22]. In [22], RFCC features were used as one of the front end features for the 2012 NIST SRE. It was studied that the overall recognition performance was very successful. The RFCC feature extraction technique is inspired by perceptual linear prediction cepstral features [22]. In RFCC extraction, integration is carried out using a rectangular window and the filters spaced in linear scale [21].

## 2.8 All-pole group delay function (APGDF)

The significance of phase-based features for speaker verification was investigated in [23]. In that work, group delay function was used to derive the speaker-specific features from the phase spectrum. It was mentioned that the

group delay features using all-pole models can be utilized to compute phase information for speaker verification task. Speaker verification results using NIST 2010 SRE dataset showed that the group delay techniques are useful under the high vocal effort. Further, group delay features were comparable to usual magnitude spectrum-based MFCC features. The group delay function  $\tau(x)$  for the speech signal  $s(n)$  can be obtained as derived in [23], [24]:

$$\tau(w) = \left( \frac{S_R(w)X_R(w) + S_I(w)X_I(w)}{|S(w)|^2} \right) \quad (8)$$

where  $S(w)$  is a Fourier transform of  $S(n)$ ,  $X(w)$  is a Fourier transform of  $x(n)$ ,  $x(n) = ns(n)$ ,  $|S(w)|$  is the magnitude spectrum,  $S_R(w)$  is a real part of  $S(w)$ ,  $S_I(w)$  is an imaginary part of  $S(w)$ ,  $X_R(w)$  is a real part of  $X(w)$  and  $X_I(w)$  is an imaginary part of  $X(w)$ .

## 2.9 Sub band centroid frequency coefficients (SCFC)

Attempts have been made to obtain the alternative to the cepstral features that should provide information for speech/speaker recognition. In this direction, Paliwal [25], investigated a few formant type features for speech recognition. In [26], SCF was used for text-independent speaker authentication as a complement to cepstral based features. It was concluded that spectral subband centroids (SSC) perform somewhat better than MFCC features and also combining SSC with MFCC features enhance the performance of the authentication system in both clean and noisy environments. Further, SCFC includes complementary knowledge related to subbands which are not present in cepstral features.

Let  $S[n]$  represent a speech frame, for  $n = 0, 1, \dots, N - 1$ , and  $S[f]$  correspond to the speech frame spectrum. Further,  $S[f]$  is split into  $K$  number of subbands and each subband is described as upper frequency edge ( $u_k$ ) and lower frequency edge ( $l_k$ ).  $W_k[f]$  Denotes the frequency-sampled response of the filter. SCF defined as the weighted average frequency for a given subband [27]. The  $k^{\text{th}}$  sub band spectral centroid frequency  $F_k$  described as [25]-[27]:

$$F_k = \frac{\sum_{f=l_k}^{u_k} f |S[f] W_k[f]|}{\sum_{f=l_k}^{u_k} |S[f] W_k[f]|} \quad (9)$$

## 2.10 Sub band spectral flux coefficients (SSFC)

In [28], spectral flux based features were used for speech and music discrimination task. Spectral flux determines the frame-to-frame variation of speech in the power spectrum [28]. It is computed between normalized power spectrum of consecutive frames using the Euclidean distance measure [21].

Recently, a new feature called SSFC features are used for synthetic speech detection. It was mentioned that the SSFC features contain information connected to spectral flux in different subbands.

Experimental results showed that the SSFC features were useful compared to other spectral features considered for the study. The subband spectral flux (SSF) of the  $i^{\text{th}}$  subband of the  $m^{\text{th}}$  speech frame is [21]:

$$SSF_m^i = \sum_{k=1}^{N/2+1} \|\bar{S}_m(k) - \bar{S}_{m-1}(k)\|^2 W_i(k) \quad (10)$$



where  $W_i(k)$  denotes the spectral window function used to find the frequency response of  $i^{\text{th}}$  subband,  $\bar{S}_m(k)$  is the magnitude of  $k^{\text{th}}$  frequency element of the normalized power spectrum of  $m^{\text{th}}$  frame and  $N$  is the number DFT bins.

Then SSFCs are obtained by applying logarithmic compression and DCT on SSFs.

### III. DATABASE AND EXPERIMENTAL SETUP

All the experiments are carried out using the IITG multi-variability speaker recognition (IITG-MV) database. The speech data was collected using different speaking styles, sensors, environments and languages from 200 speakers [29].

The recording was carried out in the wide varieties of acoustic environments (office, corridors, hostel rooms, laboratories, etc.). The speech data are collected in multi-sensor (five different sensors), multilingual (any of the favorite Indian language and Indian English) and multi-style (reading and conversational styles) conditions. The languages include Indian English, Hindi, Tamil, Kannada, Oriya, Malayalam, Assami and so on [30]. The speech signal was sampled at 8000 Hz and 16 bits depth. For this work, 50 speakers (20 female and 30 male) in the IITG-MV database is used. The UBM was built using diagonal covariance matrices. To build the gender independent UBM, first 18 speech files from enroll data of all the speakers (nearly two hours) of YOHO database [31] is used. The GMM model parameters (mean vector, mixture weights, and covariance matrix) were measured using the expectation maximization iterative algorithm. Maximum a posteriori technique is used to build the speaker-dependent models (GMM) by considering only the mean parameters of the UBM [29]. Speakers are modeled using GMMs with 16, 32, 64, and 128 mixtures.

The number of speakers (50) and speech duration (20 s) is kept constant throughout the experiment to perform a relative comparison of monolingual, crosslingual and multilingual speaker identification results using different feature extraction techniques.

For feature extraction, analysis window of 20 ms duration with 10 ms intervals was considered. The dimension of all the features is 13 (excluding 0<sup>th</sup> coefficient).

### IV. SPEAKER IDENTIFICATION RESULTS

In this section, the speaker identification results are discussed in different languages, viz., monolingual, crosslingual and multilingual.

The best results in each condition ( $P_i$ ) are highlighted.

Note: A/B indicates training in language 'A' and testing with language 'B'; 'multi-language' includes Kannada, Assami, Bengali, Telugu, Tamil, Malayalam and Oriya.

Table 1-3 give the performance of LPCC, MFCC, multitaper MFCC,  $\tau^{\text{th}}$ - order MFCC, IMFCC, LFCC, RFCC, APGDF, SCFC and SSFC for monolingual, crosslingual and multilingual speaker identification.

Some of the observations from the speaker identification experiments are as follows:

**Table 1: The monolingual speaker identification performance using different features and GMM-UBM classifier.**

Training/ Testing	Features	Gaussian mixtures				$P_i$
		16	32	64	128	
E/E	LPCC	76	74	84	86	86
	MFCC	64	74	78	84	84
	multitaper MFCC	72	78	82	82	82
	$\tau^{\text{th}}$ - order MFCC	70	76	82	80	82
	IMFCC	60	64	64	74	74
	LFCC	66	70	76	84	84
	RFCC	62	70	72	78	78
	APGDF	68	68	78	76	78
	SCFC	72	84	86	86	86
	SSFC	64	68	76	78	78
H/H	LPCC	70	74	80	82	82
	MFCC	74	74	78	80	80
	multitaper MFCC	78	78	84	82	84
	$\tau^{\text{th}}$ - order MFCC	70	74	80	82	82
	IMFCC	62	68	68	76	76
	LFCC	76	80	78	84	84
	RFCC	66	70	78	80	80
	APGDF	64	72	78	76	78
	SCFC	72	78	82	82	82
	SSFC	70	76	80	76	80

- The results indicate that the recognition performance of 86% is achieved for LPCC and SCFC features when training and testing are done in English language (E/E).
- The multitaper MFCC and LFCC features give the highest performance of 84% when training and testing are done in Hindi language (H/H).
- The results indicate that the recognition performance of 80% is achieved for multitaper MFCC,  $\tau^{\text{th}}$ - order MFCC and SCFC features when training is done in English language and tested with Hindi language (E/H).
- The SCFC features give the highest performance of 78% speaker when training is done in Hindi and tested with the English language (H/E).
- The results show that the recognition performance of 82% is achieved for  $\tau^{\text{th}}$ - order MFCC, LFCC and SCFC features when the training is done in English and testing with multi language (E/multi).
- The LPCC features give the highest performance of 82% when training is done in Hindi and testing with multi language (H/multi).
- In the majority of the cases, monolingual speaker identification performs better as compared to crosslingual and multilingual scenario. These results clearly indicate that the effect of languages on speaker identification.
- The performance of multilingual based speaker identification system is better than that of the crosslingual, but poor compared to the monolingual system.
- The recognition performance significantly degraded in crosslingual may be due to the deviation in fluency and stressing of few words when the same person speaks different languages.
- Further, due to dissimilar prosodic and phonetic models of the languages [32].
- The SCFC performs better in the majority of the speaker identification experiments.

- The speaker recognition performance using LFCC and multitaper MFCC features was also found satisfactory as compared to other features.
- Concluding any relation for speaker identification performance in each language is difficult since the distribution of speakers in different languages is non-uniform [10].

**Table 2: The cross lingual speaker identification performance using different features and GMM-UBM classifier.**

Training/ Testing	Features	Gaussian mixtures				P <sub>i</sub>
		16	32	64	128	
E/H	LPCC	60	68	70	74	74
	MFCC	64	70	74	78	78
	multitaper MFCC	66	76	80	78	78
	$\tau^{\text{th}}$ - order MFCC	68	76	80	78	80
	IMFCC	60	64	70	68	70
	LFCC	64	70	70	76	76
	RFCC	62	70	72	78	78
	APGDF	60	66	70	76	76
	SCFC	70	78	80	78	80
	SSFC	58	64	72	74	74
H/E	LPCC	54	66	70	76	76
	MFCC	56	64	70	74	74
	multitaper MFCC	62	66	70	76	76
	$\tau^{\text{th}}$ - order MFCC	60	70	76	74	76
	IMFCC	62	64	70	68	70
	LFCC	64	68	74	76	76
	RFCC	58	76	74	70	74
	APGDF	62	64	70	68	70
	SCFC	66	70	78	74	78
	SSFC	60	68	74	72	74

## V. CONCLUSION AND FUTURE WORK

In this work, an extensive study with different feature extraction techniques for monolingual, crosslingual and multilingual speaker identification was performed. Results indicated that the SCFC, LFCC, and multitaper MFCC were useful. Future work shall include exploring the combination of features for speaker identification for language mismatch condition.

**Table 3: The multilingual speaker identification performance using different features and GMM-UBM classifier.**

Training/ Testing	Features	Gaussian mixtures				P <sub>i</sub>
		16	32	64	128	
E/Multi	LPCC	64	70	80	76	80
	MFCC	60	68	74	78	78
	multitaper MFCC	70	74	78	80	80
	$\tau^{\text{th}}$ - order MFCC	70	76	82	80	82
	IMFCC	64	68	74	76	76
	LFCC	64	70	80	82	82
	RFCC	68	74	80	80	80
	APGDF	66	66	74	76	76
	SCFC	68	74	80	82	82
H/Multi	LPCC	70	80	82	80	82
	MFCC	66	70	78	76	78
	multitaper MFCC	64	66	76	78	78
	$\tau^{\text{th}}$ - order MFCC	64	70	76	80	80
	IMFCC	60	64	70	74	74
	LFCC	70	70	78	80	80
	RFCC	58	68	74	70	74
	APGDF	62	64	70	72	72
	SCFC	64	72	80	76	80
	SSFC	58	66	78	78	78

## REFERENCES

1. J. P. Campbell, Speaker recognition: A tutorial, Proc. IEEE, vol. 85, no. 9, pp. 1437-1462, 1997.
2. T. Kinnunen and H. Li, An Overview of text-independent speaker recognition?: From features to super vectors, Speech Commun., vol. 1, no. 1, pp. 12-40, 2009.
3. P. H. Arjun, Speaker recognition in Indian languages: A feature based approach, Ph.D. dissertation, Indian Institute of Technology Kharagpur, Dept. of Electrical Engg., Kharagpur, India, Jul. 2005.
4. B. G. Nagaraja, Multilingual speaker identification, Ph.D. dissertation, Visvesvaraya Technological University, Belagavi, India, Oct. 2014.
5. H. Lei and E. Lopez, Mel, linear, and antime frequency cepstral coefficients in broad phonetic regions for telephone speaker recognition, Interspeech, pp. 2323-2326, 2009.
6. Y. Wang and B. Lawlor, Speaker recognition based on MFCC and BP neural networks, 28th Irish Signals Syst. Conf., pp. 1-4, 2017.
7. N. Wang and L. Wang, Robust speaker recognition based on multi-stream features, IEEE International Conference on Consumer Electronics-China (ICCE-China), pp. 1-4, 2016.
8. X. Shi, H. Yang, and P. Zhou, Robust speaker recognition based on improved GFCC, 2nd IEEE International Conference on Computer and Communications, no. 4, pp. 1927-1931, 2016.
9. U. Bhattacharjee and K. Sarmah, A multilingual speech database for speaker recognition, IEEE Int. Conf. Signal Process. Comput. Control. ISPPCC 2012, pp. 1-5, 2012.
10. S. Sarkar, K. S. Rao, D. Nandi, and S. B. S. Kumar, Multilingual speaker recognition on Indian languages, Proc. Annu. IEEE India Conf. INDICON 2013, pp. 1-5, 2013.
11. H. S. Jayanna, Limited data speaker recognition Ph.D. dissertation, Indian Institute of Technology Guwahati, Dept. of of Electronics & Communication Engg., Mar. 2009.
12. S. Chakroborty, A. Roy, and G. Saha, Improved closed set text-independent speaker identification by combining MFCC with evidence from flipped filter banks, Int. J. Signal Process., vol. 4, no. 2, pp. 114-121, 2007.
13. T. Kinnunen, R. Saeidi, F. Sedlak, K.A. Lee, J. Sandberg, M. Hansson-Sandsten and H. Li, Low-variance multitaper MFCC features: A case study in robust speaker verification, IEEE Trans. Audio, Speech Lang. Process., vol. 20, no. 7, pp. 1990-2001, 2012.
14. M. J. Alam, T. Kinnunen, P. Kenny, P. Ouellet, and D. O'Shaughnessy, Multitaper MFCC and PLP features for speaker verification using i-vectors, Speech Commun., vol. 55, no. 2, pp. 237-251, 2013.
15. T. Kinnunen, R. Saeidi, J. Sandberg, and M. Hansson-sandsten, What else is new than the Hamming window? Robust MFCCs for speaker recognition via multitapering, Proc. Interspeech, vol. 20, no. 7, pp. 2734-2737, 2010.
16. D. J. Thomson, Spectrum estimation and harmonic analysis, Proc. IEEE, vol. 70, no. 9, pp. 1055-1096, 1982.
17. M. Hansson and G. Salomonsson, A multiple window method for estimation of peaked spectra, IEEE Trans. Signal Process., vol. 45, no. 3, pp. 778-781, 1997.
18. K. S. Riedel and A. Sidorenko, Minimum bias multiple taper spectral estimation, IEEE Trans. Signal Process., vol. 43, no. 1, pp. 188-195, 1995.
19. Md. Sahidullah and G. Saha, A novel windowing technique for efficient computation of MFCC for speaker recognition, IEEE signal processing letters, vol. 20, no. 2, pp. 149-152, 2013.
20. X. Zhou, D. Garcia-Romero, R. Duraiswami, C. Espy-Wilson, and S. Shamma, Linear versus mel frequency cepstral coefficients for speaker recognition, Proc. IEEE Work. Autom. Speech Recognit. Understanding, ASRU 2011, pp. 559-564, 2011.
21. Md. Sahidullah, TomiKinnunen, and CemalHanili, A comparison of features for synthetic speech detection, Proc. Interspeech, pp. 2087-2091, 2015.
22. T. Hasan, S. O. Sadjadi, G. Liu, N. Shokouhi, H. Boril, and J. H. L. Hansen, CRSS systems for 2012 NIST speaker recognition evaluation, Proc. ICASSP, IEEE Int. Conf. Acoust. Speech Signal Process., pp. 6783-6787, 2013.
23. P. Rajan, T. Kinnunen, C. Hanilci, J. Pohjalainen, and P. Alku, Using group delay functions from all-pole models for speaker recognition, Proc. Annu. Conf. Int. Speech Commun. Assoc. INTERSPEECH, pp. 2489-2493, 2013.

24. T. Thiruvaran, E. Ambikairajah, and J. Epps, Group delay features for speaker recognition, Proc. 6th Int. Conf. Information, Commun. Signal Process. ICICS, vol. 2, no. 2, pp. 1-5, 2007.
25. K. KuldipPaliwal, Spectral subband centroid features for speech recognition, Proc. IEEE International Conference on Acoustics, Speech and Signal Processing, vol. 2, pp. 617-620, 1998.
26. N. P. H. Thian, C. Sanderson, and S. Bengio, Spectral subband centroids as complementary features for speaker authentication, Proc. Biometric Authentication, pp. 631-639, 2004.
27. J. Kua, Investigation of spectral centroid magnitude and frequency for speaker recognition, Proc. Odyssey, pp. 34-39, 2010.
28. E. Scheirer and M. Slaney, Construction and evaluation of a robust multi feature speech/music discriminator, Proc. IEEE Int. Conf. Acoust. Speech, Signal Process., vol. 2, pp. 2-5, 1997.
29. B. C. Haris, G. Pradhan, A. Misra, S. Shukla, R. Sinha, and S. R. M. Prasanna, Multi-variability speech database for robust speaker recognition, Proc. Natl. Conf. Commun., pp. 1-5, 2011.
30. G. Pradhan and S. R. M. Prasanna, Significance of vowel onset point information for speaker verification," Int. J. Comput. Comm. Tech., vol. 2, no. 6, pp. 56-61, 2011.
31. J. P. Campbell Jr, Testing with the YOHO CD-ROM voice verification corpus, Proc. Int. Conf. Acoust. Speech, Signal Process. ICASSP-95, vol. 1, pp. 341-344, 1995.
32. Geoffrey Durou, Multilingual text-independent speaker identification, Proc. MIST'99 Workshop, pp. 115-118, 1999.



See discussions, stats, and author profiles for this publication at: <https://www.researchgate.net/publication/333731054>

# Hybrid location-centric e-Commerce recommendation model using dynamic behavioral traits of customer

Article in *Iran Journal of Computer Science* · September 2019

DOI: 10.1007/s42044-019-00040-3

---

CITATIONS

12

---

READS

259

2 authors:



**Sreenivasa B R**

Bapuji Institute Of Engineering & Technology

21 PUBLICATIONS 85 CITATIONS

SEE PROFILE



**Nirmala cr**

Bapuji Institute Of Engineering & Technology

39 PUBLICATIONS 126 CITATIONS

SEE PROFILE



# Hybrid location-centric e-Commerce recommendation model using dynamic behavioral traits of customer

B. R. Sreenivasa<sup>1</sup> · C. R. Nirmala<sup>2</sup>

Received: 12 February 2019 / Accepted: 6 June 2019 / Published online: 12 June 2019  
© Springer Nature Switzerland AG 2019

## Abstract

Major e-Commerce service provider offers additional product recommendation to its customers, while they access the application, and enough evidence existing that such recommendations are cost effective for both consumer and service provider. For maximizing profit and to satisfy the user, existing e-Commerce platforms use long-term context for recommendations. In actual scenario, the recommendation can aid the user for other reason such as when the product is reminded of recent interest in or, point customer to currently discounted items. Furthermore, user preference changes over time due to weather, location, etc. As a result, the recommendation must be made based on the present behavior of the ongoing session. Many research based on location and session-based approaches has been presented to forecast user's next-item requirement. However, these models are not efficient, as they are designed either to model short-term or long-term preferences. Recently, some hybrid recommendation algorithms have been presented to model both short-term and long term, but these models are designed considering static behavior and finds difficulty in revealing the correlations among behaviors and items. Furthermore, these models do not consider location-centric information for performing recommendation. To overcome the above-mentioned challenges, our research work presents hybrid location-centric prediction (HLCP) model by considering the dynamic behavior traits of users. HLCP model can learn both short-term and long-term context efficiently. Experiment results show that HLCP attains significant performance over existing models in terms of mean reciprocal rate (MMR) and hit rate (HR).

**Keywords** Bayesian personalized recommendation · Deep learning · Feedforward neural networks · Recommender system · Recurrent neural network

## 1 Introduction

The popularity of e-Commerce has strongly driven the popularity of recommendation systems. The practice has proven that robust and accurate recommendations would enhance both satisfaction for consumers and revenue for service providers. Furthermore, the growth of the Internet and smartphone technology has resulted in the transformation the way people shop. People buy more and more products online through the Internet rather than performing traditional shopping. e-Commerce offers its user with the prospect of browsing enormous amount of product collections, being updated

with the latest information, creating a wish list for a future purchase, comparing prices, and enjoying an enhanced service based on user specific customization. This led to the growth of the digital market with high competitiveness that allows the customer to move from one e-Commerce service provider to others if their requirement is not satisfied [1]. As a result, e-Commerce buying pattern of a customer requires strong consumer behavior understanding when they browse through website or apps, along with, it has to identify the reason for the recent purchase of or not, an item [2]. Obtaining this behavior information will aid e-Commerce application to offer a more customized or personalized service to consumers, retaining consumer [3] and increasing profits [4]. However, identifying consumer's behavior and the reason that motivates their purchase practice is a very difficult task.

The e-Commerce application offers consumers with a broad feature of navigation actions and choices. That is, consumers can move freely across wide variety items categories, use different searching paths to select a particular item, or

✉ B. R. Sreenivasa  
br.sreenu@gmail.com

<sup>1</sup> Department of Computer Science and Engineering, Jain Institute of Technology, Davangere, India

<sup>2</sup> Department of Computer Science and Engineering, Bapuji Institute of Engineering and Technology, Davangere, India

use a different strategy to purchase items, for example. In general, when the customers are logged in, the cookies or web server logs store the customer information in an ordered way. The most useful of customer's behavior is concealed in these web server logs, which must be identified and analyzed. An efficient analysis can aid to enhance the application content and structure [5], to recommend an item or recognize user specific interest with respect to particular item set [8], and to adapt and customize item [6, 7]. For instance, data mining has shown their significance in identifying pattern using log files. The objective is to identify usage traits and explore the consumer's area of interest.

Various approaches and designs have been productively applied in the area of e-Commerce, such as clustering, classification, association rule, and sequential pattern or trait. In the majority of the application area, these approaches are utilized in conjunction with process mining methods. Such methods are part of BI (business intelligence) field and are applied to explore hidden pattern and its relationship with data using a specific algorithm [9]. An e-Commerce application is an open environment, where almost any consumer behavior is probable. This elasticity makes identify consumer behavior a challenging task [10]. The existing model focused on designing consumers liking based on their historical selection of products and always neglect the sequential/trait information. It is important to consider that consumer preference changes with respect to the user's behavior traits. Subsequently, rather than considering one type of behavior such as clicking on items in apps and purchasing in e-Commerce and there are many trait cases with multiple behaviors towards a product such as clicking, purchasing, adding to favorites, and so on. Therefore, it is necessary to model dynamic behavioral traits and collaboratively predict what a consumer will prefer or choose next under a particular behavior.

Recently, some efforts have been put into developing prediction methods with sequential information [11–14]. However, to the best of our knowledge, none of the existing methods are designed for modeling traits with dynamic behaviors. In addition, if we directly treat different behaviors towards one item as different elements in traits, or simply neglect the differences among behaviors, the state-of-the-art methods will have difficulty in revealing the correlations among behaviors and items. In [15–17] used machine learning and a multi-layer network such as recurrent neural networks (RNN) [30, 31] for time or session behavior-based next-item recommendation. RNN is a natural choice to solve this problem and have been productively used for sequence-based recommendation problem in the state-of-the-art methods such as translation, speech recognition, signal processing, and time series forecasting. In the recommendation system, recurrent neural networks have been applied recently to the session-based recommendation environment with efficient

outcome [30]. The advantages of the recurrent neural network over the state-of-the-art similarity-based methods for recommendation is that they can productively learn the whole session of consumer interaction such as click, views, etc., aiding in increased accuracy over the state-of-the-art model. However, for behavior prediction tasks, the state-of-the-art recurrent neural network-based prediction model does not conform to complex real situations, particularly for the most recent features in historical traits [17, 30, 31]. Since the nature of the recommendation task involves large output spaces (due to a large number of items), poses distinctive challenges that need to be taken into consideration as well when modeling an efficient recommendation model considering dynamic behavior traits which are not fixed.

For overcoming above research challenges, the proposed work aims to build an efficient customer centric recommender system using dynamic behavioral traits of users considering location-centric information. First, we capture the features of diverse categories of behaviors in past historical traits, and then, our model considers to use behavior-specific transition matrices. Second, we design Hybrid Location-Centric Prediction (HLCP) model as a recurrent structure to obtain long-term contexts in traits. It models several elements in each hidden layer and uses location-centric transition matrices to obtain short-term contexts of the past history of user traits using feedforward neural network. Then, Bayesian personalized ranking model is used to maximize the objective function of learning of HLCP model. Our HLCP model not only can model the refined features of the most recent items in traits, but also can work with long-term contexts with a recurrent architecture.

The existing recommendation model is designed considering either short-term or long-term context. However, the proposed recommendation model is designed considering both short- and long-term context. Furthermore, the existing recommendation model is designed considering static user behavior, and for modeling, location-centric recommendation location history is used. In general, user preference or behavior changes from time to time and with respect to location. Thus, it is important to model to consider dynamic behavior and location information of the user. As a result, the existing model cannot be applied for performing location-centric-based item recommendation. However, the proposed hybrid recommendation can extract long-term user's location information using RNN model and short-term context user's location information using feedforward neural network. In the existing model time, stamp information is used to extract session or time centric information. However, in the proposed model time, stamp information is used to extract location information and along with time centric information is extracted. For carrying out experiment Tmall data set is used. The Tmall data set is composed of information such as item id, user id, buys, clicks, session spent,

time stamp information, etc. Thus, location information can be extracted from Tmall data set, as it provides timestamp information. For evaluating the recommendation model, hit rate and mean reciprocal rate are considered. Since it is a widely used parameter to evaluate the recommendation model, the proposed recommendation model attains good performance in terms of hit rate and mean reciprocal rate when compared with the existing model.

The research contribution as follows:

- To the best of our knowledge, no prior work has been considered for predicting dynamic behavioral traits of users considering location-centric information of the user.
- Designing of hybrid recommendation model, namely, HLCP for modeling both short-term and long-term contexts.
- HLCP model can not only be used for location-based recommendation, but also used recommending add posting location on a website or application.
- HLCP model attains good performance in terms of HR and MMR over existing hybrid recommendation model.

The rest of this paper is organized as follows. In Sect. 2, literature survey is presented. In Sect. 3, the proposed hybrid location-centric e-Commerce recommendation model using dynamic behavior trait of customers is presented. In the penultimate section, an experimental study is carried out. The conclusion and future work are described in the last section.

## 2 Literature survey

This section presents an extensive survey of the various state-of-the-art e-Commerce recommendation system, technique, its advantage, and disadvantages. In [20], showed extensive work is carried out to model long-term behavior analysis. Then, showed that the existing model is designed using dimensionality reduction methods applied to the user-item interactions of historical data. Furthermore, they showed the importance of modeling the short-term behavior of the user. Thus, they analyzed the RNN model on both long-term and short-term recommendation cases and identified the suitable parameter for stacked RNN with layer normalization and tied item embeddings.

In [21], showed using location histories (i.e., location-based social networks) will aid better understanding of customers preferences. They presented a location-based preference aware recommendation model, where user preference is learned using user location history and social sentiments are obtained from location histories of the local authorities. They aimed to address data sparsity issues using offline

and online recommendations using the iterative model. In the offline method, each user's personal preferences are weighted hierarchy and depict user knowledge of a particular location with respect to the different categories of locations. In the online model, it chooses local knowledge that matches customer preference using the candidate selection method. Finally, top-k ranked location is recommended for the user.

In [22, 23] showed user activity (behavior) changes with respect to location. In [22], introduced spatial behavior information as the hidden factor capturing both users' behavior and location preferences using Multi-task Context-Aware RNN (MTC-RNN). The MTC-RNN is modeled to combine both sequential dependency and temporal regularity of spatial behavior information. Similarly, [23] considered both spatial and temporal contextual information for modeling user behavior and are used for forecasting future location of the user. They showed that tensor factorization suffers from cold start problem for forecasting future behavioral event and factorizing personalized Markov chain is designed considering robust independence assumption among different factors, which limits its performance. Thus, the RNN model performs better than tensor factorization and factorizing personalized Markov chain. However, all these methods have a problem in incorporating geographical distance and continuous time interval. For addressing, they presented Spatial–Temporal RNN. Their model can incorporate spatial context and local temporal in each layer with session-specific transition matrices for the varied time period and distance-specific transition matrices for varied geographic distances.

In [24], showed point of interest [25] recommendation has attained wide interest due to the rapid growth of Location-Based Social Networks (LBSNs). The LBSN aid in obtaining both explicit (such as users' moving trajectories) and implicit information of user's personal preference and corresponding life patterns based on different contexts (such as geographical locations and time). Here, they presented Attention-based RNN (ARNN) to offer an explicable recommendation system using sequential check-in information of the respective customer rather than using frequency visit, a distance parameter, and social relationship. ARNN uses a deep neural network (DNN) [17] to offer recommendations utilizing past visiting behavioral traits rather than showing top-N recommendations.

Recently, a number of hybrid recommendation models are presented by combining two different learning methods to present efficient recommendation model. In [26] presented a hybrid collaborative method by combining gradient boosting method and  $k$ -nearest neighbor algorithm. The  $k$ -nearest neighbor algorithm is used to filter similar item and customer and gradient boosting is used to forecast user's rating for the products. In [27] presented the recommendation model to solve data sparsity, cold start problem

by improving collaborative filtering using fuzzy clustering. Fuzzy clustering is used for performing user classification based on user context, and then, collaborative filtering is utilized to recommend items for similar customers. In [28], presented a hybrid algorithm, where customers are first filtered (dimension reduction) based on the customer's profile [29]. Then, clustering is performed on these filtered data using the  $k$ -means clustering algorithm. Finally, the nearest neighbor for active users is identified and builds recommendations by identifying the most common items from established clusters of subscribers. In [30], showed the recommender system is generally designed considering long-term preference profiles. However, in the real-time recommendation model aids consumer for getting a better discount that they are interested in or point the visitor to discounted items. Here, they presented a systematic statistical model to analyze what is best for designing efficient recommendation algorithm such as the overall popularity of the products in the last few days, including their match with the consumer's shopping interests in the earlier sessions, as well as information about discounts. Using this information, they presented a novel hybrid model by combining the neighborhood-based method with DNN to forecast the importance of items for a respective shopping session.

From an extensive survey conducted, it can be seen most of the existing recommendation model is designed for modeling either short-term or long-term behaviors of users. Very limited work is carried out considering both short-term and long-term context [20, 30]. Furthermore, in the Markov chain-based model, the components are independently combined. Thus, it assumes a robust independence assumption among multiple features. On other side, [20, 21] are designed using RNN model [31].

Recurrent neural network model considers that the temporal dependency changes predictably along with the location in traits and is designed considering static user behavior. Thus, they are efficient in modeling short-term context. Along with, very limited work is carried out considering modeling location-centric prediction. Thus, there is a requirement to develop a new recommendation model that can model both short-term and long-term contextual behavior traits of the user by building location-centric transition matrices to proving location-centric-based recommendation model which is presented in next section below.

### 3 Hybrid location-centric e-commerce recommendation model using dynamic behavior trait of customer

This section presents a hybrid location-centric e-Commerce recommendation model using dynamic behavior trait of customers. The work aims to build an efficient hybrid

location-centric prediction (HLCP) model for e-Commerce that models both short-term and long-term contexts considering the dynamic behavior of the user. First, the system model of HLCP is described. Second, we describe the detail of the RNN model and how it is used to model the long-term context. The behavior of user changes rapidly (short-term) when they are exposed to a new environment. That is when user travels to a different country (location) their priority changes. Similarly, user preference changes rapidly when certain ads are posted to a certain location of the application user interface (AUI). Thus, the RNN model cannot be applied to model such a short-term context. Then, this work describes the working structure of the feedforward neural network for modeling short-term context in dynamic behavior trait of the user. Furthermore, this work describes the static behavior modeling such as a customer will just view the list of item and spend some time on an e-Commerce website. Along with, we also considered more dynamic behavior such as user will view, click, buys, spend some time, etc. on an e-Commerce website. Then, we also show how this dynamic behavior model is used in proposed HLCP model. Finally, we will show how Bayesian personalized ranking is used for learning the recurrent neural network for predicting behavior trait of e-Commerce customer.

#### 3.1 System model

The basic architecture of recommendation model is composed of the following modules, such as behavior log module, a model analysis module, and recommendation algorithm module. Behavior log module: this is used to store various kinds of consumer behaviors, such as item rating and browsing history. Model analysis module: this is used to analyze probable consumer interest based on user behavior traits log. Recommendation algorithm: this is used to establish the products which consumers are interested, and then recommend them to the respective user.

Let considers a set of items such as clothes, furniture, computer accessories, etc. as follows:

$$\mathcal{U} = \{u_1, u_2, \dots, u_n\}, \quad (1)$$

where  $u_n$  depicts the number of items considered and set of users such as male, female, children, etc. as follows:

$$\mathcal{V} = \{v_1, v_2, \dots, v_n\}, \quad (2)$$

where  $v_n$  depicts the total number of user considered. This work considers e-Commerce application, which is composed of the following behavior such as:

$$\mathcal{C} = \{c_1, c_2, c_3, c_4\}, \quad (3)$$

where  $c_1$  depicts click stream,  $c_2$  depicts added items to cart list,  $c_3$  depicts adding to favorite list, and  $c_4$  depicts purchased items.

Similarly, in the application usage pattern there exist:

$$\mathcal{C} = \{c_1, c_2, c_3\}. \quad (4)$$

Behavior such as installing application, browse items, etc. Then, the task is to predict what users will purchase in the future using the proposed hybrid design.

### 3.2 Recurrent neural network architecture

The recurrent neural network architecture is composed of multiple hidden layers. The hidden layer information of the recurrent neural network is dynamic in nature with respect to behavioral traits, where the pattern is repetitive. Thus, recurrent neural network faces problems in identifying (learning) short-term contexts in behavioral traits.

The RNN model is composed of an input layer, multiple hidden layers, and output layers, along with inner weight matrices. The activation parameter of the hidden layers is obtained as follows:

$$i_\ell^v = f(\mathcal{X}i_\ell^v + \mathcal{D}s_{w_\ell^v}), \quad (5)$$

where  $i_\ell^v \in \mathbb{S}^e$  depicts the hidden illustration of user  $v$  at location  $\ell$  in a trait,  $s_{w_\ell^v} \in \mathbb{S}^e$  depicts the illustration of the  $\ell^{th}$  input item of user  $v$ . The activation function is represented by  $f(i)$  and transition matrix of the present item is represented as follows:

$$\mathcal{D} \in \mathbb{S}^e \quad (6)$$

and the previous status is represented as follows:

$$\mathcal{W} \in \mathbb{S}^e. \quad (7)$$

$\mathcal{D}$  can obtain users' present behavior and  $\mathcal{X}$  can propagate traits signals. Equation (5) shows executed iteratively to obtain or compute the status of each location in traits. The architecture of the recurrent neural network is shown in Fig. 1.

### 3.3 Short-term context modeling

As described in the previous section, RNN is not efficient in learning short-term contexts in behavioral traits. For modeling such case, this work presents a feedforward neural network (FFNN) with a solitary linear hidden layer. Therefore, in this work, it is considered a deterministic model. Using FFNN for behavior trait prediction problem, the absolute prediction representation of traits is constructed based on items input and transition matrices at each location. The next location is a linear prediction can be depicted using following equation:

$$i_\ell^v = \sum_{j=0}^{o-1} \mathcal{D}_j s_{w_{\ell-j}^v}, \quad (8)$$

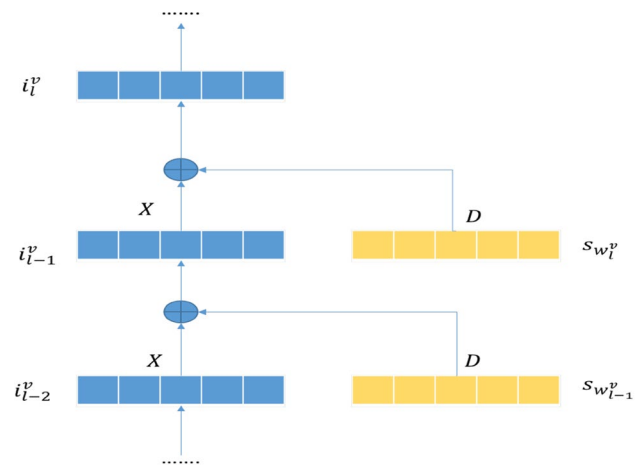


Fig. 1 Architecture of the RNN model

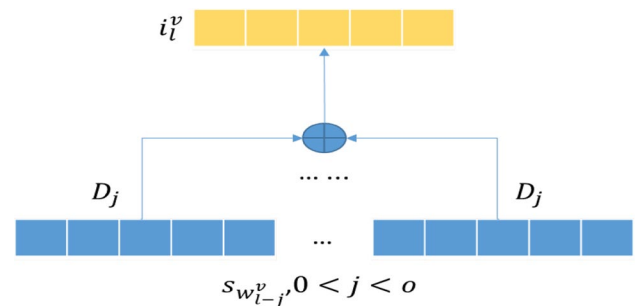


Fig. 2 Architecture of the FFNN model

where  $\mathcal{D}_j \in \mathbb{S}^{e \times e}$  depicts the transition matrix for the respective location in a behavior trait, and  $o$  is the number of components modeled in a trait. The architecture of the FFNN model to model short-term contexts in behavioral traits is shown in Fig. 2.

Here, each location in the sequence is modeled with a precise transition matrix. In general, FFNN finds difficulty in efficiently learning long-term contexts in behavioral traits.

### 3.4 User static behavior modeling

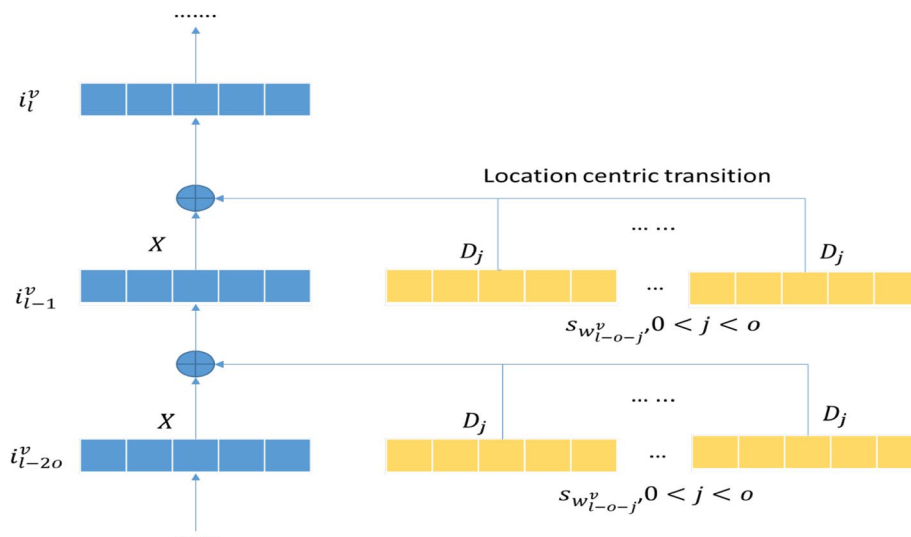
This section presents the static behavior model that captures both long- and short-term context in the past data traits simultaneously, rather than one component in each hidden layer in the recurrent neural network. This working model takes multiple components in each hidden layer and adds location-centric matrices into the RNN structure, which is described in Fig. 3.

Let us consider a user  $v$ , the hidden description of the user at the location  $\ell$  in a trait can be evaluated as follows:

$$i_\ell^v = \mathcal{X}i_{\ell-1}^v + \sum_{j=0}^{o-1} \mathcal{D}_j s_{w_{\ell-j}^v}, \quad (9)$$



**Fig. 3** Architecture of HLCP: HLCP is modeled to capture both short-term and long-term contexts in behavior trait



where  $o$  is the number of input items considered or used in each layer of HLCP; in this work, we call it an adaptive size. The location-centric transition matrices are given below:

$$D_j \in \mathbb{S}^{e \times e}. \quad (10)$$

Equation (10) obtains the influence factor of short-term contexts, that is, the  $j$ th item in each layer of HLCP, on consumer behavior, and the feature of consumer's long-term history is learned using recurrent neural network architecture. In addition, if we consider only one input for each layer and set the adaptive size  $o = 1$ , the outcome of HLCP will be similar to RNN neglecting the non-linear activation function. An important thing to be seen here is when the traits are shorter than the adaptive size or the predicted location is at the very initial segment of a trait, that is,  $\ell < o$ . Therefore, Eq. (9) can be reformulated as follows:

$$i_\ell^v = \mathcal{X}_0^v + \sum_{j=0}^{\ell-1} D_j s_{w_{\ell-j}^v}, \quad (11)$$

where  $i_0^v = u_0$ , representing the preliminary status of consumers. The preliminary status of the entire consumer must be similar. Since individual information does not come into picture when the consumer does not select an item. This consideration  $v_o$  aid in addressing the cold start problem.

### 3.5 User dynamic behavior modeling

Let us consider a case, where a user will click, add to cart and purchase an item. Similarly, they will use the application, use it and then uninstall the application. Therefore, it is important to model multi or dynamic behavioral traits of the user for collaborative prediction of user future choice under precise behavior. Considering the case, we can neglect a different kind of behavior, or just considers different behavior

towards one product as different components in the state-of-the-art model. However, it is difficult to design and obtain correlation among such dynamic behavior towards a particular product. In this work, we consider behavior-based matrices to obtain features of different kind of behaviors. Then, the illustration of subscriber  $v$  at location  $\ell$  can be computed as follows:

$$i_\ell^v = \mathcal{X}_\ell^v + \sum_{j=0}^{o-1} D_j \mathcal{N}_{c_{\ell-j}^v, r_{\ell-j}^v}, \quad (12)$$

where  $\mathcal{N}_{c_{\ell-j}^v} \in \mathbb{S}^{e \times e}$  depicts a behavior-based transition matrix design with respect to behavior on the  $j$ th product of subscriber  $v$ . An important thing to be seen here is if there is only one kind of behavior, then the behavior-based matrices can be eliminated. LCP can obtain the underlying features of whether of different kinds of behavior in past traits. Furthermore, by computing whether subscriber  $v$  would perform behavior  $c$  on product  $w$  at traits location  $\ell + 1$  can be obtained as:

$$z_{v, \ell+1, c, w} = (t_\ell^v)^\mathcal{U} \mathcal{N}_{c, s_w} = (i_\ell^v + v_v)^\mathcal{U} \mathcal{N}_{c, s_w}, \quad (13)$$

where  $t_\ell^v$  depicts the illustration for the current position of subscriber  $v$  at the traits position  $\ell$ , static hidden representation  $v_v \in \mathbb{S}^e$  and containing dynamic representation  $i_\ell^v$ .

### 3.6 Learning of hybrid location-centric prediction model

Bayesian personalized ranking model [32] is a pairwise ranking method used for the implicit feedback information. The Bayesian personalized ranking has been used as an objective parameter that is widely applied for learning

recurrent neural network for predicting behavior trait of e-Commerce customer. In general Bayesian, personalized ranking considers that a customer desires a chosen set than a negative one. That is, it aims to maximize the probability using below equation:

$$p(v, l+1, c, w > w') = h(z_{v,l+1,c,w} - z_{v,l+1,c,w'}), \quad (14)$$

where  $w'$  depicts negative features,  $h(y)$  is a non-linear function selected using below equation:

$$h(y) = \frac{1}{1 + e^{-y}}. \quad (15)$$

Thus, by considering negative log likelihood, the fourth coming objective function can be minimized equivalently as follows:

$$K_1 = \sum \log \left( 1 + e^{-(z_{v,l+1,c,w} - z_{v,l+1,c,w'})} \right) + \frac{\mu}{2} \theta_1^2, \quad (16)$$

where  $\mu$  depicts regularization power control parameter and  $\theta_1 = \{V, S, X, D, N\}$  depicts parameter to be computed. The experiment is conducted to evaluate the outcome of HLCP shows significant performance which is experimentally proven in the next section in terms of Hit Rate (HR) and Mean Reciprocal Rank (MRR) performance.

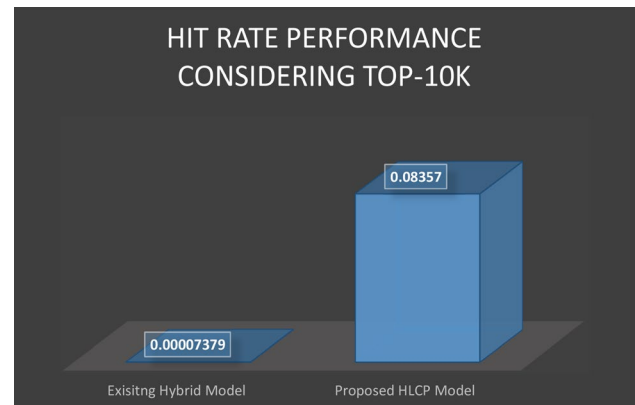
## 4 Simulation result and analysis

This section presents a performance evaluation of the proposed HLCP recommendation model over existing hybrid recommendation model [30]. The existing model combines the nearest neighbor and RNN algorithm [31] to construct a hybrid recommendation model considering static user behavior. On the other side, the developed model combines RNN with feedforward neural network. Then, the RNN learning is performed with maximizing objective function using BPR [12, 32]. The HLCP and the existing hybrid model is implemented using python programming language.

For performance evaluation, Tmall data set [18] is considered. The Tmall data set is collected from Tmall [19], one of the biggest online shopping websites in China. It contains about 200,000 shopping records belonging to 1000 users on 10,000 items. The temporal information of the data set is extracted based on the day level. It is composed of four different categories of behaviors such as purchasing, clicking, and adding to the shopping cart and adding to favorites. It suits for the task of multi-domain collective prediction on multi-behavioral traits. The data set obtained is preprocessed into training and test set. We considered four test cases, where, in each case first 70% of data is considered for training, and the remaining 30% of data is considered for testing. The regularization parameter  $\mu$  is set to 0.01. Then, on these test cases, we aim to predict what users will purchase in the

**Table 1** Hit rate@10 performance attained for Tmall data set

Baseline Metric@ 10	Existing hybrid model [30] HR	Proposed HLCP HR
Case 1	0.0001745	0.0755046
Case 2	0.00006747	0.09454
Case 3	0.000066649	0.08828
Case 4	0.00007379	0.08357
Average	0.00009560225	0.08547365



**Fig. 4** Average hit rate performance attained by the proposed HLCP model over the existing model considering the top-10k recommendation

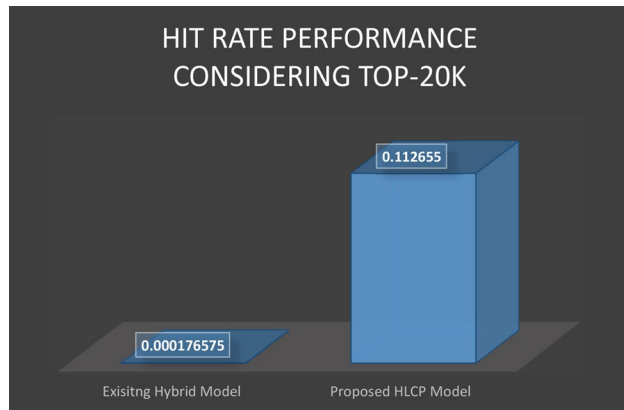
future. The performance of the prediction task carried out using HLCP recommendation and existing hybrid model is evaluated in terms of hit rate (HR) and mean reciprocal rate (MRR).

### 4.1 Hit rate performance evaluation

This section presents performance evaluation based on the accuracy of the HLCP model and existing hybrid model. The performance of both models is evaluated in terms of HR which is tabulated in Table 1. The average hit rate performance attained by the proposed HLCP model over existing hybrid model is shown in Fig. 4 considering the top-10k recommendation. From Fig. 4 and Table 1, it is seen that the proposed hybrid model attains significant performance when compared with the existing model in terms of HR considering top-10k recommendation/iteration. Similarly, an experiment is conducted considering top-20k recommendation, as shown in Table 2. The average hit rate performance attained by the proposed HLCP model over existing hybrid model is shown in Fig. 5 considering the top-20k recommendation. The outcome shows that the HLCP model attains significant performance than the existing model in terms of HR.

**Table 2** Hit rate@20 performance attained for Tmall data set

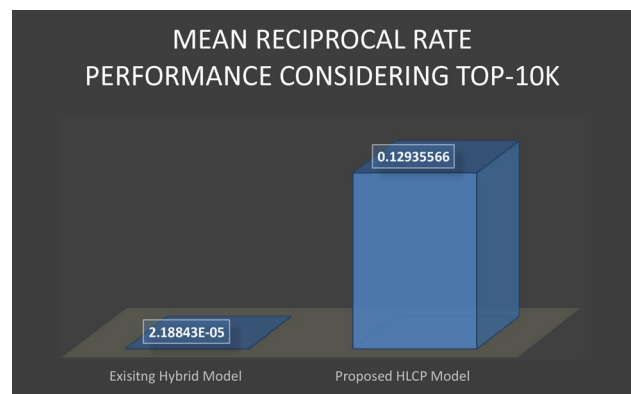
Baseline Metric@ 20	Existing hybrid model [30]	Proposed HLCP
	HR	HR
Case 1	0.0002811	0.10107
Case 2	0.000168	0.1228
Case 3	0.0001466	0.11577
Case 4	0.0001106	0.11098
Average	0.000176575	0.112655

**Fig. 5** Average hit rate performance attained by the proposed HLCP model over the existing model considering the top-20k recommendation**Table 3** Mean reciprocal rate@10 performance attained for Tmall data set

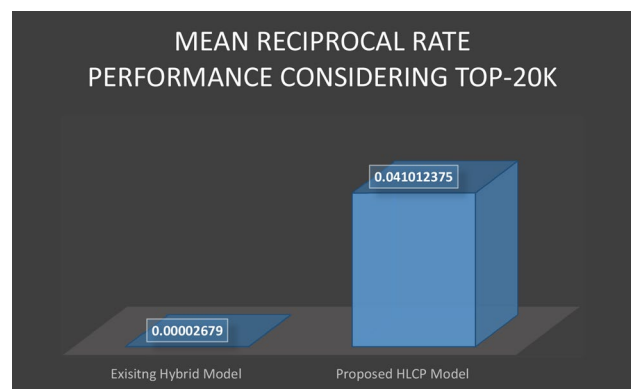
Baseline Metric@ 10	Existing hybrid model [30]	Proposed HLCP
	MRR	MRR
Case 1	0.0000391	0.0339255
Case 2	0.00001299	0.044203
Case 3	0.0000129	0.40099
Case 4	0.000022547	0.03830414
Average	0.00002188425	0.12935566

## 4.2 Mean reciprocal rate performance evaluation

This section presents performance evaluation based on the accuracy of the HLCP model and existing hybrid model. The accuracy performance of both models is evaluated in terms of MRR which is tabulated in Table 3. The average MRR performance attained by the proposed HLCP model over existing hybrid model is shown in Fig. 6 considering the top-10k recommendation. From Fig. 6 and Table 3, it is seen that the hybrid model attains significant performance when compared with the existing model in terms of

**Fig. 6** Average mean reciprocal rate performance attained by the proposed HLCP model over the existing model considering the top-10k recommendation**Table 4** Mean reciprocal rate@20 performance attained for Tmall data set

Baseline Metric@ 20	Existing Hybrid Model [30]	Proposed HLCP
	MRR	MRR
Case 1	0.0000461	0.03568
Case 2	0.00001926	0.046157
Case 3	0.0000169	0.0420215
Case 4	0.0000249	0.040191
Average	0.00002679	0.041012375

**Fig. 7** Average mean reciprocal rate performance attained by the proposed HLCP model over the existing model considering the top-20k recommendation

MRR with top-10k recommendation/iteration. Similarly, the experiment is conducted with a top-20k recommendation, as shown in Table 4. The average MRR performance attained by the proposed HLCP model over existing hybrid model is shown in Fig. 7 considering the top-20k recommendation. The outcome shows that the HLCP model

attains significant performance than the existing model in terms of MMR.

### 4.3 Results and discussion

The overall result attained shows the efficiency of the hybrid model, namely, HLCP when compared to the state-of-the-art models [12, 17, 30–32]. The significant results attained are due to consideration of location-centric-based item recommendation model with the dynamic behavior of the user by proposed design. Whereas the existing model is designed with static behavior of user and location-centric information is neglected by the state-of-the-art models.

## 5 Conclusion

The work presents an efficient recommendation model for e-Commerce industries. This hybrid recommendation model considers location-centric information and dynamic behavior of the user. No other existing research has considered the dynamic behavior of user and location-centric-based recommendation model. The Hybrid model is designed by combining RNN with FFNN for modeling short term and long term, respectively. Then, BPR is used maximizing learning objective function of HLCP model. The HLCP is designed as a recurrent structure to obtain long context in traits and it models several elements in each hidden layer and uses location-centric transition matrices to obtain short-term contexts of the past history of user traits. Our HLCP model not only can model the refined features of the most recent items in traits, but also can work with long-term contexts with a recurrent architecture considering the dynamic behavior of users. The experiment is conducted to evaluate the performance of HLCP over existing hybrid model. The outcome shows that an average hit rate performance of 0.00009560225 and 0.08547365 for top-10k recommendation is attained by the proposed HLCP and existing hybrid model, respectively. Similarly, for top-20k recommendation an average hit rate performance of 0.000176575, 0.112655 is attained by HLCP and existing hybrid model, respectively. Furthermore, an average mean reciprocal rate performance of 0.00002188425, 0.12935566 for top-k recommendation is attained by HLCP and existing hybrid model, respectively. Similarly, for top-20k recommendation an average mean reciprocal rate performance of 0.00002679, 0.041012375 is attained by HLCP and existing hybrid model, respectively. The overall result attained shows significant performance attained by HLCP over the existing model in terms of MMR and HR. The future work would consider evaluating under different data set such as MovieLens, Amazon, Youchoose etc. Furthermore, consider incorporating time

centric information for behavior analysis for attaining effective recommendation.

## References

1. Poggi, N., Carrera, D., Gavalda, R., Torres, J., Ayguadé, E.: Characterization of workload and resource consumption for an online travel and booking site. In: *Proceeding IEEE Int. Symp. workload characterization (IISWC)*, pp. 1–10, 2010
2. Liu, G., et al.: Repeat buyer prediction for e-Commerce. In: *Proceeding 22nd ACM SIGKDD Int. Conf. Knowl. discovery data mining*, New York, NY, USA, pp. 155–164, 2016
3. Xu, J.D.: Retaining customers by utilizing technology-facilitated chat: mitigating website anxiety and task complexity. *Inf. Manag.* **53**(5), 554–569 (2016)
4. Kim, Y.S., Yum, B.-J.: Recommender system based on clickstream data using association rule mining. *Expert Syst. Appl.* **38**(10), 13320–13327 (2011)
5. Carmona, C.J., Ramírez Gallego, S., Torres, F., Bernal, E., del Jesus, M.J., García, S.: Web usage mining to improve the design of an e-Commerce website: OrOliveSur.com. *Expert Syst. Appl.* **39**(12), 11243–11249 (2012)
6. Arbelaitz, O., Gurrutxaga, I., Lojo, A., Muguerza, J., Pérez, J.M., Perona, I.: Web usage and content mining to extract knowledge for modelling the users of the bidasoia turismo website and to adapt it. *Expert Syst. Appl.* **40**(18), 7478–7491 (2013)
7. Gerrikagoitia, J.K., Castander, I., Rebón, F., Alzua-Sorzabal, A.: New trends of intelligent e-marketing based on web mining for e-shops. *Proc. Soc. Behav. Sci.* **175**, 75–83 (2015)
8. Su, Q., Chen, L.: A method for discovering clusters of e-Commerce interest patterns using click-stream data. *Electron. Commer. Res. Appl.* **14**(1), 1–13 (2015)
9. van der Aalst, W.M.P.: *Process mining: discovery, conformance, and enhancement of business processes*, 1st edn. Springer, Heidelberg (2011)
10. Poggi, N., Muthusamy, V., Carrera, D., Khalaf, R.: Business process mining from e-Commerce Weblogs. In: *Proceeding 11th Int. Conf. Bus. process manage*, Berlin, Germany, pp. 65–80, 2013
11. Hernández, S., Álvarez, P., Fabra, J., Ezpeleta, J.: Analysis of users' behavior in structured e-commerce websites. *IEEE Access* **5**, 11941–11958 (2017)
12. He, Y., Wang, C., Jiang, C.: Correlated matrix factorization for recommendation with implicit feedback. *IEEE Trans. Knowl. Data Eng.* **1**, 2 (2017). <https://doi.org/10.1109/tkde.2018.2840993>
13. Castro, J., Lu, J., Zhang, G., Dong, Y., Martínez, L.: Opinion dynamics-based group recommender systems. *IEEE Trans. Syst. Man Cybern. Syst.* **1**, 2 (2017). <https://doi.org/10.1109/tsmc.2017.2695158>
14. Yu, X., Jiang, F., Du, J., Gong, D.: A user-based cross domain collaborative filtering algorithm based on a linear decomposition model. *IEEE Access* **5**, 27582–27589 (2017)
15. Zeng, Z., Rao, H.K., Liu, A.P.: Research on personalized referral service and big data mining for e-Commerce with machine learning. 2018 4th International Conference on computer and technology applications (ICCTA), Istanbul, Turkey, pp. 35–38, 2018
16. Mu, D., Guo, L., Cai, X., Hao, F.: Query-focused personalized citation recommendation with mutually reinforced ranking. *IEEE Access* **6**, 3107–3119 (2018)
17. Fu, M., Qu, H., Yi, Z., Lu, L., Liu, Y.: A novel deep learning-based collaborative filtering model for recommendation system. *IEEE Trans. Cybern.* (2018). <https://doi.org/10.1109/tcyb.2018.2795041>
18. <https://102.alibaba.com/competition/addDiscovery/index.htm>

19. <https://www.tmall.com/>
20. Villatel, K., Smirnova, E., Mary, J., Preux, P.: Recurrent neural networks for long and short-term sequential recommendation. *arXiv.org > cs > arXiv:1807.09142*
21. Bao, J., Zheng, Y., Mokbel, M.F.: Location-based and preference-aware recommendation using sparse geo-social networking data. *SIGSPATIAL/GIS* (2012)
22. Liao, D., Liu, W., Zhong, Y., Li, J., Wang, G.: Predicting activity and location with multi-task context aware recurrent neural network. *Twenty-Seventh International Joint Conference on artificial intelligence*, 3435–3441. <https://doi.org/10.24963/ijcai.2018/477>, 2016
23. Liu, Q., Wu, S., Wang, L., Tan, T.: Predicting the next location: a recurrent model with spatial and temporal contexts. In *AAAI Conference on artificial intelligence*, pages 194–200, 2016
24. Xia, B., Li, Y., Li, Q., Li, T.: Attention-based recurrent neural network for location recommendation. *2017 12th International Conference on intelligent systems and knowledge engineering (ISKE)*, Nanjing, 2017, pp 1–6
25. Zheng, H., Zhou, Y., Liang, N., Xiao, X., Sangaiah, A.K., Zhao, C.: Exploiting user mobility for time-aware POI recommendation in social networks. In *IEEE Access*. (2017). <https://doi.org/10.1109/access.2017.2764074>
26. Lu, S., Wang, B., Wang, H., Hong, Q.: A hybrid collaborative filtering algorithm based on KNN and gradient boosting. 1–5. (2018). <https://doi.org/10.1109/iccse.2018.8468751>
27. Lu, P., Wu, X., Teng, D.: Hybrid recommendation algorithm for e-commerce website. *2015 8th International Symposium on computational intelligence and design (ISCID)*, Hangzhou, 2015, pp. 197–200
28. Prabhu, P., Anbazhagan, N.: A new hybrid algorithm for business intelligence recommender system. *Int. J. Netw. Secur. Appl.* (2014). <https://doi.org/10.5121/ijnsa.2014.6204>
29. Guo, Y., Wang, M., Li, X.: An interactive personalized recommendation system using the hybrid algorithm model. *Symmetry* **9**, 216 (2017). <https://doi.org/10.3390/sym9100216>
30. Jannach, D., Ludewig, M., Lerche, L.: Session-based item recommendation in e-Commerce: on short-term intents, reminders, trends, and discounts. *User Model. User-Adapt. Interact.* **27**(3–5), 351–392 (2017). <https://doi.org/10.1007/s11257-017-9194-1>
31. Yu, F., Liu, Q., Wu, S., Wang, L., Tan, T.: A dynamic recurrent model for next basket recommendation. In: *Proceedings of the 39th International ACM SIGIR*, 2016
32. Rendle, S., Freudenthaler, C., Gantner, Z., Schmidt-Thieme, L. BPR: Bayesian personalized ranking from implicit feedback. In: *Proceedings of the 25th Conference on uncertainty in artificial intelligence, UAI'09*, pp. 452–461, 2009

**Publisher's Note** Springer Nature remains neutral with regard to jurisdictional claims in published maps and institutional affiliations.



# Implementation of Ant-Lion Optimization Algorithm in Energy Management Problem and Comparison

P. S. Preetha<sup>1,2(✉)</sup> and Ashok Kusagur<sup>3(✉)</sup>

<sup>1</sup> VTU, Belagavi, India

ps.preetha@gmail.com

<sup>2</sup> Department of Electrical and Electronics Engineering,

Jain Institute of Technology, Davanagere 577003, India

<sup>3</sup> Department of Studies in Electrical and Electronics Engineering,

UBDT College of Engineering, Davanagere 577004, India

ashok.kusagur@gmail.com

**Abstract.** The Antlion algorithm (ALO) is used here for solution of energy management problem. This algorithm is compared with particle swarm optimization (PSO), genetic algorithm (GA) and BAT algorithms. The need of energy management increases as the power system loses more power due to wrong management of power. The energy management in industrial loads can save more for industry. Due to the recent tariff plans by Indian government makes the energy management mandatory in the industry to save the peak time load. Many management techniques are provided by the researchers. The segregation of loads to fixed, shiftable and uninterruptable load makes the management of load easy but when it is planned hourly it is not easy to schedule. The proper constraints also have to be considered to make the scheduling more practical. So, the problem is formulated and solved using meta-heuristic techniques in MATLAB.

**Keywords:** Ant-lion optimization · Particle swarm optimization · Genetic algorithm · BAT algorithm · Energy management system

## 1 Introduction

There might be a huge increase in energy demand in 2020 as per [1]. This shows the requirement of power. So, there is a huge need in optimal power scheduling, renewable resources base power generation [2] etc. Based on renewable resources the smart grids play important role. It uses the recent technologies to communicate between the customer and the generator [3]. The advanced metering concepts improves the optimal power delivery to the homes with smart meters.

Another important factor is demand side management for improving the power deliver [4]. This concept uses a program which gives incentives to the customer if they are avoiding peak load. It communicates in two-way and it keeps informing the smart grid regarding pricing, load on utility, load shedding and any failures. Each customer

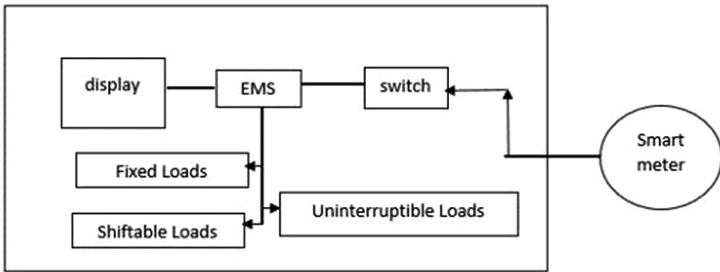


can choose their load timing. The user comfort also should not be spoiled due to the scheduling. So, there is a tradeoff between cost of energy and user comfort.

To give solution to the above problem the energy management problem is formulated and solved for industrial load. In this paper the new ant-lion optimization algorithm [8] is implemented to solve this energy management issue and compared with PSO [6], GA [6] and BAT [7] algorithm.

## 2 Problem Formulation

In the energy management recent technology play important role. As the power of each devices are known already, the switching of the load can be done easily. In [5] the embedded scheduler is done for EMS system. Recent smart meters can transfer data two way. So, it transfers between customer and utility. The data can be transferred between, pricing signal from the energy market and the load demand. The architecture of EMS system for an industry is shown in Fig. 1.



**Fig. 1.** Proposed system

**Table 1.** Load type

Load type	Devices	Power in Kwh	Hours operated
Fixed load	Furnace	5	16
	Refrigerator	4.5	19
	Air conditioner	7.2	14
Shiftable	Driller	3.5	13
	Water heater	2.5	17
	Water pump	0.8	14
	Fans	0.7	16
Uninterruptible	Tank cleaner	3.5	10
	Lights	1.5	5
	Dryer	1.4	4
	Mixer	1	20

Table 1 shows the load type and separated it as fixed, shiftable and uninterruptible and 11 loads are considered with its power rating and operating hours.

## 2.1 Fixed Devices

$$U(t) = \sum_{f_a \in F_{ap}} \left( \sum_{t=1}^{24} \rho f_a \times \gamma f_a(t) \right) \quad (1)$$

where  $a = \{1, 2, \dots, n\}$  and  $t = \{1, 2, \dots, 24\}$ .

$\gamma f_a(t)$  is *ON/OFF* state of the appliance in that timeslot.

## 2.2 Shiftable Devices

$$V(t) = \sum_{s_a \in S_{ap}} \left( \sum_{t=1}^{24} \rho s_a \times \gamma s_a(t) \right) \quad (2)$$

where  $\gamma s_a(t)$  is the *ON/OFF* state of the appliance in that hour. Our focus is to minimize the per hour cost of each appliance, as a result the overall cost will be reduced.

## 2.3 Uninterruptible Devices

$$W(t) = \sum_{ui_a \in UI_{ap}} \left( \sum_{t=1}^{24} \rho ui_a \times \gamma ui_a(t) \right) \quad (3)$$

$UI_{ap}$  is the set of un-interruptible appliances such that  $ui_a \in UI_{ap}$  and  $ui_a$  is the power rating of each appliance. The total power consumption  $W$  of this category appliances can be calculated using Eq. 3.

## 2.4 Energy Consumption Model

The total energy consumption of all the devices in each hour can be calculated using the following equation.

$$\begin{aligned} P_T(t) = & \sum_{f_a \in F_{ap}} \left( \sum_{t=1}^{24} \rho f_a \times \gamma f_a(t) \right) \\ & + \sum_{s_a \in S_{ap}} \left( \sum_{t=1}^{24} \rho s_a \times \gamma s_a(t) \right) \\ & + \sum_{ui_a \in UI_{ap}} \left( \sum_{t=1}^{24} \rho ui_a \times \gamma ui_a(t) \right) \end{aligned} \quad (4)$$

## 2.5 Energy Cost Model

$$C_T = \sum_{t=1}^T (P(t) \times \lambda(t)) \quad (5)$$

Where  $\lambda$  is pricing signal used in our work.

## 3 Antlion Algorithm

The hunting behavior of antlion is formed as algorithm for optimization solutions. Here ants are the population as per the power system term it is control signal. Here, Prey is the objective function. The hunting of objective function with random walks of the control signal, building the control traps, entrapment of population, catching the objective function and rebuilding the trap as known as control and rebuild new population are the different steps involved in it. The algorithm is given below,

**Step1:** randomly populate the ants and antlions

**Step2:** calculate control error or fitness function

**Step3:** find the antlion which finds prey faster and name it as elite.

**Step4:** while the stop criteria are not satisfied then,

Do (for loop) every ant as below,

Roulette wheel selection of antlion

Update C and D using below equations,

$$c^t = \frac{c^t}{I}$$

$$d^t = \frac{d^t}{I}$$

Create a random search and normalize it using

$$X(t) = [0, \text{cumsum}(2r(t_1) - 1), \text{cumsum}(2r(t_2) - 1), \dots, \text{cumsum}(2r(t_n) - 1)]$$

$$X_i^t = \frac{(X_i - a_i)X(d_i - c_i)}{(d_i^t - a_i)} + c_i$$

Update the position of each ant using

$$Ant_i = \frac{R_A^t + R_E^t}{2}$$

**end for**

Calculate the fitness of all the control variables

Replace the antlion with the corresponding ant if the

$$Antlion_j^t = Ant_i^t \text{ if } f(Ant_i^t) > f(Antlion_j^t)$$

Update elite if newer is fitter  
End the while

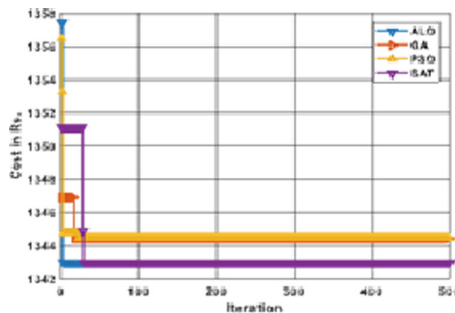
## 4 Results and Discussion

The data is collected in local sugar factory in Karnataka. The Karnataka tariff is provided in Table 2. The average cost of electricity taken is Rs. 3.50. The scheduling is done as per the load data available. There are 11 loads considered and it is separated as fixed, shiftable and uninterruptable. Fixed load cannot be scheduled. Shiftable can be scheduled at any time. Uninterruptable can be scheduled without switching it off intermittently.

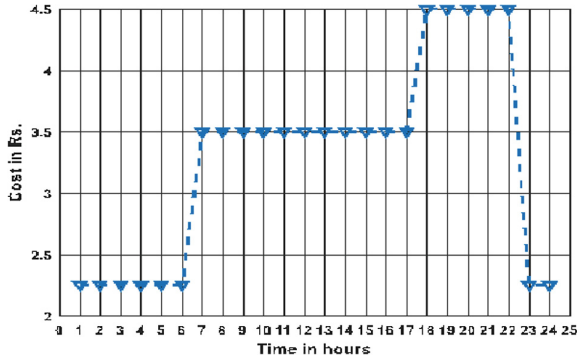
**Table 2.** Tariff in Karnataka, India

Time of day	Tariff
22.00 h to 06.00 h	(-) 125 paise per unit
06.00 h to 18.00 h	0
18.00 h to 22.00 h	(+) 100 paise per unit

There are four algorithms used for solving the problem. GA, PSO, BAT and ALO. These four algorithms used here and solutions are shown in the figures. Figure 2 shows the convergence of all the four algorithms. Tables 3, 4, 5 and 6 shows the scheduling in that '1' means on and '0' means off. The electricity tariff in India is shown in Fig. 3.



**Fig. 2.** Compared cost function



**Fig. 3.** BESCOM electricity tariff

**Table 3.** GA Algorithm results

Time		0:00	1:00	2:00	3:00	4:00	5:00	6:00	7:00	8:00	9:00	10:00	11:00	12:00	13:00	14:00	15:00	16:00	17:00	18:00	19:00	20:00	21:00	22:00	23:00
Hours		1	2	3	4	5	6	7	8	9	10	11	12	13	14	15	16	17	18	19	20	21	22	23	24
Load type	Fixed Load																0	0	0	0	0	0	0	0	0
	Shiftable load																0	0	0	0	0	0	0	0	0
		1	1	1	1	1	0	1	1	0	1	1	1	1	0	1	0	1	0	0	1	1	1	1	1
		0	0	0	0	0	1	1	1	0	1	1	1	1	0	1	0	1	0	1	0	1	0	1	0
	0	0	0	0	0	1	1	1	0	1	1	1	1	0	1	0	1	0	1	0	1	0	1	0	
	Un-interruptable	1			0	0	0	0	0	0	0	0	0	0	0	0	0	0	0	0	0	0	0	0	1
		1			0	0	0	0	0	0	0	0	0	0	0	0	0	0	0	0	0	0	0	0	1
		1			0	0	0	0	0	0	0	0	0	0	0	0	0	0	0	0	0	0	0	0	1
		1			0	0	0	0	0	0	0	0	0	0	0	0	0	0	0	0	0	0	0	0	1
		1			0	0	0	0	0	0	0	0	0	0	0	0	0	0	0	0	0	0	0	0	1
		1			0	0	0	0	0	0	0	0	0	0	0	0	0	0	0	0	0	0	0	0	1
		1			0	0	0	0	0	0	0	0	0	0	0	0	0	0	0	0	0	0	0	0	1
		1			0	0	0	0	0	0	0	0	0	0	0	0	0	0	0	0	0	0	0	0	1
		1			0	0	0	0	0	0	0	0	0	0	0	0	0	0	0	0	0	0	0	0	1
		1			0	0	0	0	0	0	0	0	0	0	0	0	0	0	0	0	0	0	0	0	1
		1			0	0	0	0	0	0	0	0	0	0	0	0	0	0	0	0	0	0	0	0	1
		1			0	0	0	0	0	0	0	0	0	0	0	0	0	0	0	0	0	0	0	0	1
		1			0	0	0	0	0	0	0	0	0	0	0	0	0	0	0	0	0	0	0	0	1
		1			0	0	0	0	0	0	0	0	0	0	0	0	0	0	0	0	0	0	0	0	1
		1			0	0	0	0	0	0	0	0	0	0	0	0	0	0	0	0	0	0	0	0	1
		1			0	0	0	0	0	0	0	0	0	0	0	0	0	0	0	0	0	0	0	0	1
		1			0	0	0	0	0	0	0	0	0	0	0	0	0	0	0	0	0	0	0	0	1
		1			0	0	0	0	0	0	0	0	0	0	0	0	0	0	0	0	0	0	0	0	1
		1			0	0	0	0	0	0	0	0	0	0	0	0	0	0	0	0	0	0	0	0	1
		1			0	0	0	0	0	0	0	0	0	0	0	0	0	0	0	0	0	0	0	0	1
		1			0	0	0	0	0	0	0	0	0	0	0	0	0	0	0	0	0	0	0	0	1
		1			0	0	0	0	0	0	0	0	0	0	0	0	0	0	0	0	0	0	0	0	1
		1			0	0	0	0	0	0	0	0	0	0	0	0	0	0	0	0	0	0	0	0	1
		1			0	0	0	0	0	0	0	0	0	0	0	0	0	0	0	0	0	0	0	0	1
		1			0	0	0	0	0	0	0	0	0	0	0	0	0	0	0	0	0	0	0	0	1
		1			0	0	0	0	0	0	0	0	0	0	0	0	0	0	0	0	0	0	0	0	1
		1			0	0	0	0	0	0	0	0	0	0	0	0	0	0	0	0	0	0	0	0	1
		1			0	0	0	0	0	0	0	0	0	0	0	0	0	0	0	0	0	0	0	0	1
		1			0	0	0	0	0	0	0	0	0	0	0	0	0	0	0	0	0	0	0	0	1
		1			0	0	0	0	0	0	0	0	0	0	0	0	0	0	0	0	0	0	0	0	1
		1			0	0	0	0	0	0	0	0	0	0	0	0	0	0	0	0	0	0	0	0	1
		1			0	0	0	0	0	0	0	0	0	0	0	0	0	0	0	0	0	0	0	0	1
		1			0	0	0	0	0	0	0	0	0	0	0	0	0	0	0	0	0	0	0	0	1
		1			0	0	0	0	0	0	0	0	0	0	0	0	0	0	0	0	0	0	0	0	1
		1			0	0	0	0	0	0	0	0	0	0	0	0	0	0	0	0	0	0	0	0	1
		1			0	0	0	0	0	0	0	0	0	0	0	0	0	0	0	0	0	0	0	0	1
		1			0	0	0	0	0	0	0	0	0	0	0	0	0	0	0	0	0	0	0	0	1
		1			0	0	0	0	0	0	0	0	0	0	0	0	0	0	0	0	0	0	0	0	1
		1			0	0	0	0	0	0	0	0	0	0	0	0	0	0	0	0	0	0	0	0	1
		1			0	0	0	0	0	0	0	0	0	0	0	0	0	0	0	0	0	0	0	0	1
		1			0	0	0	0	0	0	0	0	0	0	0	0	0	0	0	0	0	0	0	0	1
		1			0	0	0	0	0	0	0	0	0	0	0	0	0	0	0	0	0	0	0	0	1
		1			0	0	0	0	0	0	0	0	0	0	0	0	0	0	0	0	0	0	0	0	1
		1			0	0	0	0	0	0	0	0	0	0	0	0	0	0	0	0	0	0	0	0	1
		1			0	0	0	0	0	0	0	0	0	0	0	0	0	0	0	0	0	0	0	0	1
		1			0	0	0	0	0	0	0	0	0	0	0	0	0	0	0	0	0	0	0	0	1
		1			0	0	0	0	0	0	0	0	0	0	0	0	0	0	0	0	0	0	0	0	1
		1			0	0	0	0	0	0	0	0	0	0	0	0	0	0	0	0	0	0	0	0	1
		1			0	0	0	0	0	0	0	0	0	0	0	0	0	0	0	0	0	0	0	0	1
		1			0	0	0	0	0	0	0	0	0	0	0	0	0	0	0	0	0	0	0	0	1
		1			0	0	0	0	0	0	0	0	0	0	0	0	0	0	0	0	0	0	0	0	1
		1			0	0	0	0	0	0	0	0	0	0	0	0	0	0	0	0	0	0	0	0	1
		1			0	0	0	0	0	0	0	0	0	0	0	0	0	0	0	0	0	0	0	0	1
		1			0	0	0	0	0	0	0	0	0	0	0	0	0	0	0	0	0	0	0	0	1
		1			0	0	0	0	0	0	0	0	0	0	0	0	0	0	0	0	0	0	0	0	1
		1			0	0	0	0	0	0	0	0	0	0	0	0	0	0	0	0	0	0	0	0	1
		1			0	0	0	0	0	0	0	0	0	0	0	0	0	0	0	0	0	0	0	0	1
		1			0	0	0	0	0	0	0	0	0	0	0	0	0	0	0	0	0	0	0	0	1
		1			0	0	0	0	0	0	0	0	0	0	0	0	0	0	0	0	0	0	0	0	1
		1			0	0	0	0	0	0	0	0	0	0	0	0	0	0	0	0	0	0	0	0	1
		1			0	0	0	0	0	0	0	0	0	0	0	0	0	0	0	0	0	0	0	0	1
		1			0	0	0	0	0	0	0	0	0	0	0	0	0	0	0	0	0	0	0	0	1
		1			0	0	0	0	0	0	0	0	0	0	0	0	0	0	0	0	0	0	0	0	1
		1			0	0	0	0	0	0	0	0	0	0	0	0	0	0	0	0	0	0	0	0	1
		1			0	0	0	0	0	0	0	0	0	0	0	0	0	0	0	0	0	0	0	0	1
		1			0	0	0	0	0	0	0	0	0	0	0	0	0	0	0	0	0	0	0	0	1
		1			0	0	0	0	0	0	0	0	0	0	0	0	0	0	0	0	0	0	0	0	1
		1			0	0	0	0	0	0	0	0	0	0	0	0	0	0	0	0	0	0	0	0	1
		1			0	0	0	0	0	0	0	0	0	0	0	0	0	0	0	0	0	0	0	0	1
		1			0	0	0	0	0	0	0	0	0	0	0	0	0	0	0	0	0	0	0	0	1
		1			0	0	0	0	0	0	0	0	0	0	0	0	0	0	0	0	0	0	0	0	1
		1			0	0	0	0	0	0	0	0	0	0	0	0	0	0	0	0	0	0	0	0	1
		1			0	0	0	0	0	0	0	0	0	0	0	0	0	0	0	0	0	0	0	0	1
		1			0	0	0	0	0	0	0	0	0	0	0	0	0	0	0	0	0	0	0	0</	

**Table 4.** PSO Algorithm results[illegible]**Table 5.** BAT Algorithm results[illegible]

**Table 6.** ALO Algorithm results

Time		2:00	3:00	3:30	4:00	5:00	6:00	6:30	7:00	8:00	9:00	10:00	11:00	12:00	13:00	14:00	15:00	16:00	17:00	18:00	19:00	20:00	21:00	22:00	23:00
Hours		1	2	3	4	5	6	7	8	9	10	11	12	13	14	15	16	17	18	19	20	21	22	23	24
Load type	Fixed	1	1	1	1	1	1	1	1	1	1	1	1	1	1	1	1	0	0	0	0	0	0	0	0
	Load	1	1	1	1	1	1	1	1	1	1	1	1	1	1	1	0	0	0	0	0	0	0	0	0
	Shiftable load	0	0	1	1	1	1	1	0	1	0	0	0	0	1	1	0	0	1	0	0	0	0	0	0
	0	0	1	1	1	1	1	0	0	0	0	0	0	1	1	0	1	0	1	1	0	1	1	0	
	0	0	1	1	1	1	1	0	0	0	0	0	0	0	1	1	0	1	1	1	0	1	1	0	
	0	0	1	1	1	1	1	0	0	0	0	0	0	0	1	1	0	1	1	1	0	1	1	0	
Uninterruptable	1	1	1	1	1	1	1	1	1	1	1	1	1	1	1	1	0	0	0	0	0	0	0	0	0

**Table 7.** Comparison

Algorithms	Cost in Rs.	Time in Sec
GA	1344.5	15.293922
PSO	1344.45	16.32405
BAT	1343	15.910565
ALO	<b>1342.97</b>	<b>12.394</b>

Table 7 shows the final cost value with execution time. It shows that ALO algorithm shows the best result with lesser cost and time.

## 5 Conclusion

The industrial loads are considered here for energy management problem. The loads are separated as different types by considering the requirement of the industries like fixed, shiftable and uninterruptable. Then the cost formula is formulated as objective function and the type of load are considered as constraints. The problem is solved by four different algorithms and the results are graphed and tabulated. Finally, the Ant-lion algorithm is identified as solution for this energy management problem.

## References

1. Deploying a smarter grid through cable solutions and services (2010). [http://www.nexans.com/Corporate/2010/WHITE-PAPERSMART-GRIDS-\(2010\).pdf](http://www.nexans.com/Corporate/2010/WHITE-PAPERSMART-GRIDS-(2010).pdf). Accessed 31 Jan 2016
2. Guo Y, Pan M, Fang Y (2012) Optimal power management of residential customers in the smart grid. IEEE Trans Parallel Distrib Syst 23(9):1593–1606
3. Agnetis A, de Pascale G, Detti P, Vicino A (2013) Load scheduling for household energy consumption optimization. IEEE Trans Smart Grid 4(4):2364–2373
4. Nilsson H (1994) The many faces of demand-side management. Power Eng J 8(5):207–210
5. Logenthiran T, Srinivasan D, Shun TZ (2012) Demand side management in smart grid using heuristic optimization. IEEE Trans Smart Grid 3(3):1244–1252
6. Rao SS (2009) Engineering optimization: theory and practice, 4th edn. Wiley, Hoboken



7. Yang XS (2010) A new metaheuristic bat-inspired algorithm. In: Nature inspired cooperative strategies for optimization (NISCO 2010). Studies in computational intelligence, vol 284, pp 65–74
8. Fathy A, Abdelaziz AY (2018) Single and multi-objective operation management of micro-grid using krill herd optimization and ant lion optimizer algorithms. *Int J Energy Environ Eng* 9:257
9. Manjunath TG, Kusagur A (2018) Robust fault detection of multilevel inverter using optimized radial basis function based artificial neural network in renewable energy power generation application. *Int J Comput Appl* 180(48):8–15
10. Manjunath TG, Kusagur A (2018) Analysis of different metaheuristics method in intelligent fault detection of multilevel inverter with photovoltaic power generation source. *Int J Power Electron Drive Syst* 9(3):1214–1222

# A Research of Noise Estimation and Removal Techniques for Speech Signal

B.P. Mishra, Laxman Singh, Spoorti J. Jainar, Nagaraja B. G.

**ABSTRACT---** In this paper, authors made an attempt to implement the active noise control technique (ANC) to decrease the amplitude of noise communicating through the environment using an electro-acoustic (EA) system with the help of measurement sensors such as microphones and output actuators such as loudspeakers. In general, the noise signal is generated from ambient; therefore, it is easy to detect the noise in the vicinity of its source. The main objective of developing the ANC system is to generate an "anti-noise" that reduce the unwanted noise in a desired quiet region using an appropriate adaptive filter. The simulations were performed in the MATLAB 2015 environment and satisfactory results were obtained using the proposed technique. The problem under study is different from traditional adaptive noise cancellation techniques in two ways. Firstly, it is not possible to measure the desired response of a signal directly measured; only the signal with reduced magnitude is present. Secondly, the ANC system is required to take into consideration the secondary loudspeaker-to-microphone error (LME) path in its adaptation.

## 1. INTRODUCTION

In case of electrical noise cancellation, Adaptive filters are mostly used wherein the desired signal is considered as a filter output. In control applications, the adaptive filter serves as a controller with the capability to control the dynamic systems containing actuators and amplifiers. In such types of systems, estimate (anti sound) is considered as the electrical quantity received from a dynamic system. Since dynamic system exists between the filter output and estimate, the selection of adaptive filter is done with utmost care. In this work, the ANC technique has been proposed to reduce the magnitude of an unwanted noise communicating through the environment using an EA system using measurement sensors such as microphones and output actuators such as loudspeakers. As we know that the noise signal generally comes from environment; therefore, it is possible to detect the noise close to its source. The ultimate goal of developing the ANC is to attenuate the noise signal in a desired quiet region by using an "anti-

noise" that could be produced using an appropriate adaptive filter. After implementation of the proposed technique, the simulation results were obtained in MATLAB and the results seems to be quite satisfactory. The problem under study is different from traditional adaptive noise cancellation techniques in two ways. Firstly, it is not possible to measure the desired response of a signal directly measured; only the signal with reduced magnitude is available. Secondly, the ANC system is required to take into consideration the secondary LME path in its adaptation.

## 2. METHODOLOGY USED & RESULTS

In control applications, the adaptive filter is used as a controller with the capability to control the dynamic systems containing actuators and amplifiers. In such sort of systems, estimate (anti sound) is considered as the output signal received from a dynamic system. Since dynamic system exists between the filter output and estimate, the selection of adaptive filter is done with utmost care. In this case, a conventional adaptive LMS algorithm is found to be unstable due to the delay provided by the forward path [1, 2]. The x-LMS algorithm is well known adaptive filter algorithm that has proven its worth for active control (AC) applications [3]. LMS algorithm is the foundation of filtered x-LMS algorithm, which is illustrated by Figure 1. In this algorithm, a forward path is introduced between the input signal and the algorithm for the adaptation of the coefficient vectors [3, 4].

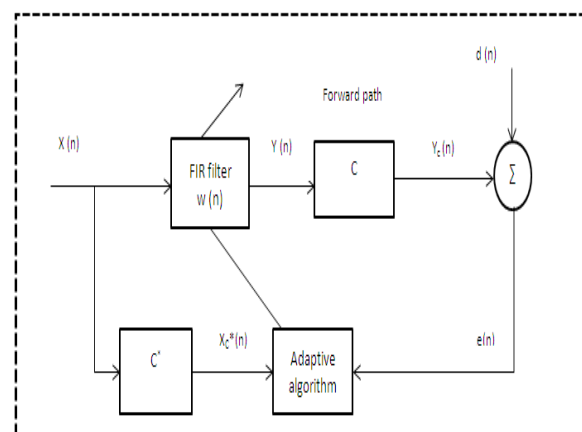


Fig.1. Active control system based on a filtered x-LMS algorithm

The implementation of active noise control technique is discussed as follows step by step:

Revised Manuscript Received on July 10, 2019.

**B.P. Mishra**, Dept. of Elect. & Comm. Engineering, JSS Academy of Technical Education, Noida. India.(email: bpmishra@jssaten.ac.in)

**Laxman Singh**, Dept. of Elect. & Comm. Engineering, Noida Institute of Engg., & Technology, Greater Noida. India (email: laxman.mehlawat2@gmail.com)

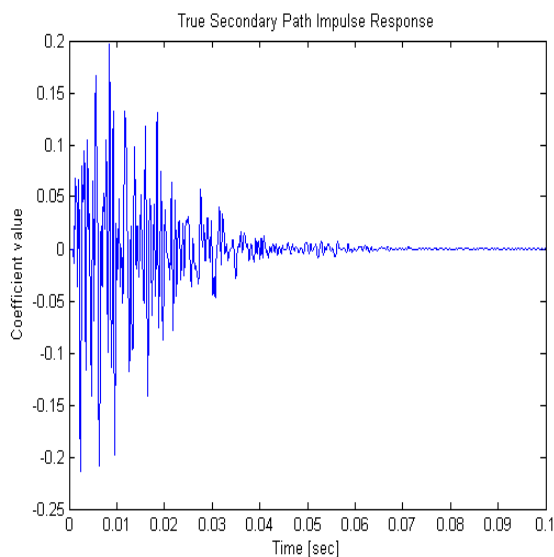
**Spoorti J. Jainar**, Dept. of Elect. & Comm. Engineering, JSS Academy of Technical Education, Noida. India (email: spoorti@jssaten.ac.in)

**Dr Nagaraja B. G.** Dept. of Elect. & Comm. Engineering, Jain Institute of Technology, Davanagere, Karnataka. India (email: nagarajbg@gmail.com)

- (a) The Secondary Communication Path
- (b) Determination of Secondary Propagation Path (SPP)
- (c) SPP Design
- (d) Performance evaluation of SPP Estimate
- (e) The Primary Communication Path
- (f) The Noise Cancellation
- (g) ANC Using the Filtered-X LMS
- (h) Residual Error Signal (RES) Spectrum

#### (a) The Secondary Communication Path

SPP is considered as the path that is followed by anti-noise from the output loudspeaker to the error microphone (LTEM). A LTEM impulse response of frequency range 160 - 2000 Hz was produced with a filter of length 0.1[1-2]. In order to perform this operation, a sampling frequency of 8000 Hz was used.



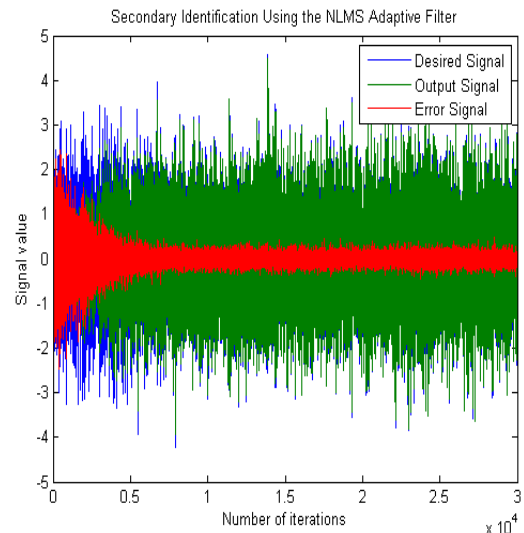
**Figure 2: Impulse Response of True SPP**

#### (b) Determination of SPP

In the ANC system, first we calculate impulse response of the secondary communication path. This step is generally implemented before controlling the noise through generation of random signal. It is obtained from the output loudspeaker in absence of noise. To accomplish this, the random signal of 3.75 seconds time duration along with the measured signal at the error microphone was generated [3]. The impulse response of secondary path is illustrated in Figure 2.

#### (c) SPP Design

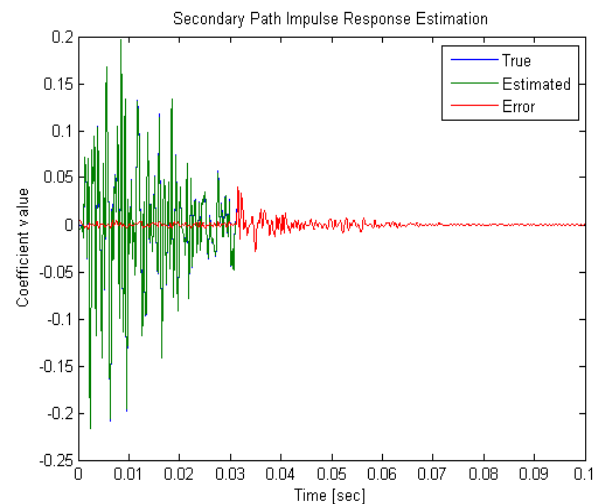
Most often, the length of the secondary communicating path filter is not equal to the length of the actual secondary communicating path. It does not require being so for an effective control in major active noise control techniques. A secondary filter with a length of 250 taps was used. This was used in response to an impulse response that has the length of 31 msec. While any adaptive FIR filtering technique may be used to perform it, the LMS algorithm is mostly preferred due to its reliability, robustness and higher efficiency [4-6]. The secondary path impulse response is plotted and illustrated in figre2. The output response of the normalized LMS filter is presented in Figure 3.



**Figure 3: Output Response of Normalized LMS Filter**

#### (d) Performance evaluation of SPP Estimate

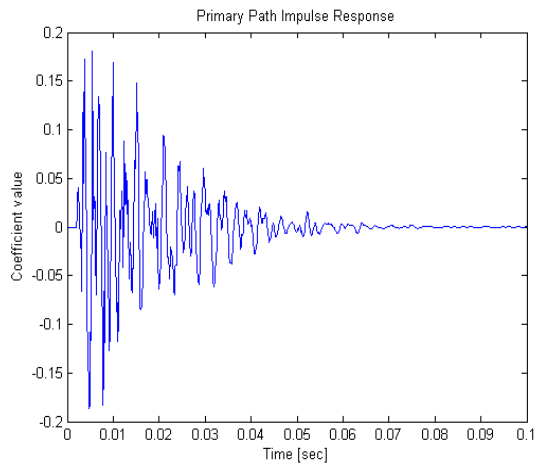
The accuracy of the SP impulse output response is calculated from the plot that depicts the coefficients of both the actual and approximated path. However, it was not possible to estimate the actual output of the tail accurately. The ANC system remains unaffected due to this error while deployed for a particular task [7].The output impulse response for a secondary communicating path is displayed as figure 4.



**Figure 4: Output Impulse Response for Secondary Communicating Path**

#### (e) The Primary Communicating Path

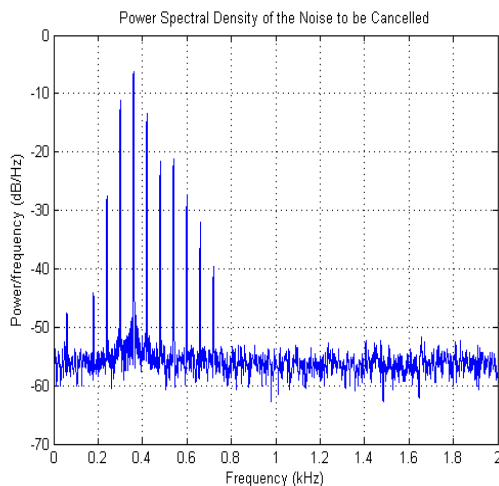
A linear filter was designed for the cancellation of noise in the propagation path. For this, the impulse response was generated that is shown in Figure 5 in the band of 200-800 Hertz.



**Figure 5: Output Response of Primary Communicating Path**

*(f) The Noise Cancellation*

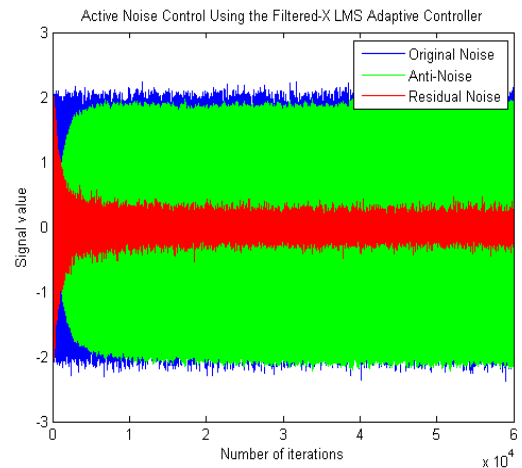
In our research work, a typical active noise control application was applied by synthetically generating 7.5 seconds of an ambient noise [8]. The spectrum of the sound was also generated. The plot for the power spectral density (PSD) of the estimated noise is given in Figure 6.



**Figure 6: PSD of the Estimated Noise**

*(g) ANC Using the Filtered-X LMS*

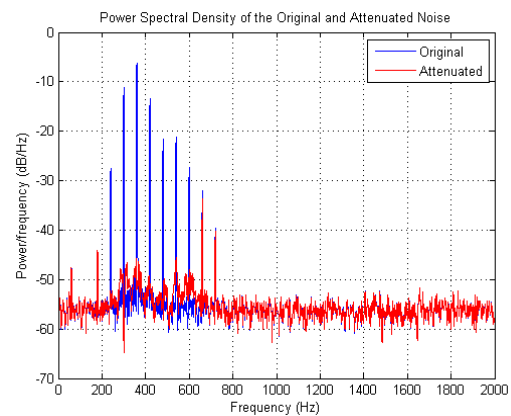
The filtered-X LMS algorithm is very popular adaptive system for ANC. In this we approximated the secondary path to yield an electrical output response which get mixed with the noise at the error sensor. Here, we get the noisy signal. In this, a controller filter length of about 44 msec with a size of 0.0001 has been incorporated for this signal [9, 10]. The resulting algorithms tend to converge after 5 seconds. With the error signal, the output volume level is decreased significantly. The output response of Filtered LMS is illustrated in Figure 7.



**Figure 7: ANC Using the Filtered LMS Adaptive Controller**

*(h) REC Spectrum*

After having compared the spectrum of the RE signal with the original one, we found that most of the periodic components were suppressed highly. The noise cancellation was not done equally over all frequencies range; however, this is acceptable for real-world systems applied to ANC systems [19-20]. PSD plot of original and suppressed noise signal is given in Figure 8.



**Fig. 8: PSD of the Original and suppressed Noise Signal**

### 3. CONCLUSION

In the current work, a filter of 0.1 seconds duration was generated for SSP by using a LTEM impulse response having band limit range from 160 - 2000 Hz. A sampling frequency of 8000 Hz was used in this. To approximate the secondary propagation path, 3.75 seconds of random noise signal was activated along with the detected signal at the microphone. SPP was designed using a secondary communicating path filter with a length of 250 taps, in response to an impulse signal 31 milliseconds duration. The LMS filter has been employed here due to its better performance and robustness. The output and error illustrated by different figures demonstrates that the algorithm converges after running 10,000 iterations. For creating the primary propagation path, a filter with a length of 0.1

seconds was employed using an input-to-error microphone impulse response in the frequency range of 200 - 800 Hz. In our research work, a typical ANC application has been applied by synthetically generating 7.5 seconds of an ambient noise.

## REFERENCES

1. P. A. Nelson and S. J. Elliott, Active control of sound. New York, NY, USA: Imperial College Press, 1992.
2. S. M. Kuo and D. R. Morgan, "Active noise control: A tutorial review," *Proc. IEEE*, vol. 87, no. 6, pp. 943–973, Jun. 1999.
3. S. J. Elliott and P. A. Nelson, "Active noise control," *IEEE Signal Process. Mag.*, vol. 10, no. 4, pp. 12–35, Oct. 1994.
4. S. Haykin, Adaptive filter theory. Englewood Cliffs, NJ, USA: Prentice-Hall, 1986.
5. S. J. Elliott, I. M. Stothers, and P. A. Nelson, "A multiple error LMS algorithm and its application to the active control of sound and vibration," *IEEE Trans. Acoust., Speech, Signal Process.*, vol. 35, no. 10, pp. 1423–1434, Oct. 1987.
6. B. Widrow and S. D. Stearns, Adaptive signal processing. Englewood Cliffs, New Jersey, USA: Prentice-Hall, 1985.
7. S. Elliott, I. M. Stothers, P. A. Nelson, A. M. McDonald, and D. C. Quinn, "The active control of engine noise inside cars," in *Proc. InterNoise Conf.*, New York, 1998, pp. 987–990.
8. A. Gonzalez, M. Ferrer, M. D. Diego, G. Pinero, and J. J. GarciaBonito, "Sound quality of low-frequency and car engine noises after active noise control," *J. Sound Vibr.*, vol. 265, pp. 663–679, 2003.
9. S. Elliott, P. Nelson, I. Stothers, and C. Boucher, "In flight experiments on the active control of propeller-induced cabin noise," *J. Sound Vibr.*, vol. 140, pp. 219–238, 1990.
10. S. M. Kuo and D. R. Morgan, Active Noise Control, Algorithms and DSP Implementations. New York, NY, USA: Wiley, 1996.
11. J. Lorente, M. Ferrer, M. de Diego, J. A. Belloch, and A. Gonzalez, "GPU implementation of a frequency-domain modified filtered-x LMS algorithm for multichannel local active noise control," in *Proc. 52nd Audio Eng. Soc. Int. Conf.*, Sep 2013.
12. Q. Shen and A. S. Spanias, "Time and frequency domain x block LMS algorithms for single channel active noise control," in *Proc. 2nd Int. Congr. Recent Develop. Air-and Structure-Borne Sound Vibr.*, 1992, pp. 353–360.
13. S. C. Douglas, "Fast implementations of the filtered-x LMS and LMS algorithms for multichannel active noise control," *IEEE Trans. Speech Audio Process.*, vol. 7, no. 4, pp. 454–465, Jul. 1999.
14. J. P. Borrallo and M. G. Otero, "On the implementation of a partitioned block frequency domain adaptive filter (PBFDAF) for long acoustic echo cancellation," *Signal Process.*, vol. 27, no. 3, pp. 301–315, 1992.
15. P. Sommen, "Partitioned frequency domain adaptive filters," in *Proc. 23rd Asilomar Conf. Signals, Syst., Comput.*, 1989, vol. 2, pp. 677–681.
16. E. Bjarnason, "Active noise cancellation using a modified form of the filtered-x LMS algorithm," in *Proc. 6th Eur. Signal Process. Conf.*, 1992, vol. 2, pp. 1053–1056.
17. M. Pawełczyk, "Feedforward algorithms with simplified plant model for active noise control," *J. Sound Vibr.*, vol. 225, pp. 77–95, 2003.
18. R. Burdisso, J. Viperman, and C. Fuller, "Causality analysis of feedforward-controlled systems with broadband inputs," *J. Acoust. Soc. Amer.*, vol. 94, no. 1, pp. 234–242, 1993.
19. D. P. Das, G. Panda, and S. M. Kuo, "New block filtered-x lms algorithms for active noise control systems," *IET Signal Process.*, vol. 1, no. 2, pp. 73–81, 2007. P. Cardinal, P. Dumcoulhel, and G. Boulianne, "Large vocabulary speech recognition on parallel architectures," *IEEE Trans. Acoust., Speech, Signal Process.*, vol. 21, no. 11, pp. 2290–2300, Nov. 2013.
20. R. Mazur, J. O. Jungmann, and A. Mertins, "On CUDA implementation of a multichannel room impulse response reshaping algorithm based on p-norm optimization," in *Proc. IEEE Workshop Appl. Signal Process. Audio Acoust. (WASPAA)*, 2011, vol. 24, pp. 305–308.



## Improved Alpha Blending Algorithm for the Authentication of Medical Images Using LWT & QR Code

Kavitha K. J.<sup>1</sup> and Priestly B Shan<sup>2</sup>

1. ECE Dept, Jain Institute of Technology,
2. Davangere & CSE Dept, Sathyabama University, Chennai  
Email: kavithakj219@gmail.com, kavithakj192@gmail.com
3. Eranad Knowledge City-Technical Campus, Manjeri, Kerala  
Email: priestlyshan@gmail.com

### ABSTRACT

Telemedicine is widely practicing applications in the field of healthcare system because of its easiness in accessing the patient detail without wasting much time and money. National Health Portal in India is about to launch 'Myhealthrecord' (MHR) to store and access prescriptions, laboratory test results, medical images and wellness related information of patient's with the help of Information technology. With this development, protecting MHR becomes a challenging task for the health organizations being stolen by the fraud to make illegal money. Many measures may be taken by the Government to avoid such cases. In that case, Digital watermarking (DWM) techniques may play a major role to claim authenticity and assure security to the MHR of a person. Although many DWM techniques are developed, no complete algorithm is available to make this technique robust. Hence still DWM remains an open research for the scientists. In this paper an approach of digital watermarking is proposed to enhance the security to the n-dimensional medical images (MI) along with other details of MHR. In this paper, Digital watermarking technique based on LWT & alpha blending algorithm is proposed for MI to enhance the security, authenticity while maintaining the perception of the watermarked image as that of the original medical image transmitted. A modified alpha blending embedding and extraction method is proposed to make the system more robust and QR code of a MHR is used as watermark and a secret key is incorporated to increase the security. The proposed technique is applied to 2-D and 3-D MI and subjected to various attacks and then the performance of the system is evaluated. The experimental result shows that, the efficiency of the proposed system increased in terms of the quality metrics PSNR, average square error, Correlation coefficient and absolute error. With the use of modified alpha blending algorithm and secret key, the system robustness is increased and QR code together with the secret key increases the security.

**Keywords:** DWM, QR code, Alpha blending algorithm.

**Mathematics Subject Classification:** 62J12, 62G99

**Journal of Economic Literature (JEL) Classification:** Q12, D24

### 1. INTRODUCTION

The growth of network has made the multimedia data transmission very easy. Basically an analog data is converted in to Digital data to transfer over the network. Once the analog data is converted to digital, the digital process is reversible and no longer protected. This allows the unauthorized use of

ISSN 2231-525X  
[www.ceser.in/ceserp](http://www.ceser.in/ceserp)  
[www.ceserp.com/cp-jour](http://www.ceserp.com/cp-jour)



the digital media and leads to fraud actions. To overcome such problems, the scientists have come with the solution of Digital watermarking technique. It does not stop the illegal activities done by the fraud but instead it can alert someone really who is authorized. Until the watermarking techniques become robust, the research on this topic will continue.

In healthcare applications, patient's data security is a major concern. Many fraud cases have been reported worldwide. To avoid such cases, much research has been done using DWM technique.

Irrespective of simple implementation and low computational complexity, the spatial based watermarking having low bit capacity and less robust to image compression. These kinds of watermark can be easily removed by cropping. For the optimization of embedding capacity, transform methods are evolved. This method is optimized for robustness to sustain the effect of many attacks including noise, Gaussian filter and compression etc. The lifting wavelet transform is the substitution for the other existing frequency domain techniques.

## 2. THE RESEARCH METHOD

The flowchart used for medical image watermarking is as shown in Figure1. The scanned medical image is read from the database and is subjected to segmentation to separate ROI & RONI region. The RONI region is subjected to 3-Level decomposition. At the same time, the MHR is read from the database, converted to QR code and subjected 3-Level decomposition. Then an improved alpha blending embedding algorithm is applied followed by inverse decomposition to get the watermarked image. A public key is used for enhancing the security and authentication and key information is generated which further improves the security to the system. At the receiver side, the exact opposite function is performed to extract the water mark image and reconstruct the original image.

### 2.1 Pre-processing

#### ***Segmentation at the cover image:***

As a first step in the process, the cover image (jpg, png, tiff, gif) is read from the database. The color image is converted to gray image so as to reduce noise, low complexity of the code, and to increase the speed of processing. Now the image is subjected to polygon based segmentation as it is a powerful tool as expected by many of the radiologists and more over it is technically not complicated and it separates the ROI region from RONI region.

#### ***QR code generation at the watermark:***

In this work, 3-watermarks are used; The ID of patient, Hospital logo and patient's MHR; each of them is encoded as a separate QR code and concatenated in to a single QR code and then it is embedded at different levels of the Cover medical Image(MI) so as to maintain data payload. The process of QR generation is shown below:

#### **Generate**

QR1 → Patient Aadhaar ID

QR2 → Hospital logo

QR3 → Patient details

Concatenate

$QRC = cat(3, R, G, B) \rightarrow \text{Embedded in MI at different levels}$

## 2.2 Decomposition

The proposed system uses LWT to divide the image into 4-sub bands (LL, LH, HL & HH) as it gives the detailed information of both frequency and spatial components of information. Among the 4 frequency bands, LL band is chosen for embedding the watermark; as it contains maximum information and large amount of energy of the image; embedding in this part increases the robustness. Also, the decomposition is repeated at 3-levels as the underneath levels contain more information and less noise. The subsequent levels may be used for storing different watermarks and later can be extracted at the corresponding levels at the receiver side.

## 2.3 Watermark Embedding Process

As stated above LWT is applied to both MI and QR code of the watermark at 3-levels and QR watermark is embedded in LL of the MI using modified Alpha blending Embedding Algorithm described as:

$$wmi = \alpha(LL \text{ of } MI) + (\beta/\alpha)(LL \text{ of } wm)$$

Where  $\alpha = \text{scaling factor} = 1 \leq \alpha \leq 2$

$\beta = \text{payload factor} = 0.5 \leq \beta \leq 1$

$wm = \text{watermark/PHR}$

$MI = \text{scanned medical image (US, MRI, CT)}$

$wmi = \text{watermarked medical image}$

The flowchart of watermark embedding process is as shown in Figure1. After this process, inverse LWT is applied to generate the watermarked medical image.

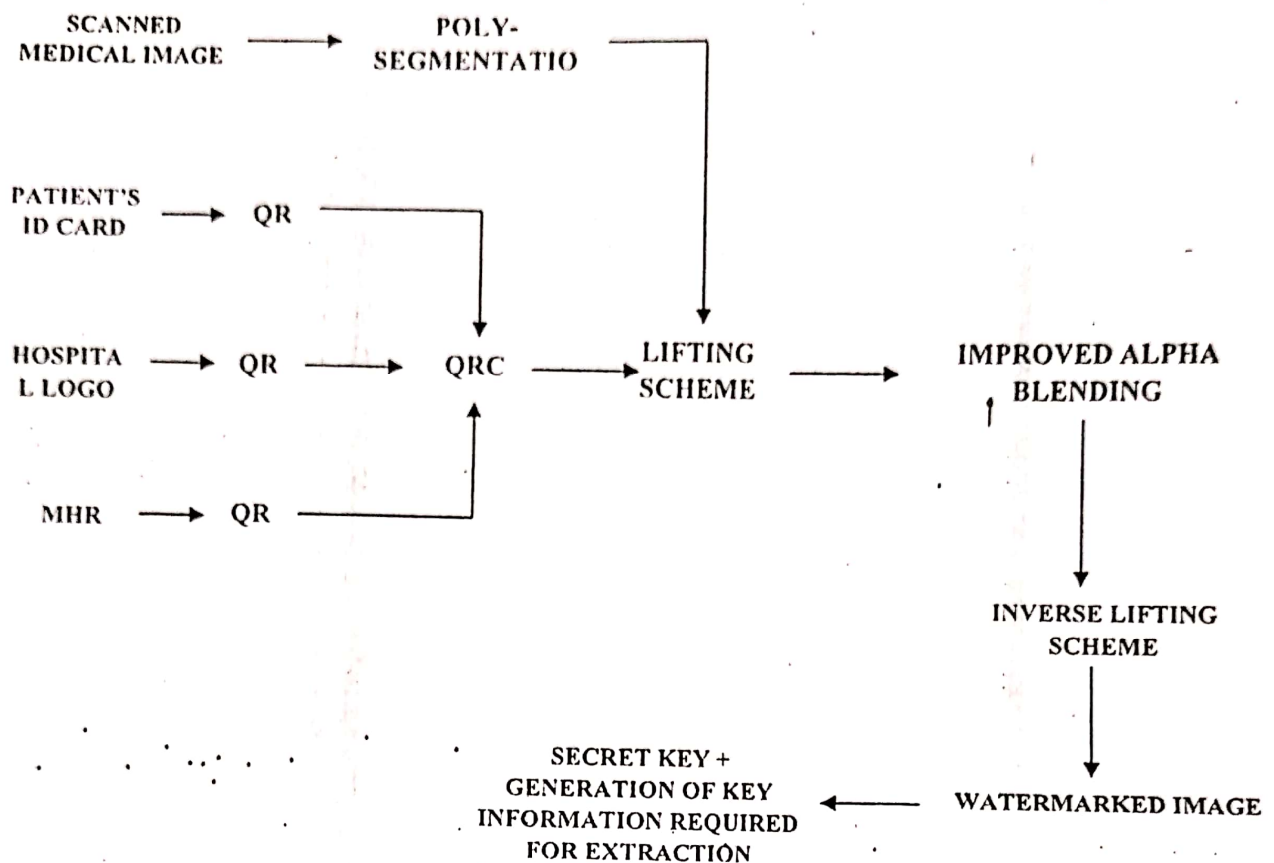


Figure 1: Proposed Watermarking System for Medical data

## 2.4 Key Generation

After embedding process, a secret key is to be transmitted in a convenient way (either over phone or using any communication) for accessing the information and also 3-key information are generated so that it can be used at the extraction side to retrieve the watermark and by thus constructing the original MI and watermark. The key generation is described as below:

- ❖ A public key is issued for the authentication purpose at the receiver side and then, key information is generated using modulo 2 addition at the sender side as:

$$k1 = \text{mod}(ll1 \text{ of } CI + ll11 \text{ of } wm, 2)$$

$$k2 = \text{mod}(ll2 \text{ of } CI + ll22 \text{ of } wm, 2)$$

$$k3 = \text{mod}(ll3 \text{ of } CI + ll33 \text{ of } wm, 2)$$

## 2.4 Watermark extraction Process

At the receiver side, the received watermarked scanned medical image undergoes decomposition using LWT transform function and authentication is done by matching the received public key. After the gaining authentication, the keys are generated:

$$W = \text{lwt}(wmi) \text{ at } 3 - \text{levels}$$



As a result it will yield,

$ll1\_1, ll2\_2$  &  $ll3\_3$  -----Low frequency bands of wmi.

Generation of key information using modulo 2 subtraction process is as shown below:

$$ll3 = \text{mod}(k3 - ll3\_3 \text{ of wmi}, 2)$$

$$ll2 = \text{mod}(k2 - ll2\_2 \text{ of wmi}, 2)$$

$$ll1 = \text{mod}(k1 - ll3\_1 \text{ of wmi}, 2)$$

Now the modified alpha blending extraction algorithm is applied as:

$$RW = ll3\_3 \text{ of } W \times \alpha - ll3 \times (\beta/\alpha)$$

### Watermark extraction:

The flowchart of watermark extraction process is shown in Figure2. After the above process, inverse LWT is applied on Keys generated at the receiver side and other sub bands of watermarked image 'W' to extract the watermark.

$$\text{Extracted}_{\text{image1}} = \text{ilwt}(ll3 \text{ and } 3_{\text{level sub bands of } W}) \text{ --- (1)}$$

$$\text{Extracted}_{\text{image2}} = \text{ilwt}(ll2, \text{ and } 2_{\text{level sub bands of } W}) \text{ --- (2)}$$

$$\text{Extracted}_{\text{image3}} = \text{ilwt}(ll1, \text{ and } 1_{\text{level sub bands of } W}) \text{ --- (3)}$$

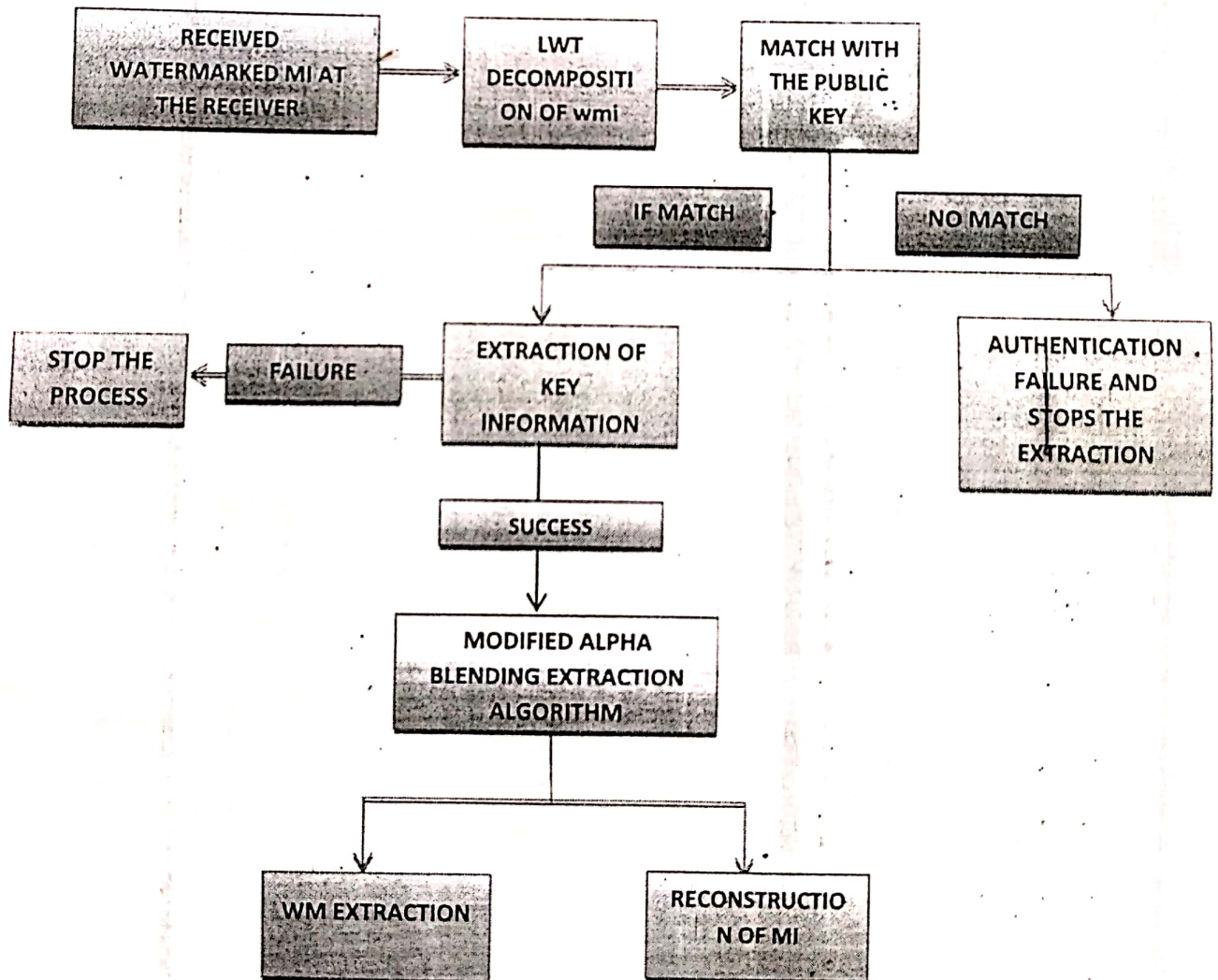


Figure 2: Block Diagram of watermark extraction process

### Original image Construction:

The scanned MI is constructed by performing inverse LWT RW and on other frequency components of LWT of watermarked image 'W' as below:

$$\text{Reconstructed}_{\text{image1}} = \text{ilwt}(\text{RW and } 3_{\text{level subbands of W}})$$

### 3. Results

The proposed system is evaluated nearly hundred US medical images, fifty MRI images and the Table1 shows the results of watermark embedding and extraction process. The result of the proposed method is compared with other methods and is as shown in Table2; Bit-plane method using IWT-QR, DWT-SVD method and 3-level LWT with alpha blending algorithm watermarking techniques: The quality metrics evaluated in the system are calculated as:

$$\text{PSNR} = (10 \log_{10} 255^2) / \text{MSE}$$

$$\text{MSE} = \frac{\sum_{i=1}^n \sum_{j=1}^n (CI(i,j) - wmi(i,j))^2}{M \times N}$$


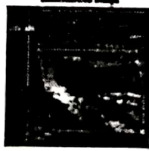







$$\text{NCC} = \frac{\sum \sum CI \times wmi}{\sum \sum wmi \times wmi}$$

$$\text{Error} = wmi - CI$$

$$\text{NAE} = \frac{\sum \sum \text{abs}(\text{Error})}{\sum \sum wmi}$$

The system is also evaluated for various attacks. The results obtained after the comparison between attacked watermarked image and the original watermarked image is shown in Table3.

Table 1: Results of WM embedding and extraction process

Type of image	Cover Image	Invisible watermark	Reconstructed MI
Image 1			
Image 2			
Image 3			






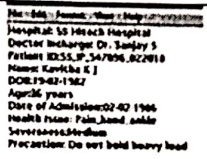
Original watermark	Extracted watermark	WM1 & WM2	WM3
			

Table2: Evaluation and comparison of the Proposed System

METHOD	PSNR (dB)	SSIM	MSE	NCC
BIT-PLANE METHOD USING IWT-QR	55.4684	0.8211	0.5920	0.7987
DWT-SVD	45.0682	0.6524	2.040	0.899
3-LEVEL LWT WITH ALPHA BLENDING ALGORITHM	77.2854	0.9078	0.012	0.997
PROPOSED SYSTEM WITH MODIFIED ALPHA BLENDING ALGORITHM	75.14	0.8721	0.021	0.912

Table3: Evaluation of the proposed system against various attacks

PROPOSED SYSTEM WITH MODIFIED ALPHA BLENDING ALGORITHM	PSNR (dB)		
Filter size	[3 3]	[6 6]	[10 10]
MEDIAN FILTER	85.683	76.592	75.514
WEINER FILTER	79.729	78.923	77.2466
GAUSSIAN FILTER (Q=0.5)	90.93	87.967	88.997
JPEG attack	69.27		

#### 4. Discussions

Based on the results obtained for the proposed system, we can observe that, the system yields optimum results and is applied for almost all types of MI: US, MRI, CT and X-ray. The system was tested for nearly hundred US and fifty MRI images.

As we know that the polygon based segmentation process is used to separate the ROI and RONI region in the case of MI, so that the diagnosis part should not be disturbed. The embedding of watermark is done in the RONI part of the image.

The conventional methods considered for comparison uses a single watermark for the embedding purpose whereas the implemented method embeds 3 different watermarks in the MI; Patient ID (E-Aadhar card is used) of size 32.4KB of dimension 252 × 365, Hospital Logo (Our institute logo is used) of size 2.75 KB with dimension 47 × 43 and PHR of size 9.47 KB with dimension 268 × 218. These watermarks are converted to QR code to reduce the number of bits hidden in the MI.

LWT is used for the compression purpose in this paper as it has many advantages over other transform domain techniques such as: Increase in smoothness, reduced aliasing effect, Information loss is very small, Increases the integrity of the embedded watermark, Increases the robustness of the system & Yields smooth image after reconstruction. In order to provide privacy, authenticity and



security to the patient's data, a public key along with Key information is used which is generated using modulo two addition and subtraction.

The alpha blending algorithm is more suitable compared to other methods whenever merging of two images is required. Hence in this work, improved alpha blending embedding and extraction algorithm is used in which the scaling factors have a wide range of values. The system is evaluated against various attacks and the result show that the system is reasonably proves to be robust.

## 5. Conclusions

Medical data transmission has become very popular all over the world. So, it becomes necessary for the health care centers to protect the privacy, integrity and authenticity of the patient details. The proposed system gives better results compared to other techniques in terms of PSNR, SSIM, MSE and NCC, but the disadvantage of the system is that, the system uses alpha blending algorithm to embed the watermark and is easily decodable if alpha and beta range is known and moreover if anyone able to decode the QR code and get the information, the patient's privacy is lost and may lead to the fraud cases.

Therefore, we can see that Digital watermarking techniques won't stop fraud activities until the system becomes 100% robust and hence to avoid such cases, we can adopt the encoding and encryption techniques along with DWM and the system can be made more robust by combining spatial & frequency domains and will considered as the future scope of the system.

## 6. References

- Michael Cobb, 2013, an article "The advantages of digital watermarking in enterprise data protection" July.
- C. Su, J. Huang, C. Shih, and Y. Chen, 2015, "Reversible and Embedded Watermarking of Medical Images for Telemedicine," SESA, EAI publisher, pp. 145-150.
- N.Nikolaidis et.al, 1998, "Robust image watermarking in the spatial domain", Elsevier, vol. 66, issue. 3, pp. 385-403.
- M. S. Goli et.al, 2017, Introducing a new method robust against crop attack in digital image watermarking using two-step sudoku, *3rd International Conference on Pattern Recognition and Image Analysis (IPRIA)*, Shahrekord, pp. 237-242.
- C. N. Sujatha et.al, 2016, Analysis of robust watermarking techniques: A retrospective, *International Conference on Communication and Signal Processing (ICCSP)*, Melmaruvathur, pp. 0336-0341.
- Wang, et.al, 2015, A novel scrambling digital image watermark algorithm based on double transform domains." *Mathematical problems in engineering*
- C. Zhang, et.al, 2008, Digital Image Watermarking Algorithm with Double Encryption by Arnold Transform and Logistic, *Fourth International Conference on Networked Computing and Advanced Information Management*, Gyeongju, pp. 329-334.
- M. Malonia et.al, 2016, Digital Image Watermarking using Discrete Wavelet Transform and Arithmetic Progression technique, *IEEE Students' Conference on Electrical, Electronics and Computer Science (SCEECS)*, Bhopal, pp. 1-6.
- Chen, et.al, 2000, Digital watermarking using DCT transformation, *Department of Electronic Engineering National ChinYi Institute of Technology*.
- C. m. Pun, 2006, A Novel DFT-based Digital Watermarking System for Images, *8th international Conference on Signal Processing*, Beijing.

## Research Article

K. J. Santhosh Kumar\* and Rajaneesh N. Marigoudar

# Comparative study of cutting force development during the machining of un-hybridized and hybridized ZA43 based metal matrix composites

<https://doi.org/10.1515/jmbm-2019-0016>

Received Nov 02, 2019; accepted Nov 14, 2019

**Abstract:** In the present study, turning of two grades of composites such as ZA43 silicon carbide and ZA43 silicon carbide and graphite was carried out. The fabrication of both categories of composites were done using stir casting technique. The silicon carbide of grit size  $60\mu\text{m}$  with concentration of 5% was reinforced for one category of the composite and for the other grade of composite, 5% silicon carbide and graphite were added. Thus fabricated materials were turned on a conventional lathe using coated carbide tools (SNMG). Dry turning of the fabricated composite was carried out with varying cutting parameters. Measurement of cutting force was done for the both compositions of fabricated materials using lathe tool dynamometer. It was observed that, while machining composite containing silicon carbide and graphite, tool experience more cutting force than composite containing silicon carbide alone.

**Keywords:** Hybrid metal matrix composites, turning, coated carbide tool, graphite, cutting force

## 1 Introduction

Aluminium metal matrix composites find wide range of applications in the field of automobile industries, aerospace applications, defence etc. due to their excellent properties such as light weight, high strength, wear resistance, strength – weight ratio, strength to cost ratio and low thermal expansion [1]. A lot of efforts have been made to mix the hard particulates such as SiC,  $\text{Al}_2\text{O}_3$ ,  $\text{B}_4\text{C}$  into aluminium based MMCs. Literature survey reveals that, SiC is the best reinforcement for aluminium based MMCs due

to its chemical affinity towards the aluminium and forms a good bond with the matrix without developing inter-metallic phase. Nowadays, due to increased industrial requirement of engineering materials which are having high strength and high wear resistance, hybrid MMCs are developed [2, 3]. The main factor that prevents embracing the MMCs is the difficulty in machining them due to high abrasive and intermittent nature of the reinforcements. Generally MMC components are mostly manufactured near to the close dimensions and then machined to the final dimensions and final surface finishes. Conventional tool materials such as high speed steel cannot be used for the machining of MMCs because of the rapid tool wear. Coated or uncoated carbide tools and ceramic tools sustain the tool wear significantly and are best choice for the machining of MMCs [4–7].

Zinc and Aluminium based alloys have very good wear resistance properties which are comparable with properties of cast iron. Commercially available ZA alloy has 27% of aluminium which has favourable properties. When the presence of aluminium in the alloy increased to 43%, the wear resistance and hardness increases, at the same time fluidity and elasticity decreases. Adding the ceramic particulate particles to such a high wear resistant alloy makes the resultant alloy to have superior wear resistant property [8–11]. Machining such composite with commercially available tool is very difficult because of hard reinforcement. The important factor which influence the tool life is supply of lubrication during the machining process. Instead of applying fluid externally for machining process, solid lubricant is introduced into the matrix during fabrication stage itself so that the friction during machining process get reduced and life span of cutting tool improves. Adding graphite to ZA alloy reduces the tool wear at all working conditions because it offers less coefficient of friction between work piece and tool [12].

In this paper importance is given to analyze the development of cutting force during the machining of MMC. When an alloy alone comes in contact with the cutting tool during the process of machining, forces developed on

\*Corresponding Author: K. J. Santhosh Kumar: Dept. of Mechanical Engineering, G M Institute Technology, Davanagere – 577006, Karnataka, India; Email: kjsanthu1991@gmail.com

Rajaneesh N. Marigoudar: Dept. of Mechanical Engineering, Jain Institute Technology, Davanagere – 577003, Karnataka, India

the cutting tool is somewhat predictable. But when the reinforcements embedded in the same alloy come in contact with the tool forces acting on the tool become unpredictable. The soft matrix phase in the matrix deforms plastically easily and show good machinability characteristics, whereas the hard reinforcement phase behaves unnaturally. Many researchers have studied and presented their ideas theoretically and experimentally regarding the cutting force developed while machining these heterogeneous materials.

Anandkrishnan and Mahamani [13] investigated on machinability of Al6061-TiB<sub>2</sub> MMC fabricated through flux-assisted synthesis. The result shows that higher reinforcement ratio produces higher tool wear, surface roughness and minimizes the cutting forces. Increase in cutting force and the rate of flank wear with depth of cut and feed rate was observed. Paulo Devim [14, 15] investigated on machinability of Al-356 reinforced with SiC composite. Dry turning was done using PCD tools. The results of the work show that feed rate affects the surface roughness and cutting speed affects the cutting force.

Manna and Bhattacharya [16, 17] worked on machinability characteristics of aluminium MMC reinforced with SiC particles. Turning was done using rhombic coated and uncoated carbide tools and investigated the effect of feed rate, cutting speed and depth of cut on cutting force was analyzed. The results shows that increase in cutting force with the increase in feed and decrease in cutting speed. Chou [18] worked on the MMC and investigated the effect of speed and feed on cutting force. The results of the study reveal that the cutting force was decreased with increase in cutting speed and increased with increase in feed rate.

Kishway *et al.* [19, 20] investigated on MMC and observed that the linear increase in the cutting force with the feed rate and decrease in cutting force with the cutting speed. Rajaneesh and Sadashivappa [21] analysed the cutting forces developed while machining the MMC using ceramic tool. The results of study reveal that increasing depth of cut, particle size and volume fraction increase the cutting force significantly and increasing cutting speed cause the decrease in cutting force. Suhas Joshi *et al.* [22, 23] developed a mathematical model in order to determine the cutting forces developed during the machining of aluminium based MMC reinforced with SiC. According to the model, the reinforcement particles present in the MMC are responsible for the variation in values of cutting force during machining. Zhang [24] developed a mathematical model to predict the cutting force and thrust force while machining the MMC reinforced with hard particulates. The cutting force was considered that it consist of components due to formation of chips, ploughing and particle fracture,

and displacement. Merchant's shear plane theory, slip line field theory and Griffith theory were used for the calculation of these components respectively. The study revealed that the cutting force developed due to ploughing and particle fracture is much more less than the cutting force developed due to chip formation. Sikdar [25] proposed the similar type of model to determine the cutting force developed while machining the MMC reinforced with hard particulates by considering particle fracture force, ploughing force and frictional characteristics at tool-chip and tool-work interfaces. The effect of volume fraction of reinforcements in the MMC on cutting force can also be calculated using this model. In this model, only 3% cutting force and 15% thrust force variation was observed between the experimental and mathematical values.

Looking at the observations proposed by the various researchers mentioned above, it is clear that there is a lot of scope for the analysis of machinability of MMC reinforced with hard particulates using various types of cutting tools. In this paper, effect of graphite and machining parameters on cutting force development during machining of two different categories of materials was compared.

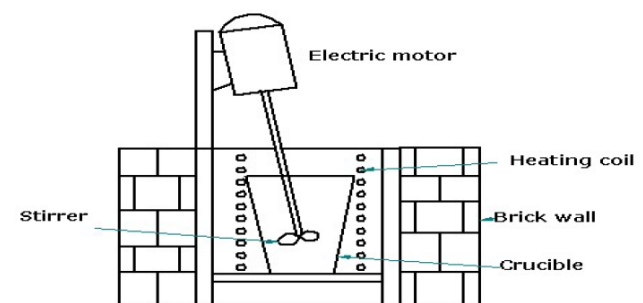
## 2 Materials and testing

The composition of zinc aluminium matrix alloy is as given in the Table 1.

Both the categories of composites were fabricated by stir casting method. The setup of stir casting is as shown in Figure 1. The weighed amount of metal as per the alloy composition is taken in the crucible and heated above the melting temperature of aluminium till whole mass in

**Table 1:** Composition of matrix in their weight percentages

Element	Al	Cu	Mg	Zn
Percentage (wt.)	43	2.5	0.02	Rest



**Figure 1:** Stir casting mechanism for casting MMC



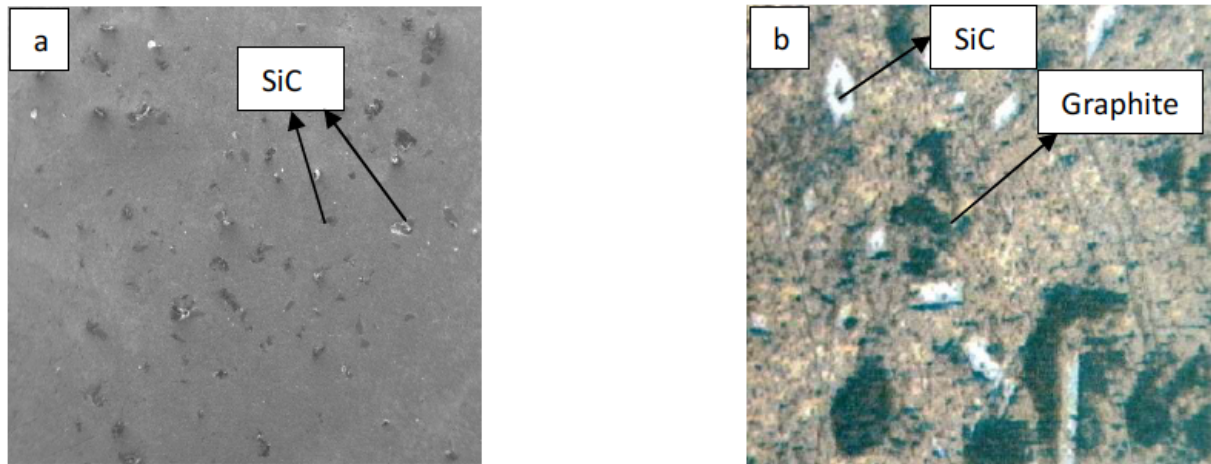


Figure 2: a) SEM image of Un-hybridised MMC b) SEM image of hybridised MMC

Table 2: Cutting tool inserts specifications


Tool specification	Tool image
Coated Tungsten Carbide – SNMG – 090308 (Kennametal WIDIA Tool)	
Square insert with 9mm × 9mm square, thickness of 3mm and 0.8mm corner radius – Normal clearance of 0° – Tolerance of nose height ±0.08 – ±0.18, Tolerance of inscribed circle ±0.05 – ±0.15, Tolerance of thickness ±0.13, Double sided chip breaker. Triple layer CVD coated with Al <sub>2</sub> O <sub>3</sub> , TiN and TiCN.	

Table 3: Selection of machining parameters and their levels

Parameters	Units	Level 1	Level 2	Level 3
Speed	m/min	95	125	175
Feed	mm/rev	0.05	0.1	0.15
Depth of cut	mm	0.25	0.50	0.75

the crucible come to liquid phase. To have unhybridized composite, pre heated silicon carbide particles (60  $\mu\text{m}$ , 5% by weight) were introduced in to the molten matrix and stirred well using coated stainless steel blade at a speed of around 600 rpm. The coating to the stainless blade was done to prevent the diffusion of blade material in to the matrix material. To have hybridized material, to the molten matrix, pre heated silicon carbide (60  $\mu\text{m}$ , 5% by weight) and graphite (10  $\mu\text{m}$ , 5% by weight) powder both were introduced and stirred.

The preheating of the SiC and graphite was done to improve the wettability of the composite. A small percentage of magnesium was added into the liquid metal which will also help to increase the wettability [26, 27]. The stirring was done for the uniform distribution of reinforcing materials in to the molten matrix. Thus stirred mass was transferred to suitable metallic dies and allowed for solidification. Once material attain the room temperature, specimen

were removed from the dies and subjected to further testing conditions. The fabricated specimen bear dimensions with 300 mm length and 54 mm diameter.

Microscopic study of the MMCs was carried out using Scanning Electron Microscope (SEM) to know the distribution of the reinforcing particles in the matrix. SEM images of the composites are shown in Figure 2(a) and 2(b). The distribution of the particles was found uniform and at some portions clustering of Graphite and SiC particles was observed.

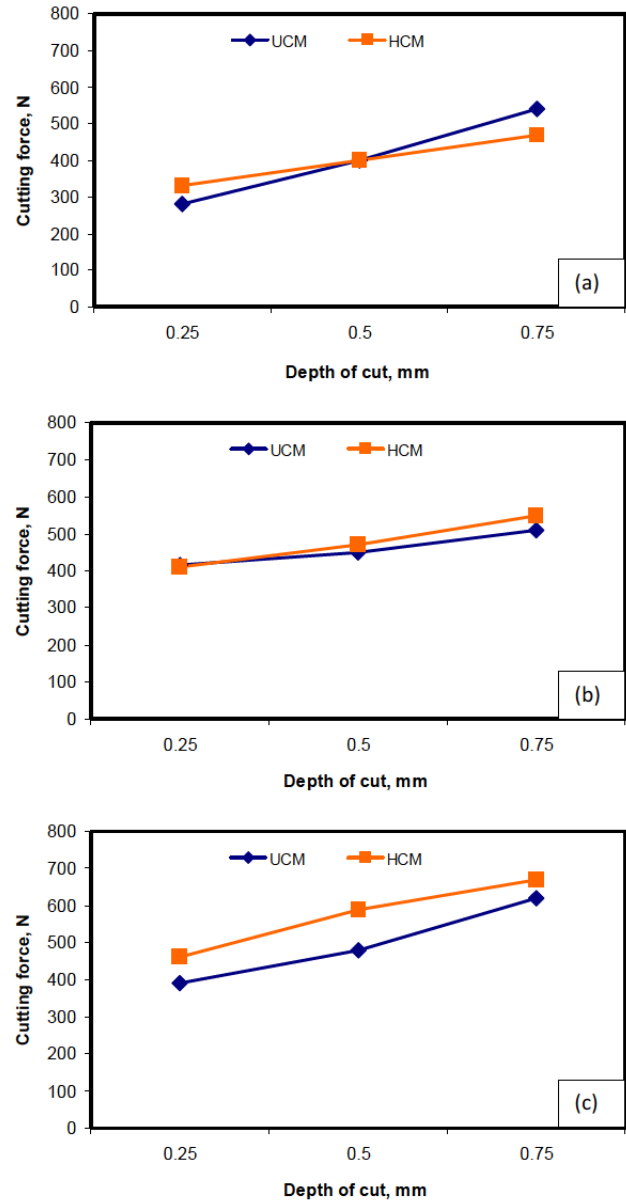
The main aim of the study is to compare the cutting force development while machining hybridised and un-hybridised composites in order to identify the effect of Graphite on the cutting force development. Dry turning test was done on both categories of materials using coated carbide tool multilayered coated carbide insert SNMG 090308 K15 with TiN, TiCN, Al<sub>2</sub>O<sub>3</sub>, and TiN coating. The specifications of the cutting tool used in the experimental work is given in the following Table 2. For each trial fresh edge of the tool insert was used to turn a length of 75 mm. The cutting force ( $F_x$ ) was measured during turning process using lathe tool dynamometer and the values were recorded and compared. The machining parameters considered for the experimentation and their corresponding levels are presented in Table 3.

### 3 Results and discussions

The force required to shear off the material plastically from the workpiece depends on various factors such as hardness, composition and microstructure of the material to be machined, type and material of the cutting tool used, heat generated during machining and machining parameters. Experiment was done to determine the cutting force developed during machining process by considering three cutting parameters such as speed, feed and DOC. For each trial, the cutting force was measured by keeping any two parameters as constant and third parameter was varied. Experiment was carried out both on hybridised and un-hybridised composites and graphs were plotted and compared to determine the effect of graphite on cutting force.

#### 3.1 Effect of depth of cut on cutting force

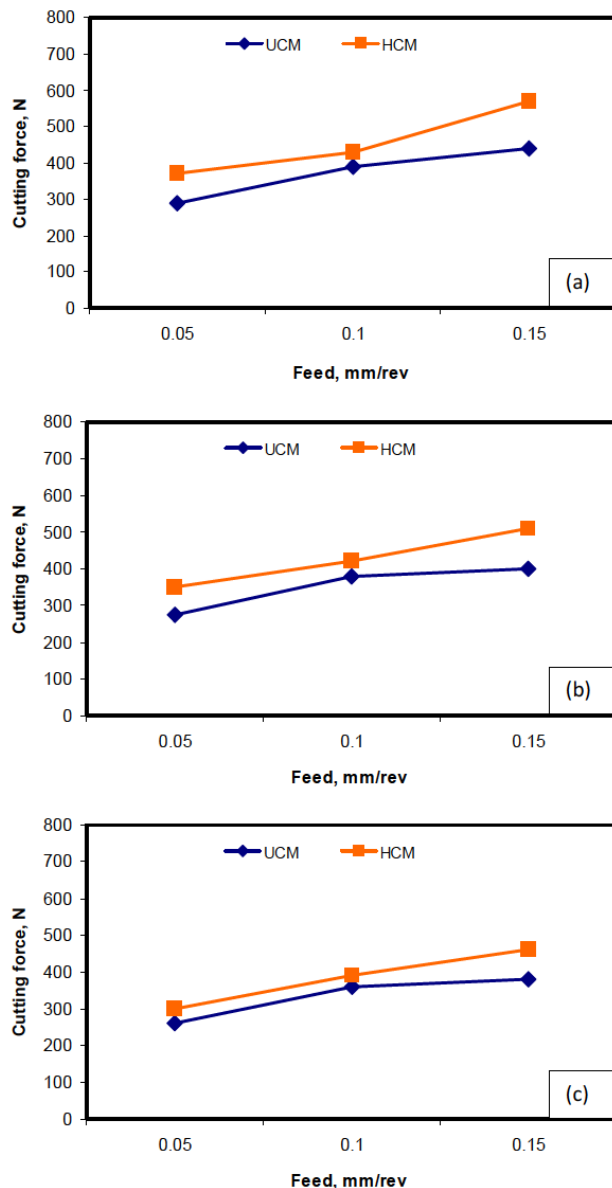
Figures 3(a), (b), and (c) show the variation of cutting force with DOC for constant feed rate of 0.05 m/rev and cutting speeds of 95 m/min, 125 m/min and 175 m/min respectively for both hybridised (HC) and un-hybridised (UHC) composites. The graph clearly indicates the increasing trend with increase in depth of cut. Similar machining tests were done on fabricated composite specimen keeping feed constant and varying cutting speed at three different levels as mentioned earlier. In all the cases of experimentation, upon increase in the depth of cut, increased cutting force is noticed. Same trend is noticed even for hybridized composite with higher cutting force. Approximately 30% increase in the cutting force is noticed between two consecutive depth of cuts and nearly 20% increase in the cutting force between unhybridized and hybridized composite material. When the DOC increases, tool penetrates more into the workpiece and hence there will be more area of contact between the workpiece and tool. This results more friction between the two surfaces which causes increase in cutting force. The cutting force developed at higher depth of cut is more for hybridised composites than un-hybridised. The reason for higher cutting force for hybridized composite is, addition of graphite as a secondary reinforcement along with SiC which increases the hardness level of the composite [12]. Increased material hardness certainly offers high resistance for the material deformation. The presence of more reinforcement concentration packed inside the metal matrix impinges the cutting tool inturn increases the cutting force.



**Figure 3:** Variation of cutting force with depth of cut, (a) cutting speed 95 m/min, feed 0.05 mm/rev (b) cutting speed 125 m/min, feed 0.05 mm/rev (c) cutting speed 175 m/min, feed 0.05 mm/rev

#### 3.2 Effect of feed on cutting force

During the machining process, feed rate has great influence on variation in cutting force. The machining tests were done on both the categories of materials with increasing feed viz. 0.05 mm/rev, 0.1 mm/rev and 0.15 mm/rev respectively by keeping constant depth of cut of 0.25 mm and three cutting speeds as mentioned earlier. The following graphs were plotted considering recorded values of the experimental work.



**Figure 4:** Variation of cutting force with increasing feed rate (a) cutting speed 95 m/min, depth of cut 0.25 mm (b) cutting speed 125 m/min, depth of cut 0.25 mm (c) cutting speed 175 m/min, depth of cut 0.25 mm

By observing the trend, it is clear that increase in the cutting force is noticed for increase in the feed rate. For a cutting speed of 95 m/min and constant depth of cut of 0.25 mm and for the feed of 0.05 mm/rev, cutting force noticed was 290 N. When feed is increased to 0.1 mm/rev, cutting force was increased to 390 N and further increasing feed to 0.15 mm/rev, cutting force was increased to 440 N. This increasing trend recorded for unhybrid composite material. With same set of machining conditions, hybrid composite specimen was turned and cutting force values were recorded. The values were 370 N, 430 N and 570 N re-

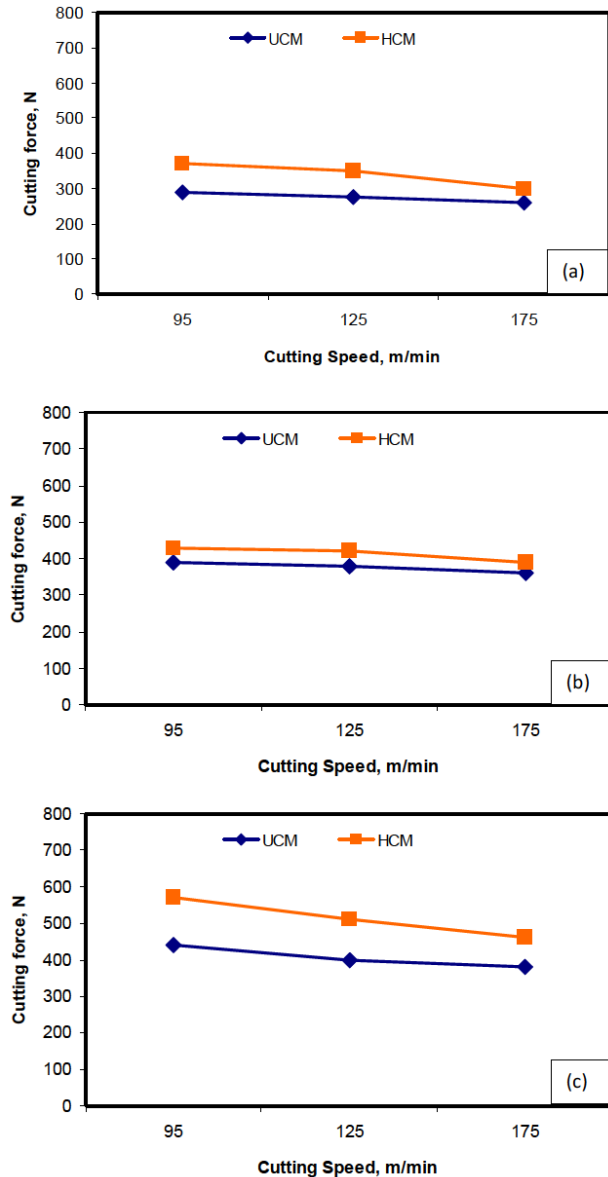
spectively for 0.05 mm/rev, 0.1 mm/rev and 0.15 mm/rev feed. Similar machining trials were executed for cutting speed of 125 m/min and 175 m/min. In all the cases, approximately 20% to 25% increase in the cutting force values were noticed between unhybridized and hybridized composite materials. As the feed rate increases, the relative movement between the tool and workpiece along the workpiece length increases. Tool tries to advance through the hard phase of the workpiece resulting in cutting force development. The variation in the cutting force is because of hard reinforcement phase in the composite material. The hybrid composite offers higher resistance for the deformation compared to unhybrid composite. This may be due to the presence of dual reinforcement in the matrix which shows still higher resistance to the deformation compared to unhybrid composite material. Packing of reinforcements takes place in the unit mass of matrix alloy which leads to increased hardness which in turn increases the cutting force.

### 3.3 Effect of cutting speed on cutting force

To study the variation of cutting force with variation of cutting speed, both feed and depth of cut is kept constant for each set of machining trial and cutting speed is varied. All the three cutting speeds 95 m/min, 125 m/min and 175 m/min were employed and variation is studied. Figure 5 shows the variation of cutting force for varying cutting speed.

The feed of 0.05 mm/rev and depth of cut of 0.25 mm with all three cutting speeds shows declining trend of cutting force. For 95 m/min, 125 m/min and 175 m/min, the cutting force development for unhybridized composites were 290 N, 275 N, 260 N respectively. By observing the variation it is clear that cutting force decreases with increase in cutting speed. Same machining tests were done on hybridized composite specimen and similar declining trend was recorded. For the cutting speed of 95 m/min, 125 m/min and 175 m/min, the cutting force developed was 370 N, 350 N, 300 N for hybridized composite respectively. Approximately 25% to 30% variation in the cutting force was noticed between hybridized and unhybridized composite material machining. Similar experimental trials were done by varying feed and results were recorded. The declining trend may be due to the fact that the rise in temperature while machining the composite increases with the increase in cutting speed. At elevated temperature levels, the matrix phase becomes soft, hence the force required to cut the metal will be less. It can also be observed from the graph that the cutting force developed for hy-





**Figure 5:** Variation of cutting force with increasing cutting speed (a) feed 0.05 mm/rev, depth of cut 0.25 mm (b) feed 0.1 mm/rev, depth of cut 0.25 mm (c) feed 0.15 mm/rev, depth of cut 0.25 mm

bridised composite is more compared to the un-hybridised composite. This may be due to the increased friction during machining process leading to higher temperature development. As cutting temperature increases, the force required to deform the material decreases. The hybridized composite develops higher cutting force at lower temperature and lower cutting force at higher temperature. The presence of graphite in the matrix may reduce the tool wear during the machining process where as it increases the cutting force.

## 4 Conclusions

The present paper deals with fabrication of hybridized and un-hybridized composites i.e. ZA43 alloy reinforced SiC particulate composite and ZA43 alloy reinforced SiC and graphite composites. Both the categories of materials were machined with coated carbide tool under selected set of machining conditions. While machining, the cutting force was measured using three axis lathe tool dynamometer. Forces developed are compared and conclusions are drawn as follows.

1. The depth of cut has direct effect on the cutting force development. As depth of cut is increased, cutting force increases correspondingly. The cutting force developed during machining of hybridized composite was higher compared to un-hybridized composites for a particular depth of cut.
2. The variation of feed during machining has direct impact on the cutting force. The value of the cutting force increases with the increase in feed rate. The cutting force developed during the machining of hybridized composite was higher than as obtained during the machining of un-hybridized composite for the same feed.
3. The cutting speed affects the cutting force in declining way. For both the types of composites, the cutting force developed during the machining tends to decrease with the increase in cutting speed. The development of higher cutting force was observed for hybridized composite over the un-hybridized composite.
4. By observing and analysing all the results obtained during the machining of both the types of composites, it was obvious that the addition of graphite into the matrix phase as the secondary reinforcing element increases the cutting force for all the experiments conducted.

## References

- [1] Das S., Development of aluminium alloy composite for engineering applications Trans. Ind. Instit. Mater., 2004, 27 (4), 325-334.
- [2] Umakanth K., Palani Kumar K., Selvamani S.T., Analysis of dry sliding wear behaviour of Al6061/SiC/Al<sub>2</sub>O<sub>3</sub> hybrid metal matrix composites, Compos. Eng. Part B, 2013, 53, 159-168.
- [3] James S.J., Venkatesan K., Kuppan P., Ramanujam R., Hybrid aluminium metal matrix composite reinforced with SiC and TiB<sub>2</sub>, Proc. Eng., 2014, 97, 1018-1026.
- [4] Davim J.P., Baptista A.M., Relationship between cutting force and PCD cutting tool wear in machining silicon carbide reinforced

- aluminium, *J. Material Proc. Technol.*, 2000, 103, 417-423.
- [5] Kannan S., Kishawy H.A., Brunswick N., On the role of reinforcements on tool performance during cutting of metal matrix composites, *J. Manuf. Proc.*, 2006, 8(2), 67-71.
  - [6] Ozben T., Kilickap E., Orhan C., Investigation of mechanical and machinability properties of SiC particle reinforced Al-MMC, *J. Mater. Proc. Technol.*, 2007, 8, 220-225.
  - [7] Marigoudar R.N., Kanakuppi S., Investigation of tool wear and surface roughness during machining of ZA43-SiCp composite using full factorial approach, *J. Eng. Manuf.*, 2013, 27, 321-331.
  - [8] Aydin M., High cycle fatigue behaviour of severe plastically deformed binary Zn-60Al alloy by equal-channel angular extrusion, *J. Mater. Proc. Technol.*, 2012, 212(8), 1780-1789.
  - [9] Ares E., Schvezov C.E., The effect of structure on tensile properties of directionally solidified Zn-based alloys, *J. Cryst. Growth*, 2011, 318(1), 56-65.
  - [10] Zhu Y.H., Biao Y., Wei H., Bearing wear resistance of monotectoid Zn-Al based alloy (ZA-35), *J. Mater. Sci. Technol.*, 1995, 11, 109-113.
  - [11] Purcek G., Saray O., Kucukomeroglu T., Haouaoui M., Karaman I., Effect of equal-channel angular extrusion on the mechanical and tribological properties of as cast Zn-40Al-2Cu-2Si alloy, *Mater. Sci. Eng. A*, 2010, 527(15), 3480-3488.
  - [12] Basavarajappa S., Chandramohan G., Rao K.V.N., Turning of particulate metal matrix composite-review and discussion, *Proc. Inst. Mech. Eng., Part B: J Eng. Manuf.*, 2006, 220, 1189-1204.
  - [13] Anandkrishnan V., Mahamani A., Investigations of flank wear, cutting force and surface roughness in the machining of Al-6061-TiB<sub>2</sub> in situ metal matrix composites produced by flux assisted synthesis, *Int. J. Adv. Manuf. Technol.*, 2010, 55 (1-4), 65-73.
  - [14] Davim J.P., Anto A., Conceic C.A., Optimal cutting conditions in turning of particulate metal matrix composites based on experiment and genetic search model, *Compos. Part A*, 2002, 33, 213-219.
  - [15] Davim J.P., Turning metal matrix composites: Experimental study of the evaluation of cutting forces, tool wear and work piece surface roughness with the cutting time, *Proc. Instit. Mech. Eng., Part B: J. Eng. Manuf.*, 2001, 215B, 371-376.
  - [16] Manna A., Battacharya B., Influence of machining parameters on the machinability of particulate reinforced Al/SiC-MMC, *Int. J. Adv. Manuf. Technol.*, 2004, 25, 850-856.
  - [17] Manna A., Battacharya B., A study on machinability of Al/SiC-MMC, *J. Adv. Manuf. Technol.*, 2003, 140, 711-716.
  - [18] Chou Y.R.K., Liu J., CVD diamond tool performance in metal matrix composite machining, *Surf. Coat. Technol.*, 2005, 200, 1872-1878.
  - [19] Kannan S., Kishwy H. A., Deiab I., Cutting forces and TEM analysis of the generated surface, *J. Mater. Process. Technol.*, 2008, 9, 2260-2269.
  - [20] Zhu Y., Kishwy H.A., Influence of the alumina particles on the mechanics of machining metal matrix composites, *Int. J. Mach. Tool Manuf.*, 2005, 45, 389-398.
  - [21] Marigoudar R.N., Kanakuppi S., Analysis of cutting forces developed during turning of SiC reinforced ZA43 mmc with ceramic tool using design of experiments, *J. Manuf. Sci. Prod.*, 2012, 12, 129-137.
  - [22] Dabade U.A., Dapkekar D., Joshi S.S., Modelling of chip-tool interface friction to predict cutting forces in machining of Al/SiC composites, *Int. J. Mach. Tool Manuf.*, 2009, 49, 690-700.
  - [23] Dabade U.A., Joshi S.S., Balasubramaniam R., Bhanuprasad V.V., Surface finish and integrity of machined surfaces on Al/SiC composites, *J. Mater. Process. Technol.*, 2007, 193, 166-174.
  - [24] Pramanik L., Zhang C.A., Arsecularatne J.A., Machining of metal matrix composites: Effect of ceramic particles on residual stress, surface roughness and chip formation, *Int. J. Mach. Tool Manuf.*, 2008, 48, 1613-1625.
  - [25] Sikder S., Kishwy H.A., Analytical model for force prediction when machining metal matrix composite, *Int. J. Mech. Sci.*, 2012, 59, 95-103.
  - [26] Lim S.C., Gupta M., Ren L., Kwok J.K.M., The tribological properties of Al+Cu/SiC metal matrix composites fabricated using the rheocasting technique, *J. Mater. Process. Technol.*, 1991, 90, 591-596.
  - [27] Hashim J., Looney L., Hashmi M.S.J., Wettability of SiC particles by molten aluminium alloy, *J. Mater. Process. Technol.*, 2001, 119, 324-328.

## Investigation and Study of Mechanical Properties of Areca Shell Fiber and Palm Powder Natural Composites

Somashekhara J<sup>1</sup>, Ramesh B T<sup>2</sup>, Vinay Belagavi<sup>3</sup> & Madhu H T<sup>4</sup>

<sup>1,2</sup> Assistant Professor, MED, Jain Institutes of Technology, Davangere, Karnataka-577003

<sup>3,4</sup> Assistant Professor, MED, Jain Institutes of Technology, Davangere, Karnataka-577003

Corresponding Author: Ramesh B T

---

**Abstract:** Natural fibers are considered to have potential use as reinforcing material in polymer matrix composites because of their good strength, stiffness, low cost, less weight and environment friendly. The interest in natural fiber-reinforced polymer composite materials is rapidly growing both in terms of their industrial applications and fundamental research. They are renewable, cheap, completely or partially recyclable, inexpensive, moderate weight, eco-friendly and biodegradable. In the present work an effort has been made to study the mechanical properties of Areca shell fiber, Areca palm powder and Epoxy reinforced natural composites. It is found from the result that, the mechanical properties of tensile, flexural and impact test of treated areca shell fiber composites is more compared to untreated areca shell fiber composites. In compression and hardness test the untreated areca shell fiber composites have shown better results than compare to treated areca shell fiber composites. From the investigation it is better identified that mechanical properties of Areca shell fiber and Areca palm powder composites shown better strength properties compared to commercially available Nuwood.

---

Date of Submission: 26-12-2018

Date of acceptance: 11-01-2019

---

### I. Introduction

A Composite Material is a macroscopic combination of two or more distinct materials, having a recognizable interface between them. Composites are used not only for their structural properties, but also for electrical, thermal, tribological, and environmental applications. Modern composite materials are usually optimized to achieve a particular balance of properties for a given range of applications. Given the vast range of materials that may be considered as composites and the broad range of uses for which composite materials may be designed, it is difficult to agree upon a single, simple, and useful definition. The resulting composite material has a balance of structural properties that is superior to either constituent material alone. The improved structural properties generally result from a load-sharing mechanism. Although composites optimized for other functional properties (besides high structural efficiency) could be produced from completely different constituent combinations than fit this structural definition, it has been found that composites developed for structural applications also provide attractive performance in these other functional areas as well. Thus, composites typically have a fiber or particle phase that is stiffer and stronger than the continuous matrix phase. There are, however, exceptions that may still be considered composites, such as rubber-modified polymers, where the discontinuous phase is more compliant and more ductile than the polymer, resulting in improved toughness. Similarly, steel wires have been used to reinforce gray cast iron in truck and trailer brake drums [1].

#### 1.1 Natural Fiber Reinforced Composites

The interest in natural fiber-reinforced polymer composite materials is rapidly growing both in terms of their industrial applications and fundamental research. They are renewable, cheap, completely or partially recyclable, and biodegradable. Plants, such as flax, cotton, hemp, jute, sisal, kenaf, pineapple, ramie, bamboo, banana, etc., as well as wood, used from time immemorial as a source of lignocelluloses fibers, are more and more often applied as the reinforcement of composites. Their availability, renew ability, low density, and price as well as satisfactory mechanical properties make them an attractive ecological alternative to glass, carbon and man-made fibers used for the manufacturing of composites. The natural fiber containing composites are more environmentally friendly, and are used in transportation (automobiles, railway coaches, aerospace), military applications, building and construction industries (ceiling panelling, partition boards), packaging, consumer products, etc [2-4]. Therefore natural fibers (sisal, areca, etc.) have attracted the attention of scientists & technologists for application in consumer goods, low cost housing and other civil structures. It has been found that these natural fiber composites possess good mechanical properties with low specific mass, better electrical resistance, good thermal & acoustic insulating properties. Despite the attractiveness of natural fiber reinforced

polymer matrix composites they suffer from lower modulus, lower strength & relatively poor moisture resistance compared to synthetic fiber reinforced composites such as glass fiber reinforced plastics [5].

## 1.2 Natural Areca Shell Fibers

Among all the natural fiber-reinforcing materials, areca appears to be a promising material because it is inexpensive, availability is abundant and a very high potential perennial crop. It belongs to the species *Areca catechu* L., under the family palmecea and originated in the Malaya peninsular, East India. Major industrial cultivation is in East India and other countries in Asia. In India, areca nut cultivation is coming up on a large scale basis with a view to attaining self sufficiency in medicine, paint, chocolate, Gutka, etc. It is estimated that about 6 Lakh tonnes of areca husk is available in south West-India. The husk of the Areca is a hard fibrous portion covering the endosperm. It constitutes 30–45% of the total volume of the fruit. Areca husk fibers are predominantly composed of hemicelluloses and not of cellulose. In Table 1 the chemical composition of Areca fibers is shown along with few known fibers. Areca fibers contain 13 to 24.6% of lignin, 35 to 64.8% of hemicelluloses, 4.4% of ash content and remaining 8 to 25% of water content. The fibers adjoining the inner layer are irregularly lignified group of cells called hard fibers and the portions of the middle layer contain soft fibers. Table 1 compares the chemical composition of Areca fiber with some other important natural fibers. Areca fiber is highly hemicellulosic and is much greater than that of any other fibers. Coir has higher lignin content than fibers. Therefore extensive planning for the disposal of this material is required. The present use of this highly hemicellulosic material is as a boiler fuel when sufficiently dried. However for the use of these fibers as a reinforcing material for composites, a study of the chemical and physical characteristics is required [6] and [7].

**Table 1 Chemical composition of natural fibers**

Fiber	Lignin %	Cellulose %	Hemicellulose %
Areca	13-24.6	----	35-64.8
Maize Stalk	10-13	38-42	21-23
Coir	40-45	32-43	0.15-0.25
Sisal	10-14	66-72	12
Banana	5	63-64	19



**Fig. 1 Areca shell fiber and powder**

## 1.3 Areca Palm (Areca Catechu)

Among all the natural fiber-reinforcing materials, betel palm appears to be a promising material because it is inexpensive, availability is abundant and a very high potential perennial crop. It belongs to the species *Areca catechu* L., under the family palmecea and originated in the Malaya peninsular, East India. Major industrial cultivation is in East India and other countries in Asia. In India betel palm is used in the preparation of the Tiffin plates unlike paper plates. Betel palm powder is predominantly composed of cellulose and hemicelluloses. Betel palm contain 35.91% of cellulose, 26.6% of hemicelluloses, 16.6% of lignin, 9.19% of ash content and remaining 11.7% of moisture content.

## 1.4 Epoxy Resins

Epoxy resins are a class of thermoset materials used extensively in structural and specialty composite applications because they offer a unique combination of properties that are unattainable with other thermoset resins. Available in a wide variety of physical forms from low-viscosity liquid to high-melting solids, they are amenable to a wide range of processes and applications. Epoxies offer high strength, low shrinkage, and excellent adhesion to various substrates, effective electrical insulation, chemical and solvent resistance, low cost, and low toxicity. They are easily cured without evolution of volatiles or by-products by a broad range of chemical specie. Epoxy resins are also chemically compatible with most substrates and tend to wet surfaces easily, making them especially well suited to composites applications. Epoxy resins (ER) are one of the most important classes of thermosetting polymers which are widely used as matrices for fiber-reinforced composite

materials and as structural adhesives. The three basic elements of an epoxy resin formulation that must be understood when selecting a thermoset system are the base resin, curatives, and the modifiers. When formulating an epoxy resin for a particular use, it is necessary to know what each of these components contributes to the physical and mechanical performance of the part during and after fabrication [1]. Epoxy resin is a widely used polymer matrix for advanced composites where good stiffness, dimensional stability and chemical resistance are required.

### 1.5 Problem Identification

The interest in natural fiber reinforced polymer composite materials is rapidly growing both in terms of their industrial applications and fundamental research. They are renewable, cheap, completely or partially recyclable, and can be incinerated at the end of their life cycle for energy recovery as they possess a good deal of calorific value. They are also very safe during handling, processing and use. Therefore focus on the natural fibers than that of the other is given as more research work has not been done on areca palm powder and areca shell fiber reinforced composite. It looks hard to define a problem before doing an experiment. In the present work an effort has been made in order to prepare the composites using areca shell fiber and areca palm powder as reinforcement materials and study the mechanical properties such as tensile, compression, flexural, impact and hardness of that prepared polymer matrix composites.

## II. Materials And Specimen Preparations

### 2.1 MATERIALS

In the present work following materials have been used for the preparation of specimens as per requirements. The methodology used for the preparation is also explained.

#### 2.1.1 Matrix Material

Epoxy resin is widely used in industrial application because of their high strength and mechanical adhesiveness characteristic. It is also good solvent and has good chemical resistance over a wide range of temperature. The purpose of using this as Epoxy is that, it is having a medium viscosity, non-crystallizing epoxy material, with room temperature curing properties. Atul Ltd. Lapox L-12 and hardener K-6 purchased from Yuje Marketing, Bangalore, India, is used in the present investigation. The purpose of using hardener is it acts as curing agent. The weight percentage of hardener used in the present investigation is in the ratio of 10:1.

#### 2.1.2 Reinforcement Materials

Reinforcements can be both natural and man-made. Many materials are capable of reinforcing polymers. Some materials, such as the cellulose in wood, are naturally occurring products. Most commercial reinforcements are manmade. As opposed to common metal materials, fibers have anisotropic properties. In this work Areca shell fiber is used as reinforcement material and betel palm powder used as a filler material.

#### 2.1.3 Areca shell fiber

The Areca fibers obtained from Areca shell. In the extraction process first, the shell was soaked in water for 1 days to soften the fibers. The soaking process loosens the fibers and can be extracted out easily. Finally, the fibers were washed again with water and dried at room temperature for about 3 days. The dried fibers are designated as untreated fibers. These fibers are cut to short fibers (5-10mm) for the preparation of composites. The density of Areca shell fiber is found to be  $1.05 \text{ g/cm}^3$ . The chemical composition of Areca shell fiber used in the present work was found to be as shown in Table 2.

**Table2. Chemical composition of Areca shell fiber**

Composition	Weight in %
Cellulose	-----
Hemicellulose	35-64.8
Lignin	13-26
Moisture content	-----
Ash	-----

#### 2.1.4 Areca palm powder

The betel palms are available in local region. The collected betel palm were dried in atmosphere (Sun light) for duration of two weeks and subsequently broken into small pieces. It is then converted in to fine powder form with a grinder. The formed powder was sieved and grain size chosen in the range of 425 to 500 microns randomly. The density of betel palm is found to be  $0.81 \text{ g/cm}^3$ . The chemical composition of betel palm powder used in the present work is shown in Table 3.

**Table 3 Chemical composition of Areca palm powder**

Composition	Weight in %
Cellulose	35.91
Hemicellulose	26.6
Lignin	16.6
Moisture Content	11.7
Ash	9.19

## 2.2 ARECA SHELL FIBER TREATMENT

Chemical treatment on Areca shell fiber will usually remove the moisture content thereby increasing its strength and also enhances the mechanical properties. This treatment clears all the impurities and also stabilizes the molecular orientation. In view of this, the Areca shell fiber used in the preparation of the composite is pretreated with acidic solutions. Based on the literature, the Areca shell fiber is treated with acidic solutions namely HCl (Hydrochloric acid) which have 0.1 normality. The treatment is made for time duration of 5 hours. After chemical treatment the Areca shell fiber was washed thoroughly with deionised water to remove the residues of the chemical content in it. The washed Areca shell fiber is dried at room temperature.

## 2.3 FABRICATION

The fabrication of present work done by following steps,

- Moulds were prepared to fabricate the specimens as per the requirements of the tests to be conducted
- The inner surface of the mold was initially smeared with a releasing agent to prevent the composites from sticking on to the mold wall
- Areca palm powder, Areca shell fiber (in chopped form) with Epoxy and hardener were mixed in a container and stirred well for 5 – 7 minutes
- The prepared mixture is poured in to the prepared moulds
- The samples so prepared are kept for drying for a duration of 48 hours at room temperature
- After drying the samples were cut in accordance with ASTM standards and Specimens are prepared as per requirements

**Table 4 Details of combinations used for preparation of composite specimens**

Specimen Code	Specimen Composition		
	Epoxy Resin	Areca Shell Fiber	Areca Palm Powder
<b>Untreated Areca Fiber And Areca Palm Powder</b>			
Untreated F5% P20%	75%	05%	20%
Untreated F10% P15%	75%	10%	15%
Untreated F15% P10%	75%	15%	10%
<b>Treated Areca Fiber And Untreated Areca Palm Powder</b>			
Treated F5% P20%	75%	05%	20%
Treated F10% P15%	75%	10%	15%
Treated F15% P10%	75%	15%	10%

## 2.4 SPECIMEN PREPERATION

The composite specimens prepared were marked for required dimensions and then cut to the markings using a wire saw. The cut edges of composites were finished with emery paper in order to bring them to the exact size. Specimens of different sizes required for different tests according to ASTM standards were made ready. The test specimen along with their dimensions and standards for different tests are discussed below.

### 2.4.1 Tensile Test Specimens

Tensile test specimens were prepared according to ASTM D3039 standard. The photographic view of specimen is shown in Fig. 2 below. The specimen used is a rectangular bar of length 250mm, width 25mm and thickness 6.5mm.

**Fig. 2** Tensile Test Specimens Prepared by ASTM standards



#### **2.4.2 Compression Test Specimens**

Compression test specimens were prepared according to ASTM D695 standard. The photographic view of specimen is shown in Fig. 3 below. The specimen used is a rectangular bar of length 25.4mm, width 12.7mm and thickness 12.7mm.



**Fig. 3** Tensile Test Specimens as per ASTM standards

#### **2.4.3 Flexural Test Specimens**

Flexural test specimens were prepared according to ASTM D790 standard. The photographic view of specimen is shown in Fig. 4. The specimen used is a rectangular bar of 130mm length, 25mm width and 6.5mm thickness.



**Fig. 4** Flexural test specimens as per ASTM standards

#### **2.4.4 Impact Test Specimens**

Impact test specimens were prepared according to ASTM D256 standard. The photographic view of specimen is shown in Fig. 5. The specimen used is a rectangular bar of 63.5mm length, 10mm width and 10mm thickness.



**Fig. 5** Impact test specimens as per ASTM standards

#### **2.4.5 Hardness Test Specimens**

Hardness test specimens were prepared according to ASTM D785 standard. The photographic view of specimen is shown in Fig. 6. The specimen used is a rectangular bar of 10mm length, 10mm width and 6mm thickness.



**Fig. 6** Hardness test specimens as per ASTM standards

### **III. Experimental Setup And Result Discussion**

The experimental set has been made to conduct different experiments to find out different mechanical properties. In present work Universal Testing Machine was used For Tensile test, Flexural strength and compression test, Charpy test to analysis of Impact strength and vicker Hardness machine to know hardness. In fig. 7 shows that different testing setup to analysis mechanical properties of natural composites.



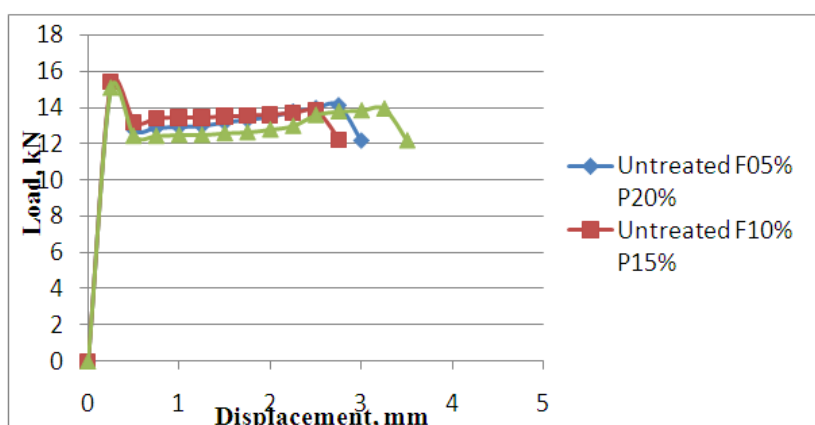
**Fig. 7** UTM and other testing set to find mechanical properties of natural composites

Analysis of the mechanical behaviour and moisture absorption of composites are the most important aspects. Performance testing of mechanical behavior and moisture absorption of composites depend on the nature of matrix material, the distribution and orientation of the reinforcing fibers, the nature of the fiber-matrix interfaces. Even small changes in the physical nature of the reinforcement for a given matrix may result in prominent changes in the overall mechanical behaviour and moisture absorption of composites.

### 3.1 MECHANICAL BEHAVIOUR OF COMPOSITES

In the present work, the mechanical behaviour of the composites was investigated by conducting the Tensile, Compressive, Flexural, Impact and Hardness tests. The tensile, compressive, and flexural tests were carried out by using Universal Testing Machine. The Izod test was done using impact testing machine and hardness (Rockwell hardness B) tester for finding the hardness value. The Machinability test for finding the roundness of the different compositional composite materials is carried out by using Profile Projector. The composite specimens which were prepared according to the ASTM standards tested for each property. The three different composition contents by weight ratio used are F05% P20%, F10% P15% and F15% P10% with epoxy.

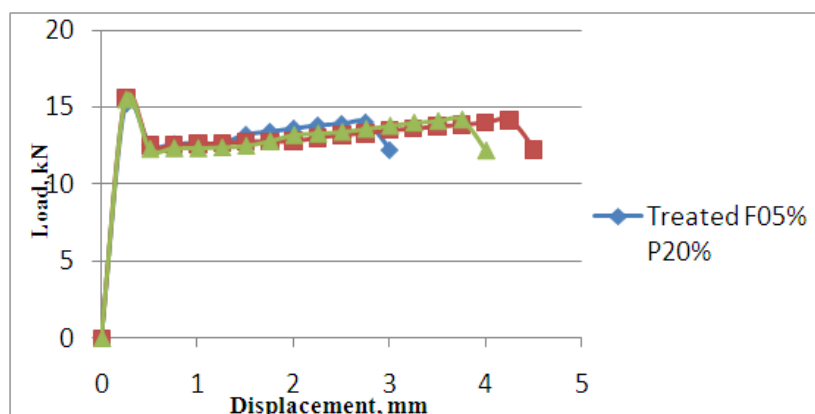
#### 3.1.1. Effect of Load on Tensile Strength of Natural Composites



**Fig. 8** Effect of Un-treated fiber content on the tensile strength of natural composites

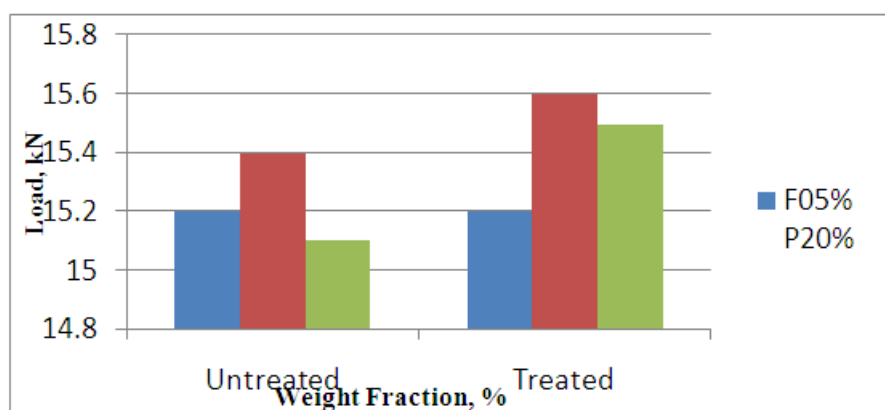
The effect of Un-treated fiber content on the tensile strength of all the combination of composites is shown In Fig. 8. It is evident from Fig. 8 that as the load goes on increasing the deformation increases. Maximum load of 15.4kN was observed in un-treated composite specimen having composition F10% P15% compared to other two specimens. The specimen with the composition indicated above withstands maximum part of load and by consequence raise the tensile strength of composite material. This might be the reason that the matrix material is well distributed with the fiber and filler particles. However, for 15% fiber composite the tensile strength decreases as it might be due to the presence of the void content [5]. These voids are expected to

be due to the proper squeezing pressure which had not been applied on the top surface of the material which might have caused the generation of voids and also during the exothermic reaction between matrix and reinforcement material at the rate of high temperature condition the gas absorption capacity will be more. This will also influences the generation of voids.



**Fig. 9** Effect of HCl-treated fiber content on the tensile strength of natural composites

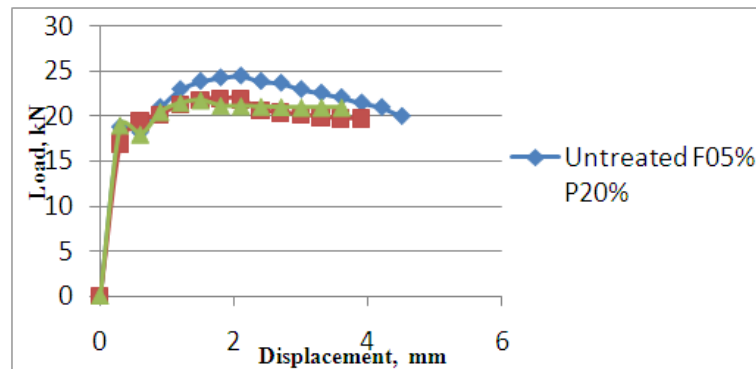
The Fig. 9 shows the effect of HCl-treated Areca shell fiber with three different combinations on the composite specimens. From the Fig 9 it can be observed that the composite specimen with the composition of F10% P15% sustain more load 15.6kN and more deformation compare to the other two specimens with compositions of F05% P20% and F15% P10% sustain loads up to 15.2kN and 15.5kN respectively. The specimen with composition of F15% P10% has high tensile strength compare to other two compositions of specimens because of high fiber content. The effect of alkali treatment improves the fiber strength, fiber matrix adhesion and the performance of the natural fiber composites by removing the natural and artificial impurities as well as softens the fiber which will gives high tensile strength to the fiber. This observation indicate that the fiber rich reinforced composites will sustain more tensile load and at the same time the chemical treatment of areca shell fiber allows rich bonding with the Palm powder filler by soaking the fibers in a known concentration of HCL.



**Fig. 10** Comparison of tensile strength of un-treated and treated specimens of three different combinations

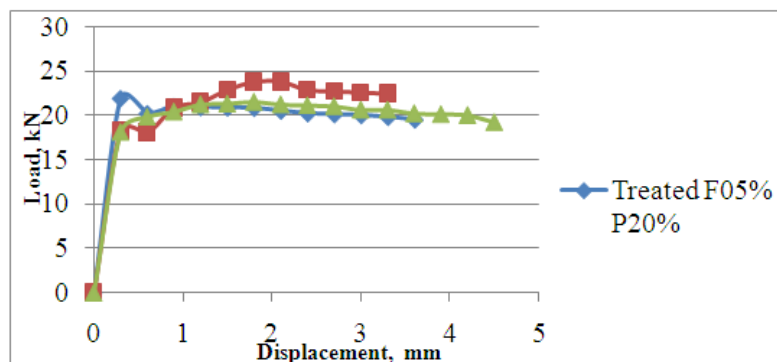
The tensile properties of untreated and treated composites at different percentages of fiber and filler contents are shown in Fig. 10. Comparison of the untreated fiber composites, with the acid-treated fiber composites on observation indicate that there is no much variation in the tensile load. The composition of F10% P15% treated and untreated composites sustain the load of 15.6kN and 15.4kN respectively. This is due to the well segregation of the filler and fiber particles with the matrix and also the interfacial bonding between the fiber and matrix is high. Un-treated composites sustain more load in the order of their composition F10% P15% as first, F05% P20% as second and F15% P10% as the last compared to the treated composites again in the order F10% P15%, F15% P10%, F05% P20% respectively. The results indicate that, increase in tensile strength in treated fiber content composite assumed to be due to the increase in fiber percentage which resists the pull out.

### 3.1.2 Effect of Load on Compressive Strength of Natural Composites



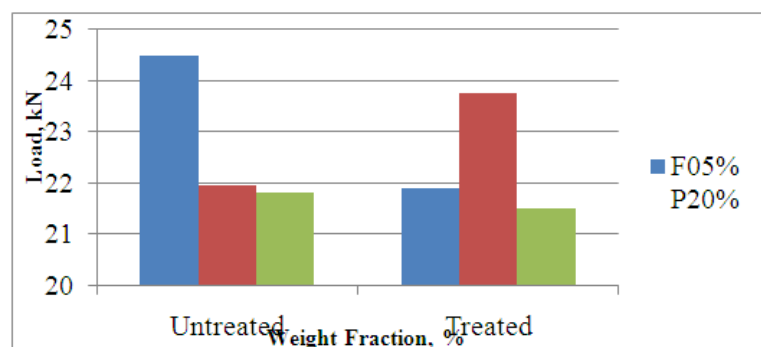
**Fig. 11** Effect of Untreated fiber and untreated filler content on the compressive strength of natural composites

The compression strength of un-treated composite at three different percentage compositions of fiber and filler content is shown in the above Fig. 11. It is observed from the figure that 20% of the betel palm filler content composite exhibited high compressive load of 24.5kN and more deformation. After reaching the yield load of about 17kN, the composites start to deform at faster rate. This situation is assumed to be due to the betel palm filler content particles strengthening the interface adhesion with the matrix and fiber materials, high fiber matrix compatibility and wetting [27]. And also presumed that the matrix material which is distributed over the surface of the solid particles of the untreated fiber which gives high brittleness to the composites.



**Fig. 12** Effect of Treated fiber and untreated filler content on the compressive strength of natural composites

In Fig. 12 shows the relation between the load and displacement for treated composite of different combinations under compressive load. The Fig. 12 clearly shows that load bearing capacity of the composite with treated 10% fiber content is comparatively higher than the other two composites which sustained a load of 23.75kN and its compressive strength is also higher than the rest of the composites. It may be due to high fiber-matrix compatibility, good fiber-matrix interaction.

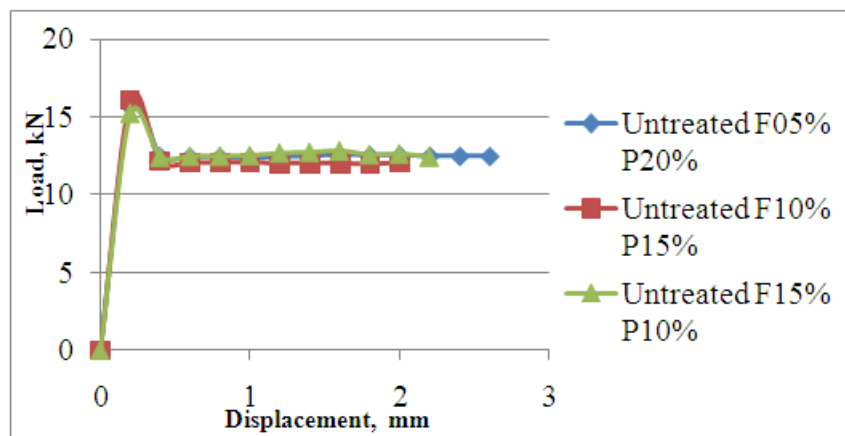


**Fig. 13** Comparison of compressive strength of un-treated and treated Specimen of three different combinations

The compressive strength of three different combinations of natural composites both un-treated and treated is shown in the Fig.13 The un-treated composite with 05% fiber content observed to be having more compressive strength compared to the treated ones. This might be due to the chemical treatment effect on the fiber content. Hence the composite with treated fiber content is exhibiting decrease in compressive strength. The composite with un-treated content of composition (F05% P20%) shows more load absorbing capacity compared to the treated composite of composition (F05% P20%). This might be due to the betel palm filler content particles strengthening the interface adhesion with the matrix and fiber materials, high fiber matrix compatibility and wetting.

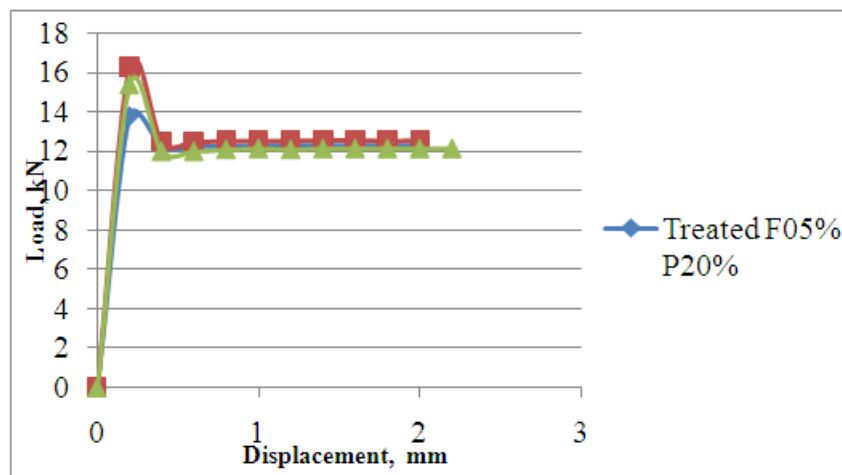
### 3.1.3 Effect of Load on Flexural Bending Strength of Natural Composites

The flexural strength of un-treated composite at three different percentage compositions of fiber and filler content is shown in the Fig. 14. The figure clearly indicates that, the variation in weight fraction of filler contents does not have greater effect on the load bearing capacity and the ability to withstand bending of the composites. The composite with F10% P15% shows maximum flexural load of 16.1kN and less deformation and F05% P20% composition composite shows comparatively less load and more deformation



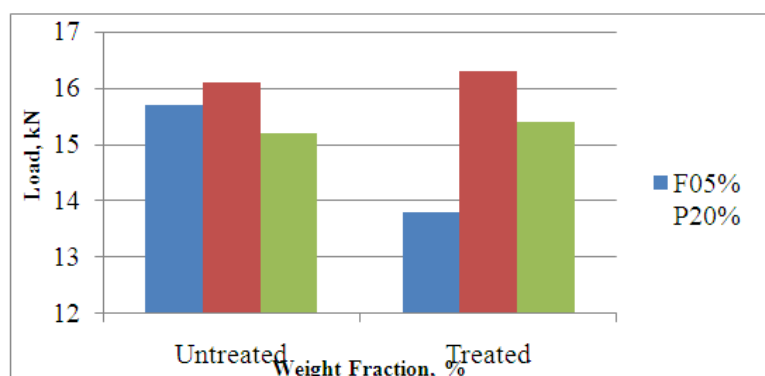
**Fig. 14** Effect of Un-treated fiber content on the flexural strength of natural composites

It may be due to the reason that the improper segregation of the fiber and filler particles with the matrix material. The composite with composition of F15% P10% has shown more deformation at the yield point than the other two composites. This might be due to the reason that the fiber will deform more compare to the composite with more percentage of betel palm powder as filler. The upper portion of composite will first undergo compression and bottom portion of the composite will then deform under tension [4].



**Fig. 15** Effect of Treated fiber and untreated filler content on the Flexural strength of natural composites

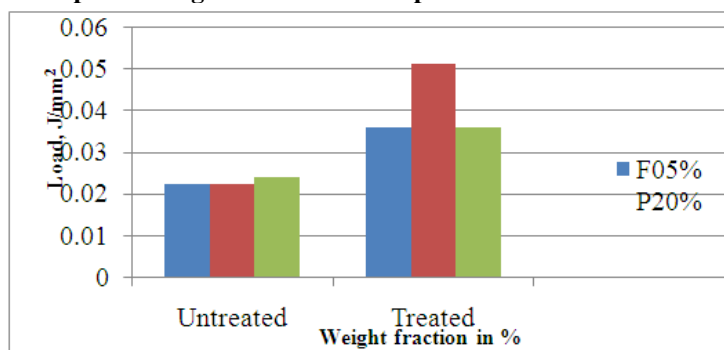
The Fig.15 shows the results of flexural strength testing of chemical treated specimens with different combination of composites. Fig. 5.8 shows that flexural strength increases with increase in Areca fiber content composite. The flexural strength decreases with increase in filler percentage. It was observed that 10% volume of treated fibers composite had a higher flexural strength than 05% & 15% treated composites due to high fiber-matrix compatibility, good fiber-matrix interaction & wetting. It is reasonable that enhanced fiber-matrix interaction due to high fiber-matrix compatibility and alkali treatment at 10% fabric content will lead to an increased transfer of stress from matrix to fibers and thus flexural strength increases. At 10% volume of treated fibers composite, value of the flexural strength was found to be higher and optimum than the untreated composites. This was because alkali treatments have been proven effective in cleaning fiber's surface by removing impurities from fibers, decreasing moisture sorption, enabling mechanical bonding and thereby improves matrix reinforcement interaction. Thus the alkali treatment enables and improves the fiber fitness, adhesive characteristics of the surface of the areca fibers, fiber-matrix polar interaction & wetting, hence surface offers a good fiber-matrix interface adhesion and an increase in the mechanical properties [27, 24].



**Fig. 16** Comparison of flexural strength of un-treated and treated Specimen of three different combinations

In Fig.16 shows the treated fiber having a more flexural load and deformation compared to the Untreated ones. From the Fig 5.9 it is observed that, the composition of F10% P15% Untreated and Treated composites have higher flexural load than other two composites. At 10% volume of treated fibers composite, value of the flexural strength was found to be higher and optimum than the untreated composites. This may be due to alkali treatments that had been proven effective in cleaning fiber's surface by removing impurities from fibers, decreasing moisture sorption, enabling mechanical bonding and thereby improves matrix reinforcement interaction. Thus the alkali treatment enable and improves the fiber fitness, adhesive characteristics of the surface of the areca fibers, fiber-matrix interaction & wetting, hence surface offers a good fiber-matrix interface adhesion and an increase in the mechanical properties [27, 24].

### 3.1.4 Effect of Load on Impact Strength of Natural Composites



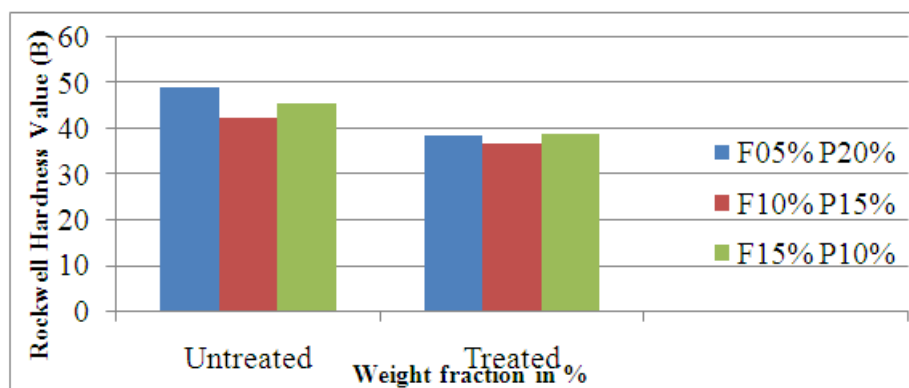
**Fig. 17** Variation of impact strength of the untreated and treated three different combination natural composites

It clearly shows the comparable results of impact strength for un- treated and treated of three different combination composites. Generally impact strength found to increase with the increase of the fiber content and the maximum impact value was observed in the untreated fiber content of 15%. In case of treated combination it was observed that 10% of fiber content of the composite had higher values of the impact strength than 05%, and 15% volume of treated fiber composites. Higher impact strength of treated composites is due to a better



mechanical interlocking of the fiber-matrix, which results in the fracture of fiber at the crack-plane with less fiber pullout. As the alkali treatments have been proven effective not only in cleaning fiber's surface by removing impurities & hemicellulose from fibers but also will render the fiber surface coarser leading to better interface and interlocking between fibers and matrix blend [27]. From the above result 20% filler content of treated and untreated composites have lesser impact strength is due to the presence of so many filler ends in the composites, which could cause crack initiation and hence potential composite failure [20].

### 3.1.5 Effect of Chemical Treatment on the Hardness Value of Natural Composites



**Fig. 18.** Variation of Hardness value of the untreated and treated composites for three different combinations

From Fig.18 it can be observed that the hardness value increases with increase in filler content of composite. This is due to proper distribution of filler material; due to interaction of the filler with fiber in the interfacial bonding the ductile viscous is turned to brittle in nature. This is causing a continuous increase in the hardness with the increase in filler content. The 10% fiber content composite has shown a lower trend in hardness. This is due to the fact that the fiber becomes the predominant than the base material and as the percentage of fiber increases, the interaction between the fibers inside the composite increases i.e. there will be higher fiber to fiber contact which leads to poor interfacial bonding between the fiber and the matrix. Due to this poor interfacial bonding effective load transfer may not take place and leads to quick failure and such reduction in strength may be attributed to increasing porosity and air void which brought about insufficient compaction of the high fiber content mixture. The untreated fiber content composite shows maximum hardness value i.e., 49 compared to the treated composite. This might be due to the presence of high loading solid particles embedded with untreated areca shell fibers.

**Table 5** Comparison Of Commercial Nuwood With Untreated And Treated Areca Shell Fiber And Areca Palm Powder – Epoxy Resin Natural Composites

Composite	Tensile Strength in N	Compressive strength in N	Flexural strength in N	Impact strength in J/mm <sup>2</sup>	Hardness in (RHNB)
<b>Untreated Areca Fiber And Areca Palm Powder</b>					
Untreated F5% P20%	15200	24500	15700	0.0225	49
Untreated F10% P15%	15400	22000	16100	0.0225	42.5
Untreated F15% P10%	15100	21800	15200	0.0243	45.5
<b>Treated Areca Fiber And Untreated Areca Palm Powder</b>					
Treated F5% P20%	15200	21900	13800	0.03625	38.5
Treated F10% P15%	15600	23750	16300	0.051225	37
Treated F15% P10%	15500	21500	15400	0.036225	39
Commercial Nuwood	2200	2000	225	0.189	2

## IV. Conclusion

Based on the results of the experimental investigation the following conclusions are drawn.

- The amount of areca shell fiber content positively affects the tensile strength of composites. The treated specimen with F10% P15% composition found to have a greater tensile load of 15.6kN and tensile strength of 0.123kN/mm<sup>2</sup>
- The compressive load of the untreated specimen with composition F05% P20% shown greater value of 24.5kN and greater compressive strength of 0.145kN/mm<sup>2</sup>
- The flexural load of the composites increases with increase in the amount of Areca shell fiber content. The treated specimen with F10% P15% composition found to have more flexural load of 16.3kN and Flexural strength of 0.100kN/mm<sup>2</sup>

- The treated composite specimen with F10% P15% composition observed to be sustaining higher impact strength of 0.051225 J/mm<sup>2</sup> compared to F05% P20% and F15% P10% composition specimens
- Hardness increases with increase in betel palm powder content. Composites with F05% P20% Untreated composition as shown maximum hardness of 49 (HV+30) compared to F10% P15% and F15% P10% compositional specimens
- The specimen with composition of F10% P15% (Treated) shown 1.3% increase in tensile strength compared to F10% P15% (untreated)
- The specimen with composition of F05% P20% (un-treated) shown 4% increase in compression strength compared to F10% P15% (treated)
- The specimen with F10% P15% (Treated) composition found to possess 1.5% increase in flexural strength compared to F10% P15% (Untreated)
- The specimen with composition of F15% P10% (Untreated) shown 58% decrease in impact strength compared to F10% P15% (Treated)
- The composite specimen with F05% P20% (un-treated) shown 21% increase in hardness value compared to F15% P10% (treated) combination composites

### References

- [1]. "ASM Handbook for Composites", ASM International Committee, Volume 21, 2001, pp. 1-2605.
- [2]. Prof Pandey P C., "Composite Materials", Dept of Civil Eng, IISc, Bangalore. syllabus version 2.0 - 17, August 2004.
- [3]. Abdul Khalil H P S, Firoozian P, Bakare I O, Hazizan Md. Akil and Ahmad Md. Noor., "Exploring Biomass Based Carbon Black as Filler in Epoxy Composites: Flexural and Thermal Properties", Materials and Design, 31, 2010, pp. 3419-3425.
- [4]. Alamari H and Low I., "Mechanical Properties and Water Absorption Behaviour of Recycled Cellulose Fibre Reinforced Epoxy Composites", Polymer Testing, 31, (2012), pp.620-628.
- [5]. Ali J Salaman., "Tensile and Impact Properties of Polystyrene Matrix Composites Reinforced by Palm Natural Fibers And Carbon Fibers", Academic Research International, Vol. 3, No. 2, September 2012, pp. 114-116.
- [6]. Arun Kumar Rout and Alok Satapathy., " Study on Mechanical and Tribo-Performance of Rice-Husk Filled Glass-Epoxy Hybrid Composites", Materials and Design, 41, (2012), pp. 131-141.
- [7]. Cheng Jung Lina, Salim Hiziroglu, Shu Min Kana and Hsien W., "Manufacturing Particle Board Panels from Betel Palm (Areca catechu Linn.)", Journal of Materials Processing Technology, 197, 2008, pp. 445-448.
- [8]. Dhanalakshmi Sampathkumar, Ramadevi Punyamurthy, Srinivasa Venkateshappa C, and Basavaraju Bennehalli., "Effect of Chemical Treatment on Water Absorption of Areca Fiber", Journal of Applied Sciences Research, 8(11), 2012, pp. 5298-5305.
- [9]. Fatima S and Mohanty A R., "Acoustical and Fire-Retardant Properties of Jute Composite Materials", Applied Acoustics, 72, 2011, pp. 108-114.
- [10]. Hayes B S and Gammon L M., "Optical Microscopy of Fiber-Reinforced Composites", ASM International, [www.asminternational.org](http://www.asminternational.org), 2010.
- [11]. Jinchun Zhu, Huijun Zhu, James Njuguna and Hrushikesh Abhyankar., "Recent Development of Flax Fibres and their Reinforced Composites Based on Different Polymeric Matrices", Open Access Materials, 6, 2013, pp. 5171-5198.
- [12]. Joshi S V, Drzal L T, Mohanty A K and Arora S., "Are Natural Composites Environmentally Superior to Glass Fibre Reinforced Composites?", Composites: Part A, 35, 2004, pp. 371-376.
- [13]. Manjunath B H and Prahlad Rao K., "Influence of Fiber/Filler Particles Reinforcement on Epoxy Composites", Vol. 3, Issue 3, May-Jun 2013, pp.1147-1151.
- [14]. Mohan Kumar G C., Member IAENG, "A Study of Short Areca Fiber Reinforced PF Composites", Vol II, WCE 2008, July 2008, pp. 3-7.
- [15]. Mwaikambo L Y and Ansell M P., "The Effect of Chemical Treatment on the Properties of Hemp, Sisal, Jute and Kapok Fibres for Composite Reinforcement" 2<sup>nd</sup> International Wood and Natural Composites Symposium, June 28-29, 1999 in Kassel.
- [16]. Naveen P N E, Yasaswi M and Prasad R V., " Experimental Investigation of Drilling Parameters on Composite Materials", IOSR Journal of Mechanical and Civil Engineering (IOSRJMCE), ISSN : 2278-1684, Volume 2, Issue 3 (Sep-Oct. 2012), pp. 30-37.
- [17]. Oladele I O, Omotoyinbo J A and Adewara J O T., "Investigating the Effect of Chemical Treatment on the Constituents and Tensile Properties of Sisal Fibre", Journal of Minerals & Materials Characterization & Engineering, Vol. 9, No.6, 2010, pp.569-582.
- [18]. Omar Faruk, Andrzej K. Bledzki, Hans-Peter Fink and Mohin Sain., "Composites Reinforced With Natural Fibers", Progress in Polymer Science 37 : 2012, pp 1552- 1596.
- [19]. Penpun Wetvitayaklung, Thawatchai Phaechamud, Chutima Limmatvapirat, Sindhchai and Keokitichai., "A Study of Antioxidant Capacity in Various Parts of Areca Catechu L", Naresuan University Journal, 14 (1), 2006, pp. 1-14.
- [20]. Ramachandra Reddy G, Ashok Kumar M and Chakradhar K V P., " Fabrication and Performance of Hybrid Betel Nut (Areca catechu) Short Fiber/ Sansevieria Cylindrica (Agavaceae) Epoxy Composites" International Journal of Materials and Biomaterials Applications, 1 (1), 2011, pp. 6-13.
- [21]. Ratna Prasad A V and Mohana Rao k., "Mechanical Properties of Natural Fiber Reinforced Polyester Composites", Materials and Design 32 2011, pp. 4658-4663.

Ramesh B T. "Investigation and Study of Mechanical Properties of Areca Shell Fiber and Palm Powder Natural Composites." IOSR Journal of Mechanical and Civil Engineering (IOSR-JMCE), vol. 15, no. 6, 2018, pp. 62-73.

